Czech Technical University in Prague
Faculty of Electrical Engineering

Doctoral Thesis

Ing. Michal Voldán

Prague, March 2023

Czech Technical University in Prague
Faculty of Electrical Engineering
Department of Measurement

Advances in Acoustic Thermometry

Doctoral Thesis

Ing. Michal Voldán

Supervisor:	doc. Ing. Antonín Platil, Ph.D.
Supervisor-Specialist:	Dr. Ing. Libor Husník
Study programme:	DSP - P2612, Electrical Engineering and Informatics
Branch of study:	2601V006, Measurement and Instrumentation

Prague, March 2023

Declaration

I declare that I elaborated this thesis on my own and that I mentioned all the information sources that have been used in accordance with the Guideline no. 1/2009 for adhering to ethical principles in the course of elaborating an academic final thesis.

In Prague on …… ……

Michal Voldán

Acknowledgements

All the material and measurements were mostly provided by and done in the laboratories of the Czech Metrology Institute. I would especially like to thank my supervisor doc. Ing. Antonín Platil, Ph.D. for leadership and patience. I would like to express my gratitude to Dr. Ing. Libor Husník for his constant encouragement, insightful comments, and technical support and for always being available for advice and discussions. Many thanks to Dr. Roberto Maria Gavioso and Dr. Daniele Madonna Ripa for patient training in primary acoustic thermometry and for lending the spherical resonator, their friendship and helpful advices. I thank Dr. Ing. Radek Strnad, PhD. for his honest, objective and ruthless criticism of all the technical shortcomings found during the development of the practical acoustic thermometer. I thank Ing. Jan Kučera, Ph.D. for all advice related to the SW solution in the LabView environment. The biggest thanks go to my wife Markéta for her great patience and immense support throughout my studies and to my son Vilém for his patience while I was writing my doctoral thesis at home. Part of the research described in Chapter 5.1 was funded by the SGS17/192/OHK4/3T/13 grant project, covered by the Czech Technical University in Prague. The research described in Section 5.2.1 was partially funded by the 18SIB02-RMG4 Researcher Mobility Grant (RMG) project, covered by the Euramet (see [1]).

Abstract

This thesis deals with the theory and practice of temperature measurement using acoustic waves. The temperature metrology in the Czech Republic is briefly described, and then principles of existing primary thermometers are presented along with the thermometer using sound. Following short introduction to the principles and methods of acoustic gas thermometry, the development of the practical acoustic thermometer is described and complemented by measurement results and total measurement uncertainty budget. In the second part of the thesis, the primary acoustic gas thermometry efforts with an objective of returning the kelvin unit realisation back to Czech Republic are shown.

At the beginning of the work, the practical acoustic thermometer uses the simple impulse-echo method to determine the time of flight of short 75 kHz acoustic bursts travelling through a waveguide in order to determine the speed of sound and calculate the temperature of the environment around the stainless-steel waveguide. After the initial calibration, the mechanical stability of employed transducer is enhanced by the lid, fixing all the mechanical parts of thermometer together and allowing work with monatomic gas. Improvement in shielding and grounding allowed the influence of frequency to be measured. The analysis of the results of these measurements led to a change in the working frequency and a subsequent change of the used waveguide. The efficiency of an interpolation was then tested, leading to ten-times enhancement in time measurement resolution. In order to make the system portable, originally static measurement system was replaced by a combination of waveform generator with oscilloscope. Finally, a comprehensive temperature- and pressure- dependence measurement was performed in the range of (-80 to 220) °C, showing the upper temperature limit of the system. Last section dedicated to the total measurement uncertainty estimations suggests that the length determination remains the largest measurement uncertainty contributor. It is typical for practical acoustic thermometers and probably causes the deviation between measured thermodynamic temperature and temperature of standard platinum resistance thermometer. The thermometer prototype is unique in its design in which one electrostatic transducer (in this case one measuring microphone) is used both to transmit and receive acoustic signal without the need of complex supporting electronics or time synchronisation between signals.

Another objective (in Section 5.2.1) was to assemble the high-temperature apparatus in the Italian Metrological Institute INRiM and to perform the acoustic measurement at the elevated pressure above 430 K to obtain an isotherm and to show the effectiveness of this apparatus and acoustic gas thermometry at high temperatures. After the description of the system, results of preliminary acoustic measurements during assembling the apparatus, followed by acoustic measurements in Ar gas up to 550 K and the isotherm at 294 K between 100 kPa and 430 kPa are shown, demonstrating the potential of high temperature acoustic gas thermometry.

In addition, the corresponding training in INRiM allowed the beginnings of acoustic gas thermometry at Czech Metrology Institute, with the preliminary measurements described in Section 5.2.2. All the control and measurement applications in this research were created in the LabView environment.

Keywords: acoustic thermometry, temperature measurement, thermodynamics, kelvin, AGT, PAT

Abstrakt

Tato práce se zabývá teorií a praxí měření teploty pomocí akustických vln. Stručně je popsána metrologie teploty v České republice a následně jsou představeny principy stávajících primárních teploměrů spolu s teploměrem, který k měření teploty využívá zvuk. Po krátkém seznámení s principy a metodami akustické plynové termometrie je popsán vývoj praktického akustického teploměru, spolu s výsledky měření a celkovým rozpočtem nejistot měření. V druhé části práce jsou prezentovány snahy o primární akustickou plynovou termometrii s cílem vrátit realizaci jednotky kelvin zpět do České republiky.

Praktický akustický teploměr na začátku práce používá jednoduchou metodu impuls-echo k určení doby průletu krátkých 75 kHz akustických pulzů, procházejících vlnovodem za účelem určení rychlosti zvuku a výpočtu teploty v okolí tohoto vlnovodu z nerezové oceli. Po úvodní kalibraci je mechanická stabilita použitého měniče zvýšena víkem, které spojuje všechny mechanické části teploměru k sobě a umožňuje práci s jednoatomovým plynem. Díky zlepšení stínění a zemnění systému se stalo možným přesně změřit vliv frekvence. Analýza výsledků tohoto měření pak vedla ke změně pracovní frekvence a následné změně použitého vlnovodu. Poté byla testována účinnost interpolace, což vedlo k desetinásobnému zlepšení rozlišení měření času. Aby byl systém přenosný, byl původní statický měřicí systém nahrazen kombinací signálového generátoru a osciloskopu. Nakonec bylo provedeno rozsáhlé měření teplotní a tlakové závislosti v rozsahu (-80 až 220) °C, což ukázalo i maximální měřitelnou teplotu systému. Poslední část věnovaná odhadům celkové nejistoty měření naznačuje, že určení délky zůstává největším příspěvkem nejistoty měření. To je typické pro praktické akustické teploměry a pravděpodobně způsobuje odchylku mezi naměřenou termodynamickou teplotou a teplotou etalonového platinového odporového teploměru. Prototyp teploměru je unikátní konstrukcí, využívající elektrostatický měnič, který umožňuje použít jeden mikrofon pro vysílání i příjem akustického signálu bez nutnosti využití složité podpůrné elektroniky nebo časové synchronizace mezi signály.

Dalším cílem (v části 5.2.1) bylo sestavení vysokoteplotní aparatury v italském metrologickém institutu INRiM a provedení akustického měření při zvýšeném tlaku nad 430 K pro získání izotermy a demonstrace účinnosti této aparatury a akustické plynové termometrie při vysokých teplotách. Po popisu systému jsou uvedeny výsledky předběžných akustických měření v průběhu sestavování aparatury, následovaných měřeními v argonu do 550 K a izotermou při 294 K mezi 100 kPa a 430 kPa, prokazující potenciál vysokoteplotní akustické plynové termometrie.

Související stáž v institutu INRiM navíc umožnil zavedení koncepce akustické plynové termometrie v Českém metrologickém institutu s předběžnými měřeními popsanými v části 5.2.2. Všechny řídicí a měřicí aplikace v rámci této práce byly vytvořeny v prostředí LabView.

Klíčová slova: akustická termometrie, měření teploty, termodynamika, kelvin, AGT, PAT

Table of Contents

Czech Technical University in Prague 2
Table of Contents 7
List of Figures 9
List of Tables 13
List of Symbols and Abbreviations 14
1. Introduction 16
2. State-of-the-Art 20
2.1. The Most Advanced Primary Thermometry Methods 20
2.1.1. Johnson Noise Thermometer 20
2.1.2. Dielectric-Constant Gas Thermometer 22
2.1.3. Doppler-Broadening Thermometer 23
2.1.4. Acoustic Gas Thermometer 24
2.1.4.1. Motivation for high-temperature AGT 29
2.1.4.2. Practical AGT 30
3. Objectives of the doctoral thesis 33
4. Selection of usable methods 34
4.1. The use of an electrostatic actuator (PAT) 34
4.2. The impulse echo method of sound velocity measurement in hollow waveguides (PAT) 34
4.3. Localization of the measurement region (PAT) 35
4.4. The temperature computation from PAT measurement using air media 35
4.5. Fitting of acoustic radial modes (AGT) 35
4.6. Thermal boundary layer correction (AGT) 36
5. Practical part 38
5.1. Practical Acoustic Thermometer (PAT) 38
5.1.1. Single transducer ultrasonic thermometer using an electrostatic actuator 39
5.1.1.1. The initial burst 39
5.1.1.2. Waveguide 40
5.1.1.3. Measurement and data acquisition 42
5.1.1.4. Data evaluation 42
5.1.1.5. Results of the initial calibration 45
5.1.1.6. Interpolation 46
5.1.2. PAT working with argon gas 47
5.1.2.1. Shielding and grounding 49
5.1.2.2. Influence of working frequency 51

5.1.2.3. Time resolution and interpolation test 53
5.1.3. Transformation to a portable system 56
5.1.3.1. Vacuum and gas tightness 58
5.1.3.2. Temperature and pressure characterisation 60
5.1.3.3. Total measurement uncertainty budget 65
5.2. Primary acoustic gas thermometry 70
5.2.1. Extending the high temperature range of acoustic gas thermometry 70
5.2.1.1. Description of the HTAGT apparatus 70
5.2.1.2. Measurement equipment 74
5.2.1.3. Measurement procedure 74
5.2.1.4. Measurement at ambient air 75
5.2.1.5. Measurement in vessel using argon gas and strip heaters 76
5.2.1.6. Measurement in the vacuum furnace 78
5.2.2. Primary Acoustic Gas Thermometry at CMI 82
5.2.2.1. Measurement in ambient environment 84
5.2.2.2. Measurement in climatic chamber 86
6. Conclusion 88
6.1. Meeting the objectives 88
6.2. Further work 88
7. References 89
8. List of Publications 98
8.1. Author’s publication on the topic of the doctoral thesis 98
8.2. Other author’s publications 98
9. Annex A – Uncertainty budgets for practical acoustic thermometer 99

List of Figures

Figure 1: A traceability chain for contact thermometry in the CMI – a state before kelvin redefinition. Red parts are not implemented. 17

Figure 2: A traceability chain for non-contact thermometry in the CMI – a state before kelvin redefinition. Red parts are not implemented. 18

Figure 3: A proposed change in the Czech temperature traceability scheme 19

Figure 4: Temperature range covered by primary thermometers in 2005 as mentioned in [46] 20

Figure 5: The switching correlator noise thermometer, "PA" denotes the preamplifier [47] .. 21

Figure 6: Schematic sketch of the DCGT system at PTB in 2011 [55] 23

Figure 7: Sketch of an essential part of the DBT gas sample and example of an absorption spectrum for $H_2{}^{18}O$. "Ph" denotes the photodiode [58]. 24

Figure 8: Principal scheme of the acoustic and electromagnetic acquisition systems as used in [64] 28

Figure 9: Differences between the ITS-90 and relative acoustic gas thermometry results for thermodynamic temperatures obtained at various laboratories [86] 29

Figure 10: PAT designs including localization of the measurement area as proposed in [89] 31

Figure 11: Example of LabView application, fitting the quadratic function to acoustic resonance mode 36

Figure 12: Principal scheme of the measurement arrangement 38

Figure 13: The excitation pulse recorded by the oscilloscope (blue) and samples of the pulse as designed by the LV application (red), published in [109]..... 39

Figure 14: Dependence of the surface temperature on the top of the waveguide on the nominal temperature in the furnace, estimated measurement uncertainty included (as published in [109]). 41

Figure 15: Waveguide design, dimensions in mm 41

Figure 16: The amplitude spectrum of the measured data before (in blue) and after (in red) high-pass filtering, as published in [109] 43

Figure 17: The typical average signal after mean filtering of the data that was obtained at the nominal temperature of 38.5 °C [109] 43

Figure 18: Typical average signal details at 38.5 °C [109]..... 44

Figure 19: Autocorrelation of the typical average signal at 38.5 °C (Detail corresponding to the echoes from the waveguide) [109]..... 44

Figure 20: Measurement setup as drawn in Figure 12. Left: Waveguide with actuator and microphone, partially immersed in the bath. Middle: Detail of actuator inside the waveguide. Right: Supplementary electronics. Figure published in [109]..... 45

Figure 21: Discrepancy between theoretical and measured τ as published in [109]..... 45

Figure 22: differences between the reference thermometer's temperature and that calculated using the fitting function, published in [109]..... 46

Figure 23: Standard deviation of the τ values that were measured and interpolated at each calibration point (ACF is the autocorrelation), published in [109]..... 47

Figure 24: The lid of the practical acoustic thermometer in the CMI 48

Figure 25: The sequential development of the mechanical part of a prototype of a practical acoustic thermometer 49

Figure 26: The original voltage source and modulator assembly (left) was supplemented with shielding and upgraded with a commercially available modulator (right) 49

Figure 27: Change in the electrode connection (from left to right) 50

Figure 28: The result of the calibration of PAT with Ar media at atmospheric pressure in the range of (-20 to 90) °C 50

Figure 29: Dependence of the standard deviation of the measured τ on the frequency of the excitation pulse. Measurement in calibration bath at 0 °C in blue, measurement in melting point of ice (0 °C) in red. 51

Figure 30: Calculation of suitable frequency for the PAT from the waveguide dimensions 52

Figure 31: Dependence of the standard deviation on the frequency of the excitation pulse, Ar gas filling, standard atmosphere, 23 °C 52

Figure 32: Dimensions of the waveguide used to move the minimum working frequency out of the audioband 53

Figure 33: PAT in Isotech ITL M17701 calibration furnace 54

Figure 34: Theoretical temperature resolution dependence on the temperature for different time resolution values from 0.015625 to 10 (in μs) that can be achieved by the interpolation process 54

Figure 35: Dependence of the standard deviation of the measured data on the interpolation factor n 55

Figure 36: The example of measured τ data after implementation of interpolation to the acquisition routine, nominal temperature 49.8 °C 55

Figure 37: Equipment used in the portable version of PAT 56

Figure 38: LabView measurement procedure used for static PAT system 57

Figure 39: LabView measurement procedure used for portable PAT system 58

Figure 40: The mobile gas management system connected to PAT 59

Figure 41: Evacuation curves 60

Figure 42: Detail of evacuation curves 60

Figure 43: Postprocessed recording of pressure and τ – measurement at -40 °C nominal 61

Figure 44: Surface temperature measurement, temperature in bath is 220 °C nominal 61

Figure 45: Results of temperature and pressure characterisation (from -80 °C to 60 °C) 62

Figure 46: Results of temperature and pressure characterisation (from 80 °C to 200 °C) 62

Figure 47: Results of temperature and pressure characterisation at 220 °C 63

Figure 48: Pressure dependence of measured Δτ at -60 °C nominal temperature 63

Figure 49: Measurement results for pressure close to 100 kPa 64

Figure 50: Measurement results for pressure close to 100 kPa and temperature range (-80 to 180) °C 64

Figure 51: Error of fitting 65

Figure 52: Total measurement uncertainty 68

Figure 53: Fitting error supplemented with measerement uncertainty 68

Figure 54: HTAGT apparatus 70

Figure 55: Cross-section of the copper resonator, dimensions in mm 71

Figure 56: Quasi-spherical resonator. MW denotes microwaves, MP microphones, TH thermometers and GP the gas port 71

Figure 57: Acoustic waveguides used for acoustic transmission between the laboratory and the resonator 72

Figure 58: Gas-tight vessel consisting of a cylindrical copper body (on left), the vessel (with cavity) inserted into the main furnace (on right) 72

Figure 59: (Left) Linear fit to three selected microwave estimates of the internal radius of the cavity in vacuum between 448 K and 510 K. (Right) Absolute residuals of the linear fit. 73

Figure 60: Heating furnace used in HTAGT research, placed on a framed supporting structure. 73

Figure 61: The initial measurement setup, resonator on the table 74

Figure 62: Simple calculations to estimate frequencies of other radial modes from known positions of (0,2) mode. (0,2) mode always found by scanning the spectrum. 75

Figure 63: (0,4) mode shape comparison for various initial configurations, selection of receiver microphone and gain of amplifier 75

Figure 64: Relative fitting precision of seven purely radial modes, (0,2) to (0,8) in air at ambient temperature and pressure with 40 cm long, 1.6 mm i.d. acoustic waveguides for several different microphonic configurations 76

Figure 65: Strip heaters mounted on the vessel 77

Figure 66: Normalised spectrum of (0,2) mode measured at various temperatures using strip heaters and ambient temperature 77

Figure 67: Comparison of spectral images for modes (0,2) to (0,10) 78

Figure 68: Vacuum and pressure tight connections to microphones and acoustic waveguides 78

Figure 69: SPRT inserted in a thermometry well that is sealed across the head flange of the furnace. 79

Figure 70: Surface thermometer attached to the flange of the furnace 79

Figure 71: Pressure (left plot) and temperature (right plot) records during 24 hours of acoustic measurements near 550 K, 270 kPa. A large thermal gradient in the order of 2 K persists along the whole record. 80

Figure 72: Relative fitting precision of three radial acoustic modes in Ar near 550 K, 270 kPa. 80

Figure 73: Relative difference of the speed of sound estimated from three radial acoustic modes in Ar near 550 K, 270 kPa 81

Figure 74: Relative differences of the speed of sound estimated from three radial acoustic modes in Ar at 294 K between 100 kPa and 430 kPa 82

Figure 75: Sketch of the spherical resonator at CMI 83

Figure 76: Characterization of the resonator on the Zeiss XENOS coordinate measuring machine 83

Figure 77: Spatial visualisation of the measured deviations from sphericity values of both hemispheres of the resonator 84

Figure 78: Measurement setup for AGT experiment in ambient environment at CMI 84

Figure 79: Resonance mode (0,2) at ambient temperature 85

Figure 80: Calculated speed of sound values for 8 resonance radial modes at ambient temperature 85

Figure 81: Spherical resonance cavity in climatic chamber 86

Figure 82: Relation between speed of sound and temperature of IPRT 86

Figure 83: Differences in temperature calculated from speed of sound and temperature measured by IPRT 87

Figure 84: Differences in temperature calculated from speed of sound (at modes (0,5) and (0,6)) and temperature measured by IPRT 87

List of Tables

Table 1: Sensitivity coefficients of thermometer to main uncertainty contributors 66

Table 2: Gas limit composition declared by the manufacturer and calculated molar mass of resulting mixture for this composition 66

Table 3: Calibration results of Rosemount 2088 pressure transducer 67

Table 4: Measurement uncertainty budget for the nominal temperature of -80 °C 69

Table 5: Measurement uncertainty budget for the nominal temperature of -80 °C 99

Table 6: Measurement uncertainty budget for the nominal temperature of -60 °C 100

Table 7: Measurement uncertainty budget for the nominal temperature of -40 °C 101

Table 8: Measurement uncertainty budget for the nominal temperature of -20 °C 102

Table 9: Measurement uncertainty budget for the nominal temperature of 0 °C 103

Table 10: Measurement uncertainty budget for the nominal temperature of 20 °C 104

Table 11: Measurement uncertainty budget for the nominal temperature of 40 °C 105

Table 12: Measurement uncertainty budget for the nominal temperature of 60 °C 106

Table 13: Measurement uncertainty budget for the nominal temperature of 80 °C 107

Table 14: Measurement uncertainty budget for the nominal temperature of 100 °C 108

Table 15: Measurement uncertainty budget for the nominal temperature of 120 °C 109

Table 16: Measurement uncertainty budget for the nominal temperature of 140 °C 110

Table 17: Measurement uncertainty budget for the nominal temperature of 160 °C 111

Table 18: Measurement uncertainty budget for the nominal temperature of 180 °C 112

Table 19: Measurement uncertainty budget for the nominal temperature of 200 °C 113

Table 20: Measurement uncertainty budget for the nominal temperature of 220 °C 114

List of Symbols and Abbreviations

AGT	Acoustic Gas Thermometer / Thermometry
e	An elementary charge equal to $1.602176634 \cdot 10^{-19}$ C
N_A	Avogadro constant equal to $6.02214076 \cdot 10^{23}$ mol^{-1}
BB	Blackbody
k_B	Boltzmann constant equal to $1.380649 \cdot 10^{-23}$ $J \cdot K^{-1}$
BIPM	Bureau International des Poids et Mesures
C	Capacitance in F
CSPRT	Capsule SPRT
CEM	Centro Español de Metrología
Z	Complex impedance in Ω
CCT	Consultative Committee for Thermometry
CMI	Czech Metrology Institute
DCGT	Dielectric-Constant Gas Thermometer / Thermometry
DBT	Doppler-Broadening Thermometer / Thermometry
κ_{eff}	Effective compressibility in Pa^{-1}
V	Electrical voltage in V
k	Expansion factor dependent on the probability distribution, dimensionless
FP	Fixed Point
F	Force in N
f	Frequency in Hz
HTFP	High-Temperature FP
HTSPRT	High-Temperature SPRT
IPRT	Industrial Platinum Resistance Thermometer
IR	Infrared
ITS-90	International Temperature Scale of 1990
INRiM	Istituto Nazionale di Ricerca Metrologica
JNT	Johnson's Noise Thermometer / Thermometry
LNE	Laboratoire national de métrologie et d'essais
LSSPRT	Long Stem SPRT
ρ	Mass density in $kg \cdot m^{-3}$
MSSPRT	Metal-Sheathed SPRT
R	molar gas constant in $J \cdot mol^{-1} \cdot K^{-1}$
M	Molar mass in $kg \cdot mol^{-1}$
NIST	National Institute of Standards and Technology
NMI	National metrology institute
NPL	National Physical Laboratory
ε	Permittivity in $F \cdot m^{-1}$
PTB	Physikalisch-Technische Bundesanstalt
h	Planck constant equal to $6.62607015 \cdot 10^{-34}$ $J \cdot Hz^{-1}$
PRT	Platinum Resistance Thermometer
PSD	Power Spectral Density
PAT	Practical acoustic thermometer
p	Pressure in Pa

RAM	Random Access Memory
ϑ	Relative capacitance change, dimensionless
ε_r	Relative permittivity, dimensionless
RMS	Root Mean Square
c	Speed of light in a vacuum equal to 299792458 $m \cdot s^{-1}$
u	Speed of sound in $m \cdot s^{-1}$
SPRT	Standard Platinum Resistance Thermometer
α_0	Static dipole polarizability in $C \cdot m^2 \cdot V^{-1}$
SI	Système international (d'unités)
CODATA	The Committee on Data for Science and Technology
ε_0	The electric permittivity of the vacuum equal to $8.8541878128 \cdot 10^{-12}$ $F \cdot m^{-1}$ with a standard uncertainty of $0.0000000013 \cdot 10^{-12}$ $F \cdot m^{-1}$
γ	The ratio of heat capacities c_p/c_V, dimensionless
t_{90}	The temperature as assigned by the ITS-90, in °C
T_{90}	The temperature as assigned by the ITS-90, in K
T	The thermodynamic temperature in K
t	The thermodynamic temperature, in °C
TC	Thermocouple
τ	Time delay between arrival of two reflected acoustic pulses in seconds
TOF	Time of Flight
TPW	Triple Point of Water
$\Delta\nu_{Cs}$	Unperturbed ground-state hyperfine transition frequency of the caesium 133 atom, equal to 9192631770 Hz
λ	Wavelength in m
u_0	Zero-pressure speed of sound in $m \cdot s^{-1}$

1. Introduction

Temperature is one of the most frequently measured quantities in the world. It influences practically all known phenomena and therefore temperature interferes with almost all human activities. Temperature measurement is an integral part of health, military and manufacturing industries and is an essential quantity in every field of scientific activity. In specific areas of business relations or as the decisive variable in some litigation, a precise temperature measurement is of utmost importance.

The accuracy and correctness of measurement result are influenced by factors such as the properties of the sensor, parameters of the surrounding environment, the suitability of the thermometer application and how the traceability of the measurement is provided.

According to [2], the temperature measurement traceability is defined as the uninterrupted sequence of transmission of the kelvin unit, from the highest metrology quality temperature standard, through temperature standards of lower metrological quality up to "working thermometers" (thermometers that are not used as standards for another thermometry calibration).

Until 20th May 2019, the definition of the unit of kelvin was the following: "The kelvin, unit of thermodynamic temperature, is the fraction 1/273.16 of the thermodynamic temperature of the triple point of water." [3]. The TPW (Triple Point of Water, details in [4]) is usually maintained as a fundamental part of the ITS-90 (the International Temperature Scale of 1990, described in [5] and [6]) realisation. Thus, before the 20th of May 2019, the realisation of the TPW was the realisation of the kelvin unit at the same time.

The temperature defined by the ITS-90 is derived from phase transitions of 17 defining FPs (Fixed Points) and methods of interpolation between them. As mentioned in [7], the ITS-90 assigns the exact value of the T_{90} temperature to the realisation (represented by inherent phase transition) of each defining FP with zero uncertainty. Most FP cells have the form of metal or quartz-glassed cells containing an extremely pure substance, kept in a graphite crucible. Unique construction with a well allows immersing the thermometer into the cell. More about the fixed points of ITS-90 can be found in [8] and [9].

Methods of interpolation include specific instruments and mathematical equations for conversion of properties of used equipment to temperature. The group of interpolation instruments includes SPRTs (Standard Platinum Resistance Thermometers) and reference radiation thermometers (more about radiation thermometry in [10]). An overall description of techniques for approximating the ITS-90 can be found in [11].

SPRTs commonly operate in the range of -189.3442 °C to 660.323 °C, HTSPRTs (High-Temperature SPRTs, of different construction) usually operate up to 961.78 °C. The platinum resistance thermometer is based on the temperature dependence of the electrical resistance of the high-purity platinum resistance element. The platinum wire is freely wound on a solid carrier (usually in SPRT) or a thin deposited Pt layer is enclosed by the insulation powder (usually in IPRTs – Industrial Platinum Resistance Thermometers, that don't follow requirements for use of ITS-90 mathematical procedures given in [12]; computations and operation according to the IEC 60751 standard [13] are provided) and protected by quartz glass or metal-sheathed stem of the thermometer. For constructional, principal and other details of SPRTs and HTSPRTs see [12]. In spite of the fact that PRTs are subject to many uncertainty sources and need to be carefully maintained, the flexibility of construction and achievable measurement uncertainty in the order of mK make it the most frequently used type of thermometer in the world (see [12], [13] and [14]).

Thermocouples (TC) usually operate in the range of (-196 to 1600) °C, using the Seebeck's effect. The principle of operation and uncertainty budget components are described in [15] and [16]. The construction of industrial base metal thermocouples differs from more precise

sensors, that are made of noble or pure metals [17] and from self-validating realisations [18]. From measured thermoelectric voltage, the temperature is usually calculated according to standards ČSN EN 60584-1 and ČSN EN 62460. In 2019, the wire-bridge method of thermocouple calibration (described in [19]) was removed from the Czech national traceability scheme, because of missing metrological traceability to the kelvin unit realisation. Thermocouples are not mentioned by the ITS-90 as the interpolation instrument.

Measurement at higher temperatures is covered by radiation thermometry and radiation laws (see [10]). Radiation thermometers are implemented in the form of measurement chains and usually, DC voltage or directly temperature is measured. Radiation thermometers can theoretically operate in a wide range from 0 K up to the highest possible temperature limited by the speed of light, practically in the range of (-50 to 3000) °C [20]. Detailed information about uncertainty and error sources associated with radiation thermometers is given in [21] and [22].

Generally, the interpolation instrument serves to provide measurement traceability for thermometers of lower metrological quality and secondary (see [19] and [23]) and alternative (e.g. Xe [24], CO_2 [25], SF_6 [26]) fixed points. It is calibrated by direct measurement in a set of FPs, selected following the ITS-90 recommendation (see [12]), according to the chosen temperature subrange. To get a satisfactory description of the thermometer behaviour at intermediate temperatures, the interpolating procedure of ITS-90 is then applied to the measured data.

The traceability of the temperature measurement in the Czech Republic is formally divided into "National Temperature Standard for Contact Thermometry" (see Figure 1) and "National Temperature Standard for Non-Contact Thermometry" (Figure 2). The temperature range of the ITS-90 realisation is (-189.3442 to 1084.62) °C.

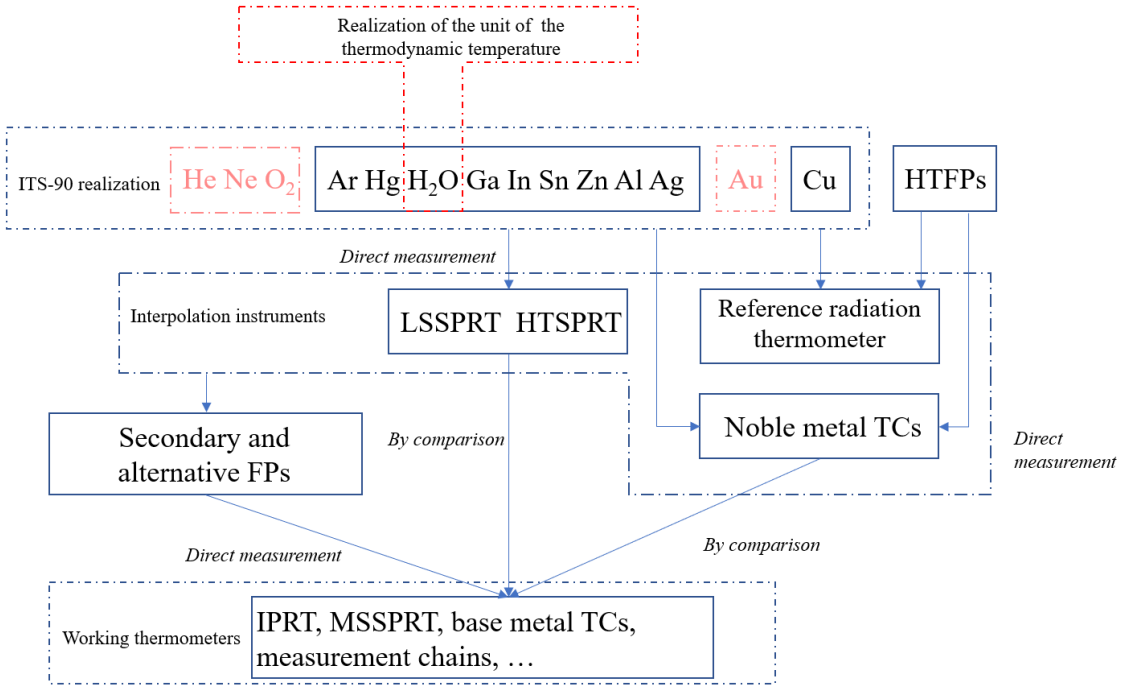

Figure 1: A traceability chain for contact thermometry in the CMI – a state before kelvin redefinition. Red parts are not implemented.

The current traceability chain for the non-contact thermometry (Figure 2) is based on the FP of Cu and HTFPs of Fe-C (1153 °C), and Co-C (1324 °C). More information about FPs for radiation thermometry can be found e.g., in [27]. The instrument (calibrated in these FPs) uses extrapolation to provide measurement traceability at higher temperatures. Through reference

radiation sources, secondary FPs and pyrometers, the traceability is provided further to transfer standards and working thermometers. More about radiation thermometers (RT) and blackbodies (BB) can be found in [10].

A set of HTFPs that can be further implemented such as Pd-C (1492 °C) is described e.g. in [28], [29], [30] and [31] and are currently in production, to allow extension of measurement capabilities and measurement of *T* at temperatures up to 1492 °C (as mentioned in [32]).

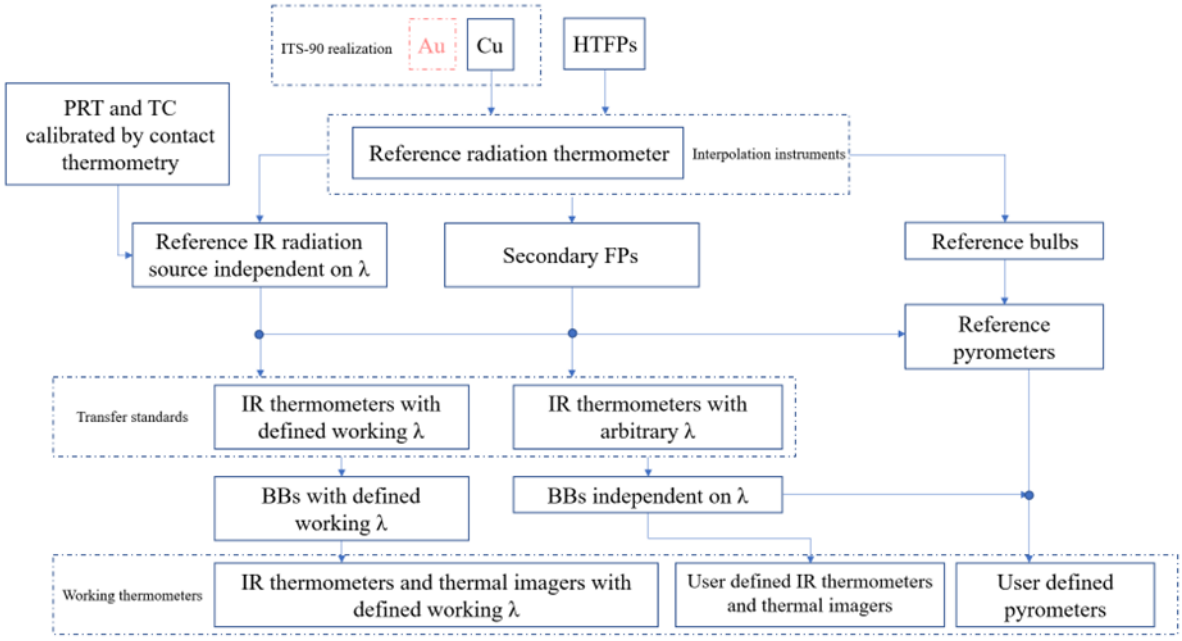

Figure 2: A traceability chain for non-contact thermometry in the CMI – a state before kelvin redefinition. Red parts are not implemented.

Fixed point temperatures were determined based on long-term research using fundamental methods of temperature measurement thus applying only to ideal high-purity FPs. Real fixed point material is not perfectly clean and contains undesirable contaminants. The temperature measurement cannot be performed on the surface of the material under phase transition but at a certain depth at which the transition temperature is affected by the hydrostatic pressure. The temperature of the fixed point is not constant during the phase transition, but slightly changes, so it is necessary to select the appropriate part of the measured (freezing or melting) curve to be used for the calibration. More about impurities can be found in [33] and hydrostatic pressure corrections are discussed in [34]. T-T_{90} differences of the ITS-90 FPs as estimated by the BIPM can be found in [35]. None of the conventional thermometers measures the temperature directly but t_{90} must be computed from other temperature-dependent property of the thermometer. Many influencing factors affect the measurand and properties of these thermometers, that additionally drift with time, thus periodical calibration is necessary. Following the ITS-90 procedures brings uncertainty sources e.g. in the form of so-called *non-uniqueness* and *sub-range inconsistency* (explained in [36]).

The previous kelvin definition was based on the TPW artifact. The temperature of the TPW realisation depends on several specific conditions, such as isotopic composition and impurities of the specific water, filled in the cell (effect of impurities on TPW realisation is discussed e.g. in [37], [38] and [39], the hydrostatic pressure effect in [40]). The artefact is not accessible to everybody, its properties slightly drift with time and one of the special procedures for the creation of the ice mantle in the TPW is necessary to be followed (details in [4]).

All these complications represent significant hindrance to metrological procedures and therefore on 20th May 2019, a new definition of the kelvin unit based on the defined and fixed value of the Boltzmann constant k_B came into force [3]. The definition can be found in [41] and

is the following: "**The kelvin, symbol K, is the SI unit of thermodynamic temperature. It is defined by taking the fixed numerical value of the Boltzmann constant k_B to be $1.380649 \cdot 10^{-23}$ when expressed in the unit $J \cdot K^{-1}$, which is equal to $kg \cdot m^2 \cdot s^{-2} \cdot K^{-1}$, where the kilogram, metre and second are defined in terms of h, c and $\Delta\nu_{Cs}$.**" The new definition is invariant with space and time and independent of any substance, material, a technique of realisation, temperature or temperature range. As mentioned in [7], it includes the equivalence of the thermal energy E and temperature T, as expressed by the Maxwell-Boltzmann equation

$$E = k_B T. \quad (1)$$

The ITS-90 does not include the thermodynamic temperature unit realisation anymore. Therefore, it is necessary to provide traceability of the ITS-90 for calibration of the practical temperature scale (ITS-90) and HTFPs (Figure 3 shows a detail of the changed part in the traceability chain that is planned for the Czech Republic) by the development of the primary thermometry.

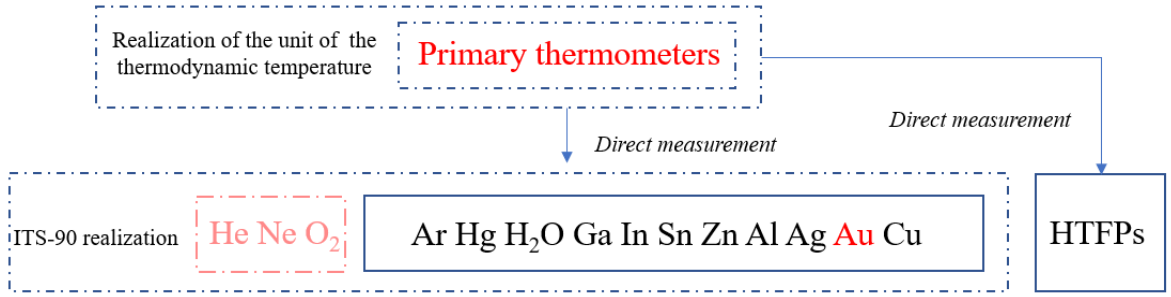

Figure 3: A proposed change in the Czech temperature traceability scheme

Ambitions to restore the kelvin unit realisation in the Czech Republic led to efforts to develop primary thermometry at the CMI. A brief description of selected primary thermometry methods forms the beginning of the theoretical part of this thesis (in Section 2), together with the description of an acoustic approach to temperature measurement.

Descriptions of major operational principles and corresponding phenomena can provide a way to understand the uniqueness, complexity and potential of acoustic thermometry to the reader in a separate subsection 2.1.4.

Unfortunately, nowadays no primary thermometer is capable of (and designed for) calibrating conventional thermometers. This fact gave birth to several "practical" prototypal realisations of thermodynamic thermometer setups, mainly at the cost of higher measurement uncertainty. Even if of lower metrological quality, such a thermometer can offer calibration to common sensors with traceability to the kelvin unit.

The main objective of the work described in this thesis is therefore the development of the practical acoustic thermometer. Here the practicality is understood as suitability for calibration of common contact thermometers using temperature enclosures that are common in industrial and temperature calibration laboratory practice and portability of the device. The resulting form created at CMI fits industrial calibration furnaces and baths. The uniqueness of this thermometer is in its design, allowing the microphone to serve both as a transmitter and receiver simultaneously, removing the uncertainty contribution connected to time synchronization between the transmitter and receiver channel.

Section 4 presents the specific methods used in practical part. The practical part (Section 5) then describes the development of Practical Acoustic Thermometer (PAT) and Acoustic Gas Thermometer (AGT) at CMI as well as achievements in the field of high-temperature AGT, reached as a part of an internship at INRiM in 2021.

Finally, the Conclusion in Section 6 summarizes the results, discusses the contribution of the mentioned work, the advantages and disadvantages of selected solutions and presents plans for further development of acoustic thermometry in CMI conditions.

2. State-of-the-Art

A practical realisation of the kelvin unit can be made via "primary methods", defined by fundamental mathematical formulas that connect thermodynamic temperature with a given Boltzmann constant value. As mentioned in [42], the so-called primary thermometers are based on sufficiently understood and characterized physical systems, for which state equations can be written explicitly without the need of introducing unknown temperature-dependent parameters. According to [32], primary thermometers can directly measure *T* (absolute primary thermometer), or the ratio of two thermodynamic temperatures (relative primary thermometer). The most developed and understood methods of primary thermometry are Johnson Noise Thermometer (JNT), Dielectric Constant Gas Thermometer (DCGT), Doppler Broadening Thermometer (DBT), and Acoustic Gas Thermometer (AGT) and at higher temperatures absolute and relative radiometry (see [43]). Measurements and methods involved in k_B determination for the 2017 CODATA adjustment can be found in [44] (for 2010 in [45]). Temperature ranges of primary thermometers (the latest found from 2005, but nowadays probably very similar) as given in [46] are shown in Figure 4.

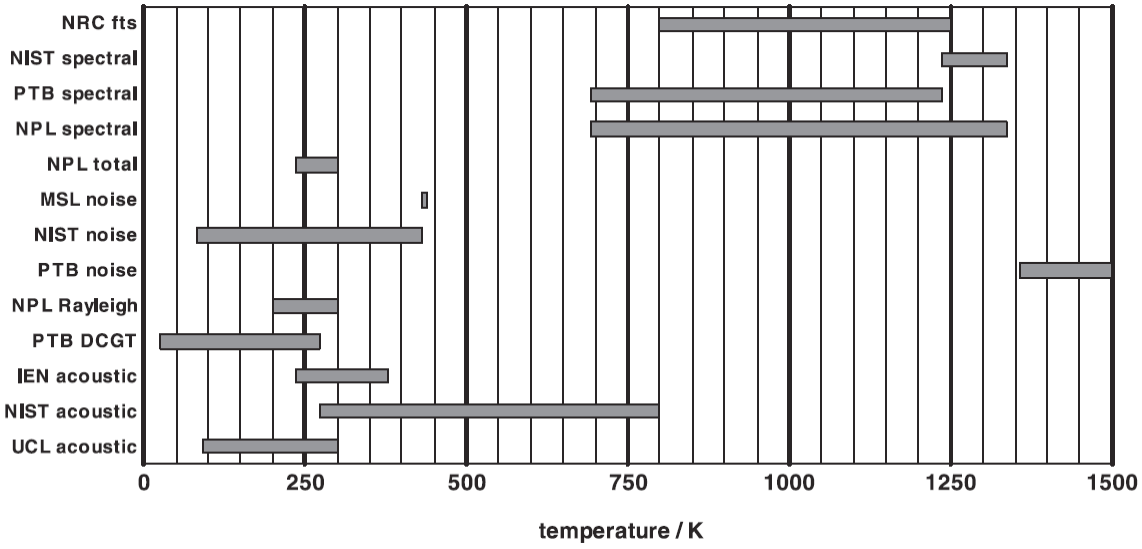

Figure 4: Temperature range covered by primary thermometers in 2005 as mentioned in [46]

The term "fts" used in Figure 4 is optical thermometry based on Fourier spectroscopy, "spectral" is spectral and "total" is total radiation thermometry, "noise" is JNT, "Rayleigh" is thermometer based on Rayleigh scattering, acoustic is AGT (all these methods are described in [46]).

2.1. The Most Advanced Primary Thermometry Methods

Several primary thermometers are already well described in accessible articles and are present at a number of European NMIs with different stages of development and temperature range.

2.1.1. Johnson Noise Thermometer

Johnson Noise Thermometer is characteristic by its purely electronic approach. It works with spontaneous thermal fluctuations of the electron gas in electrical conductors, known as Johnson noise. As mentioned in [47], the principle of operation is based on Nyquist's theorem, describing the relation between PSD of the noise across a resistor of impedance *Z* in thermal equilibrium with the surrounding environment at *T* as

$$d\overline{V_T^2} = 4hf\mathrm{Re}(Z)\left[\frac{1}{2} + \frac{1}{\exp\left(hf/k_B T\right) - 1}\right]df. \qquad (2)$$

The first term within the parentheses is equal to the zero-state energy of the system and when it is neglected, Eq. (2) can be approximated (for $f < 100$ MHz and $T > 25$ K) as

$$\overline{V_T^2} = 4k_B T R \Delta f \tag{3}$$

with the accuracy of approximation better than 0.0001 % [47]. Symbol R denotes here the electrical resistance in Ω. Johnson noise is "white" in this regime, i.e. PSD is not dependent on f, R and Δf and it is usually measured over limited bandwidth Δf at a resistor, typically with a nominal R value of 100 Ω. The simplest forms of JNT use (according to [48]) rearranged expression of Eq. (3) in the form of

$$T = \frac{1}{4k_B} \frac{\overline{V_T^2}}{R \Delta f} \tag{4}$$

to derive T from the measurement of the mean-square voltage at the resistor in defined Δf (that is usually assumed constant because of difficulties in bandwidth measurement) or from a comparison of mean-square noise voltage $\overline{V_T^2}$ measured at T and mean square noise voltage $\overline{V_{T_0}^2}$ measured at reference temperature T_0 as

$$T = T_0 \frac{\overline{V_T^2}}{\overline{V_{T_0}^2}} \frac{R(T_0)}{R(T)}. \tag{5}$$

Measured signals are typically at the level of units of μV RMS and therefore other noise sources can easily disrupt the measurement. Johnson noise is independent of all material properties of the sensor except its resistance. Sensors (optimally free of non-thermal noise) with R value independent on f, are four-wire connected to preamplifiers with complex design and of gain up to 10^6. Such low noise amplifiers must operate in wide Δf with high linearity and stability. The amplified signal is filtered by a bandpass filter that sets the operating Δf of the thermometer (typically from tenths of kHz up to units of MHz). The most common design of today's JNTs is a noise thermometer that uses a switching correlator (see Figure 5) to reduce the effect of uncorrelated amplifier input noise voltage and noise in lead-wires.

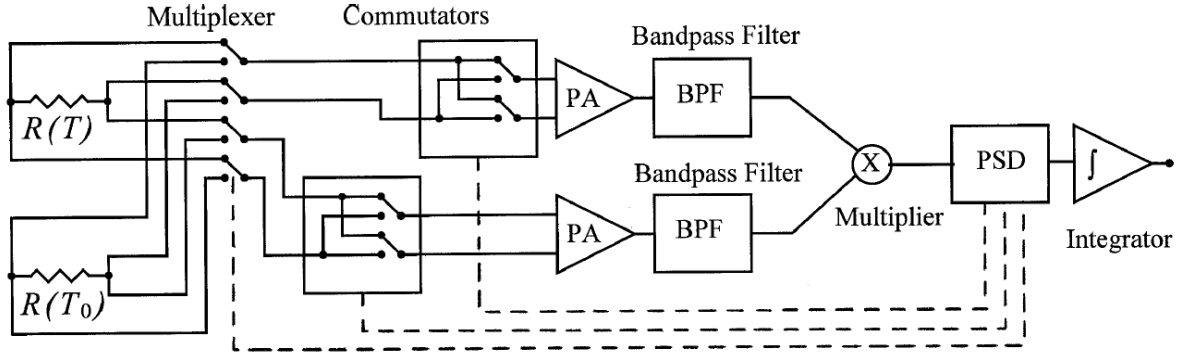

Figure 5: The switching correlator noise thermometer, "PA" denotes the preamplifier [47]

Two channels containing a preamplifier and filter are used for measurement on the same resistance ($R(T)$ or $R(T_0)$) selected by a multiplexer. As mentioned in [49], frequent switching eliminates the effects of drift of the thermometer gain and bandwidth drift. Outputs are then compared by a correlator to eliminate the noise of electronics. PSD is then computed from the output value that fluctuates around the expected value, thus long measurement time (tens of seconds for measurement uncertainty around 1 °C, tens of hours for uncertainty around 1 mK) is necessary. The use of an integrator with a low-pass (anti-aliasing) filter or digital averaging system is used as the best available averaging filter in terms of short response time in a given Δf. Commutators shown in Figure 5 serve to eliminate offset errors.

JNT has generally significant advantages compared to other primary methods. According to [49], the structure and size of the sensing probe are similar to conventional thermometers. Anyway, careful grounding and shielding must be performed. In practical realisations, sensing elements are formed by Josephson junctions or thin foil resistors with a low temperature coefficient of resistance. Current JNTs are capable of operation at temperatures from units of mK up to 1500 °C (as stated in [47]). In contrast with gas thermometry systems, JNT is not limited by the non-ideal properties of real gases [50]. JNT nonlinearity sources are discussed in [49]. Details of implementation in NIST and measurement uncertainty analysis can be found in [47]. An example of an uncertainty budget is shown in [51].

2.1.2. Dielectric-Constant Gas Thermometer

The basic idea of DCGT is to replace the density of gas ρ in the state equation with the electric permittivity of vacuum ε_0 and to measure this constant. According to [52], particles of ideal gas do not interact and behave like induced dipoles with static polarizability α_0. The equation of state can be expressed in the form of

$$p = k_B T \frac{\varepsilon - \varepsilon_0}{\alpha_0} \tag{6}$$

In real gas, interactions between particles must be considered by combining virial expansion of the state equation and the Clausius-Mossotti equation (details in [53]). The principle of DCGT operation in practice is explained in [54] as follows. The ε is determined from the measurement of capacitance, performed by a capacitor (filled between its electrodes with gas) at various pressures (to compute behaviour at zero pressure) and constant T. This process is known as the measurement of isotherms. The dependence of electrode geometry on pressure must be taken into account. According to [54], a capacitor consisting of cylindrical inner and outer electrodes with effective compressibility κ_{eff} (carefully computed by complex computer simulations from geometry and material properties of the capacitor) has this dependence linear and in the form of

$$C(p) = \varepsilon_r C(0)\left(1 + \kappa_{eff} p\right). \tag{7}$$

Therefore, now all NMIs with DCGT are using cylindrical measuring capacitors. The previous equation allows the determination of ε_{r} at a constant temperature. With relative capacitance change

$$\vartheta = \frac{(C(p) - C(0))}{C(0)} = \varepsilon_r - 1 + A_\varepsilon \kappa_{eff} p \tag{8}$$

and substitution $\mu = \vartheta/(\vartheta + 3)$, the approximation for p at fixed T is

$$p = A_1 \mu (1 + A_2 \mu + A_3 \mu + \cdots) \tag{9}$$

with

$$A_1 = \left(\frac{A_\varepsilon}{RT} + \frac{\kappa_{eff}}{3}\right)^{-1}. \tag{10}$$

R represents the molar gas constant and A_ε is the molar polarizability given by the relation

$$A_\varepsilon = \frac{N_A \alpha_0}{3\varepsilon_0}. \tag{11}$$

Other coefficients (A_2, A_3, ..) can be determined by fitting the data obtained by the measurement at constant temperature (e.g. in TPW cell). More details about the derivation of the working equation can be found in [54]. The advantage of DCGT is that ρ is determined *in-situ* via ε measurement so the ρ measurement (complicated in "dead areas", not exposed to measured temperature) and knowledge of the number of moles in the working volume is not necessary. Figure 6 shows a sketch of the DCGT system developed in the PTB and described in [55].

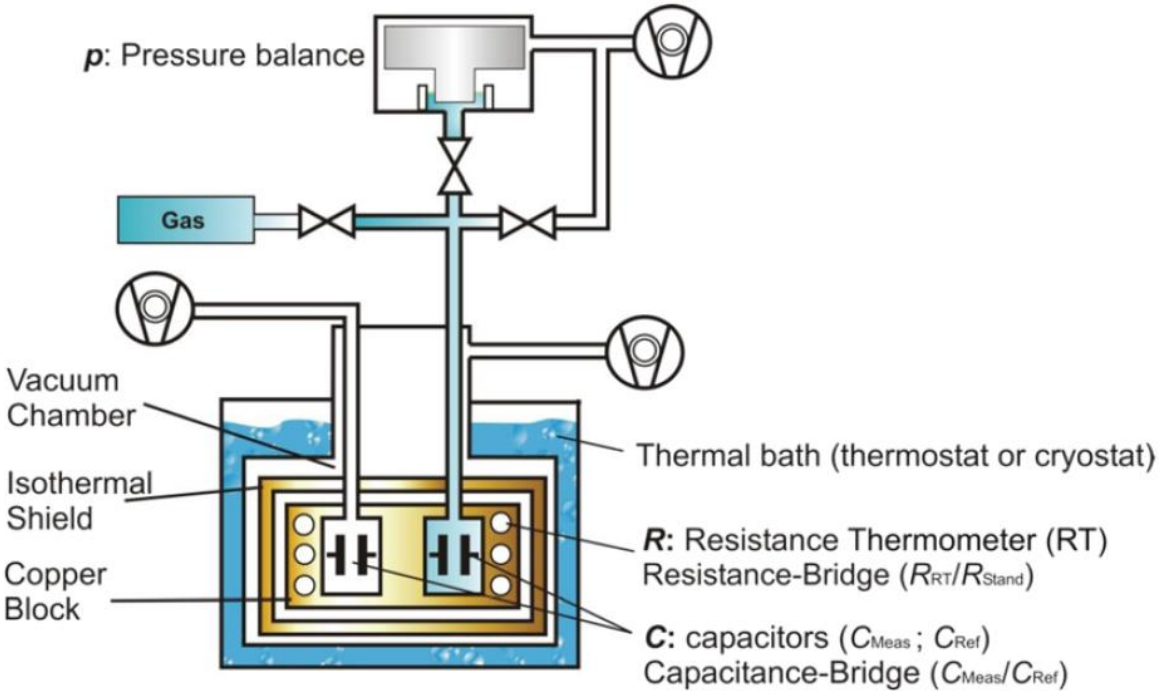

Figure 6: Schematic sketch of the DCGT system at PTB in 2011 [55]

The measuring system is vacuum-isolated from a large-volume (hundreds of litres) liquid-bath thermostat with temperature inhomogeneity and instability within 1 mK. Each capacitor is surrounded by a metallic pressure vessel that is thermally connected with supporting CSPRTs. Usually, tungsten carbide (TCA) or stainless steel (SS) electrodes with aluminium oxide isolation discs are employed (TCA has compressibility about 2x smaller than SS) in cylindrical capacitors. A very sensitive capacitance ratio bridge (with a resolution better than 10^{-9}) serves to measure ϑ as a function of p to determine the slope of isotherms. According to [56], He is the only working gas of polarizability known with sufficiently small uncertainty. The helium of 99.99999 % or better nominal purity is used as a dielectric in the measuring capacitor (on right). The gas handling system is controlled by three dry pumps (in Figure 6 sketched as three circles, connected to three different volumes). Because of the very small relative permittivity ε_r of helium, small capacitance changes are measured and therefore operation at high pressures (commonly up to 7 MPa) is necessary. Measurement uncertainty budgets can be found in [56] and [57]. At each pressure, the correction for κ_{eff} of capacitors is needed (procedure e.g. in [55]).

2.1.3. Doppler-Broadening Thermometer

According to [58], DBT (in [59] mentioned as "Doppler-broadened molecular spectroscopy") consists of retrieving the Doppler width from highly accurate observation of the spectral profile corresponding to a shape of the given atomic or molecular line in a gas sample at thermodynamic equilibrium. Involved experiments are in the linear regime of radiation-matter interaction. As mentioned in [60], from the analysis of an absorption profile, the strength of a given line, from which the transition dipole moment between two quantum states can be inferred. Also, the line centre frequency that gives information about involved energy levels can be detected. If the shape of a given line is recorded as a function of p, line broadening and shifting components can be determined. When the spectroscopic parameters of a particular line

of the specimen are known, then the absorber gas density can be accurately determined using laser absorption spectroscopy. The highest level of precision and accuracy for employed laser absorption spectroscopy in the linear regime of interaction should be followed (as stated in [58]). At low gas pressures, the main source of line broadening is the Doppler effect. This leads to the Doppler width of a spectral line, which links thermal energy to an optical frequency as follows:

$$\Delta\nu_D = \frac{\nu_0}{c}\sqrt{2\ln\left(2\frac{k_B T}{M}\right)}, \tag{12}$$

where $\Delta\nu_D$ is the Doppler half-width at half maximum, ν_0 is the line centre frequency, c is the speed of light and M is the absorber molecular mass. If ν_0 and M are known, T can be determined (see [60]). Figure 7 shows the sketch of an essential part of each DBT system and an example of an absorption spectrum for $H_2{}^{18}O$ gas, measured in [58] at a pressure of about 400 Pa.

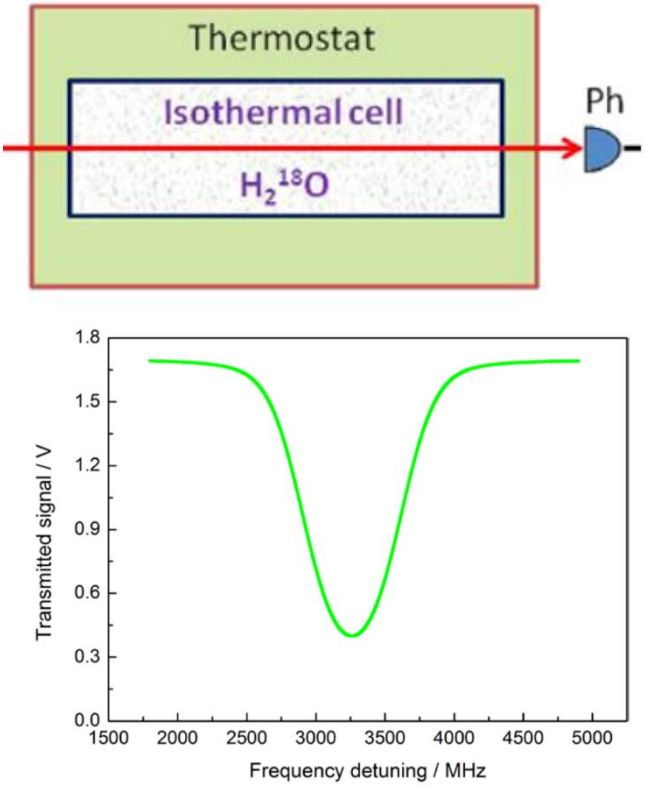

Figure 7: Sketch of an essential part of the DBT gas sample and example of an absorption spectrum for $H_2{}^{18}O$. "Ph" denotes the photodiode [58].

DBT is a relatively new method of T measurement that is (according to [61]) currently mostly limited by the uncertainty associated with the line shape model that is adopted for the nonlinear least-squares fits of experimental spectra. Details about line-shape approximation theory can be found in [60] and [61]. As mentioned in [60], several requirements must be fulfilled for a successful experiment. Generally, the spectral line must be isolated (thus the molecular target has to be as simple as possible), to avoid line interference effects and detection electronics should be highly linear and sensitive. In [58], proof-of-principle experiments were performed on NH_3 and CO_2 molecules and C_2H_2 in [62]. Components of measurement uncertainty budget are discussed in [58].

2.1.4. Acoustic Gas Thermometer

As explained in [63], the absolute AGT determines T from measurements of the speed of sound u in a low-density monatomic gas (of average molar mass equal to M). The method involves the measurement of the resonance frequencies of standing waves in cavities of simple geometry

(see [64]), made of stainless steel or copper (according to [45]). As mentioned in [65], principles of AGT are related to the basic formula, linking Laplace's definition of the zero-pressure speed of sound u_0 and T,

$$u_0^2(T) = \frac{\gamma RT}{M}, \tag{13}$$

where R is the molar gas constant. For a monatomic gas, the heat capacity ratio γ is equal to 5/3 and acoustic boundary layer corrections can be calculated with the 0.05 % accuracy. When real, non-monatomic gas is used, virial corrections depending on p must be applied to γ. These corrections must be calculated for each pressure or can be obtained by the measurement (see [44]).

The u in a real gas (described in [66]) is given as a function of ρ as follows:

$$\begin{aligned} u^2 = \left(\frac{\partial p}{\partial \rho}\right)_S &= u_0(1 + \beta_a \rho_n + \gamma_a \rho_n^2 + \cdots) \\ &= \frac{\gamma_0 k_B T}{M} + A_1(T)p + A_2(T)p^2 + \cdots, \end{aligned} \tag{14}$$

where S is the entropy, β_a and γ_a are the acoustic virial coefficients and u_0 is the value of the speed of sound at zero density that can be calculated as

$$u_0 = \frac{\gamma^{pg} RT}{M} \tag{15}$$

with γ^{pg} meaning the ratio of the isobaric and isochoric heat capacities for an ideal gas. β_a and γ_a are usually fitted to measurements of $u(p,T)$ using the equation form of

$$u^2(p,T) = \frac{\gamma_0 RT}{M}(1 + \beta_a p + \gamma_a p^2 + \ldots) \tag{16}$$

In practice, u_0 may be estimated by extrapolating to zero pressure the results of a set of measurements of $u(p)$ at different pressures along an isotherm (see [63] and [66]) or calculated from quantum mechanics and statistical mechanics (using a computer modelling). Alternatively, β_a and γ_a are independently known from theory with sufficient accuracy to correct Eq. (14) or Eq. (16), which is the case for He. Coefficients $A_1(T)$ and $A_2(T)$ are connected to the density virial coefficients and their temperature derivates.

For spherical or quasi-spherical geometry of resonator, the radial wave does not interact with any orthogonal angle, therefore the most accurate AGTs use one of these cavity shapes [59].

The speed of sound is not measured directly, but following [66], it can be calculated from the resonance frequencies of several acoustic modes in the resonance cavity as

$$f_n = \frac{u}{2\pi a_0} \times \frac{a_0}{a} z_n + \Delta f_n, \tag{17}$$

where a is the radius at pressure p, calculated (in [59]) as an effective radius $a = (a_x\, a_y\, a_z)^{1/3}$, a_0 is the zero-pressure radius, z_n is an eigenvalue (zeros of spherical Bessel function) known exactly, Δf_n is a sum of small (but important) correction terms and the subscript n indicates the mode of oscillation (for cavities having a spherical or quasi-spherical shape with internal radius a, the acoustic resonance frequencies $f_{0,n}$ of purely radial modes are identified by a single index n).

Several physical effects lead to relevant perturbations of the resonance frequencies, and only perturbed frequencies f'_n are experimentally accessible

$$f_n' = f_n + \sum \Delta f_n\,. \tag{18}$$

An acoustic model that is sufficiently comprehensive must compute and take into account the corresponding corrections. The thermal energy loss in the thin boundary layer on the interior surface of the cavity is the perturbing effect that is most important for radial acoustic modes. It is also typical practice to take into consideration the finite acoustic impedance of ducts, microphones, and shell vibrations from elastic modes propagating within the hollow cavity shell. The halfwidth g_n of a resonance curve, which is used to estimate the energy stored in the standing wave, is often a function of the same perturbing effects. The accuracy of determination of the speed of sound is indicated by the agreement between the values of g_n obtained from the experiment and those derived from the model [67][68].

Eq. (17) suggests that an accurate estimation of the cavity's internal diameter is needed. The full-dimensional characterisation of the resonator is usually achieved using coordinate measurement machines as shown in [69]. This technique replaced the procedure using gravimetric weighing (e.g., in [59]) or filling the resonator with liquid (of well-known ρ) and subsequent weighing of this liquid as mentioned in [63]. Full dimensional description can quantify the quality of manufactured cavity and provides information about corresponding uncertainty of inner radius determination but is valid only for a very limited temperature range.

The most practical way to determine inner dimensions at the current temperature and thermal expansion of the cavity is (as shown in [66]) to measure the cavity's microwave resonance frequencies

$$\langle f_N \rangle = \frac{cz_m}{2\pi a}, \tag{19}$$

where the index N generically summarizes the notation needed to distinguish the type, symmetry and order of TM and TE modes and c is the speed of light in the gas. The basic theory of microwave resonances in a spherical cavity can be found in [65]. Computation of the inner (nearly spherical) cavity volume V from microwave resonances can be done using the relation given in [63] as

$$c = \frac{n\langle f_\mathrm{m} - \Delta f_\mathrm{m} \rangle_p}{z_\mathrm{m}} (6\pi^2 V)^{1/3}. \tag{20}$$

f_m denotes the measured microwave frequency, n is the refractive index of the gas in the cavity at a pressure p, z_m is a mode-dependent microwave eigenvalue and $\langle f_\mathrm{m} - \Delta f_\mathrm{m} \rangle_p$ is the average of the corrected frequencies of the $(2l + 1)$ microwave modes that would degenerate in a perfect spherical cavity (l = 1, 2, 3, …). Index m denotes the mode of oscillation. Usually, only the lowest-order modes are used. The average frequency is sensitive to small, smooth deviations from a spherical shape in higher orders.

The lowest possible degeneracy of the electromagnetic normal modes of the cavity is triple, with corresponding notations TM_{1n} and TE_{1n}. The three resolved peaks of each mode are used to determine the arithmetic average in Eq. (19).

According to [45], the use of a quasi-spherical geometry for the shape of the resonance cavity would enhance the precision in determining microwave eigenfrequencies by removing the degeneracy associated with microwave eigenfunctions. It is explained in [70] as follows: “Previous acoustic studies of ITS-90 used resonators that were as spherical as possible; very small deviations of sphericity in all three measured Cartesian axes caused the overlapping of components of microwave modes. It complicated the measurement and resulted in higher uncertainty of the resonance frequency (f_m) measurement.”

Another discussion can be found in [66]. It says that a microwave measurement is simplified when a shape differs from spherical by just enough to enable separation of measured microwave modes, but not so much that the accurate calculation of the microwave and acoustic eigenvalues requires detailed measurements of the shape, i.e. that perturbation theory from which the

calculations are based is still applicable here. It is advantageous to have a form of a triaxial ellipsoid with axes in ratios $1 : (1 + \mathcal{E}_1) : (1 - \mathcal{E}_2)$, and with $0.0005 < \mathcal{E}_{1,2} < 0.001$, because for this case, values of z_{m} are known with extraordinarily small uncertainties (thanks to the analytical calculations of proper corrections made in [71] and [72]).

It was initially proposed in [73] that quasi-spherical shapes for resonance cavities may be used to improve the resolution of the triplets and the accuracy of their measurement. A detailed design of the quasi-spherical resonator can be found e.g. in [74] or [75].

The most relevant perturbation to the microwave frequencies accounts for the penetration of the electromagnetic field within the cavity wall, due to its finite electrical conductivity.

Due to thermal expansion and elastic compression, the dimensions of the cavity change with temperature and pressure. If an estimate of the thermal expansion coefficient α_{th} and the cavity's isothermal compressibility k_T are independently known, this variation can be corrected. Only the former correction matters, is relevant for thermometry applications, and microwave measurements in vacuum at various temperatures can accurately estimate it. Finally, for quasi-spherical cavities, an accurate estimation of the shape of the cavity is provided by the measurement of the relative separation of the frequencies of each resonance within a triplet. Calculating the appropriate geometrical perturbations and corrections may be done using this information to both f_n and $\langle f_N \rangle$ [67][68].

A microwave technique might be also used in combination with acoustic measurement simultaneously to ease the task of determining the inner cavity volume as a function of *T* and *p*. The most attractive feature of absolute AGT is shown in [63], where the following formula, connecting *c*, *u* and *T* is derived:

$$\left[\frac{f_n - \Delta f_n}{z_n}\frac{z_m c}{n\langle f_{\mathrm{m}} - \Delta f_{\mathrm{m}}\rangle_p}\right]^2 = \frac{5k_B T}{3m} + A_1(T)p + A_2(T)p^2 + \cdots, \tag{21}$$

thus, here the temperature is determined by the ratio (speed of sound)/(speed of light) which is proportional to ratios of measured frequencies: $k_B T \approx (3/5) \cdot m[f_{\mathrm{n}} z_m c/(z_n n f_{\mathrm{m}})]^2$. Dimensions and pressure appear here only in the form of corrections and f_{n} denotes measured acoustic resonance frequency. This brings the possibility for simultaneous acoustic measurement of the speed of sound and microwave measurement of current cavity dimensions.

As discussed in [70], an isotropic expansion of the resonator doesn't affect the (*u*/*c*) ratio value but anisotropic expansion does. The cavity dimensions must be stable at least over the period of every isotherm measurement. When the resonator is realised with poor geometry accuracy, additional parasitic resonances can be generated, which distorts the measurement result. The resonator is usually created by bolting quasi-hemispheres together. In [76], measured deviations from the sphericity of the spherical resonator are shown and discussed.

For thermometry applications, different cavity materials may be selected depending on the working temperature range, dimensions and type of thermostatic system. The large thermal and electrical conductivity of copper reduces heat gradients across the cavity and improves the accuracy of microwave measurements, making copper cavities the preferred choice in most cases. The quality factor of both acoustic and microwave resonances is increasing with a raising volume-to-surface ratio (i.e. larger cavities are better), reducing boundary layer and skin depth energy losses. On the other hand, the benefit of small cavities is that they can return to thermal equilibrium more rapidly after any significant changes in the temperature of the apparatus. Inner dimensions between 4 cm and 10 cm are typical.

The selection of gas is with respect to isotopic abundance, purity and cost. Over the time, these factors limited the selection to argon and helium-4 as mentioned in [44]. Molar mass *M* is determined from the measurements with a mass spectrometer (e.g., in [64]). The advantage of using helium (according to [44]) is that while boundary layer correction can be calculated for

both gases, the relative uncertainty in the correction for He is smaller than for Ar. In comparison with argon, u in helium is much more sensitive to impurities. The technique of flowing gas (see [70]) reduces possible contamination from outgassing of cavity material.

A relative determination of the thermodynamic temperature T with respect to some reference temperature T_{ref}, with $T_{ref} = T_{TPW} = 273.16$ K being the most common choice, is also possible by measuring the ratio $u_0(T)/u_0(T_{ref})$. Relative measurements require measuring ratios of lengths and frequencies. Noble gas impurities are acceptable for relative measurement, but M must not change during the measurement process (see [63]). In practice, T is determined by measuring the pressure dependence of the acoustic resonance frequencies f_n and microwave resonance frequencies f_m of the gas-filled cavity using a relation by [70]:

$$\frac{T}{T_{ref}} = \frac{\lim_{p\to 0}\left(\frac{f_n + \Delta f_n}{\langle f_m + \Delta f_m\rangle}\right)^2_T}{\lim_{p\to 0}\left(\frac{f_n + \Delta f_n}{\langle f_m + \Delta f_m\rangle}\right)^2_{T_{TPW}}} = \frac{\lim_{p\to 0}\left(\frac{u}{c}\right)^2_T}{\lim_{p\to 0}\left(\frac{u}{c}\right)^2_{T_{TPW}}}, \tag{22}$$

where Δf_n and Δf_m are corrections to the measured frequencies discussed in [70]. This approach (e.g., in [65]) brings elimination of the uncertainty of M determination. Relative AGT is usually used for (T-T_{90}) measurements and measurement of T of fixed point realisations. Relative AGT has the advantage that traceability to the units of length and time is no longer needed and several uncertainties, including those associated with κ_0/M which is assumed to remain constant as a function of temperature, cancel out as well as many instrumental uncertainties.

An example of the configuration allowing the simultaneous measurement of acoustic and microwave resonance modes can be found in [64] and is shown in Figure 8. Nowadays the lock-in amplifier is usually used instead of the part with synchronous detection and synthesizer.

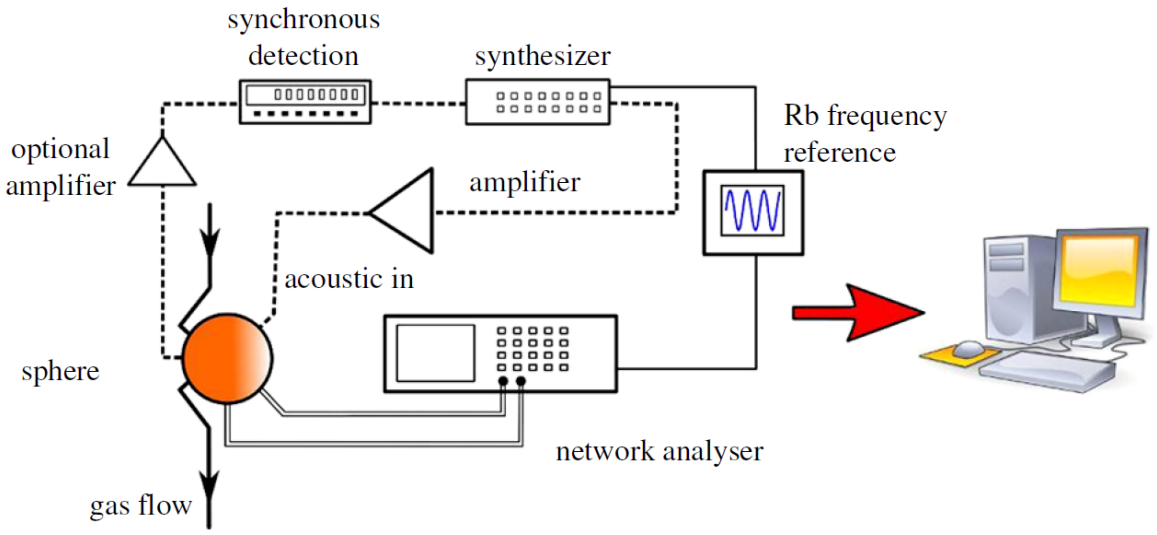

Figure 8: Principal scheme of the acoustic and electromagnetic acquisition systems as used in [64]

To excite and detect microwave modes, straight, loop or pin antennas can be used. Details of suitable microwave transducers and preamplifiers can be found e.g., in [66] and [76]. Details of involved acoustic and microwave transducers, cables, cryostat and gas handling system of AGT developed by NIST and LNE are provided e.g., in [70]. Another AGT designed in INRiM including measurement, analysis and corrections of microwave data as well as complex uncertainty analysis of the whole AGT system is described in [45] and [77]. Details of AGT by NPL are then shown in [78]. The uncertainty budget for the determination of the k_B using ^{4}He

gas in 2015 is shown in [44]. A number of error sources and corrections is also discussed in [65], [76] and [63].

According to [65], the main advantages of acoustic thermometry are its second-order dependence on p and the independence of u on the amount of gas medium. As mentioned in [63], the quasi-spherical cavity shape is not essential for accurate AGT but is the easiest to use when employing microwave dimensional measurement. A cylindrical AGT using longitudinal acoustic modes of the fixed-path-length cavity filled with argon can be combined with e.g., two-colour optical interferometry and achieve similar results as the "spherical AGT" described here. One of the cylinder length measurement principles is given in [79]. In addition, the imperfection in the cylinder shape does not affect the eigenvalues of the longitudinal modes in the first order of perturbation theory and thus a measurement of the average cavity length is sufficient for accurate AGT. Microwave measurements of the cylindrical cavity were realised in [80]. Examples of the system developed for k_B measurements with a cylindrical resonance cavity are described e.g., in [81] and [82].

2.1.4.1. Motivation for high-temperature AGT

Over three decades have passed between the adoption of the International Temperature Scale of 1990 (ITS-90) [83], which defines T_{90}, and the redefinition of the kelvin in 2019 [84], i.e., adoption of the thermodynamic temperature T scale in its final form. The AGT has importantly contributed to the determination of the differences ($T-T_{90}$) as shown in Figure 9. AGT data are the major source of information used to determine the exact value of the Boltzmann constant, which defines the kelvin [85], as no other primary thermometry method has been able to achieve a comparable level of accuracy.

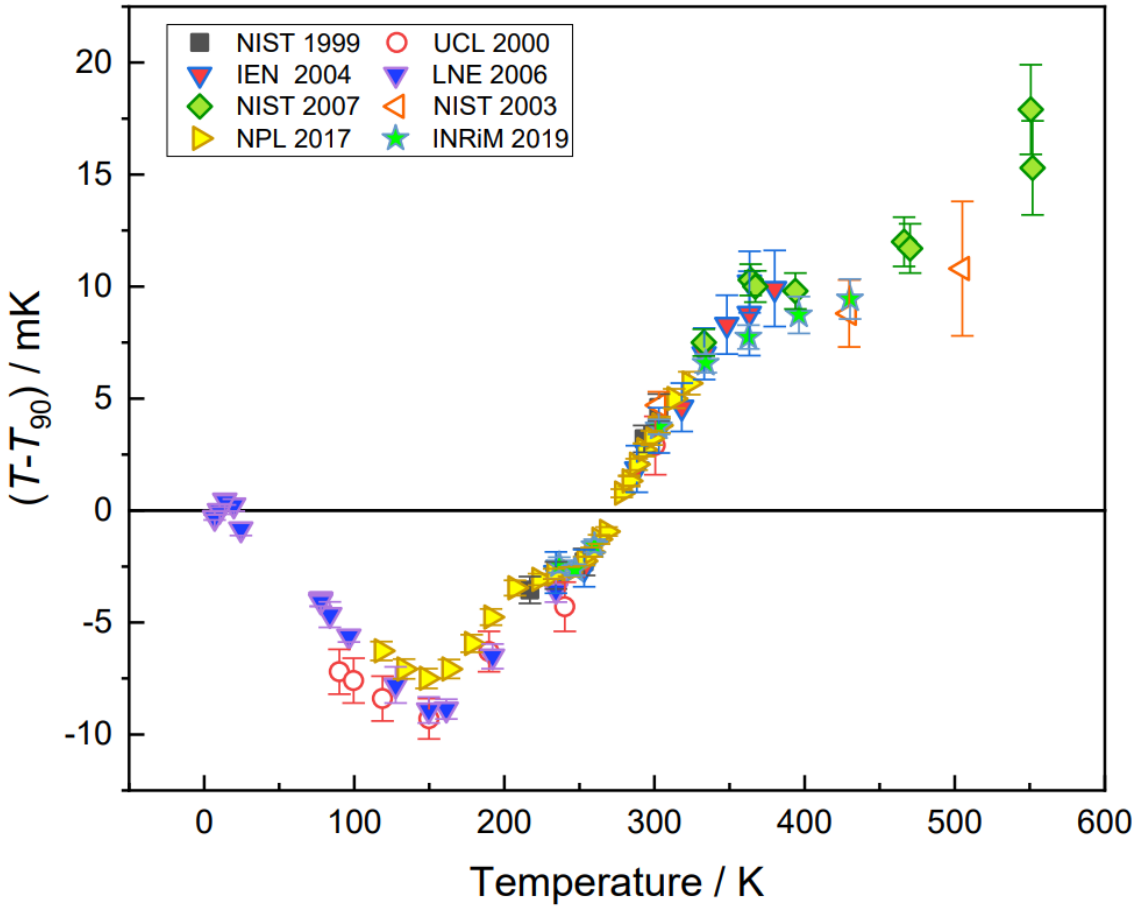

Figure 9: Differences between the ITS-90 and relative acoustic gas thermometry results for thermodynamic temperatures obtained at various laboratories [86]

Despite this remarkable success, the *Mise-en-Pratique* of the kelvin [87], i.e., the practical use of a primary approach, such as AGT, for the future direct calibration of standard thermometers onto the thermodynamic temperature scale remains to be achieved. The thermodynamic scale and ITS-90 will most certainly coexist until this goal is achieved, with the results of studies that determine the former being utilized to enhance the latter, maybe via an ITS-90 redesign that could take place in the upcoming years. Research in primary thermometry will be focused on expanding the practicality and adaptability of the primary techniques in the meantime to support the dissemination of the temperature unit.

The CCT Working Group for Strategic Planning has declared global consensus with this vision and the associated roadmap [88], with a special recommendation to continue with ($T-T_{90}$) measurements in the temperature ranges of 430 K to 1358 K and in the range of 1 K to 200 K, where results are relatively limited and partially inconsistent.

The objective of the work described in this thesis in Section 5.2.1, which is meant to contribute to this effort, is to show that AGT keeps its accuracy in the temperature range up to 550 K. This objective is particularly challenging because of some high-temperature range's inherent difficulties. These include the release of contaminants from the vessel's interior surface and the resonator that might seriously pollute the thermometric gas, the limited operating temperature range of electroacoustic and other transducers, the limited working range of the dielectric material used in microwave-compatible coaxial cables and the probable development of significant thermal gradients because of the large temperature variations between many components of the apparatus.

2.1.4.2. Practical AGT

The other part of this thesis deals with development of perhaps less accurate but more portable and practically applicable AGT or “PAT”. The practical acoustic thermometer is a common term for the application of acoustic thermometry in metrological practice using a waveguide. Most practical acoustic thermometers are based on the measurement of TOF of short acoustic pulses in a waveguide, which is generally called a “pulse-echo system”. Excluding historical realisations, NMIs have developed several versions of PAT based on designs (shown in Figure 10) proposed in 2010 in [89] and some realisations later more characterized in 2015 in [90], [91] and [92].

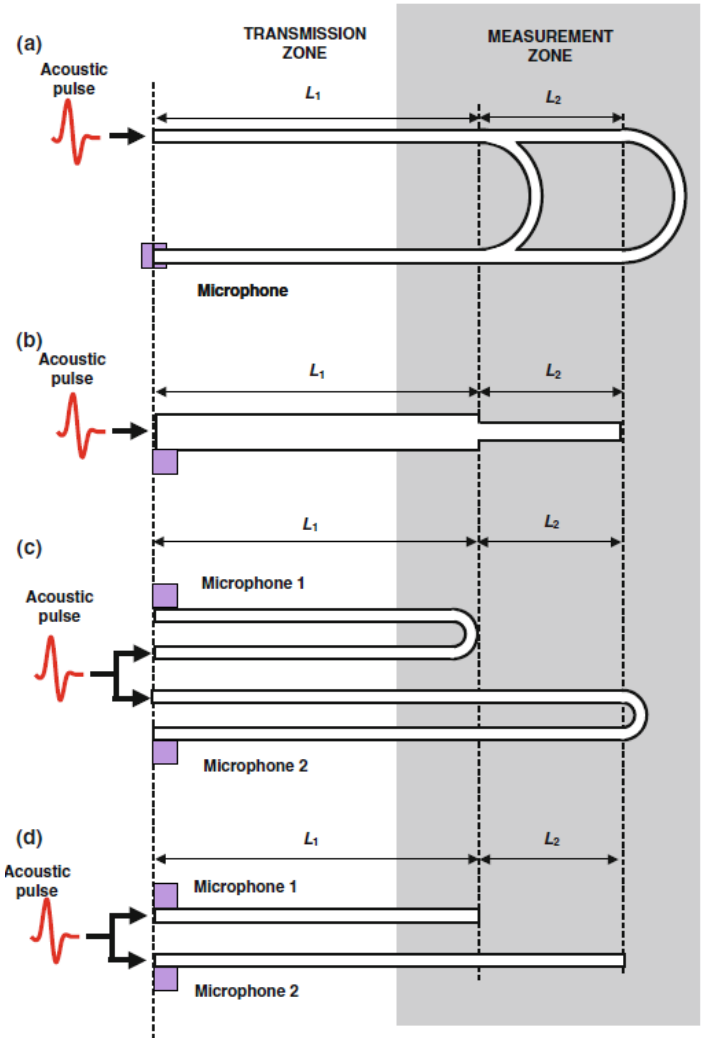

Figure 10: PAT designs including localization of the measurement area as proposed in [89]

Basic forms of PAT (in gases) work with Eq. (13) or its simplification for average air

$$u_{air} = 331.41 + 0.61 \cdot t, \tag{23}$$

(where t is thermodynamic temperature expressed in °C) or the thermometer is calibrated against a standard thermometer (SPRT or TC), thus traceable to the ITS-90 (examples in [93] and [93]). To extract a TOF from measured signals, various approaches can be used. The simplest but less reliable evaluation method is called the "threshold crossing method" (described in [95]). More common is the use of "phase detection" (e. g. in [95], [97] or [93]) or "correlation method" (e.g. in [98]).

Beside practical acoustic gas thermometers, configurations employing acoustic wave propagation in solids also exist (e.g. in [99], [99], [100] and [102]) and due to the more difficult description of wave propagation, those PATs are usually described by a polynomial resulting from $u = \mathrm{f}(t_{90})$ calibration. Also, several systems measure TOF in liquids (e. g. in [103]) for indicative T observation purposes, but with poor mathematical description and thus T evaluation with unacceptable uncertainties.

Generally, the localization of the measurement region is provided by introducing inhomogeneity into the waveguide (example e.g., in [99]). Practical acoustic thermometers are limited by the uncertainty sources connected to the measurement of the waveguide length (including its thermal expansion), accuracy and resolution of time measurement and TOF evaluation, noise, shielding and grounding of associated electronics, pressure, purity and

knowledge of used media composition (see [92]). It is concluded in [89] that smooth bends in the waveguide have a negligible effect on the amplitude and speed of the transmitted acoustic pulses. Latest achievements in the field of practical acoustic thermometry were found in [104] in 2020, where measurements of speed of sound were performed at pressures up to about 400 kPa in argon, employing the spiral-ended closed waveguide with two cross-sections and ½" prepolarized free-field microphone. The time of flight was determined in the amplitude frequency spectrum with the resulting measurement stability about 75 mK and measurement uncertainty of about 65 mK. The temperature rage of the measurement was (0 to 70) °C.

The practical acoustic thermometer presented in this thesis in Section 5.1 is therefore focused on the design that allows inserting the waveguide in vertical furnaces, that are common in industrial calibration laboratories and extending the temperature measurement range.

3. Objectives of the doctoral thesis

The main objective of the work is the development of the practical acoustic thermometer (PAT), which includes following sub-objectives:

A. Building a prototype of the practical acoustic thermometer that will use single microphone for its operation
B. Enabling portability of the measurement system
C. Calibrating the system in the temperature range bigger than the latest achievements (mentioned in section 2.1.4.2)
D. Reaching measurement uncertainty below 0.15 °C that makes the thermometer comparable to common industrial contact thermometers

Another complementary objectives, regarding primary acoustic gas thermometry (AGT) are

E. Performing an acoustic measurement at elevated pressure above 430 K to obtain an isotherm, using high-temperature AGT apparatus at INRiM, to prove an effectiveness of and acoustic gas thermometry at high temperatures.
F. Initiating acoustic gas thermometry development at CMI

4. Selection of usable methods

4.1. The use of an electrostatic actuator (PAT)

The effect of electrostatic coupling [105] is used in Section 5.1 to make the microphone act as an acoustic receiver and an acoustic source at the same time. If an electrical voltage is applied between flat electrodes, the attractive force of magnitude [105]:

$$F = \frac{-V^2 \varepsilon a}{2d} \tag{24}$$

acts between them. Symbol *a* here denotes the ratio of the area of the electrode to the area of the diaphragm and *d* denotes the distance between the actuator and diaphragm of the microphone in meters. The equivalent pressure in Pa can be calculated as:

$$p(t) = -\frac{\varepsilon a}{2d^2}(V_0 + v\sin(\omega t))^2 \tag{25}$$

where V_0 is the DC voltage between the actuator and diaphragm in V, *v* is the amplitude of the AC component of the voltage between the actuator and diaphragm in V, ω is an angular frequency in rad·s^{-1} and *t* is a time in seconds (see [106]).

An electrostatic actuator is commonly used for calibrations of condenser microphones to obtain frequency response characteristic. As described in [106], it can generate a constant electrostatic pressure acting on the metallic diaphragm of the microphone, in a wide frequency range. The actuator acts as the electrode with an electrical potential having DC and AC components. The DC component is equal to the polarisation voltage of the microphone and the AC component is formed by the initial burst (see Section 5.1.1.1) with a sinusoidal signal. The form of the actuator, that is placed in the vicinity of the diaphragm, is a flat metal plate with holes that allow its acoustic transparency.

The diaphragm of the microphone oscillates at the frequency of the AC component of the total voltage between the electrostatic actuator and the membrane. As a result, it generates acoustic waves that travel through the acoustically transparent actuator further into the waveguide.

4.2. The impulse echo method of sound velocity measurement in hollow waveguides (PAT)

To determine the speed of sound propagating inside the waveguide, some signal that is easy to identify and distinguish from other measured signals must be introduced to the sound field that is naturally already present in the given working media. The waveguide is closed by the rigid flat surface at one side while on the other side the diaphragm of the acoustic transducer is located parallel to this surface. When the possibility to distinguish the useful signal exists, such an acoustic signal of a proper amplitude and time duration is sent to the waveguide by an acoustic source. This signal, usually in the form of an acoustic impulse, travels further to the wall on the opposite side of the waveguide. When using a suitable waveguide material and working media, most of the energy is reflected back from this flat surface towards the acoustic transducer. Both the initial impulse and the echo from the waveguide can be identified in the measured signal after appropriate analysis and postprocessing of the microphone recording. As

described in [105], from the delay τ between them the mean velocity of sound u along the waveguide can be calculated as:

$$u = \frac{2 \cdot l}{\tau}, \tag{26}$$

where l is the length of the waveguide. This "impulse echo method" is applied for the measurement of the speed of sound propagating in the media inside the waveguide.

4.3. Localization of the measurement region (PAT)

To measure the speed of sound in some delimited area the waveguide must be partially inserted into this volume. It is assumed that the temperature in this volume can deviate from the temperature range that the acoustic transducer can resist. Therefore, the measuring part is connected to another part of the waveguide serving mainly as protection. Thus, the waveguide itself is partially exposed to the ambient temperature and the information about the mean sound velocity only in the measurement region should be determined. For this purpose and due to the use of a single acoustic transducer, the design where fully immersed and partially immersed waveguide parts differ in cross-section as proposed in [89], and shown in Figure 10 (b) was selected to construct a waveguide.

4.4. The temperature computation from PAT measurement using air media

When measuring using the air medium, Eq. (13), describing the relation between the speed of sound in an ideal gas and the thermodynamic temperature is simplified and used to compute the temperature estimation. This approximation does not take into account such effects as pressure, humidity, gas composition and others influencing the precision and limits of operation of the measurement experiment. The simplification was performed as follows:

$$u_{air} = \sqrt{\frac{\gamma_{air} RT}{M}}. \tag{27}$$

M here is expressed in g·mol^{-1} and the value of R that was used for measurements with air media is determined in [107]. In addition, values of γ and M for the average air, as listed in [108] were used. Substituting these specific values into Eq. (27), the following relationship is obtained:

$$u_{air} = 331.41 + \sqrt{1 + \frac{t}{273.15}} \tag{28}$$

When using only the first two terms of the Taylor expansion it reduces into the form that is given by Eq. (23) and can be expressed in K units as

$$T_{air} = \frac{u_{air} - 331.41}{0.61} + 273.15. \tag{29}$$

Similarly, the thermodynamic temperature of the ideal monatomic gas in K can be expressed as

$$T_{ideal} = \frac{M \cdot u^2}{\gamma \cdot R}, \tag{30}$$

Both Eq. (29) and Eq. (30) were used to calculate 2 estimations of the temperature from τ values that were measured in air media at ambient pressure in Section 5.1.1.

4.5. Fitting of acoustic radial modes (AGT)

When frequency positions of acoustic modes of AGT at a given temperature and pressure are known, the real and imaginary parts of an acoustic signal are recorded at a discrete number of

frequencies distributed over the frequency range wide enough to include a single or several resonance curves. For the single acoustic radial mode resonance, a few tens of points spanning a frequency range (4 to 8) times wider than the mode halfwidth g_n are typical. Recorded frequency of the acoustic signal and complex voltage data $x + iy$ are repeatedly fitted (see Figure 11) to the complex function

$$x + iy = \frac{if\boldsymbol{A}}{f^2-(f_n+ig_n)^2} + \boldsymbol{B} + \boldsymbol{C}(f - f_n) + \boldsymbol{D}(f - f_n)^2 \tag{31}$$

where $\boldsymbol{A}$ is a complex amplitude, $\boldsymbol{B}$, $\boldsymbol{C}$ and $\boldsymbol{D}$ are complex constants defining a quadratic background, and $\boldsymbol{F}_n = f_n + ig_n$ is the complex resonance frequency of the mode n. The relative fitting precision of f_n, achievable with this procedure and instrumentation (described above) is expressed in units of parts per million (ppm) [63]. The procedure of fitting is necessary to continuously measure the frequency of the given acoustic radial resonance mode and was used in Section 5.2.1.

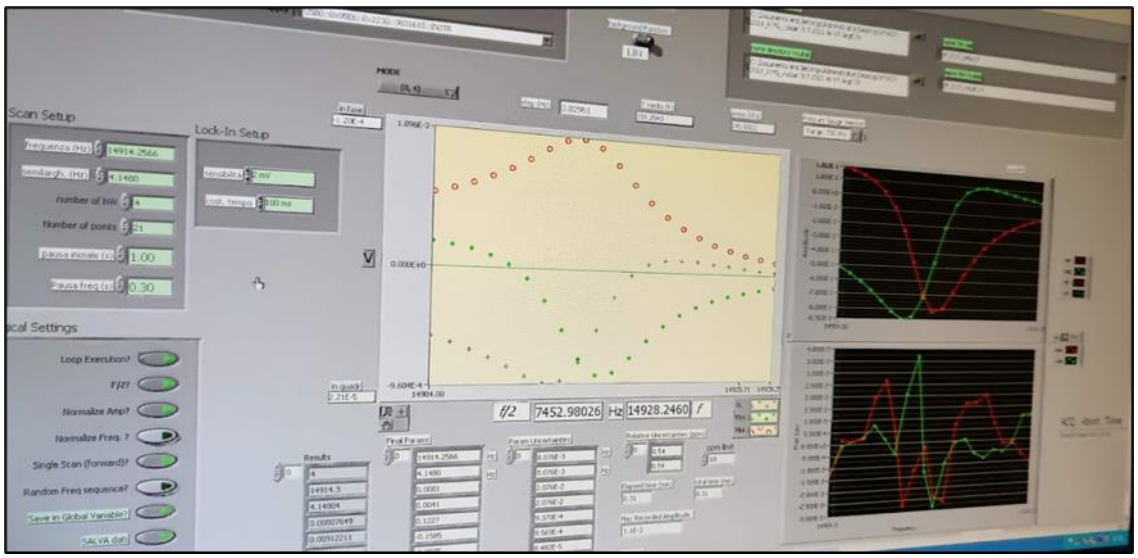

Figure 11: Example of LabView application, fitting the quadratic function to acoustic resonance mode

4.6. Thermal boundary layer correction (AGT)

In the spherical or quasi-spherical resonator, the gas develops a thermo-acoustic boundary layer characterized by the exponential decay length

$$\delta_{th} = \sqrt{\left(\frac{\lambda_{gas}}{(\rho C_P \pi f_n)}\right)} \tag{32}$$

during each acoustic cycle as a result of heat exchange with the shell enclosing the cavity. The λ_{gas} denotes the thermal conductivity of gas, ρ its density, Cp is the molar thermal capacity at a constant pressure and f_n (or $f_{0,n}$) is the original measured and uncorrected frequency value. Frequency correction to the acoustic radial resonance frequency for thermal boundary layer is for spherical cavity with the radius a (according to [63]) equal to

$$\frac{\Delta f_{th}(p,T)}{f_n} = -\frac{(\gamma-1)}{2a}\delta_{th} + \frac{(\gamma-1)}{a}l_{th} + \frac{(\gamma-1)}{2a}\delta_{th,sh}\frac{\lambda_{gas}}{\lambda_{sh}}, \tag{33}$$

where λ_{sh} is thermal conductivity of resonator material and l_{th} denotes the thermal accommodation length given by the relation

$$l_{th}(p,T) = \frac{\lambda_{sh}}{p}\left(\frac{\pi MT}{2R}\right)^{0,5}\left(\frac{2-h}{h}\right)\frac{1}{2}. \quad (34)$$

The variable h is the thermal accommodation coefficient, expressing the quality of the heat exchange between the gas molecules and the solid surface of the resonator and

$$\delta_{th,sh} = \left(\frac{\lambda_{sh}}{\pi\rho_{sh}C_{p,sh}f_n}\right)^{0,5}. \quad (35)$$

The value of $\Delta f_{th}(p,T)$ is added to the measured frequency f_n to obtain the corrected frequency value. For a typical AGT system, the value $\frac{\Delta f_{therm}}{f_n}$ is usually in the range from $50\cdot10^{-6}$ to $200\cdot10^{-6}$ and this is the most significant correction that must be performed on the raw data. This range can also be expressed in temperature, as $100\cdot10^{-6} < \Delta T/T < 400\cdot10^{-6}$. For radially symmetric acoustic modes of a spherical or quasi-spherical cavity of radius a, the contributions of the boundary layer to the real and imaginary (halfwidths) part of the resonance frequencies (Δf_{th} and g_{th}) are equal and both grow at low density according to $\rho^{-\frac{1}{2}}$. The contribution of the thermal boundary layer to the value g is g_{th} and is given by the equation

$$\frac{g_{th}(p,T)}{f_n} = \frac{(\gamma-1)}{2a}\delta_{th} + \frac{(\gamma-1)}{2a}\delta_{th,sh}\frac{\lambda_{gas}}{\lambda_{sh}} - \frac{1}{2}(\gamma-1)(2\gamma-1)\frac{\delta_{th}}{2a}. \quad (36)$$

Thermal boundary layer correction was applied to measured resonance frequencies in Section 5.2.1.

5. Practical part

5.1. Practical Acoustic Thermometer (PAT)

The main objective of this work was to develop a practical acoustic gas thermometer with parameters closer to primary realisations than already published PATs, measuring thermodynamic temperature, portable and easy to use.

The prototype of a practical acoustic thermometer with a single acoustic transducer, working with an air medium, consists of four main parts. The first part includes an electrostatic actuator (in the form of a perforated electrode), a DC voltage source providing polarisation voltage for the microphone, a signal generator and a simple electronic circuit superposing AC and DC signals into one circuit node.

The second part is a waveguide composed of two sections with different diameters. As a result, mechanical inhomogeneity is introduced into the sound path. It allows the differentiation of the measured signal, which corresponds to the measured area, from the total signal. The time difference between the arrival of reflected waves from the place of the diameter reduction and from the closed end of the waveguide determines the time of flight in the thinnest waveguide section that is fully immersed into the measurement area.

The third part provides the recording of the transmitted acoustic waves and echoes from the waveguide. It consists of a microphone with a preamplifier, a power supply for the preamplifier, a source of polarizing voltage and a measuring ADC device (in the diagram marked "Recorder"). The analysis of acquired data is maintained by the signal processing unit (the fourth part, not shown). Figure 12 shows the principal scheme of the measurement arrangement.

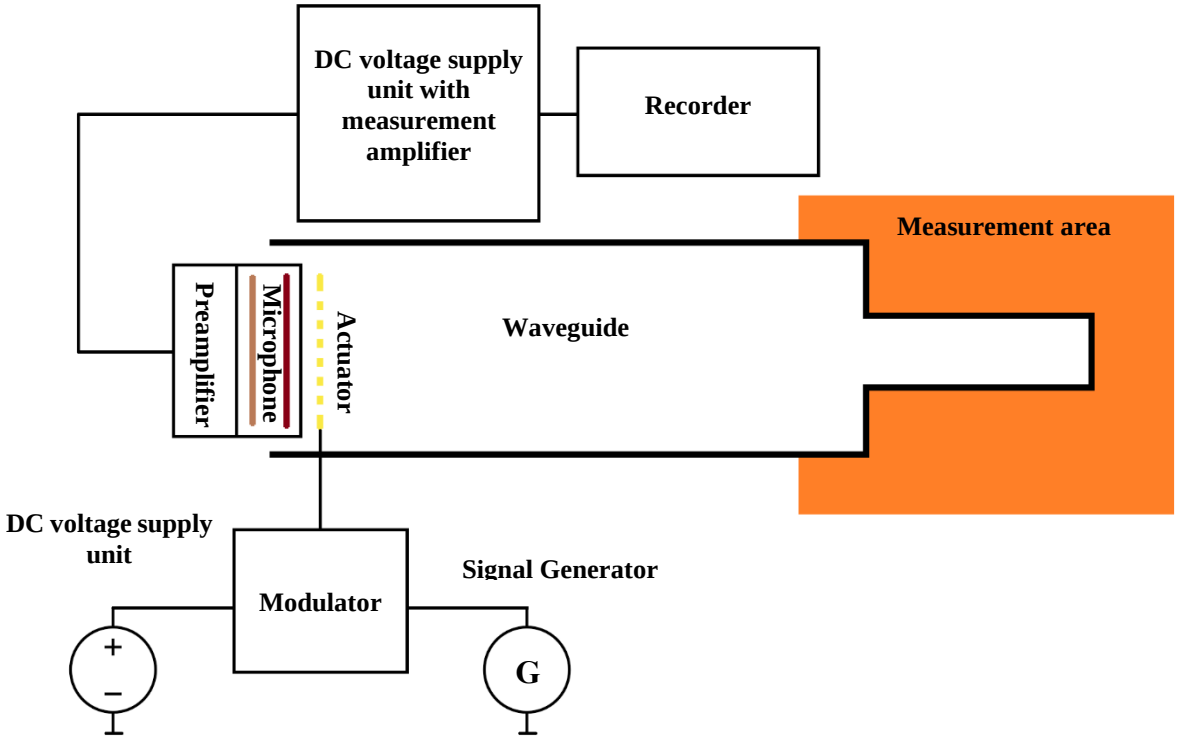

Figure 12: Principal scheme of the measurement arrangement

Both the generation of the excitation signal and the measurement of data from the thermometer are controlled by the LabVIEW application.

5.1.1. Single transducer ultrasonic thermometer using an electrostatic actuator

This section describes work published in [109], the first version of the PAT prototype and the results of the initial measurement using air media at ambient pressure in a range of (-20 to 90) °C.

5.1.1.1. The initial burst

The initial burst serves to excite the movement of the diaphragm and excitation of an acoustic pulse that travels from the microphone/actuator further into the waveguide. It was designed as a product of 10 V, 75 kHz, waveform and 0.5 ms lasting, 1 V in amplitude, square waveform. The quiescent part of signal with 0 V output was 24 ms long after each generation of an initial burst. The resulting 24.5 ms loop was continually present at the analogue output (at the differential configuration of the channel and with a sampling frequency of 200 kHz) of National Instruments NI-4461 24-bit delta-sigma type DAC converter module that was hosted in NI PXI-1031 DC, 4-slot DC-powered chassis.

Figure 13 shows the recording of 0.5 ms long region of the generated signal (nonzero part of the initial burst) as measured by 2 MSa/s digital oscilloscope (in blue) and samples that correspond to the same region as designed by the LabVIEW application. It proved the sufficiency of the available sampling rate to produce a fully-fledged excitation pulse.

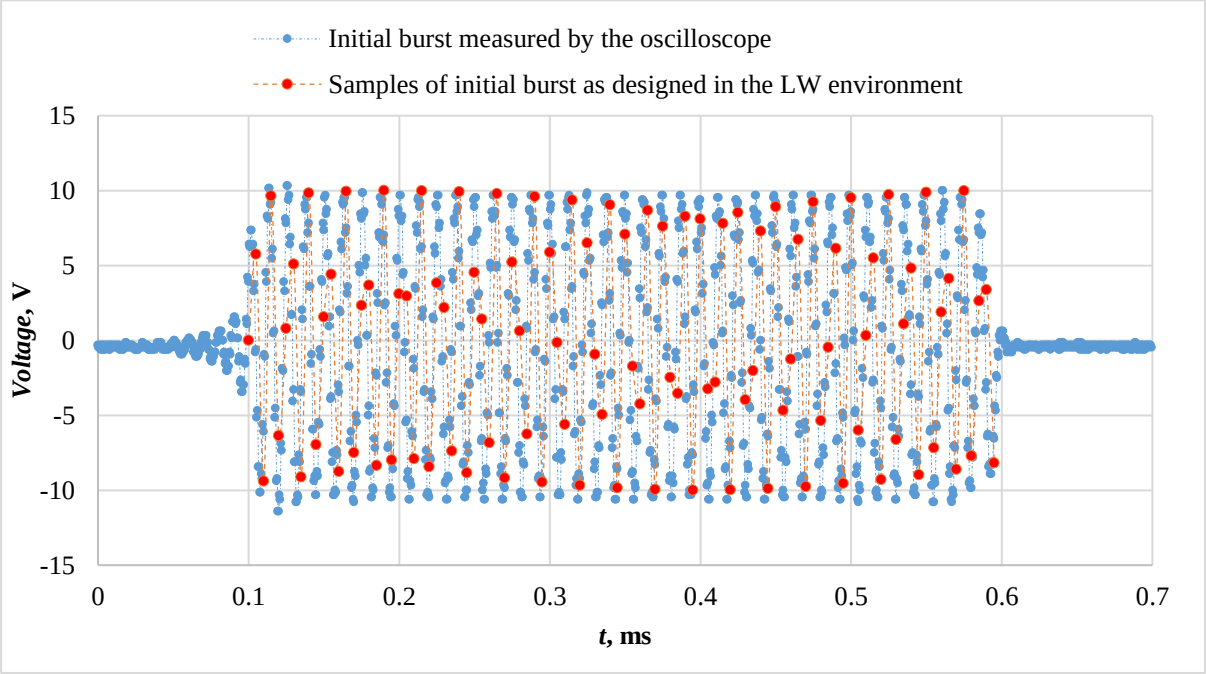

Figure 13: The excitation pulse recorded by the oscilloscope (blue) and samples of the pulse as designed by the LV application (red), published in [109]

The free-field 1/4″ Microtech Gefell MK 301 measuring microphone with a nominal polarisation voltage of 200 V DC was used as a transducer, both producing and measuring a sound field in the waveguide. Two Microtech Gefell MN 921 power supply units are employed to hold the microphone and electrostatic actuator at the equivalent electrical potential.

The existence of an eventual voltage difference in output voltage between these two units was tested by calibrated 8.5-digit reference multimeter Fluke 8508A both in battery supply operation and external power supply adapter regime. The 60 min lasting measurement (with the sampling rate of 4 s) of an output voltage at both units in both power supply modes resulted in the average voltage of 198.4 V with a maximum standard deviation of 0.04 V in all tested cases. It proved the comparability and interchangeability of both voltage sources. Despite that it

showed that there is no need for battery power supply operation, the thermometer prototype was using battery mode to prevent unexpected noise from the electrical network during its operation.

The GRAS RA0014 perforated golden electrode forming an electrostatic actuator was positioned in front of the diaphragm. The air gap between the actuator and the diaphragm was estimated to be approximately 0.01 mm. This electrode was connected with 250 MΩ resistor to the power supply unit and by 6.8 nF capacitor to the signal generator. The circuit containing the capacitor and resistor is denoted as a "Modulator" in the principal scheme in Figure 12 and allows creating the signal that contains 200 V DC component (nominal value) and superimposed 10 V (in amplitude) AC component with initial bursts for the actuator.

5.1.1.2. Waveguide

While the maximum waveguide length is limited mainly by the power loss along the sound path, an effort is made to have dimensions similar to conventional industrial resistance thermometers, which is practical for use in industrial calibration laboratories. The optimal length and diameter should allow the prototype to fit e.g., in low temperature vertical block calibration furnaces. In practice, such thermometers are typically of a diameter in a range from 3 mm to 12 mm and up to 500 mm long. The minimum length of the waveguide is mostly limited by sensitive components at its end that is not exposed to the measured environment, namely the microphone with an operating temperature in the range of (-50 to 110) °C [110], and the preamplifier with an operating temperature range of (-10 to 50) °C [111].

Three acoustic single-tube waveguides (approximately 500 mm long, with 10 mm inner diameter and 1 mm wall thickness) made of aluminium, brass and stainless steel (common and affordable materials), closed at one end and open at the other were selected for a preliminary measurement. The purpose was to estimate the approximate maximum theoretical measurable temperature of the acoustic thermometer prototype. These samples were immersed 250 mm deep in an aluminium block of the Isotech 511-Medusa-3 dry-block calibrator. The Ahlborn FTF109PH surface thermometer, employing a Dostmann P615 display unit was attached to the surface and measuring its temperature close to the open side of each waveguide at several temperatures of the furnace in the range of (100 to 500) °C. The measurement results in Figure 14 show that all tested waveguides can be used only up to about 300 °C for the safe operation of the system. Considering the indicative measurement results, the waveguide was made longer than the tested samples and of type 1.4541 stainless steel.

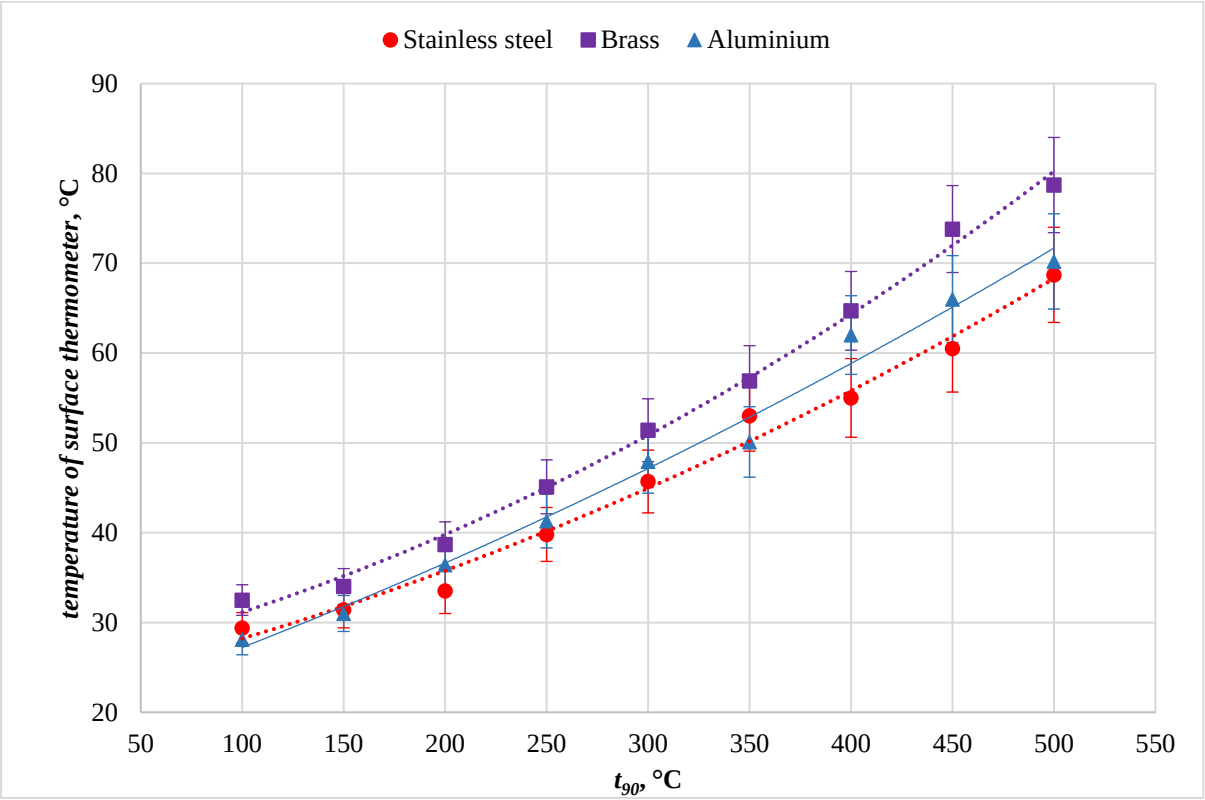

Figure 14: Dependence of the surface temperature on the top of the waveguide on the nominal temperature in the furnace, estimated measurement uncertainty included (as published in [109]).

Figure 15 shows the drawing of the waveguide (employed for the initial calibration) in cross-section. Two tubes of different diameters, made of stainless-steel, were welded together in series by laser to decrease the effects of unevennesses along the main path of acoustic waves propagation. The flat surface made by step reduction of the waveguide diameter reflects part of the sound energy back to the acoustic source while the rest of the energy propagates further to the closed end of the thinnest tube, where it is also reflected.

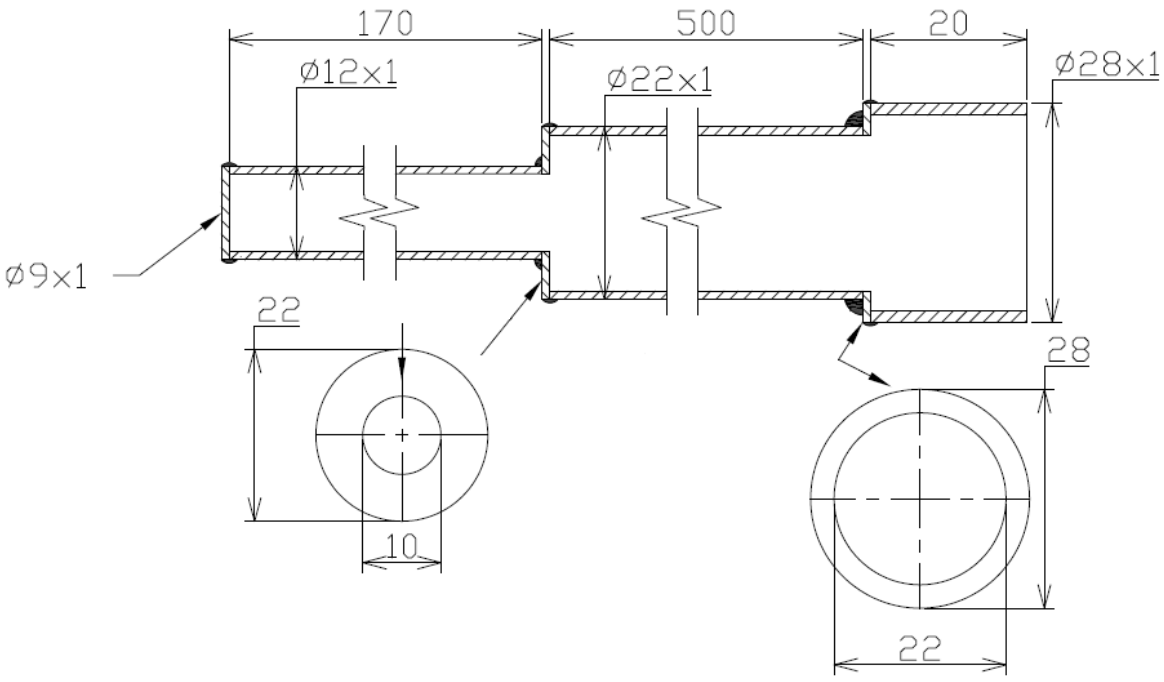

Figure 15: Waveguide design, dimensions in mm

The additional third part with the largest diameter is connected to the waveguide to serve as an electrode holder. All parts of the waveguide were laser welded to minimize any unevennesses which could otherwise modulate the sound during its propagation, reduce the transmission efficiency and introduce unwanted noise into the measured signal.

5.1.1.3. Measurement and data acquisition

Condenser measuring microphone was selected as an acoustic transducer with stable electroacoustic parameters. It is connected to a 1/4'' measuring microphone preamplifier Microtech Gefell MV 302 with a maximum inherent noise of 20 μV and gain of 0 ± 0.05 dB. The Microtech Gefell MN 921 unit provides the necessary power supply both for the preamplifier (119 V DC nominal) and the polarisation voltage for the microphone (200 V DC nominal). This unit includes the measuring amplifier with amplification that can be adjusted by the gain selection switch. The selected gain value was 128 during the measurement which corresponds to the dynamic range of 138 dB and the effective self-noise voltage value of 330 nV. The output voltage of the measuring amplifier was connected to the analogue input channel (measuring in a differential configuration, 30 dB gain and 1 MΩ input impedance) of the same PXI-4461 module that is used for generating initial bursts. The 24-bit delta-sigma converter provided the A/D conversion with a sampling rate of 200 kSa/s.

5.1.1.4. Data evaluation

The LabVIEW application controlled the whole data acquisition procedure. A total of 400 data cycles representing the transmission of the initial burst and reception of an echo from the waveguide were captured for a total period of 9.8 s in each measurement. The internal RAM of the employed PC was limiting the maximum number of those cycles during a measurement period.

The thermometer contains one acoustic transducer, therefore only one signal is obtained that includes the initial burst as well as all of the echoes from the waveguide. The controlling application performs a high-pass frequency filtering of the recorded data in the form of an inverse Chebyshev type filter of the tenth order, with a cut-off frequency of 35 kHz and the attenuation of 60 dB. The filter's main purpose is to exclude from the collected data any signals that have a frequency in the audio-frequency band. Figure 16 shows the typical amplitude frequency spectrum (of the recorded data) both before and after filtering. To prevent low-frequency noise from affecting the final average signal shape, frequency domain filtering is applied to the raw recorded data before subsequent mean filtering. The initial burst of a sine signal has a finite number of periods, which results in the stretching of the amplitude spectrum shape to the sides. Thus, in addition to the primary lobe, the lateral lobes also appear.

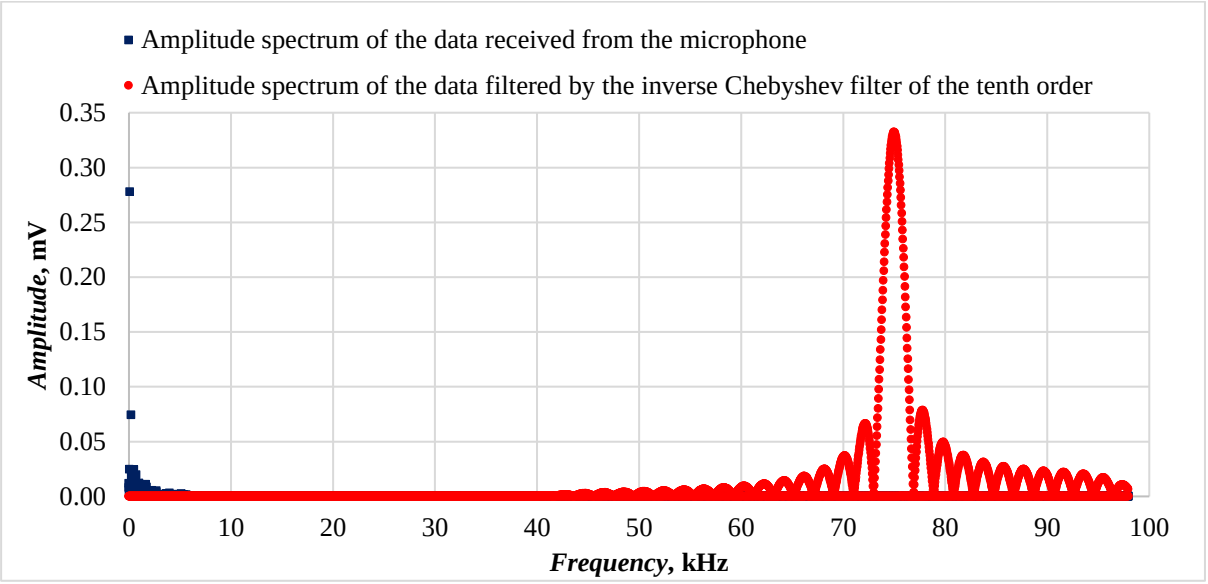

Figure 16: The amplitude spectrum of the measured data before (in blue) and after (in red) high-pass filtering, as published in [109]

The data processed by the inverse Chebyshev high-pass frequency filter is furthermore subjected to simple average filtering (a number of received signals, containing transmitted pulse and received echoes, are averaged to reduce the noise). Figure 17 illustrates the typical form of the signal for the average measurement cycle at around 38.5 °C in detail. The controlling software determines the absolute position of initial bursts at the time axis, which is not important for subsequent computations. The pulse that represents the initial burst is significantly larger than the pulses that correspond to the reflection at the waveguide diameter decrease location and the reflection at the closed end of the waveguide. As a result, the analysis based on the detection of threshold crossings is ineffective.

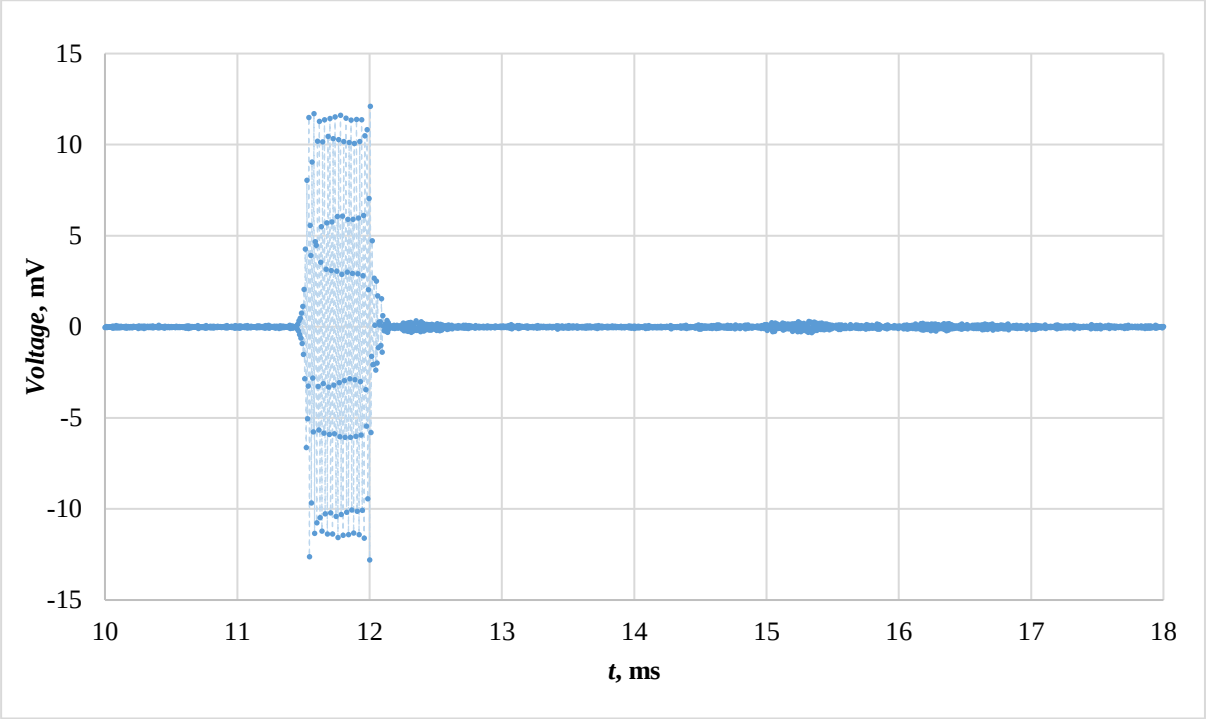

Figure 17: The typical average signal after mean filtering of the data that was obtained at the nominal temperature of 38.5 °C [109]

Figure 18 illustrates the typical average signal from Figure 17 in more detail. Eq. (28) and the environmental parameters mentioned in Section 4.4 give the theoretical time delay of about 2.8

ms between the initial pulse and the echo from the first reflection at the temperature 38.5 °C. Near the location at the time axis that corresponds to the estimated value of delay from the initial pulse, the beginning of the (stretched) pulse that corresponds to the first reflection can be identified. The theoretical delay between pulses corresponding to the first and the second reflection at this temperature is 0.96 ms.

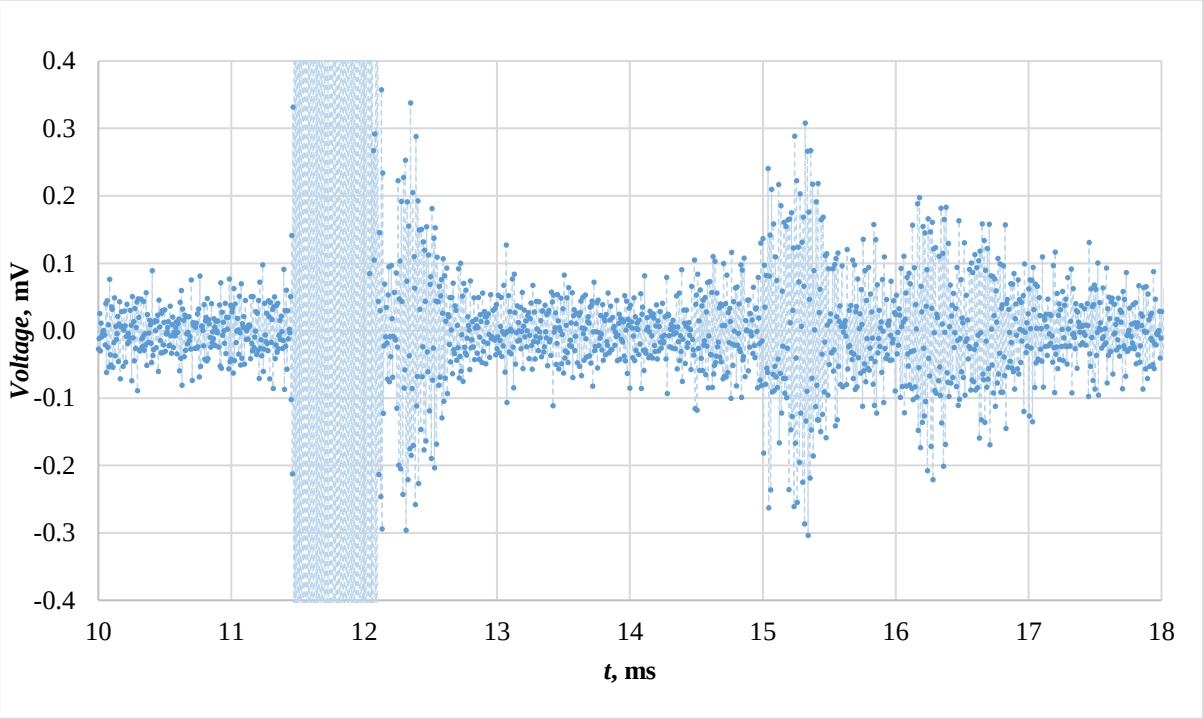

Figure 18: Typical average signal details at 38.5 °C [109]

The autocorrelation of the average signal is used to calculate the time difference between the first and second reflected pulses. Figure 19 shows the autocorrelation of the average signal that corresponds to the waveguide echoes in detail. The positions of the maximum values of the two most significant pulses at the time axis are used to calculate the time delay between the first two reflections.

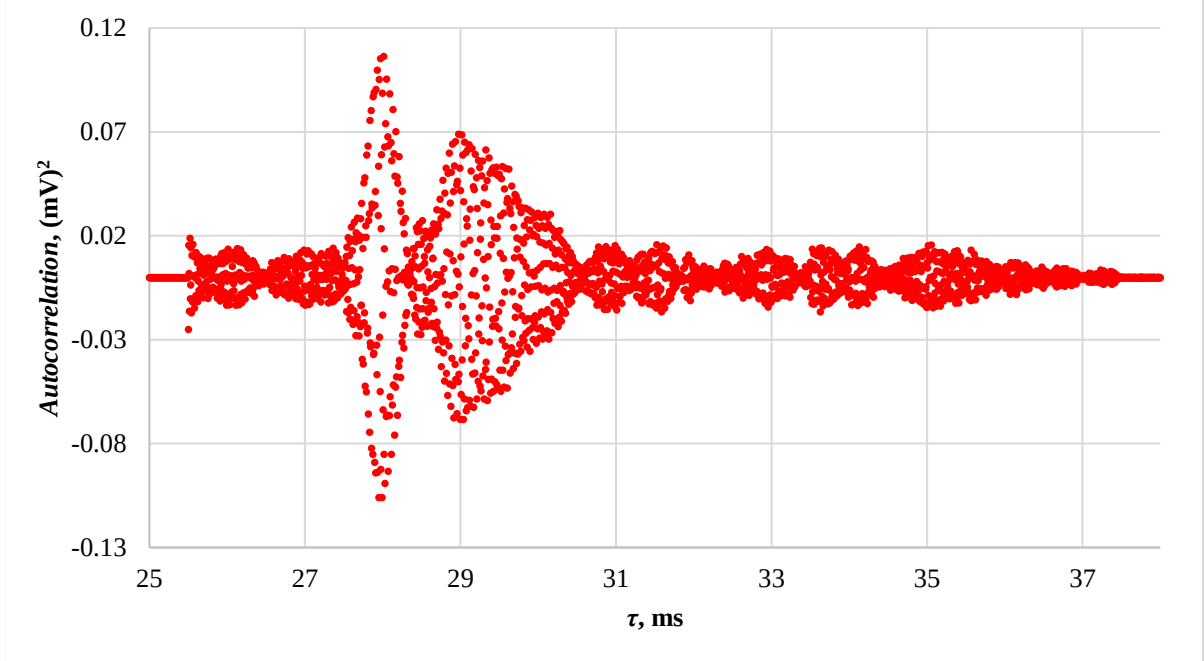

Figure 19: Autocorrelation of the typical average signal at 38.5 °C (Detail corresponding to the echoes from the waveguide) [109]

A temperature estimation can then be derived from the time delay identified by the use of the autocorrelation function.

5.1.1.5. Results of the initial calibration

During the initial calibration, the prototype used bursts at frequency 75 kHz. Following the initial measurement at the melting point of ice (0 °C), this frequency value was chosen because it exhibited the minimal difference between theoretical and measured values of τ. The thermometer was then calibrated using a Pt100 resistance thermometer (Tinsley STS100) in liquid baths (cryostat ASL LU100A and water bath Tamson T.X.V.M.B.70/230) in the temperature range of (-20 to 90) °C. The measurement setup for the initial calibration can be found in Figure 20.

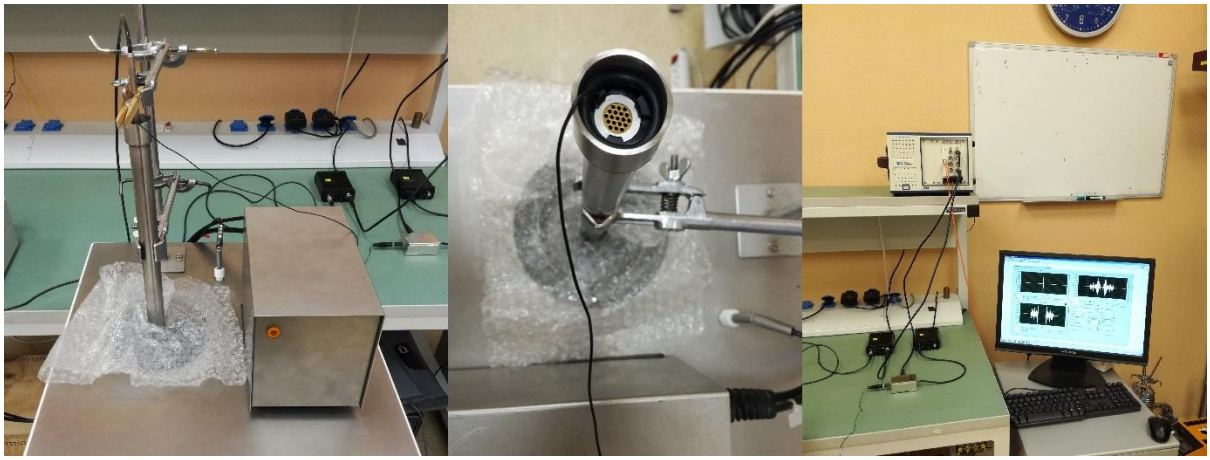

Figure 20: Measurement setup as drawn in Figure 12. Left: Waveguide with actuator and microphone, partially immersed in the bath. Middle: Detail of actuator inside the waveguide. Right: Supplementary electronics. Figure published in [109]

At each calibration temperature point, a series of 30 measurements was made. Figure 21 displays the measurement results as the mean measured $\Delta\tau$ value and corresponding standard deviation of each measured value. The discrepancy between measured and theoretical τ is represented by the symbol $\Delta\tau$. Eq. (29) is used to calculate the τ_a and Eq. (30) is used to calculate the τ_i from t_{90} (measured using a standard thermometer).

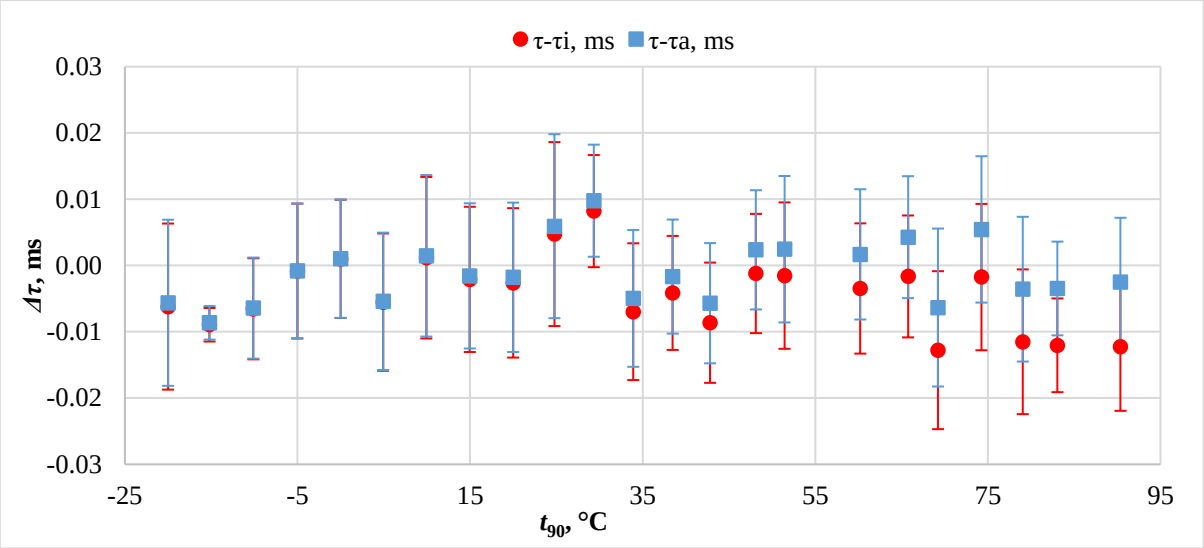

Figure 21: Discrepancy between theoretical and measured τ as published in [109]

The NI-4461 input channel has a time resolution of 5 µs, or 10 µs when calculating the time interval between two peaks of the autocorrelation of the average of the recorded signal. Figure 21 demonstrates that practically all temperature differences between measured and theoretical

values are smaller in magnitude than the time resolution. To find a more precise description of thermometer behaviour, the inverse dependency (temperature of the reference thermometer in reliance on measured τ) was fitted using a second-order polynomial function. Figure 22 shows the difference between the temperature measured using a standard thermometer and the fitting function output.

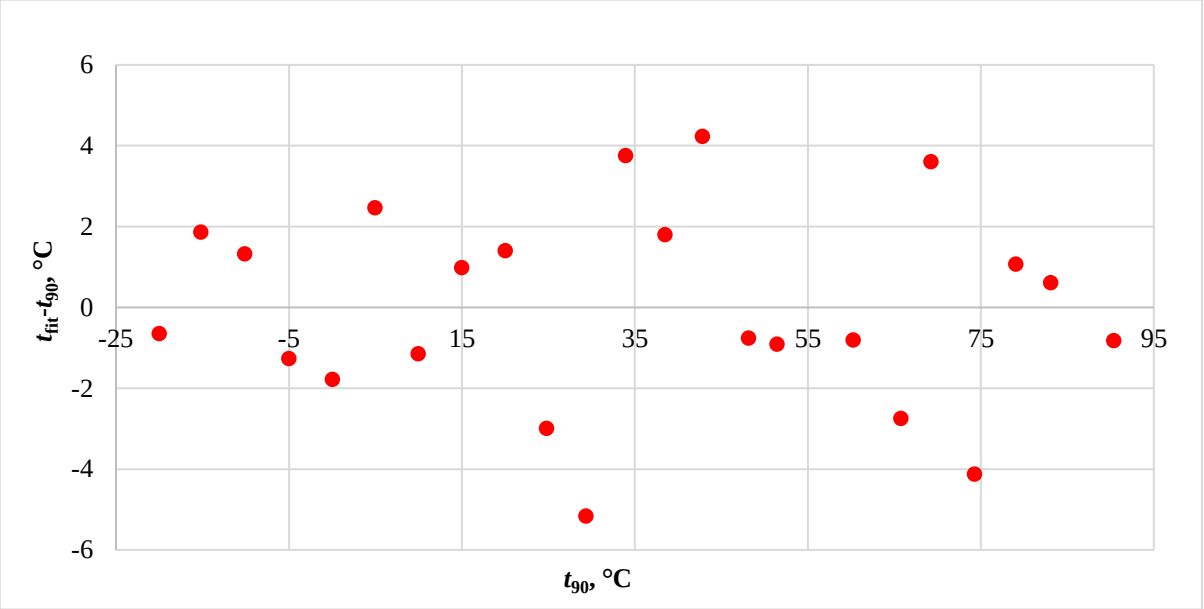

Figure 22: differences between the reference thermometer's temperature and that calculated using the fitting function, published in [109]

As suggested by [89], the temperature resolution ΔT of the PAT prototype can be given as

$$\Delta T = \frac{2\Delta\tau_R}{\tau} T \tag{37}$$

where T is the absolute temperature of measured media, $\Delta\tau_R$ is time resolution (10 µs), and τ is the measured time delay from which the temperature is computed. It yields a resolution of around 5 °C at -20 °C rising to around 7 °C at 90 °C, which is consistent with the values displayed above.

5.1.1.6. Interpolation

The average signals were interpolated using linear, cubic, and spline algorithms and the interpolated signal was analysed in the same way as the original data. The subsequent autocorrelation function cannot produce better results than those obtained from the measured data in the case of linear and cubic interpolation, because the outputs of those interpolations are never outside of the original data extremes. Theoretically, spline interpolation should produce results with a smaller standard deviation, and therefore it was applied to the measured signal as well as to the autocorrelation results. Figure 23 displays the standard deviation σ_τ values of the measured and interpolated τ values for each calibration point. Each interpolation algorithm that was tested, produced data with greater σ_τ, thus the interpolation didn't improve the results shown in Figure 22.

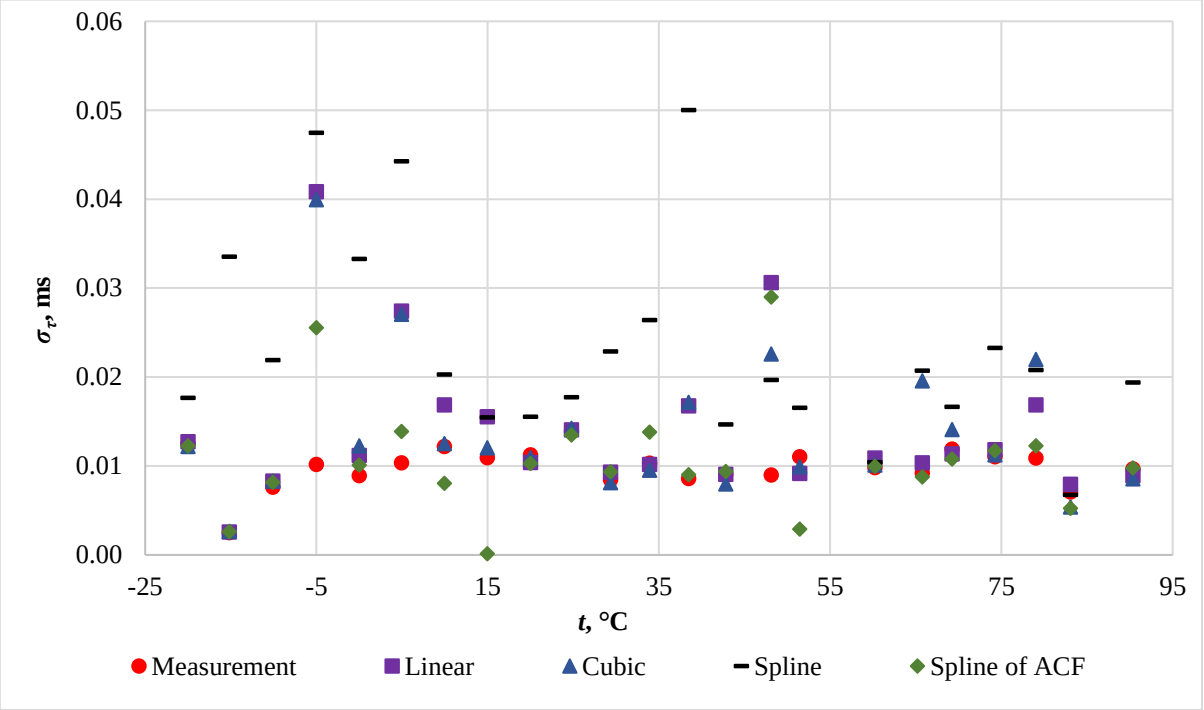

Figure 23: Standard deviation of the τ values that were measured and interpolated at each calibration point (ACF is the autocorrelation), published in [109]

The interpolation methods applied to measured data did not lead to enhancement in terms of the standard deviation of the data thus the measurement accuracy was probably not limited only by the resolution of the measurement card. Insufficient averaging time or noise was probably the cause of the significant variance of measured τ.

5.1.2. PAT working with argon gas

Eq. (13), describing the relation between the speed of sound and T applies only to an ideal gas, however, noble gases have very similar thermodynamic properties (and simple behaviour in comparison with polyatomic gases). These gases are He, Ne, Ar, Kr, Xe and Rn. The most accessible and the least problematic (maintenance, storage, safety etc.) is Ar. Therefore, this gas is used in most AGT applications. The results of the initial calibration were obtained at ambient air and pressure. To enable the possibility of working gas selection and its preservation in the waveguide, the waveguide was complemented by a lid (sketched in Figure 24) with electrical feedthrough and outlet for gas management with a flow regulator. The possibility of operation up to a maximum pressure of 2 atmospheres is assumed. Additionally, the lid provides mechanical stabilisation of the microphone and transmitter and its connection to the waveguide.

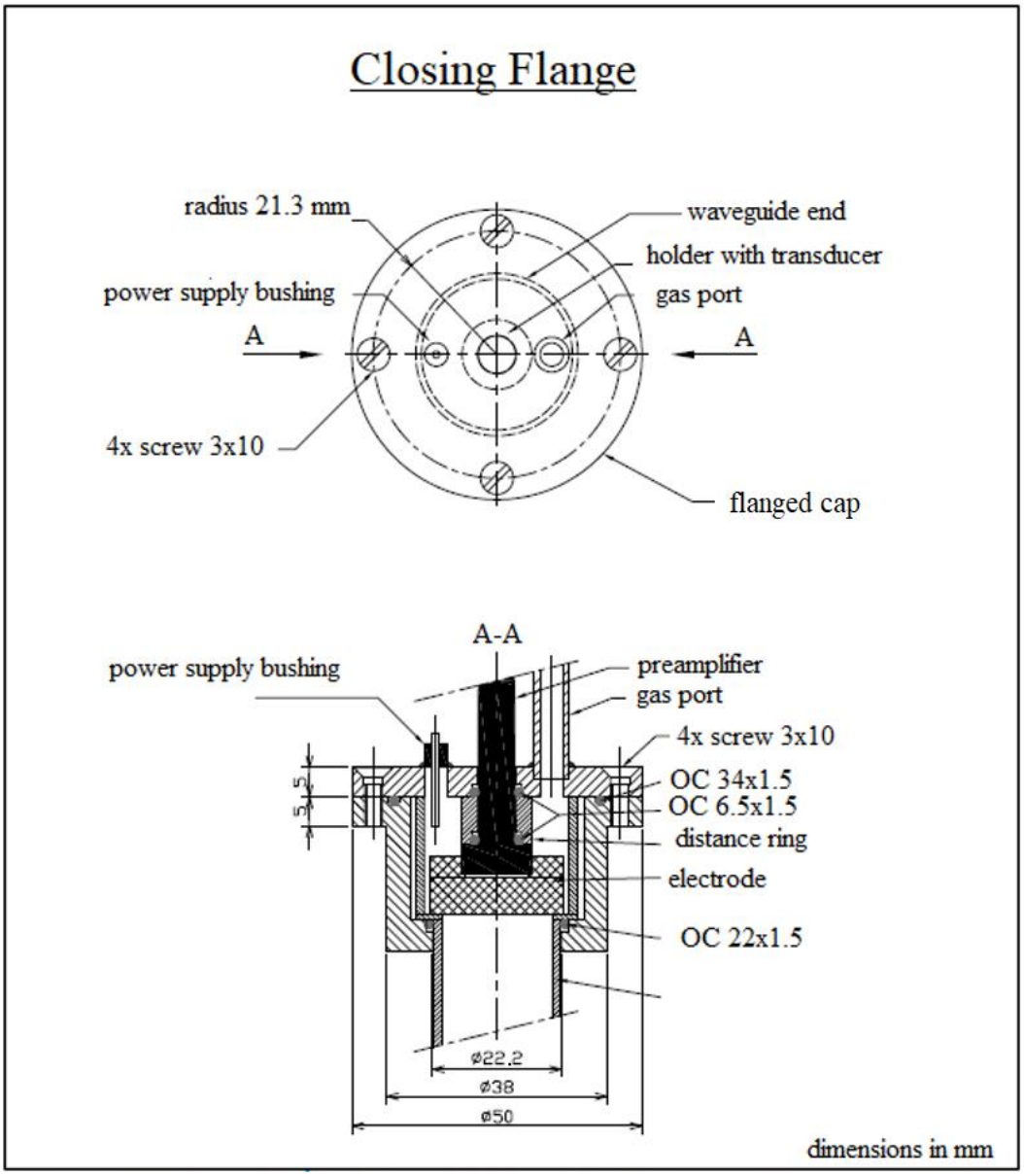

Figure 24: The lid of the practical acoustic thermometer in the CMI

Using Ar media, Eq. (13) should describe better the relationship between temperature and speed of sound in the waveguide than by using air, because the variable composition of the air is difficult to determine. The main measurement uncertainty source of the thermometer, related to the limited repeatability of microphone installation (as evident from Figure 20) was eliminated by the application of the lid, that fixes all thermometer components together. The development of the mechanical part of the prototype is shown in Figure 25. The possibility of the use of monatomic gas enabled focusing on measurement error and uncertainty sources, that cause deviation of thermometer behaviour from theory and contribute to the total measurement uncertainty of the thermometer. As a consequence of the exclusive use of Ar media, Eq. (29) is excluded from further calculations and the temperature is computed only using Eq. (30).

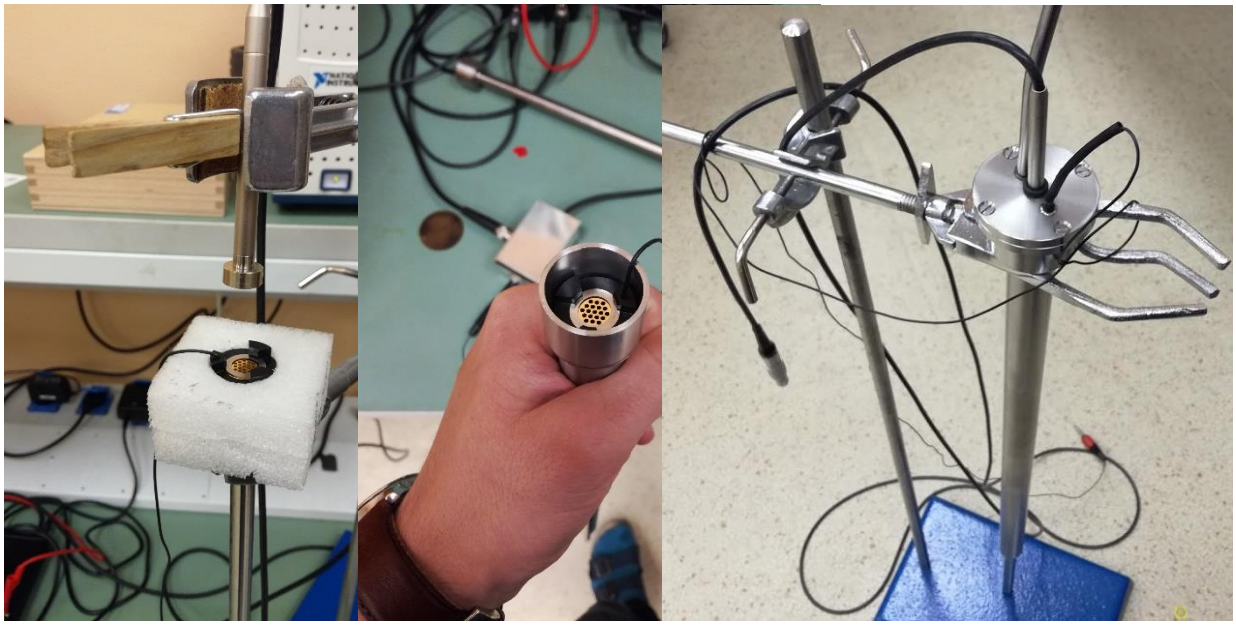

Figure 25: The sequential development of the mechanical part of a prototype of a practical acoustic thermometer

5.1.2.1. Shielding and grounding

Electronic circuits used to prepare signals for the excitation electrode, for subsequent signal amplification, and circuits providing power to individual parts of the measuring chain, were equipped with shielding. The circuit designed to sum up the DC and AC components of the signal (for the electrode) has been replaced by a commercial one (see Figure 26).

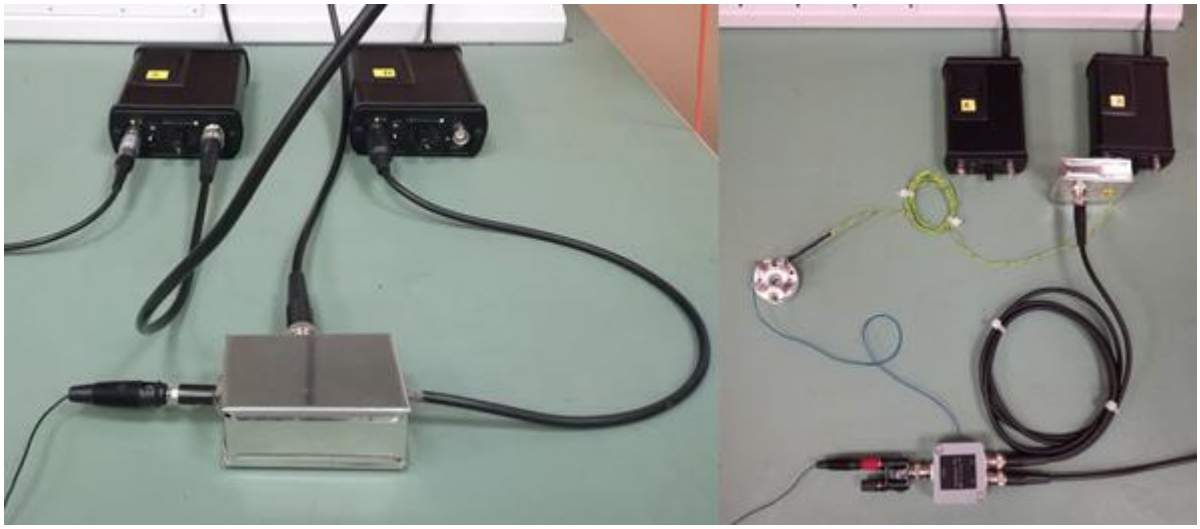

Figure 26: The original voltage source and modulator assembly (left) was supplemented with shielding and upgraded with a commercially available modulator (right)

Additionally, the connection from the modulator to the electrode was replaced by the coaxial cable (Figure 27).

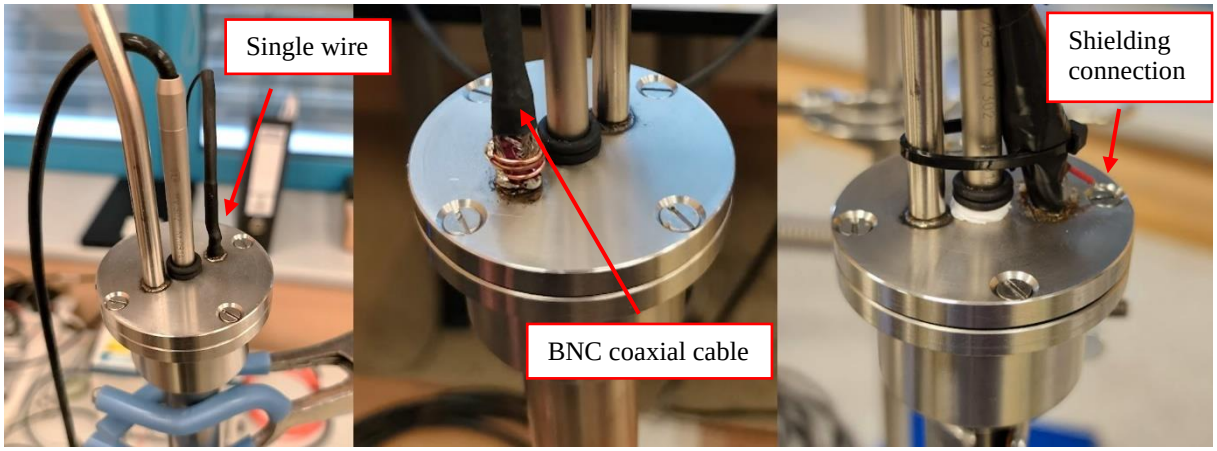

Figure 27: Change in the electrode connection (from left to right)

OWON SDS8302 300 MHz, 2.5 GSa/s digital oscilloscope was used for observations of the parasitic voltage signal, originally induced on several parts of the setup elements. It helped to see the sufficiency of shielding and grounding that was not sufficient during the initial calibration which produced large fluctuations of measured data. Results of the PAT calibration with 99.999 % pure Ar media, after the noise reduction process, are shown in Figure 28. Results of initial calibration from Section 5.1.1.5 are included also in Figure 28 to enable easy comparison. Enclosing the waveguide, use of Ar gas and shielding the waveguide body resulted to smaller standard deviation of measurement results.

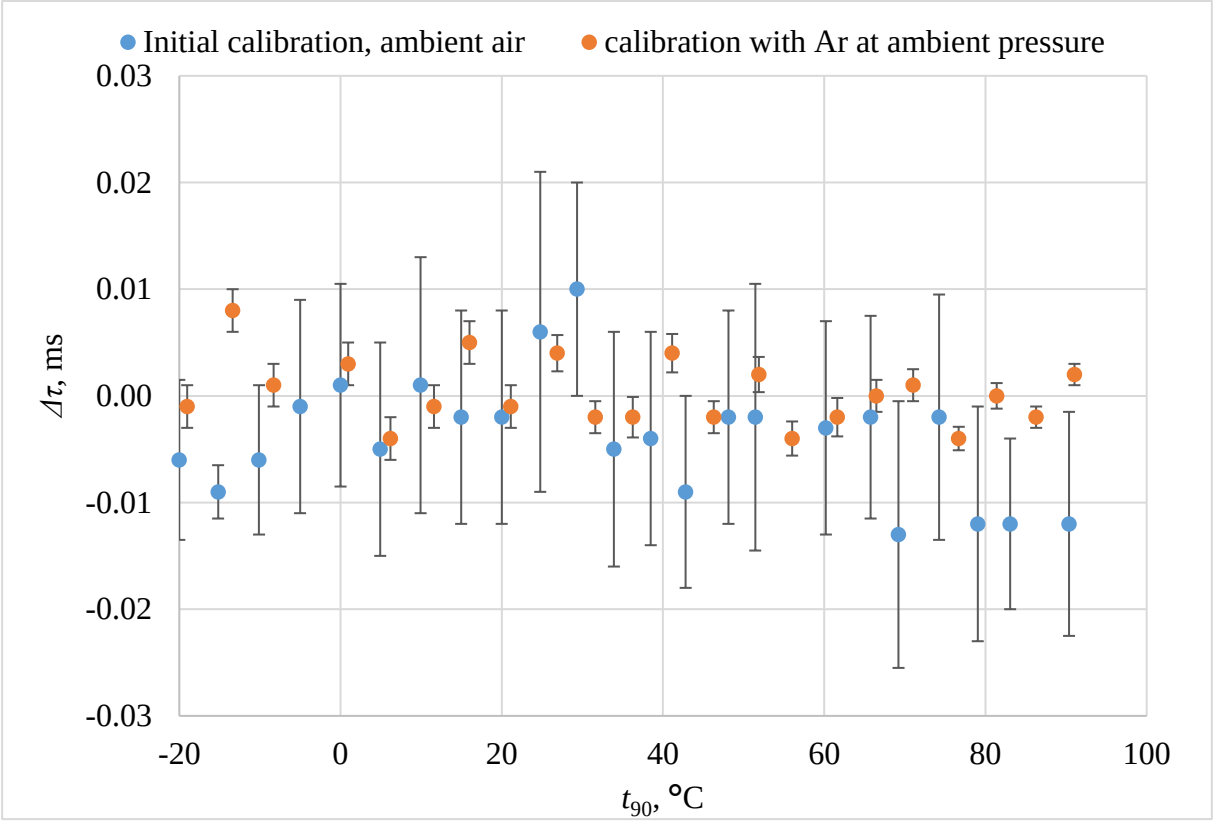

Figure 28: The result of the calibration of PAT with Ar media at atmospheric pressure in the range of (-20 to 90) °C

In the individual parts of the measuring set, chokes were tested to suppress the influence of a possible ground loop in the circuit (42 mH, 118 Ω) and (1.6 mH, 1.5 Ω) and they did not have any effect on the measured signal, so they are assumed not needed.

5.1.2.2. Influence of working frequency

Before the noise reduction (described in part 5.1.2.1), the dependency of the standard deviation (of measured τ values) on the frequency of the initial pulse was measured with the Ar media in the range of (15 to 89.5) kHz at the ice point (melting ice at 0 °C, explained in [19]) and in calibration ethanol bath Fluke at 0 °C. Measurement results are shown in Figure 29 and are caused by inner waveguide dimensions in relation to the wavelength of the sound.

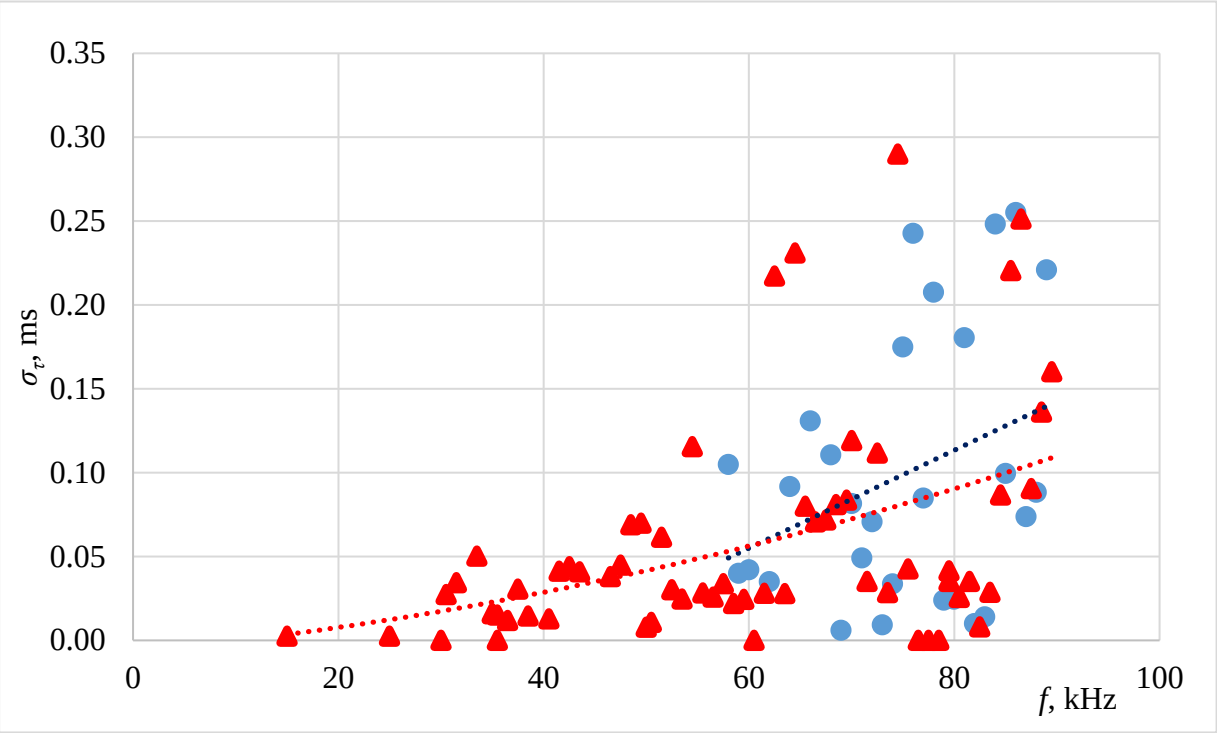

Figure 29: Dependence of the standard deviation of the measured τ on the frequency of the excitation pulse. Measurement in calibration bath at 0 °C in blue, measurement in melting point of ice (0 °C) in red.

The sound field in the waveguide can be generally divided into 3 different types, depending on the wavelength of the initial acoustic pulse in relation to the inner diameter of the thicker (of the two) waveguide sections. If the sound wavelength λ is greater than the biggest longitudinal internal dimension of the waveguide l_P, i.e.

$$l_P < \lambda, \tag{38}$$

a pressure field will be created (details in [112], Chapter 5) and energy reflections from the diameter reduction, or ends of the waveguide, will not be detectable in the signal. If such a case does not occur, but the wavelength is still greater than the largest transverse internal dimension of the waveguide l_T, thus

$$l_T < \lambda < l_P, \tag{39}$$

then ideally plane waves propagate into the waveguide from the source. In the third case for

$$\lambda < l_T \tag{40}$$

the waves propagate with spherical wavefronts and multiple reflections occur which cause interferences and with increasing difference between λ and l_T the significance of interferences

increases (see [113], chapter 13). The dimensions of the waveguide used to obtain data (shown in Figure 29) are described in Figure 15. Very simple MS Excel file calculator was created to ease the computation of suitable frequency of excitation pulse (screenshot in Figure 30).

INPUT	Waveguide length, mm	671		OUTPUT			
	Length of thicker waveguide part, mm	500					
					M_{air}	0.02897	g.mol-1
	Diameter of thinner waveguide part, mm	10			$C_{p\,air}$	1	kJ/kg.K
	Diameter of thicker waveguide part, mm	20		MAXIMUM frequency above which waves begin to propagate with spherical wavefronts and multiple reflections occur that cause interference	$C_{V\,air}$	0.718	kJ/kg
	R	8.3144598		f_{1K}, kHz 35.491	κ_{air}	1.39275766	
	κ	1.666559898		f_{2K}, kHz 17.746	l_{air}	0.172031	m
	M	0.039948	g.mol^{-1}				
	l	0.172031	m	MINIMUM frequencies below which a pressure field occurs and no reflections are detectable	M_{Ar}	0.039948	g.mol-1
	Temperature, °C	90.0		f_{3K}, kHz 0.529	$C_{p\,Ar}$	0.5203	kJ/kg.K
	Temperature, K	363.15	K	f_{4K}, kHz 0.710	$C_{V\,Ar}$	0.3122	kJ/kg
	tau, s	0.000969			κ_{Ar}	1.666559898	
	c, m/s	354.914			l_{Ar}	0.160274	m

Figure 30: Calculation of suitable frequency for the PAT from the waveguide dimensions

For the argon media, the calculated working range of usable frequencies is (0.593 to 14.816) kHz at -20 °C and (0.710 to 17.746) kHz at 90 °C. The dependence of σ on f was measured again after the noise reduction process (described in part 5.1.2.1) using argon gas at standard atmosphere and ambient temperature (23±2.5) °C. The results can be found in Figure 31 and the σ values by their magnitude prove the positive effect of the shielding and grounding process that was performed.

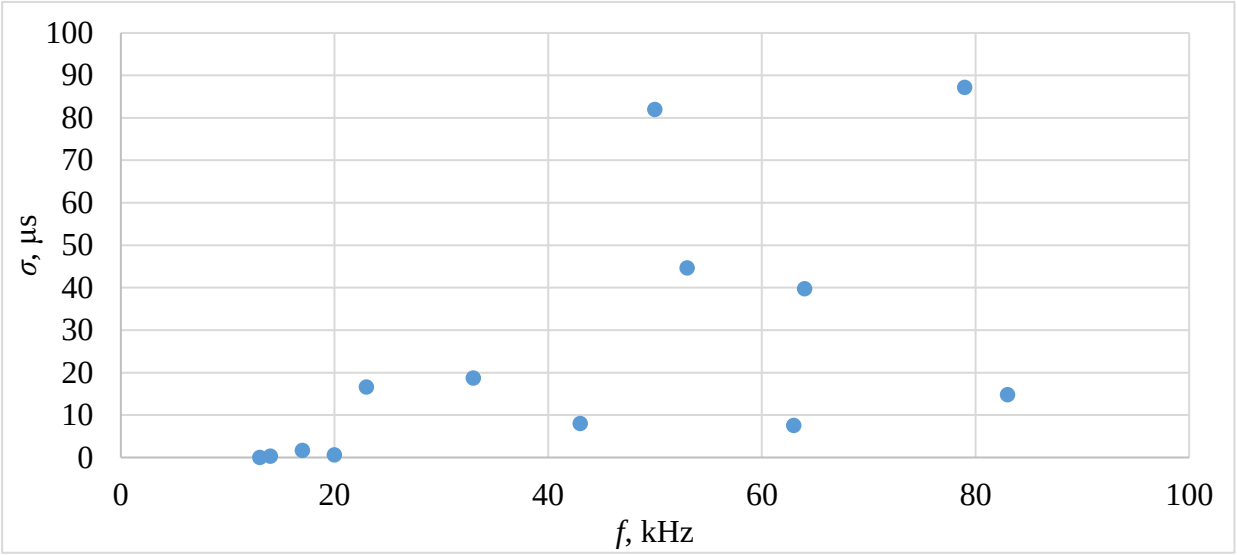

Figure 31: Dependence of the standard deviation on the frequency of the excitation pulse, Ar gas filling, standard atmosphere, 23 °C

Frequency work ranges of the waveguide depicted in Figure 32 are theoretically (0.593 to 29.633) kHz at -20 °C and (0.710 to 35.491) kHz at 90 °C. This waveguide allows operation with the working frequency outside the audio-frequency band and therefore for the following measurements, its value was set to be 25 kHz.

Repeated experiment results support the idea that to minimize the influence of the wavelength, the working frequency should be below 14.816 kHz for the given waveguide. However, the useful frequency range is unacceptable, since it is only in the audio-frequency band. This fact prevents the thermometer to operate in conditions of the common environment that includes the presence of a variety of outer parasitic sound sources.

The waveguide was therefore exchanged for the alternative (slightly thinner) model, which was supplied together with the previous one by the manufacturer. Dimensions can be found in Figure 32.

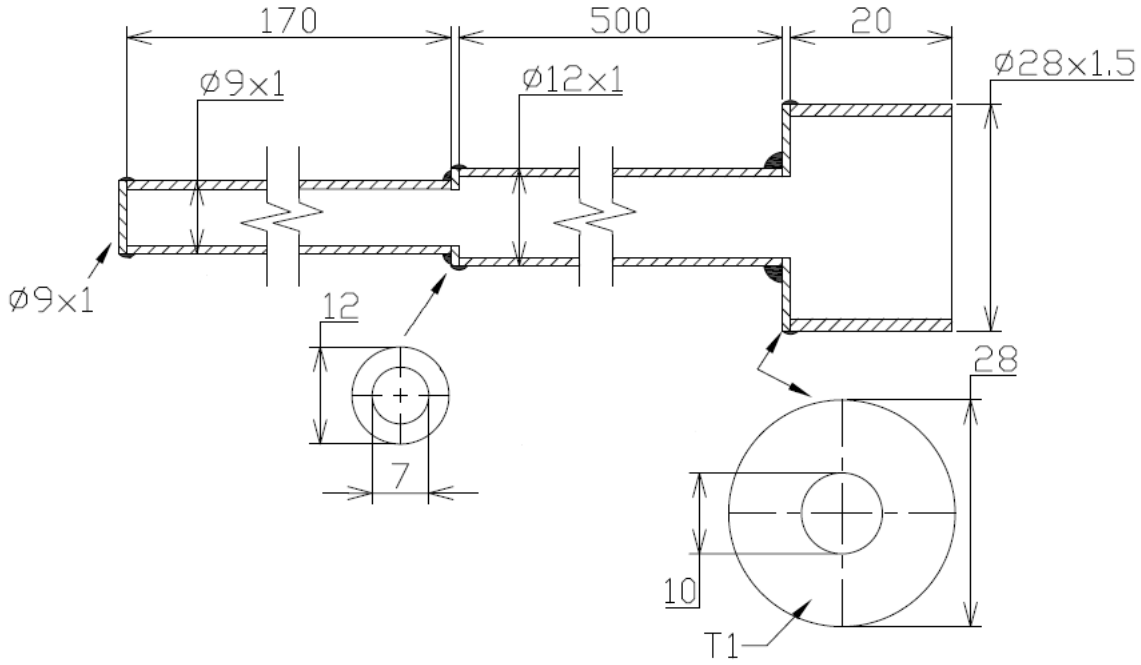

Figure 32: Dimensions of the waveguide used to move the minimum working frequency out of the audioband

5.1.2.3. Time resolution and interpolation test

The time resolution $\Delta\tau_R$ of the PXI-4461 module limits the thermometer precision and is the largest uncertainty contributor. The current measurement system (its time resolution) could be enhanced by implementing a faster acquisition system, e.g. NI PXIe-5160 oscilloscope module which is the easiest to implement but not a cost-efficient solution, since the thermometer should be an affordable system.

The interpolation of the measured data represents the possibility to enhance the time resolution up to 10x (as mentioned e.g. in [89]) and because the standard deviation (shown in Figure 31) is comparable to $\Delta\tau_R$, a success rate of the interpolation was tested in this section.

Although the entire PAT system was powered from the same power source through a voltage stabilizer with an Advance 552G filter, s.n. 101, during operation in a cryostat with an ethanol media, the measured signal was disturbed in a way that made the measurement impossible. This phenomenon was probably caused by leaks in the waveguide that were later found in Chapter 5.1.3.1. The next Chapter deals with vacuum and pressure tightness testing and the effort to eliminate eventual leaks. Therefore, the single-zone furnace Isotech ITL M17701, s.n. 13588-4 (Figure 33) in which there was no interference was selected for subsequent tests. As a standard thermometer, Fluke 5683, s.n. 4228, connected to the ratio resistance bridge ASL F300, s.n. 009017/03 was used.

The LabVIEW environment offers several interpolation methods (listed in [114]) already available in a basic setting. The "Interpolate 1D Fourier VI" function, described in [114], was selected for its simplicity of implementation and the possibility to easily set the so-called interpolation factor *n*, for which it applies that

$$L = n \cdot l, \tag{41}$$

where l is the number of vector values before interpolation and L is the number of vector values after interpolation. The function provides interpolation by transforming the input signal into the frequency domain and then zero-padding the spectrum, according to the selected interpolation factor. In the next step, the correction of the asymmetry of the spectrum and the back transformation into the time domain are done. [114]

Figure 33: PAT in Isotech ITL M17701 calibration furnace

Figure 34 shows the theoretical temperature resolution of the PAT, corresponding to the time resolution (in ms) that can be achieved by the interpolation process at various temperatures of the measured environment. According to theoretical assumptions based on [89], the minimum achievable $\Delta\tau_R$ should be equal to 1 µs, thus 10 times enhancement (red line in Figure 34).

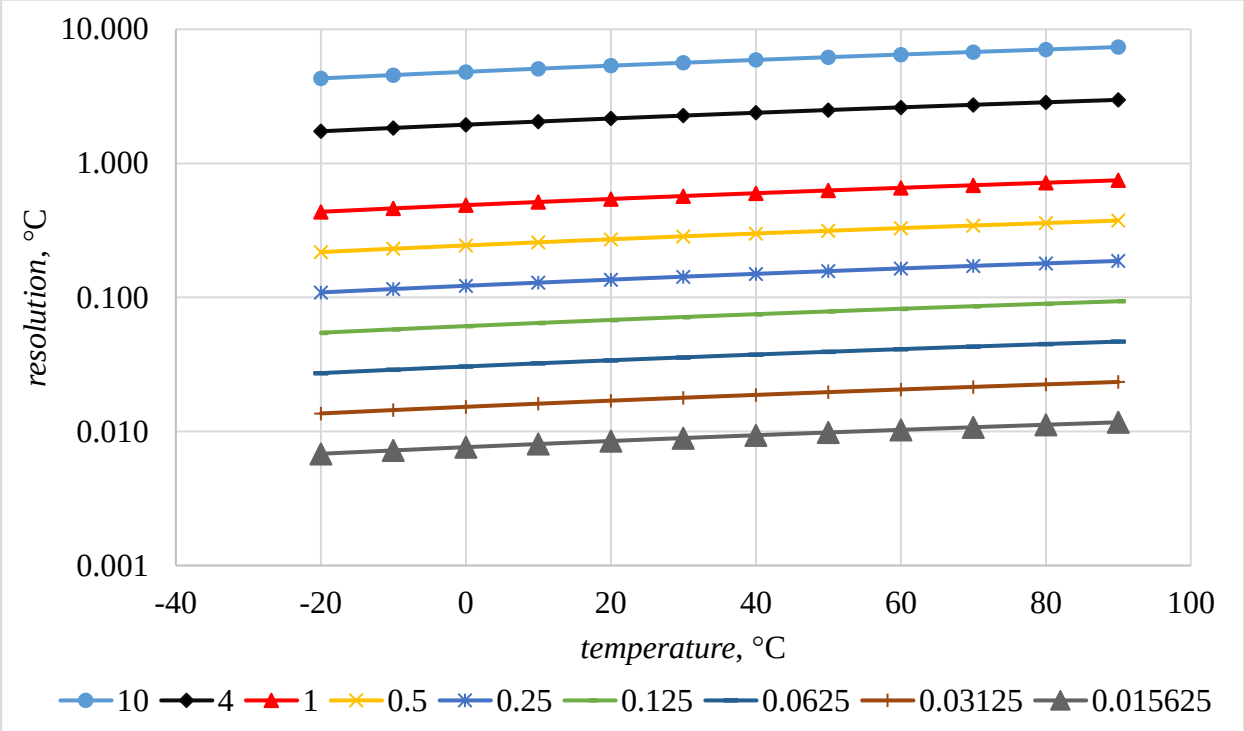

Figure 34: Theoretical temperature resolution dependence on the temperature for different time resolution values from 0.015625 to 10 (in µs) that can be achieved by the interpolation process

The results of interpolation tests at nominal temperatures of (50, 60, 70, and 80) °C are shown in Figure 35. The RAM of the desktop PC, which is part of the PAT measurement system, allows the use of an interpolation factor with a maximum value of n=1024. Although temperature resolution seems to increase with increasing time resolution infinitely, the best achieved measured time resolution, with *n* varying from 4 to 1024, was equal to 1 µs which is in agreement with the statement in [89].

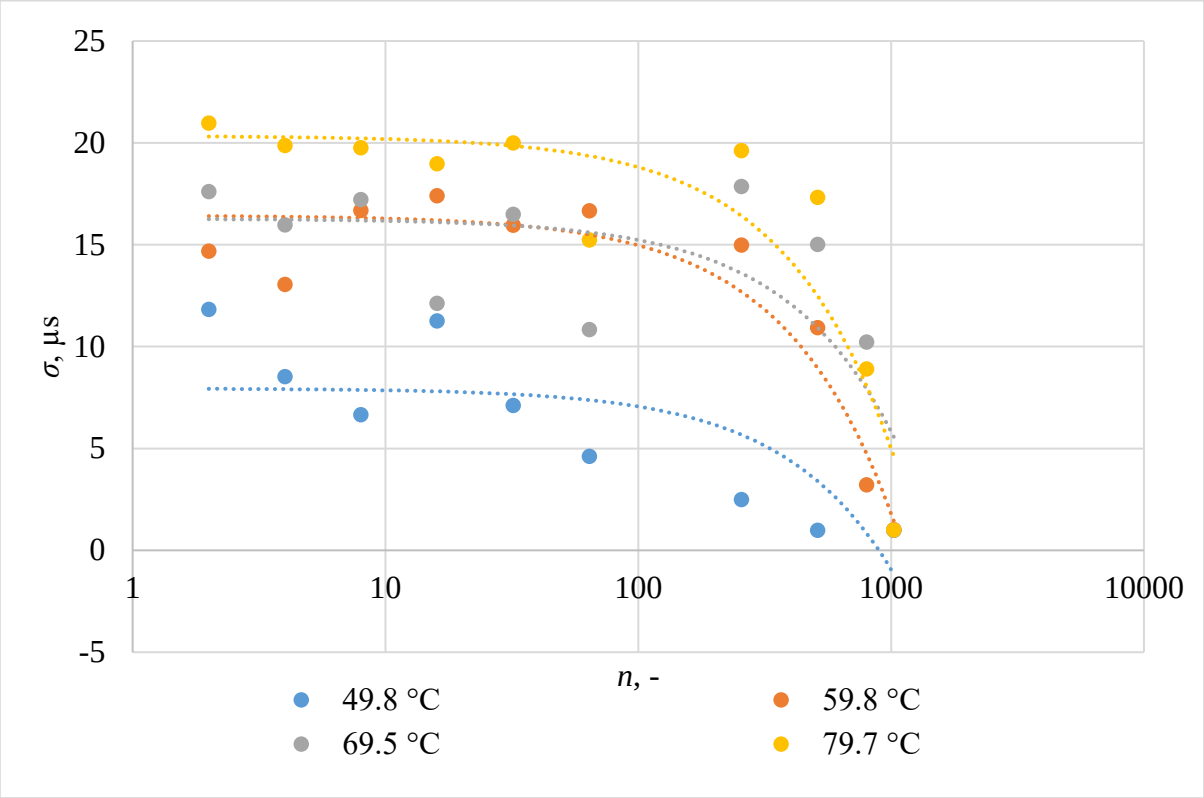

Figure 35: Dependence of the standard deviation of the measured data on the interpolation factor n

The example of measured *τ* data at 49.8 °C nominal is shown in Figure 36. The interpolation is successfully implemented and leads to results corresponding to the theoretical assumption, i.e. the resolution of 1 µs.

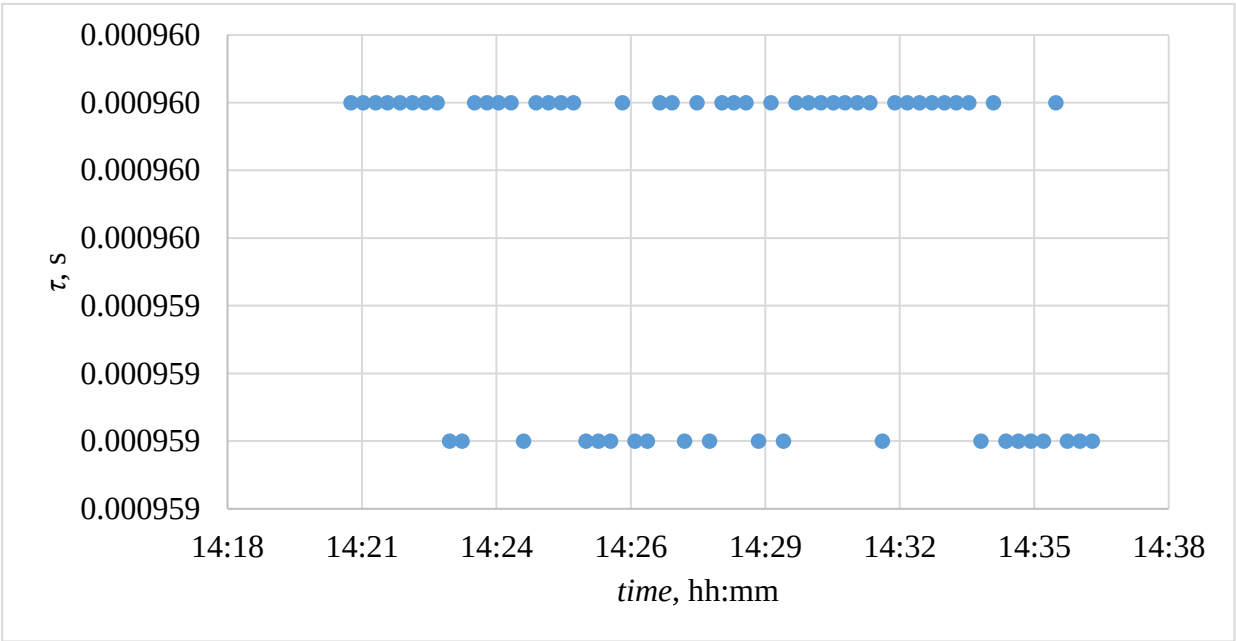

Figure 36: The example of measured τ data after implementation of interpolation to the acquisition routine, nominal temperature 49.8 °C

5.1.3. Transformation to a portable system

The original equipment was partially replaced to allow the mobility of the acoustic thermometer. The NI PXI 1031 DC chassis (used to power measurement cards and for communication with a PC) does not allow communication with laptops and therefore the PXI system was replaced by the Siglent SDG1025 Function/Arbitrary Waveform Generator and the OWON SDS8302 300 MHz, 2.5 GSa/s digital oscilloscope. Additionally, Microtech Gefell MN 921 units were replaced by Bruel & Kjaer 2690-A NEXUS Conditioning Amplifier. The current equipment is depicted in Figure 37.

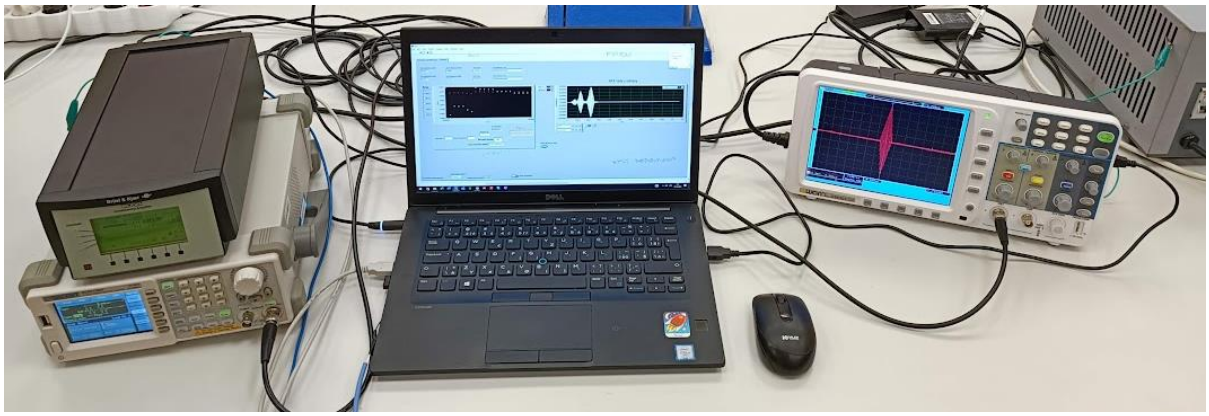

Figure 37: Equipment used in the portable version of PAT

The main difference from the previous configuration is replacing the NI PXI-4461 module continuously measuring the input channel data by the oscilloscope tracing the current signal of a limited length. Therefore, new control and measurement application was created in the LabView environment setting all the devices, performing the measurement and evaluation of the results and storing measured data into the data file. The previous measurement procedure is shown in Figure 38. The initial burst (described in Section 5.1.1.1) is continuously repeated and transmitted to the output channel of NI-4461 Dynamic Signal Analyzer that is connected to the PAT system. Voltage signal from the microphonic measurement (subsequently amplified) is acquired by the same NI-4461 module at the input channel. The measurement period is limited by RAM of associated desktop PC, allowing 10 seconds long record. After the data acquisition is completed, the bandpass filter clears the signal from components of unwanted frequencies. Whole data vector is then split into several signals, each containing one initial burst and one zero-signal part (serving to measure echoes from the waveguide).

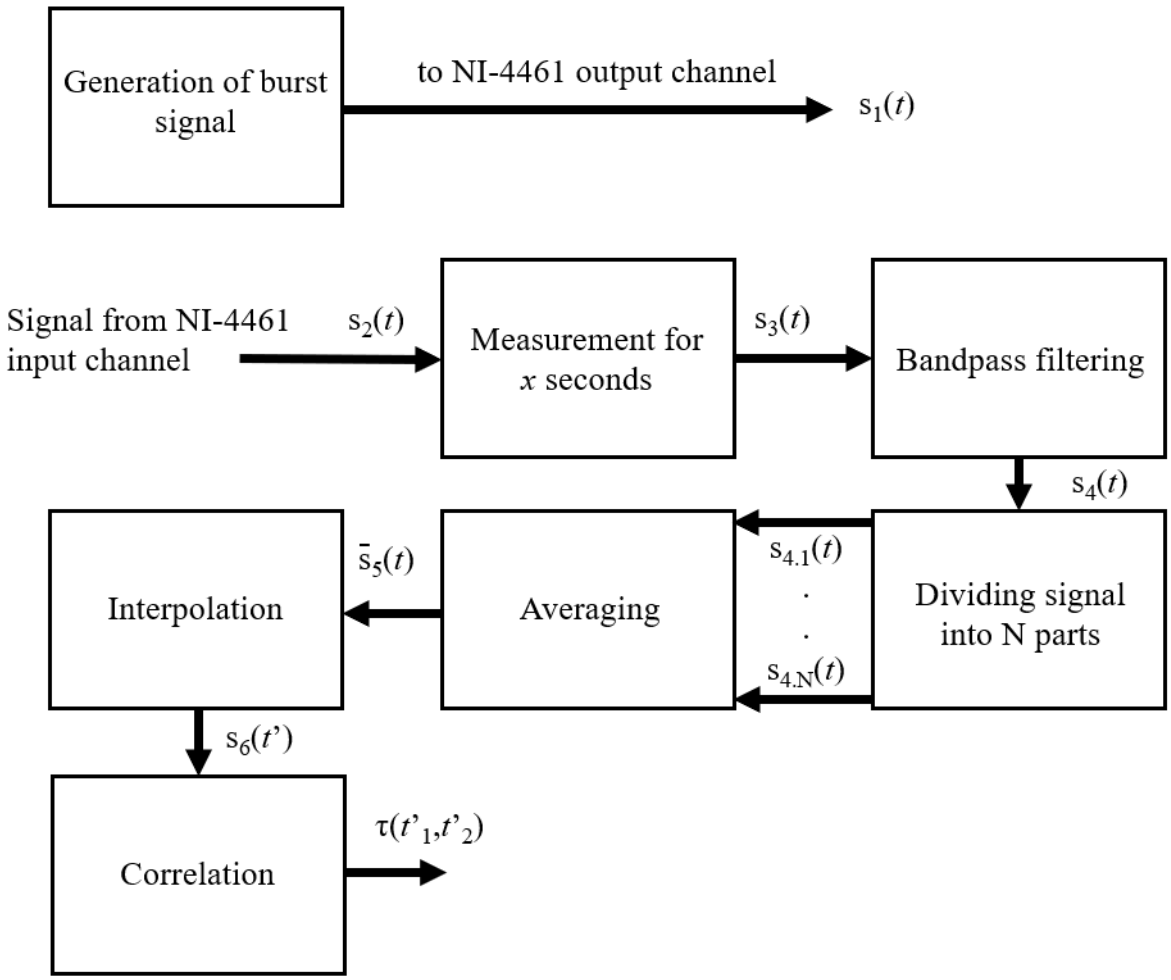

Figure 38: LabView measurement procedure used for static PAT system

The averaging removes random noise components and produces mean signal, that can be subsequently interpolated to reach a total measurement resolution of 1 μs. The time-of-flight value is calculated from the correlation function, thus the τ is calculated and the speed of sound can be derived.

A portable system was assembled with the effort to keep all the measurement settings as similar to the previous setup as possible. However, some differences result from the change of the equipment. The current measurement procedure associated with the new setup is shown in Figure 39. Although the signal is produced by standalone signal generator, the initial setup of this device (and also of the oscilloscope) preceding each measurement is carried out by the same LabView application that is providing the whole measurement process. While the initial burst is produced by the waveform generator, the oscilloscope is focused on the signal area 7.6 ms wide, containing one period of the transmitted burst and received echoes from the waveguide. Mean filtering is provided by the oscilloscope itself i.e., the acquired data are represented by currently displayed data on the oscilloscope screen. Those data are then interpolated, and to reduce the noise, the data are also subsequently subject of moving average process. The correlation then serves to work out the τ value from resulting post-processed data. During the development of the system, parameters of the initial burst were optimised. The amplitude was raised from 10 V_{PP} to 20 V_{PP} which enhanced SNR significantly. The sinusoidal part of the burst was curtailed from 0.5 ms to 0.3 ms and the "silent interval" (described in Section 5.1.1.1) was curtailed from 24 ms to 6 ms. It enabled data averaging with higher number of measurement cycles (containing transmitted burst and echoes from the waveguide) per time unit than in previous burst configuration.

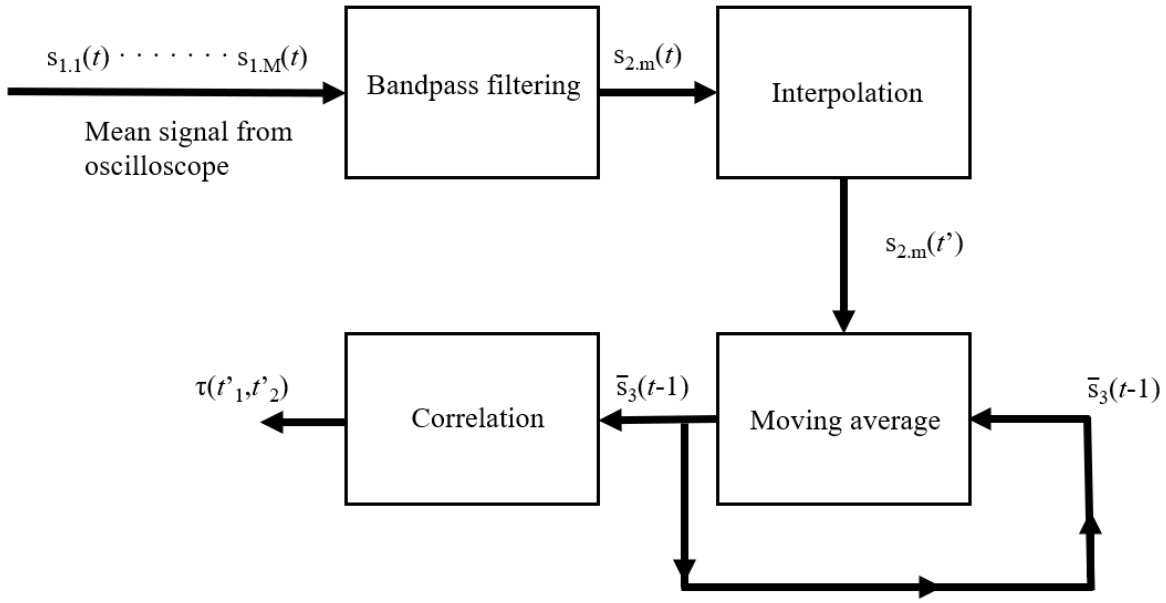

Figure 39: LabView measurement procedure used for portable PAT system

The resulting time resolution of the measured τ data is 12.5 ns, which corresponds to temperature resolution of about 6.35 mK at -20 °C, raising to approx. 9.1 mK at 90 °C.

5.1.3.1. Vacuum and gas tightness

To enable extrapolation of measurement results to the zero-pressure speed of sound, it is necessary to provide vacuum–tightness and pressure tightness of the PAT body (shown in Figure 27). It consists of the waveguide, rubber gasket, lid with gas port, electrical feedthrough and feedthrough for the microphone preamplifier. Multiple attempts were performed to make PAT vacuum and pressure tight. The PAT body was connected to the mobile gas management system (see Figure 40). It is made of aluminium construction, wearing the gas pressure vessel, tubings with valves to enable evacuation and filling the system with gas from the vessel as well as the valve to vent the system to the surrounding atmosphere, Yokogawa DPharp EJX310A pressure gauge with transmitter and Pfeiffer HiPace 80 + HiCube 80 Eco vacuum pump.

Figure 40: The mobile gas management system connected to PAT

The process of evacuating to test vacuum tightness can be seen in Figure 41 and the detail of those curves is shown in Figure 42, indicating the minimum achieved pressure levels. The process of filling with gas to about 150 kPa (absolute) was applied in order to find places where gas leaks. Linde HQ Leak Detection Spray (having the effect equivalent of soap water) was used to find locations of leakages at each overpressure state and BISON High Temp Silicone glue was then applied to seal each leakage that was found.

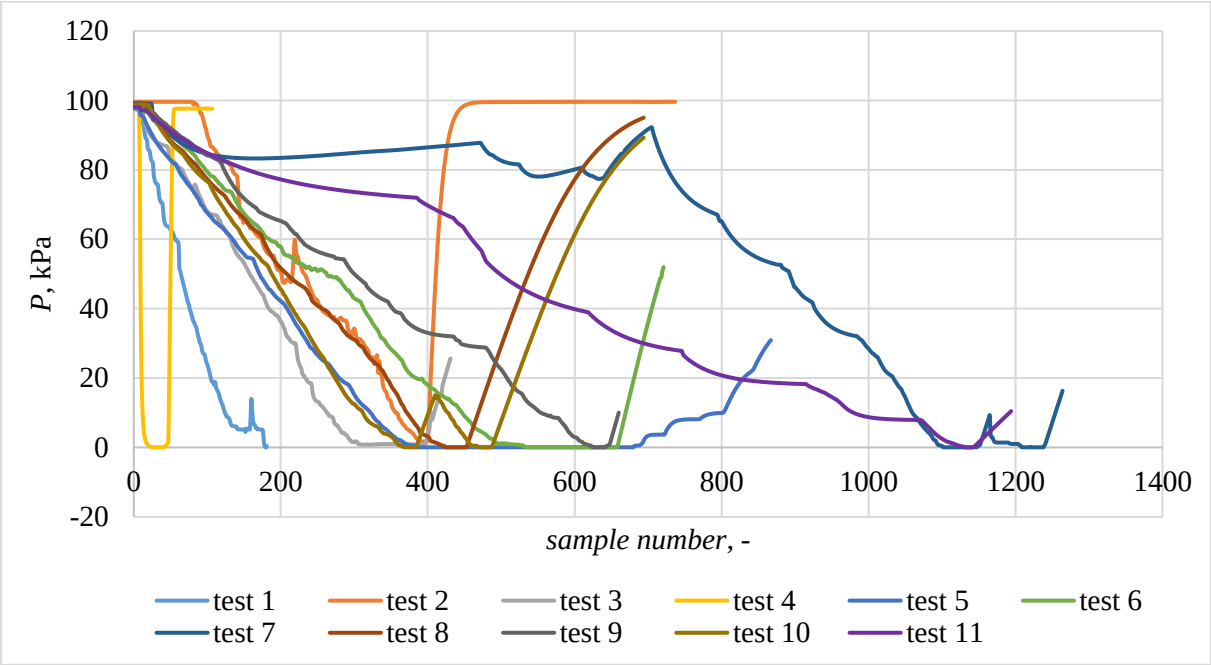

Figure 41: Evacuation curves

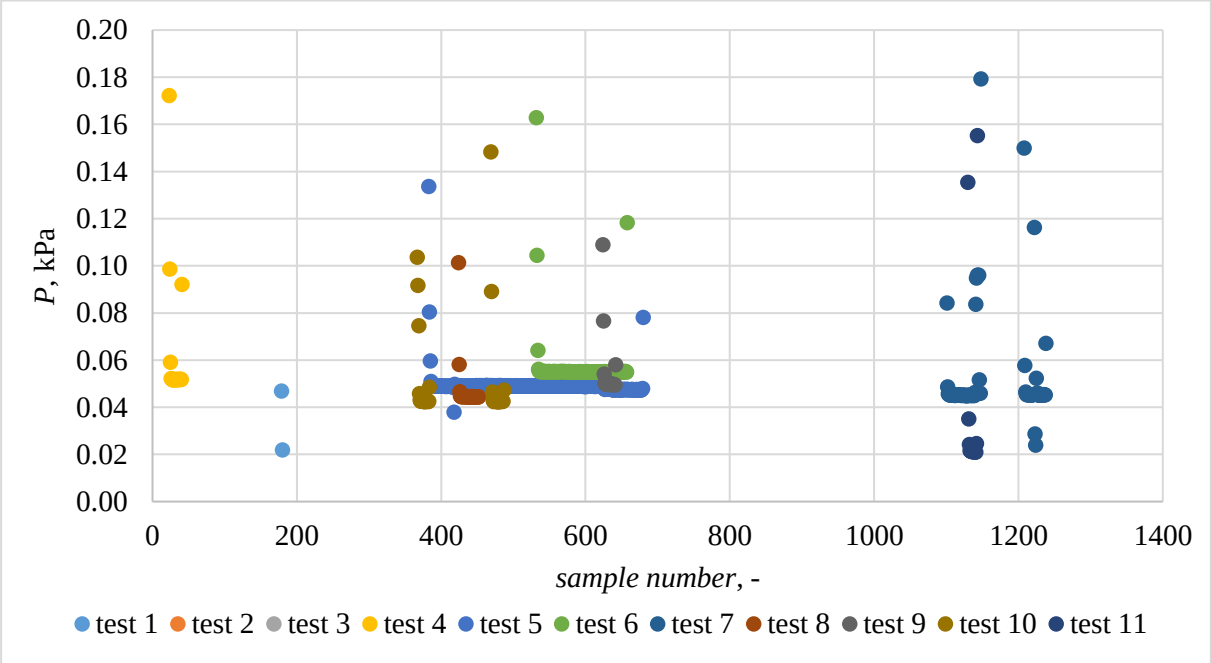

Figure 42: Detail of evacuation curves

5.1.3.2. Temperature and pressure characterisation

The lowest pressure achieved inside the waveguide was 0.021 kPa and during the last pressurization, no place with a visible gas leak was found. For each temperature calibration point, after the temperature had stabilized, the PAT was filled with argon to at least 150 kPa. Subsequently, τ was measured with decreasing pressure until the equalization with the surrounding environment, including this state. Then the thermometer was slowly evacuated and the measurement was carried out again until the pressure and temperature equalized with the surrounding environment.

Parts with stable temperature and pressure were selected for evaluation of measured data. Such postprocessed recording of pressure and τ is shown in Figure 43. Theoretical τ is calculated from t_{90} temperature measurement using SPRT. Symbol $\Delta\tau$ in graphs below denotes the measurement error, i.e. the difference between measured τ and theoretical τ.

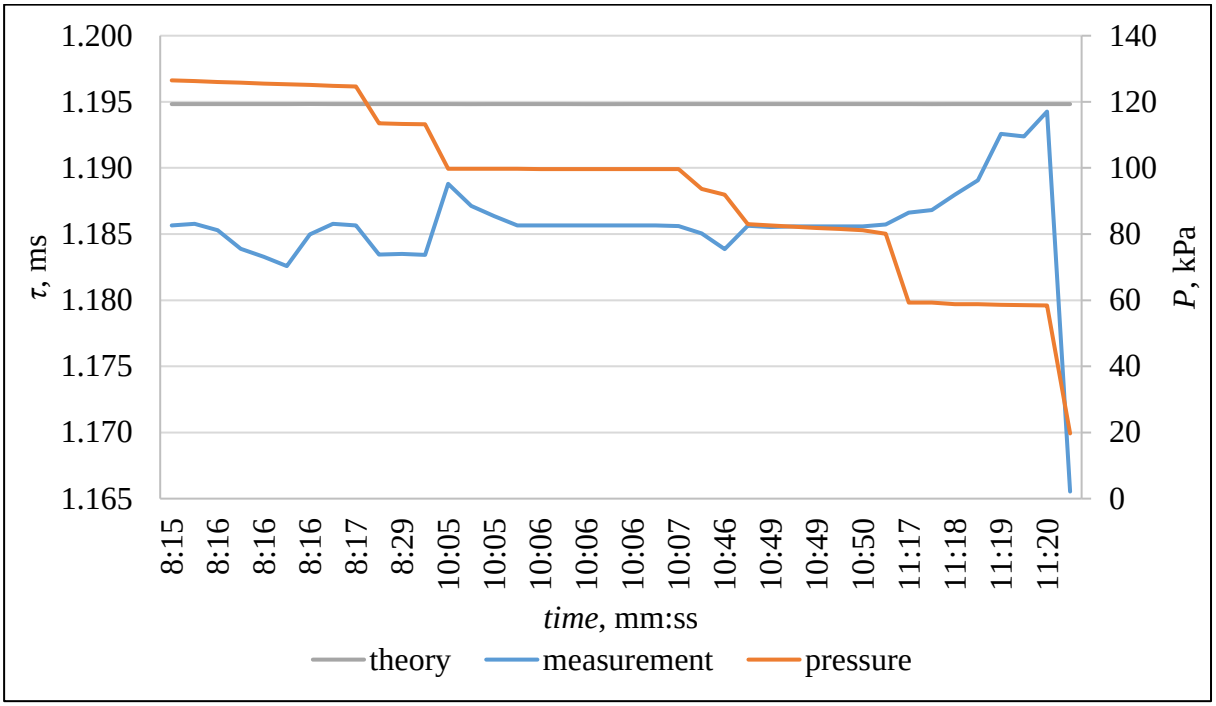

Figure 43: Postprocessed recording of pressure and τ – measurement at -40 °C nominal

The t_{90} temperature measurement was performed by Tinsley 5187SA SPRT with s.n. 268711 from -80 °C to 0 °C, Tinsley 5187SA SPRT with s.n. 238690 from 0 °C to 140 °C and Fluke 5683 SPRT with s.n. 4219 in the range from 140 °C to 220 °C. SPRTs were connected to WIKA CTR9000 resistance ratio bridge with s.n. 022759/01 and two Tinsley 5685A electrical resistance standards (25 Ω nominal resistance with s.n. 280158 and 100 Ω nominal resistance with s.n. 279875) were employed to enable resistance ratio to temperature calculations.

Three temperature-controlled enclosures were employed according to the temperature of measurement. For the range of (-80 to 20) °C, the Fluke 7381 cryostat filled with ethanol was used. The range from 40 °C to 80 °C was covered by Tamson T.X.V.M.B.70/230 thermostatic bath, filled with distilled water. Finally, the Pemit OL250 bath, using silicone oil was used to cover the range from 80 °C up to 220 °C. At temperatures above 160 °C, additional surface thermometer served to check that the temperature of the waveguide (2 cm below the location of transducer, see Figure 44) does not exceed 50 °C, which is the maximum operating temperature of the preamplifier (attached to the transducer).

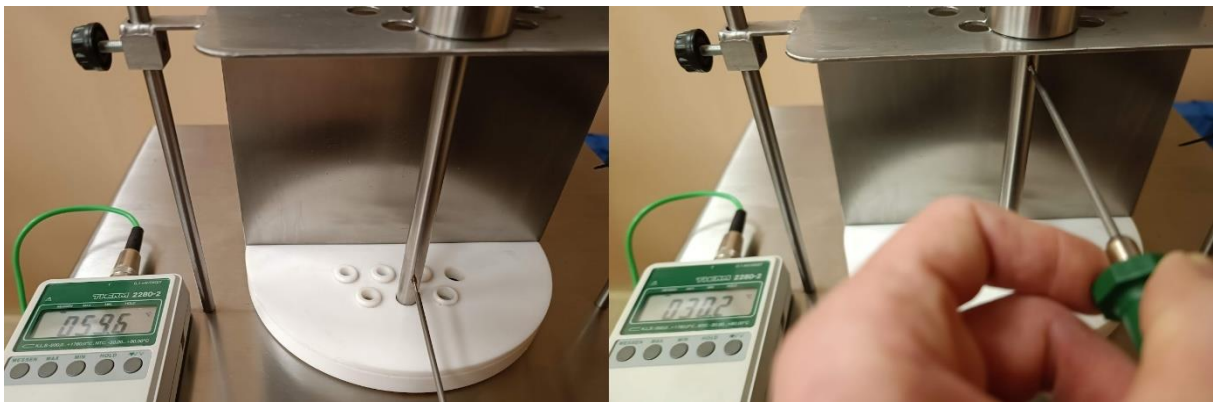

Figure 44: Surface temperature measurement, temperature in bath is 220 °C nominal

The total temperature range was (-80 to 220) °C nominal. Due to the amount of measurement points, results are shown in three figures (range (-80 to 60) °C in Figure 45, range (80 to 200) °C in Figure 46 and 220 °C in Figure 47) for better clarity. Symbol $\Delta\tau$ denotes the difference between τ measured by PAT device and τ calculated from SPRT measerement.

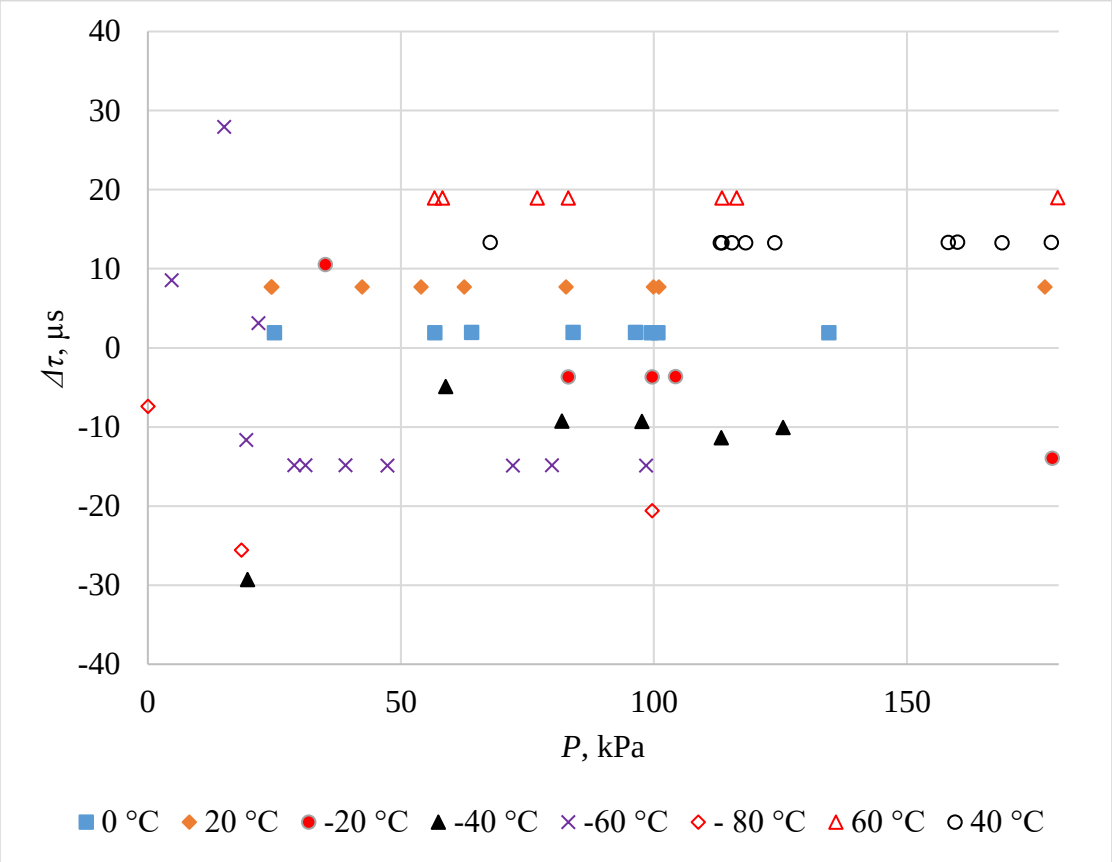

Figure 45: Results of temperature and pressure characterisation (from -80 °C to 60 °C)

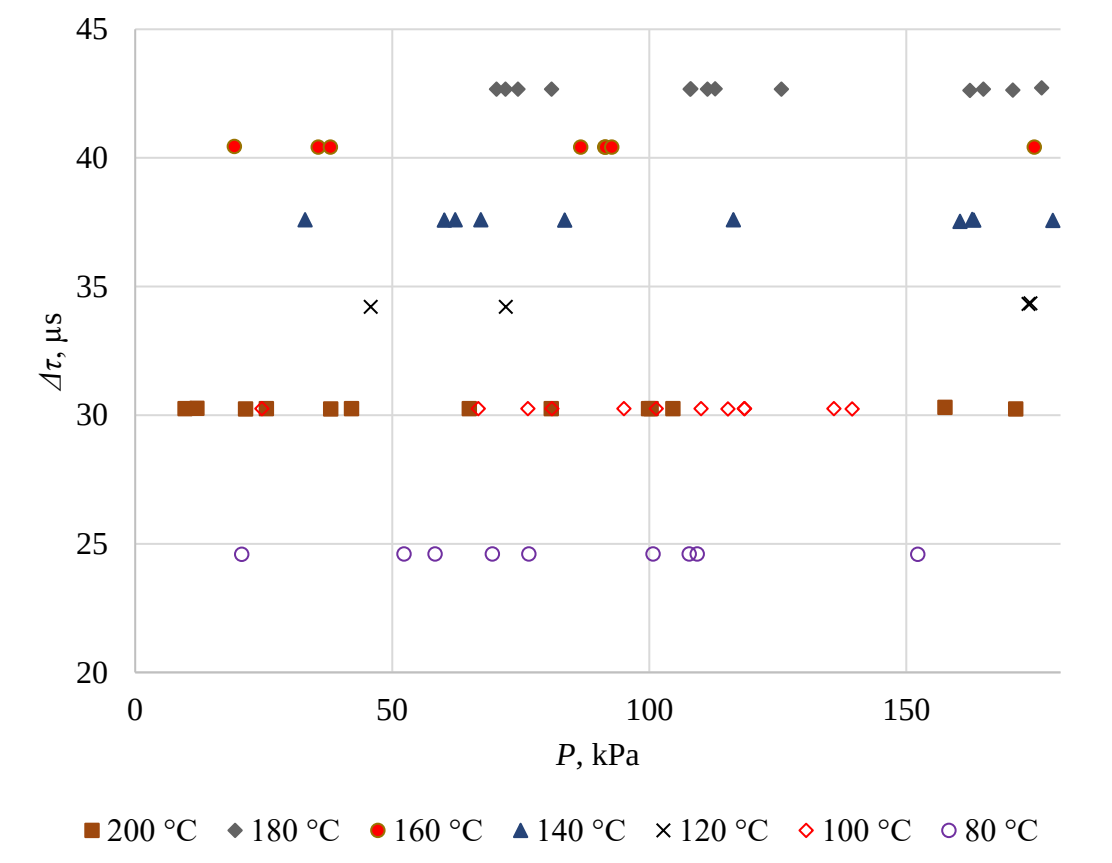

Figure 46: Results of temperature and pressure characterisation (from 80 °C to 200 °C)

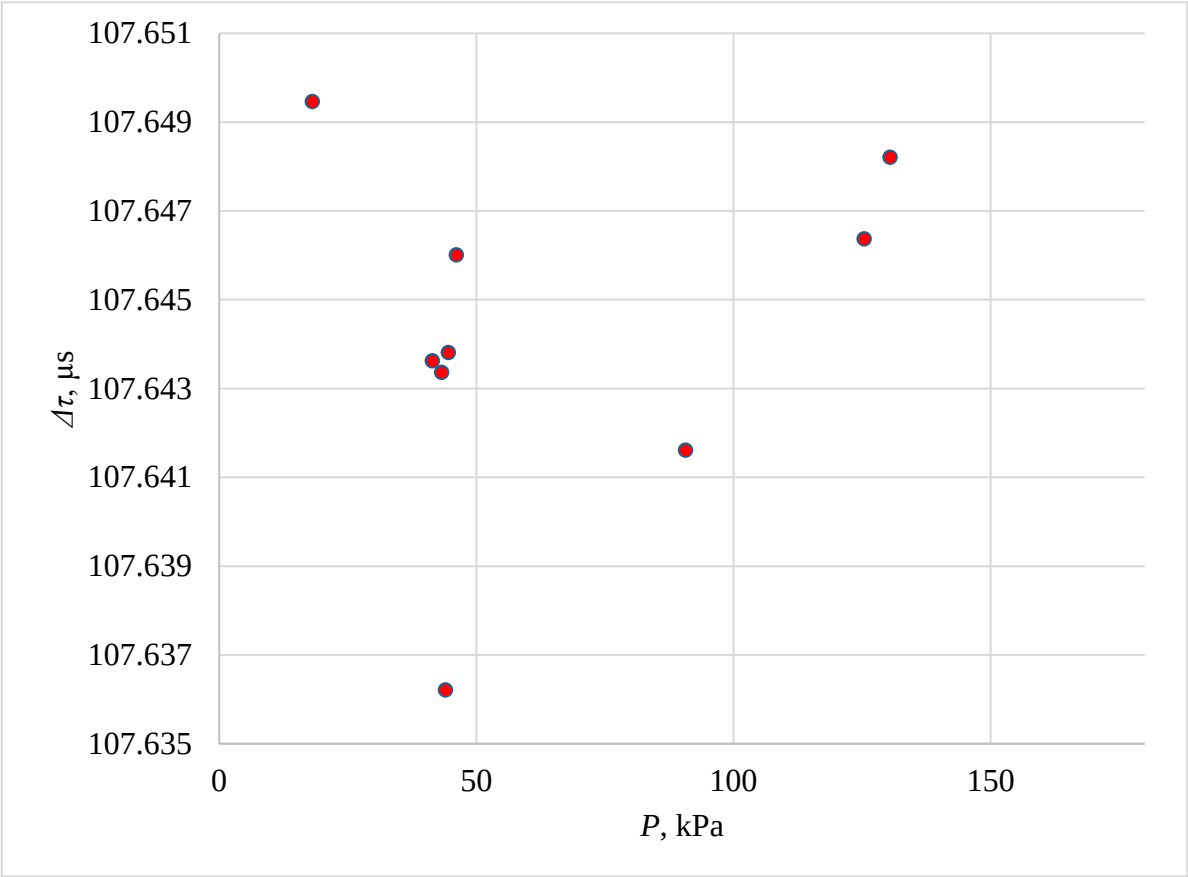

Figure 47: Results of temperature and pressure characterisation at 220 °C

It is evident that the magnitude of measurement error raises significantly below the pressure of about (20 to 40) kPa, while values above this pressure range vary only slightly, equivalent to temperature changes of the liquid bath. Example can be found in Figure 48. At higher pressure (above approximately 140 kPa), small leakages in the PAT body caused raise in absolute value of measurement error as well.

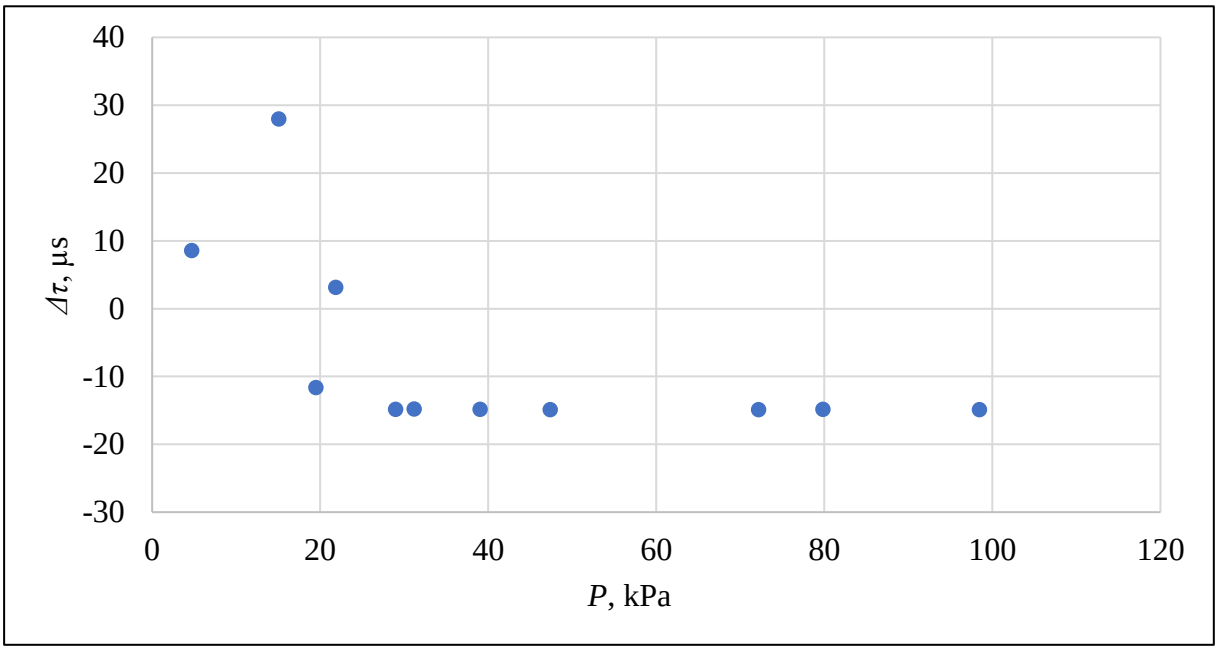

Figure 48: Pressure dependence of measured Δτ at -60 °C nominal temperature

The influence of pressure on measurement results were not found, thus variations in pressure during measurement of PAT prototype, filled with Ar at approx. 100 kPa have an effect smaller than the resolution of PAT is. Therefore, the uncertainty contribution associated to pressure variations is assumed to be zero. Measurement results for pressure close to 100 kPa are summarized in Figure 49. Upper temperature limit of the PAT prototype is probably caused by the fact that although the surface thermometer indicated sufficiently low temperature of the waveguide, the temperature was probably higher inside the waveguide resulting in operation outside the temperature limits of microphone and preamplifier.

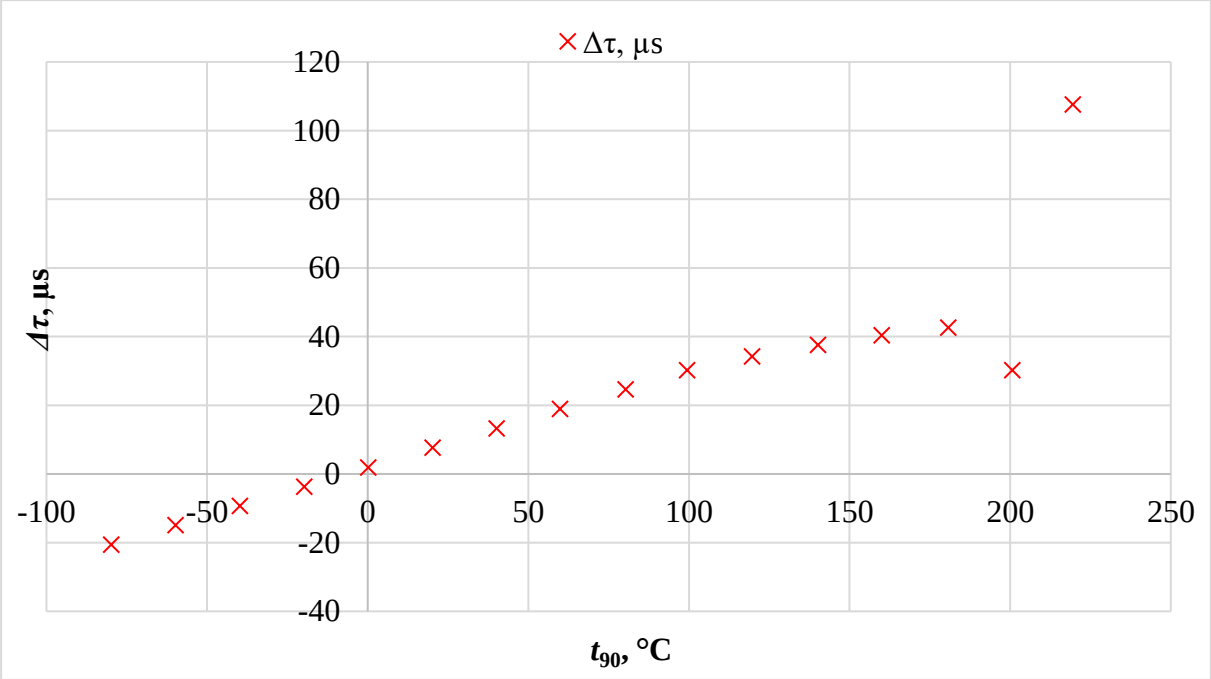

Figure 49: Measurement results for pressure close to 100 kPa

When neglecting measurement results at 200 °C and 220 °C, the $\Delta\tau$ data presented in Figure 49 can be fitted by polynomial function as shown in Figure 50.

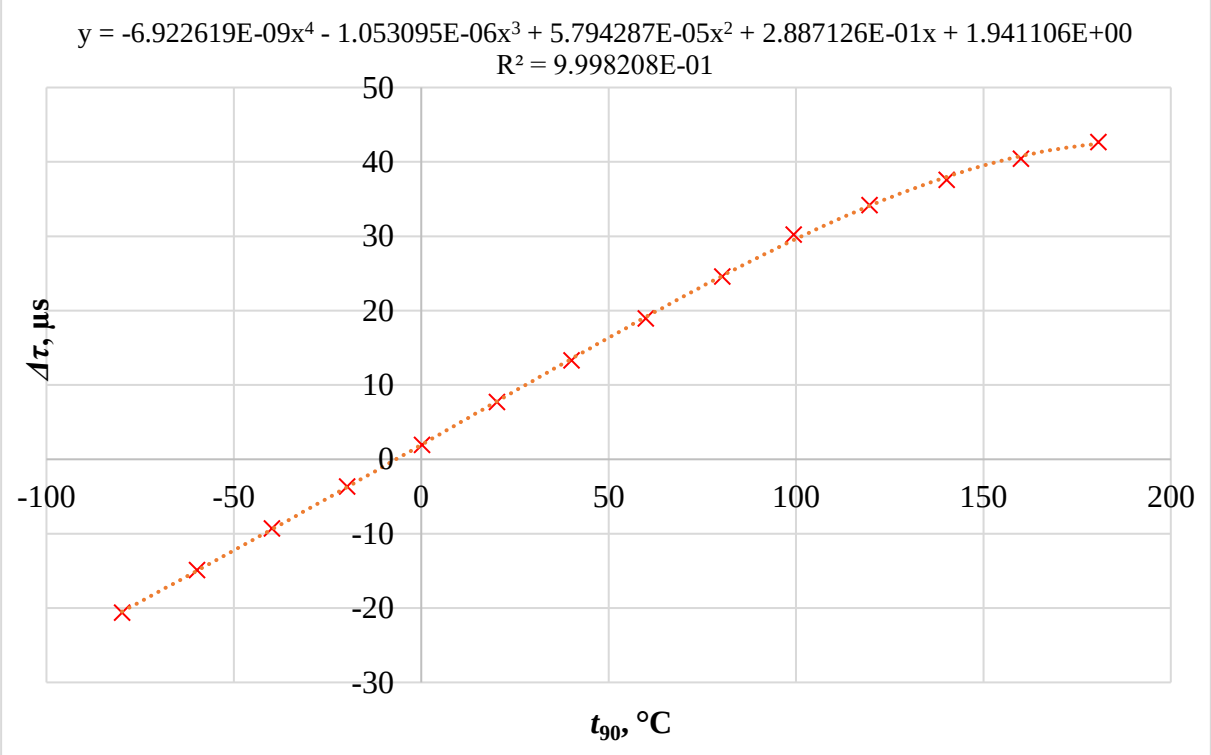

Figure 50: Measurement results for pressure close to 100 kPa and temperature range (-80 to 180) °C

Corresponding differences $\Delta\tau_{measured}$- $\Delta\tau_{fitted}$ are indicated by Figure 51.

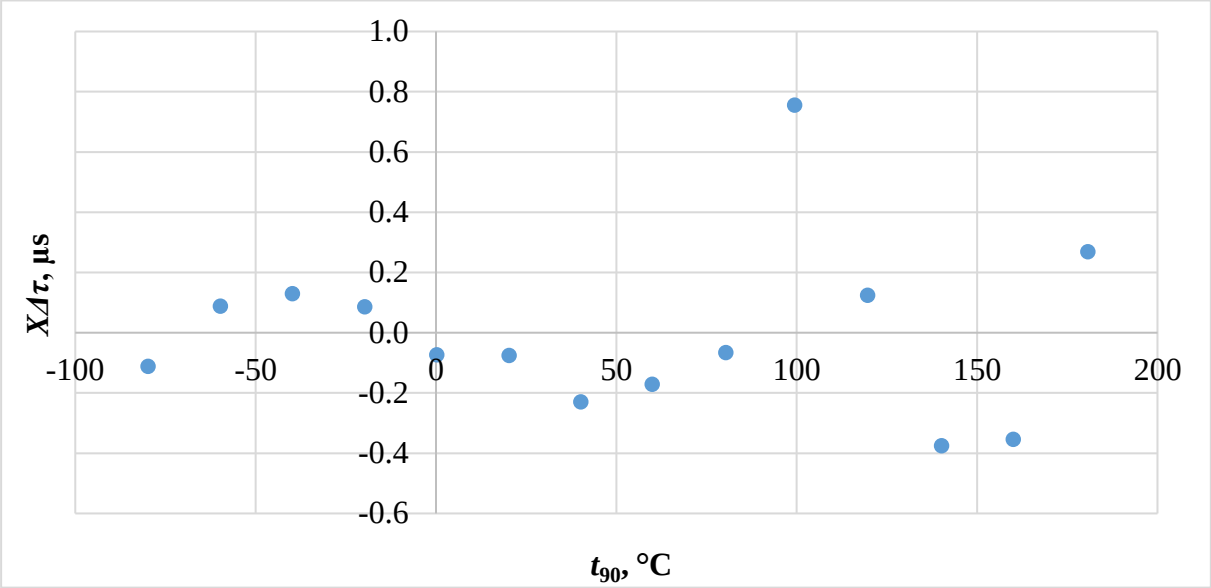

Figure 51: Error of fitting

It is evident from Figure 51 that measurement above 100 °C nominal brings higher measurement error, possibly caused by high temperature (close to maximum working temperature of the microphone) present in the waveguide. The resulting fitting error is in the range from (-0.4 to 0.8) µs.

At temperatures below the dew point of Ar gas, arising condensation effect prevents the correct operation of the electrostatic transducer and causes additional attenuation of sound field energy, therefore the measurements were not performed below -80 °C.

5.1.3.3. Total measurement uncertainty budget

The measurement uncertainty of PAT is connected to all the sources associated with the measurement of τ and subsequent temperature determination, with mechanical properties of the waveguide, sound propagation, heat transfer, and other sources that can influence measured results. Combining Eq. (13) and Eq. (26), temperature relation to the time-of-flight τ can be expressed by the equation

$$T = \frac{4Ml^2}{\gamma R\tau^2}, \tag{42}$$

that applies to zero-pressure propagation. From the equation above, several contributions together with sensitivity coefficients to the uncertainty can be identified and corresponding sensitivity coefficients are summarized in Table 1.

Table 1: Sensitivity coefficients of thermometer to main uncertainty contributors

sensitivity coefficient	value
$\frac{\partial T}{\partial M}$	$\frac{4l^2}{\gamma R\tau^2}$
$\frac{\partial T}{\partial l}$	$\frac{8Ml}{\gamma R\tau^2}$
$\frac{\partial T}{\partial \gamma}$	$-\frac{4l^2M}{\gamma^2 R\tau^2}$
$\frac{\partial T}{\partial R}$	$-\frac{4l^2M}{\gamma R^2\tau^2}$
$\frac{\partial T}{\partial \tau}$	$-\frac{8l^2M}{\gamma R\tau^3}$

The total measurement uncertainty (denoted by $\breve{u}$ to be easily distinguishable from the speed of sound) is therefore

$$\breve{u}(T) = \sqrt{\left(\breve{u}(M)\cdot\frac{\partial T}{\partial M}\right)^2 + \left(\breve{u}(l)\cdot\frac{\partial T}{\partial l}\right)^2 + \left(\breve{u}(\gamma)\cdot\frac{\partial T}{\partial \gamma}\right)^2 + \left(\breve{u}(R)\cdot\frac{\partial T}{\partial R}\right)^2 + \left(\breve{u}(\tau)\cdot\frac{\partial T}{\partial \tau}\right)^2} \qquad (43)$$

and each component includes several contributors.

The molar mass calculation of the *n*-gas mixture is described by [115] as

$$M_{MIX} = \sum_{i=1}^{i=n} x_i M_i, \qquad (44)$$

i.e., the sum of the mole fractions of each gas x_i multiplied by its molar mass M_i. The average molar mass M of pure Ar is 39.948 kg·mol^{-1} and the purity of used argon gas, guaranteed by the manufacturer Linde is 99.999 % with composition (see Table 2).

Table 2: Gas limit composition declared by the manufacturer and calculated molar mass of resulting mixture for this composition

Substance	**Amount, %**	***M*, kg·mol^{-1}**	**M_i**
Ar	> 99.9990	39.948	39.94760
N_2	< 0.0005	28.0134	0.00014
H_2O	< 0.0003	18.02	0.00005
O_2	< 0.0002	31.9988	0.00006
CO_2	< 0.00005	44.01	0.00002
C_nH_m	< 0.00002	300.1888	0.00006
H_2	< 0.00002	2.016	0.00000

M_{MIX}, kg·mol^{-1}	39.9479
M_{Ar}-M_{MIX}, kg·mol^{-1}	0.0001

As mentioned in Section 2.1.4, the heat capacity ratio of a monatomic gas is equal to 5/3. To simplify the task of uncertainty in γ determination, the γ value is assumed to possibly vary with temperature by 0.001 %, following the gas composition in Table 2.

After the redefinition of several SI units in 2019, the molar gas constant value became fixed as 8.314462618 $J \cdot mol^{-1} \cdot K^{-1}$ and with associated zero uncertainty (see [116]).

The waveguide employed in this research was manufactured with the precision of 0.5 mm. The sound path l is equal to the inner length of the thinner waveguide part i.e., the waveguide part used for the speed of sound determination. It was measured as 169.97 mm at ambient temperature (23 °C) by a combination of a thin alumina rod, rubber O-ring and ProsKit PD-151 digital sliding scale with a resolution of 0.01 mm and calibration with an uncertainty of 0.01 mm. The waveguide is made of 1.4541 stainless steel with coefficient of linear thermal expansion between 20 °C and 200 °C equal (according to [117]) to $16.5 \cdot 10^{-6}$ K^{-1}. Assuming this value for the range from (-80 to 220) °C, the possible half-length of the sound path was calculated to vary from 169.29 mm to 170.52 mm. Corresponding correction is applied on τ measurement results that are shown in Section 5.1.3.2, Figure 50. If not applied, the uncertainty caused by thermal expansion would be ranging from 0.02 µs to 6.92 µs depending on measured temperature. During its normal operation, the PAT is employed with calibrated Rosemount 2088 pressure transducer, with the characteristics and uncertainty values shown in Table 3.

Table 3: Calibration results of Rosemount 2088 pressure transducer

***Nominal pressure*, kPa**	***ΔP* (pressurizing), kPa**	***ΔP* (evacuation), kPa**	***U*, kPa**
0.000	-0.080	-0.082	0.001
20.000	-0.092	-0.118	0.005
40.000	-0.101	-0.125	0.005
60.000	-0.103	-0.124	0.005
80.000	-0.112	-0.131	0.007
100.000	-0.105	-0.124	0.008
120.000	-0.102	-0.122	0.010
140.000	-0.115	-0.134	0.011
160.000	-0.113	-0.124	0.013
180.000	-0.122	-0.130	0.014
200.000	-0.122	-0.122	0.016

Calibration allows further corrections for errors in the indication of the device ΔP and the calibration uncertainty U is considered in the PAT uncertainty budget. The sensitivity of temperature measurement to pressure measurement uncertainty is given by pressure characteristics, determined in Section 5.1.3.2 as zero (or smaller than the resolution of the PAT prototype) in the range from 40 kPa to 140 kPa.

Uncertainty of Time of Flight τ resolution of the system, includes uncertainty of oscilloscope time determination, averaging during the measurement, precision of τ calculation and short-term drift of oscilloscope time base.

The total measurement uncertainty for the temperature range (-80 to 180) °C is shown in Figure 52 and the total measurement uncertainty budget for -80 °C nominal is shown in Table 4.

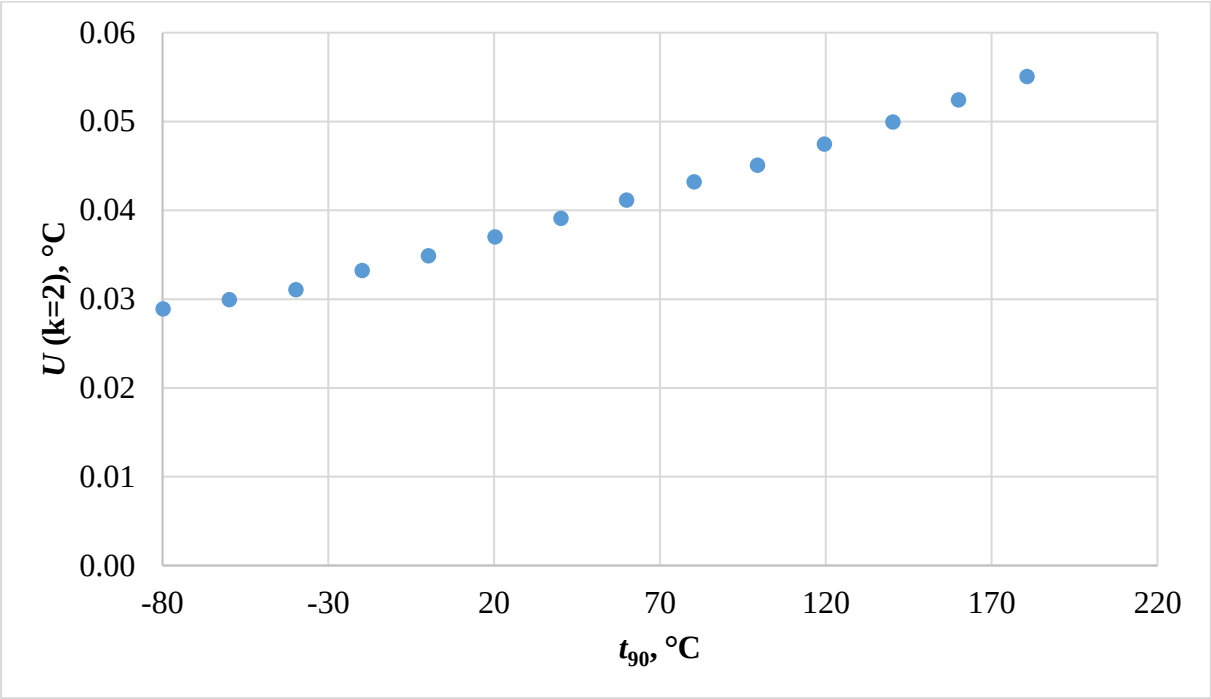

Figure 52: Total measurement uncertainty

It is evident from Figure 52 that the measurement uncertainty level is well below 0.15 °C which corresponds to IEC 60751 requirements for IPRT tolerance class A. Fitting error from Figure 51, expressed in °C and supplemented with measurement uncertainty is shown in Figure 53. It can be concluded, that in the range of (-80 to 80) °C the thermometer follows the IEC 60751 requirements for IPRT tolerance class A and IEC 60751 requirements for class B in the most of other measurement points.

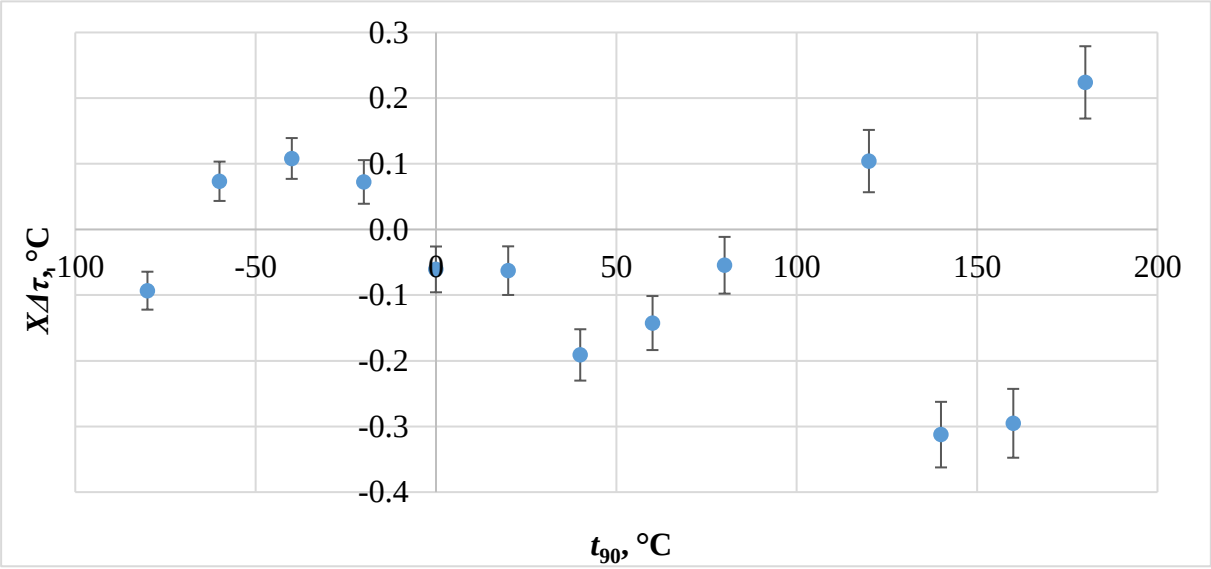

Figure 53: Fitting error supplemented with measerement uncertainty

Table 4: Measurement uncertainty budget for the nominal temperature of -80 °C

Uncertainty source	Value	z_{max}	Dimension	Distribution	k	u_x		Sensitivity	Dimension	u_x for k=1, °C	Source
Molar mass from gas composition	0.0399479	3.99E-07	g·mol^{-1}	rectangular	1.732050808	0.0000	g·mol^{-1}	5.0E+03	°C·mol·g^{-1}	0.001	gas datasheet
Length of sound path determination	170.88	1.00E-02	mm	Gaussian	2	0.005	mm	2.3E+00	°C·mm^{-1}	0.012	measurement
thermal expansion	0.00056	5.00E-08	m	rectangular	1.732050808	0.000	m	2.3E+03	°C·m^{-1}	0.000	calculation
Heat capacity ratio	1.667	1.67E-05	-	rectangular	1.732050808	0.00001	-	1.2E+02	°C	0.001	gas datasheet
Molar gas constant	8.314462618	0.00E+00	J·mol^{-1}·K^{-1}	rectangular	1.732050808	0.0000	J·mol^{-1}·K^{-1}	2.4E+01	°C·J^{-1}·mol·K	0.000	fixed value, zero uncertainty
Immersion of sensor	0.005	5.00E-03	°C	rectangular	1.732050808	0.003	°C	1.0E+00	°C·°C^{-1}	0.003	estimation
Pressure measurement	100.000	8.00E-03	kPa	Gaussian	2	0.004	kPa	0.0E+00	°C·kPa^{-1}	0.000	measurement
Resolution of τ	12.5	1.25E+01	ns	rectangular	1.732050808	0.000	s	3.1E+05	°C·s^{-1}	0.002	observation and calculation
Time base (short term drift od oscillocope)	1	1.00E+00	ns	rectangular	1.732050808	0.000	s	3.1E+05	°C·s^{-1}	0.000	device specification
Short term drift of the generator	1	1.00E+00	µHz	rectangular	1.732050808	0.577	µHz	0.0E+00	°C·µHz^{-1}	0.000	estimation
Parasitic voltage noise	0	4.00E-03	°C	rectangular	1.732050808	0.002	°C	1.0E+00	°C·°C^{-1}	0.002	estimation
Interpolation	-0.112	0.00E+00	µs	Gaussian	2	0.000	s	3.1E+05	°C·s^{-1}	0.000	not applicable
Instability of measured environment	0.003	3.00E-03	°C	rectangular	1.732050808	0.002	°C	1.0E+00	°C·°C^{-1}	0.002	estimation
Inhomogeneity of measured environment	0.005	5.00E-03	°C	rectangular	1.732050808	0.003	°C	1.0E+00	°C·°C^{-1}	0.003	estimation
Microphone Characteristic	0	2.00E-03	°C	rectangular	1.732050808	0.001	°C	1.0E+00	°C·°C^{-1}	0.001	estimation
Acoustic noise	0.001	1.00E-03	°C	rectangular	1.732050808	0.001	°C	1.0E+00	°C·°C^{-1}	0.001	estimation
t_{90} temperature measurement	0.008	8.00E-03	°C	rectangular	1.732050808	0.005	°C	1.0E+00	°C·°C^{-1}	0.005	measurement
Other influences	0.001	1.00E-03	°C	rectangular	1.732050808	0.001	°C	1.0E+00	°C·°C^{-1}	0.001	estimation
Uncertainty source	Value	z_{max}	Dimension	Distribution	k	u_x		Sensitivity	Dimension	u_x for k=1, °C	Source
A type uncertainty	0.1	0.1	µs	Gaussian	1	0.089	µs	0.044	°C/µs	0.004	data
								Total uncertainty		0.014	
Temperature, K	193.316							*Expansion coefficient*		2	
Temperature, °C	-79.834					*Total rounded expanded uncertainty*, °C				0.029	

5.2. Primary acoustic gas thermometry

5.2.1. Extending the high temperature range of acoustic gas thermometry

This chapter describes the research (which took place from June to August 2021 at INRiM) carried out to prove the effectiveness and accuracy of AGT above 430 K.

5.2.1.1. Description of the HTAGT apparatus

Figure 54 shows the principal sketch of the complete high-temperature AGT apparatus in the longitudinal section and front view that was designed by INRiM. It consists of a vacuum-tight stainless-steel furnace, vacuum- and pressure-tight vessel with a copper cylindrical body and head stainless steel flanges, and copper resonance cavity, with the notable difference that the cavity sketched in Figure 54 differs in dimension and shape from that used in this research.

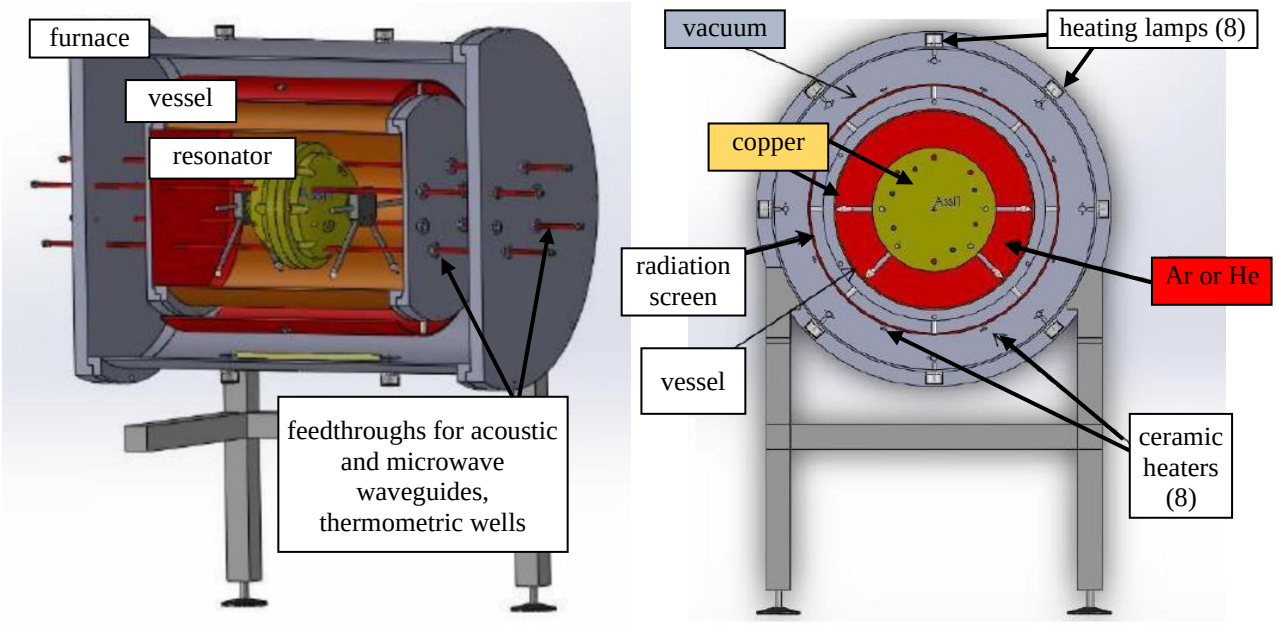

Figure 54: HTAGT apparatus

The acoustic resonator (with the internal volume of about 0.27 litres) employed in this research is made of two hemispheres, machined from an oxygen-free high-conductivity copper (OFHC) billet and assembled to create an inner triaxial ellipsoid cavity with a shape described as follows

$$\frac{x^2}{a^2(1+\varepsilon_2)^2}+\frac{y^2}{a^2(1+\varepsilon_1)^2}+\frac{z^2}{a^2}=1 \qquad (45)$$

where nominally, a = 40 mm, ε_1 = 0.001 and ε_2 = 0.002. The external geometry of the resonance cavity is cylindrical, approximately 240 mm in length and 160 mm in diameter. To minimize the amplitude and frequency of the elastic resonances of the shell (which may disturb the acoustic modes of the cavity), the resulting thickness of the shell is significantly greater than what is typical for acoustic resonators used in temperature metrology (see Figure 55).

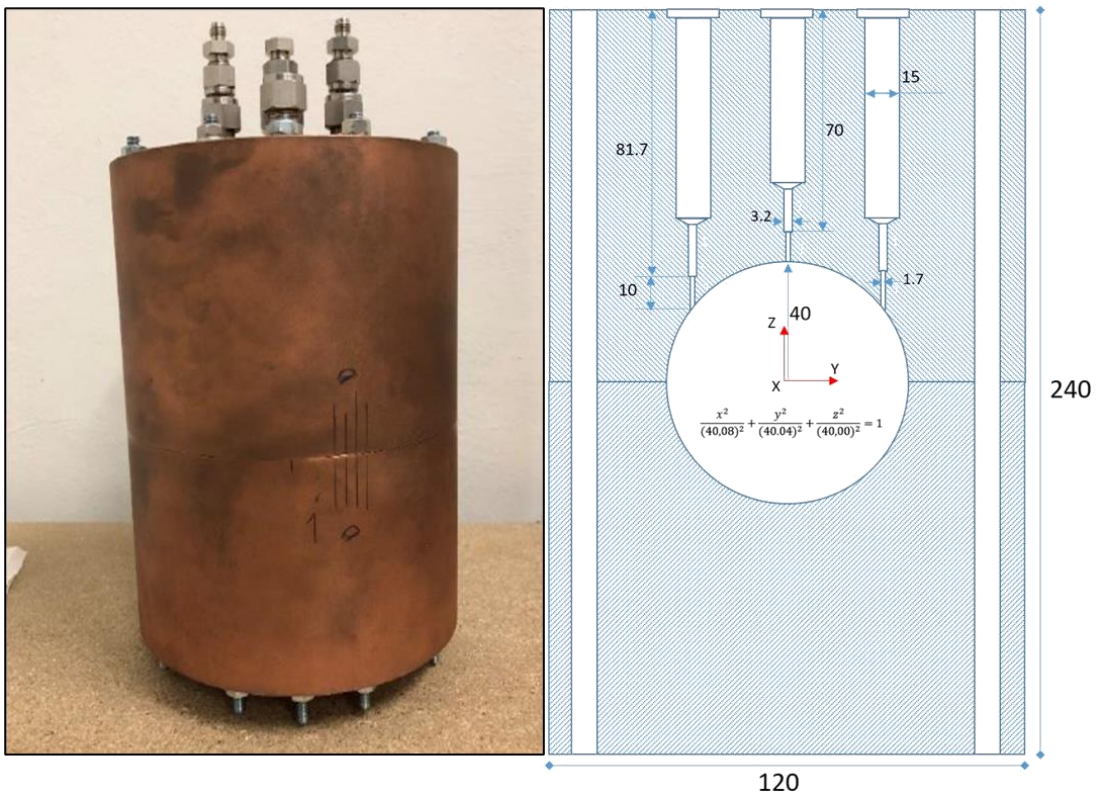

Figure 55: Outer shape (left) and cross-section (drawing, right) of the copper resonator, dimensions in mm

To enable access into the cavity and mounting the support (welded 3/8" Swagelok connectors and fittings) for two acoustic waveguides, two microwave cables, and a duct that can be used to fill and evacuate the cavity with gas, five cylindrical wells with a diameter of 9.6 mm are bored in the resonator wall (see Figure 55 and Figure 56). The bore diameter decreases to 1.75 mm before entering into the cavity to match the internal diameter (i.d.) of the acoustic waveguides and the gas filling tube.

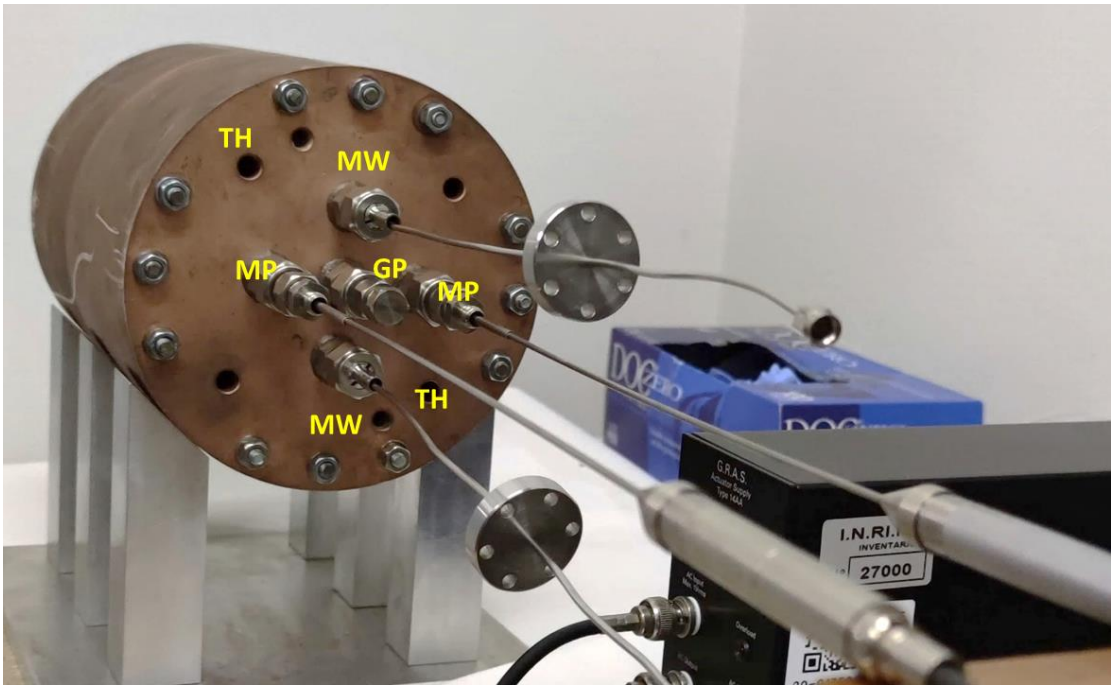

Figure 56: Quasi-spherical resonator. MW denotes microwaves, MP microphones, TH thermometers and GP the gas port

The acoustic transducers are acoustically coupled to the resonator by waveguides. This way microphones are protected from possible damage from heat when the resonance cavity is

exposed to high temperatures. Waveguides selected in 2019 for final measurement setup have an internal diameter of 1.6 mm and a total length of 600 mm and are terminated in a small coupling cylindrical chamber with a diameter of 12 mm, separated by 0.5 mm from the front-facing diaphragm of two ½" free-field condenser microphones (see Figure 57).

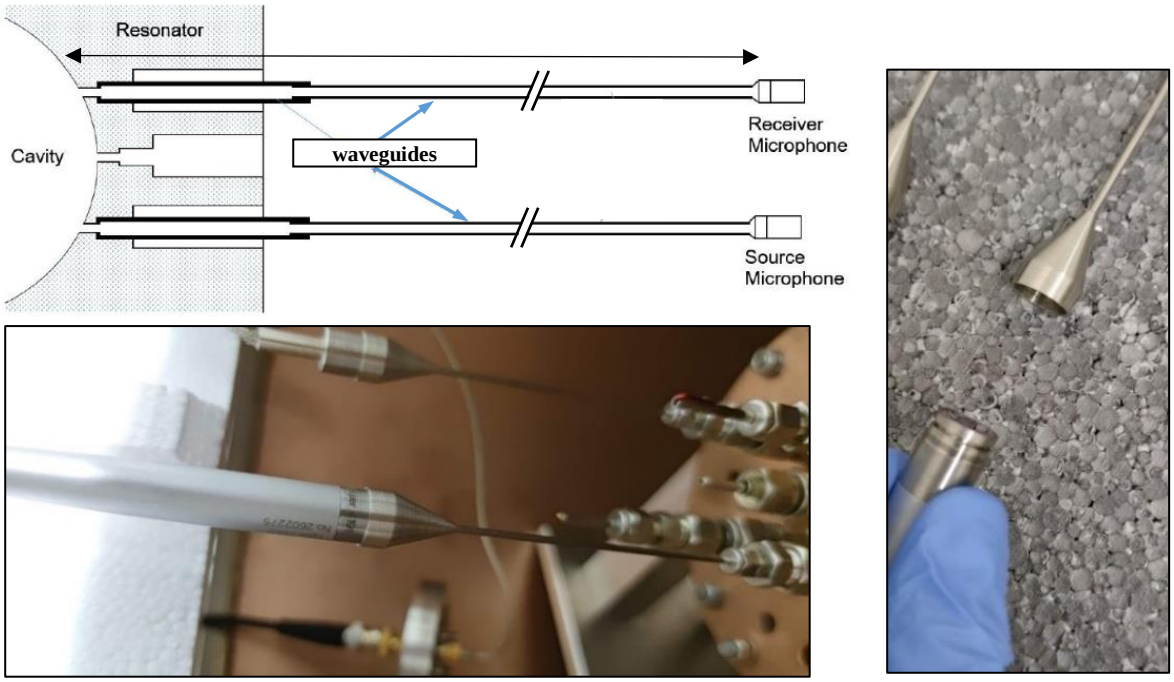

Figure 57: Acoustic waveguides used for acoustic transmission between the laboratory and the resonator

The resonator is placed horizontally inside the surrounding cylindrical vessel (see Figure 58), approximately in the centre of the longitudinal axis. Cavity support is made of stainless steel with low heat conductivity. The vessel (400 mm in diameter and length of 450 mm) consists of a cylindrical copper body and stainless-steel head flanges and is shown in Figure 58. The flanges are employed with thermometer wells, and gas- and vacuum-tight feedthroughs for the acoustic waveguides. The maximum operating pressure (according to the manufacturer) is 1.5 MPa at ambient temperature, decreasing to 1 MPa at around 600 °C. The copper wire ring gaskets are used to seal the main head flanges.

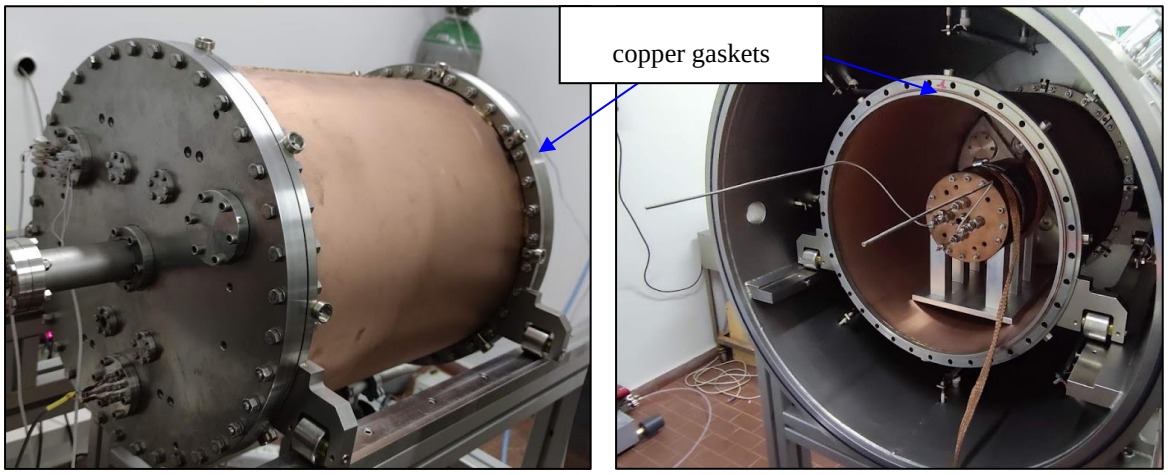

Figure 58: Gas-tight vessel consisting of a cylindrical copper body (on left), the vessel (with cavity) inserted into the main furnace (on right)

From measurement in the microwave domain, performed in 2019 ([118]), simple fitting function

$$a(T) = a_{480K} + m(T - 480\ \mathrm{K}), \tag{46}$$

was derived to describe the thermal expansion of the cavity. In the equation above, $a_{480\mathrm{K}}$ = (40.1400 ± 0.0022) mm is the fitted estimate of the radius of the cavity at 206.85 °C (480 K), and m = (6.8 ± 0.9)×10^{-4} mm·K^{-1}. The ratio $m/a_{480\mathrm{K}}$ = (16.9 ± 2.9) K^{-1} estimates the linear thermal expansion coefficient (see Figure 59) of the cavity and is in accordance with published estimates of copper in the same temperature range in [119].

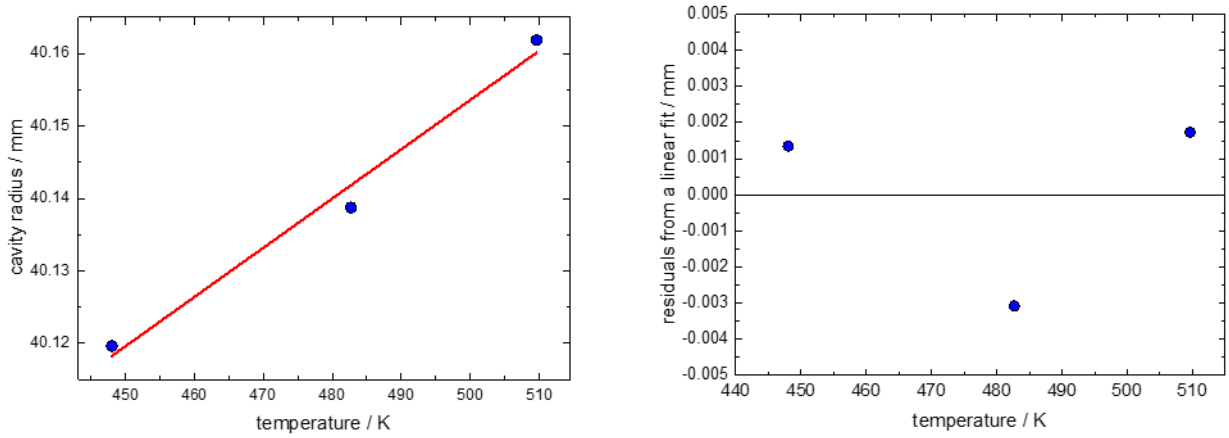

Figure 59: (Left) Linear fit to three selected microwave estimates of the internal radius of the cavity in vacuum between 448 K and 510 K. (Right) Absolute residuals of the linear fit.

The main furnace (shown in Figure 60) with the theoretical temperature range up to 1000 K, is a stainless steel cylindrical (650 mm long) vacuum-tight chamber equipped with 8 halogen infrared lamps (USHIO QIR235-500/VZB) that are controlled by 4 AC variable transformers. The lamps provide total maximum radiating power of 4 kW with 85 % in the infra-red and 7 % in the visible part of the spectrum. Electrical power is supplied to eight lamps, connected in parallel groups of two, by a set of four variable (0 to 240) VAC transformers that can be independently manually operated. To prevent heat transfer outside from the furnace, the water is circulating inside its walls. Two horizontal rails are welded internally to allow insertion and positioning of the vessel.

Figure 60: Heating furnace used in HTAGT research, placed on a framed supporting structure.

The furnace has two head flanges with necessary feedthroughs for acoustic and microwave measurements, 2 wells for inserting SPRTs, gas inlets and wells for SPRTs.

5.2.1.2. Measurement equipment

In initial configuration there were two ½'' microphones serving to transmit and receive acoustic signal through the quasi-spherical resonator. The source microphone was attached to the G.R.A.S RA0086 Transmitter Adapter, enabling the microphone to be connected to the Keysight 33210A function generator via GRAS 14AA Electrostatic Actuator Amplifier and the microphonic receiver was connected to the preamplifier B&K 2669. The initial waveform for the source microphone served as a reference signal for the STANFORD RESEARCH SYSTEMS SR830 lock-in amplifier. The B&K 4166 source microphone is connected to the resonator using waveguide of 1 mm inner (2 mm outer) diameter and receiver B&K 4165 microphone was connected using waveguide of 0.8 mm inner (1 mm outer) diameter. The receiver microphone was connected via B&K 5935 microphone supply unit to the input channel of the lock-in amplifier. The initial measurement setup is in Figure 61.

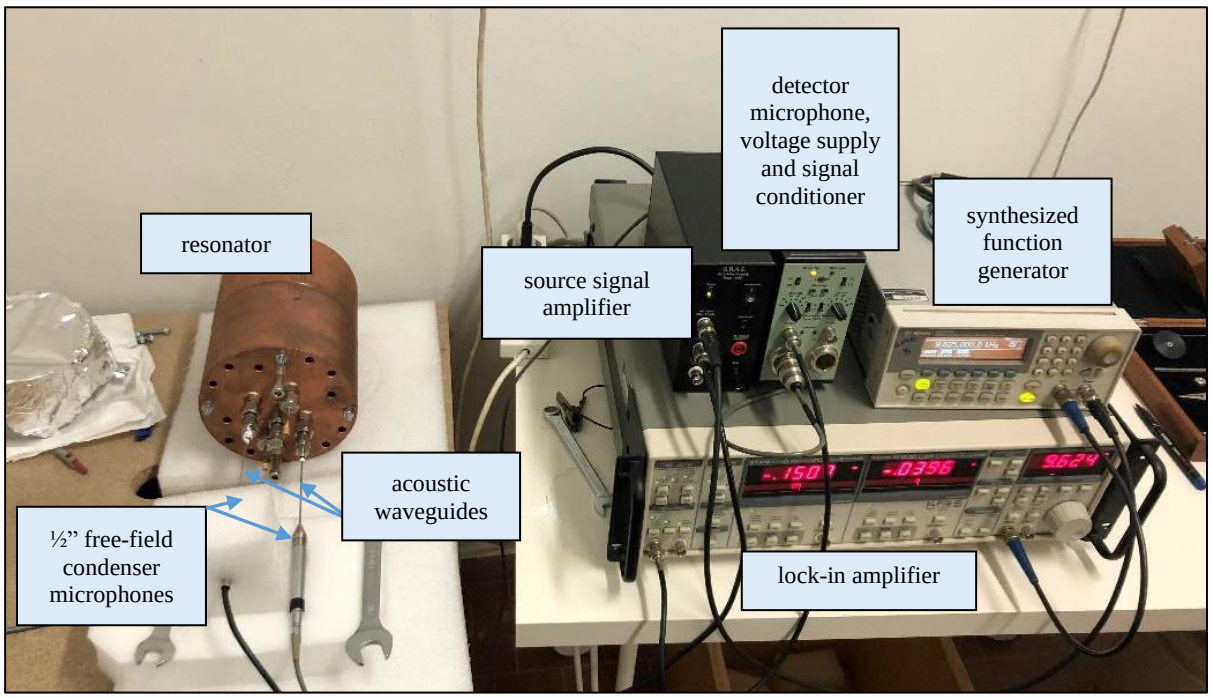

Figure 61: The initial measurement setup, resonator on the table

5.2.1.3. Measurement procedure

Frequency positions of radial resonance modes (for $l = 0$) can be estimated (according to [63]) by measurement of (0,2) resonance frequency and using given $z_{l,n}$ values as

$$f_{0,n+1} = f_{0,n} \cdot \frac{z_{0,n+1}}{z_{0,n}}. \tag{47}$$

To estimate the speed of sound, following equation was used

$$f_{0,n} = \frac{z_{0,n} u}{2\pi a} \rightarrow u = \frac{f_{0,n} a 2\pi}{z_{0,n}} \tag{48}$$

where $z_{0,n}$ is the root of Bessel function, u is the speed of sound (340 m·s^{-1}) at ambient temperature and a is the radius of the resonator which is 40 mm in z direction. Example of

measured frequency positions of radial acoustic modes together with its predictions is shown in Figure 62.

			constants, turning points of the spherical Bessel functions								
			$z_{(0,2)}$, -	$z_{(0,3)}$, -	$z_{(0,4)}$, -	$z_{(0,5)}$, -	$z_{(0,6)}$, -	$z_{(0,7)}$, -	$z_{(0,8)}$, -	$z_{(0,9)}$, -	$z_{(0,10)}$, -
			4.4934094579	7.7252518369	10.904121659	14.066193913	17.220755272	20.371302959	23.519452499	26.666054259	29.811598791
initial inputs			outputs calculated from measured $f_{(0,2)}$								
$f_{(0,2)}$, Hz	u, m/s	a, m		$f_{(0,3)}$, Hz	$f_{(0,4)}$, Hz	$f_{(0,5)}$, Hz	$f_{(0,6)}$, Hz	$f_{(0,7)}$, Hz	$f_{(0,8)}$, Hz	$f_{(0,9)}$, Hz	$f_{(0,10)}$, Hz
6154.69	344.59	0.04004		10581.39	14935.54	19266.68	23587.53	27902.88	32214.95	36524.89	40833.39
			outputs dependent on theoretical speed of sound								
	estimation	to be corrected	$f_{(0,2)}$, Hz	$f_{(0,3)}$, Hz	$f_{(0,4)}$, Hz	$f_{(0,5)}$, Hz	$f_{(0,6)}$, Hz	$f_{(0,7)}$, Hz	$f_{(0,8)}$, Hz	$f_{(0,9)}$, Hz	$f_{(0,10)}$, Hz
			6154.69	10581.39	14935.54	19266.68	23587.53	27902.88	32214.95	36524.89	40833.39
$f_{(3,1)}$, Hz			speed of sound calculated from measured modes								
6175.14											
inputs from spectrum measurement			$f_{(0,2)}$, Hz	$f_{(0,3)}$, Hz	$f_{(0,4)}$, Hz	$f_{(0,5)}$, Hz	$f_{(0,6)}$, Hz	$f_{(0,7)}$, Hz	$f_{(0,8)}$, Hz	$f_{(0,9)}$, Hz	$f_{(0,10)}$, Hz
		inputs ->	6154.69	10582.80	14939.33	19270.80	23587.98	27901.44			
			error, Hz	1.41	3.79	4.12	0.45	-1.44	-32214.95	-36524.89	-40833.39
							invalid result	invalid result			

Figure 62: Simple calculations to estimate frequencies of other radial modes from known positions of (0,2) mode. (0,2) mode always found by scanning the spectrum.

Figure 63 displays the initial measurement of the (0,4) mode for the resonator in ambient air environment.

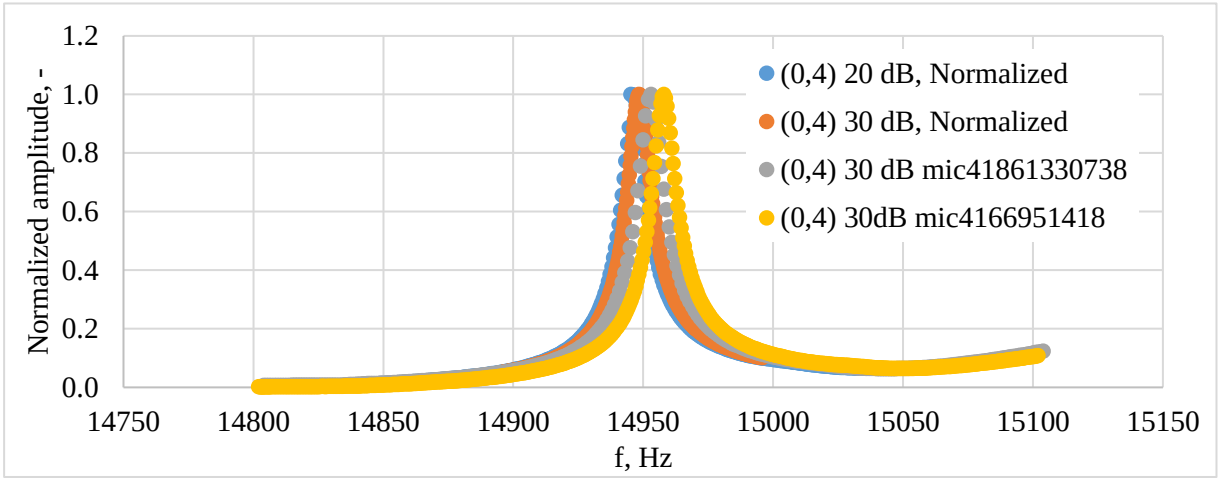

Figure 63: (0,4) mode shape comparison for various initial configurations, selection of receiver microphone and gain of amplifier

5.2.1.4. Measurement at ambient air

Results of comparison of the precision which were achieved in fitting (described in Section 4.5) of several purely radial modes after various minor modifications to the assembly of the waveguides and by using different types of ½" condenser microphones are illustrated in Figure 64. It shows that relative fitting precision (fitting error) in the order of 1 ppm or below was achieved for modes (0,2) to (0,8) that are in the frequency range between 6 kHz and 32 kHz.

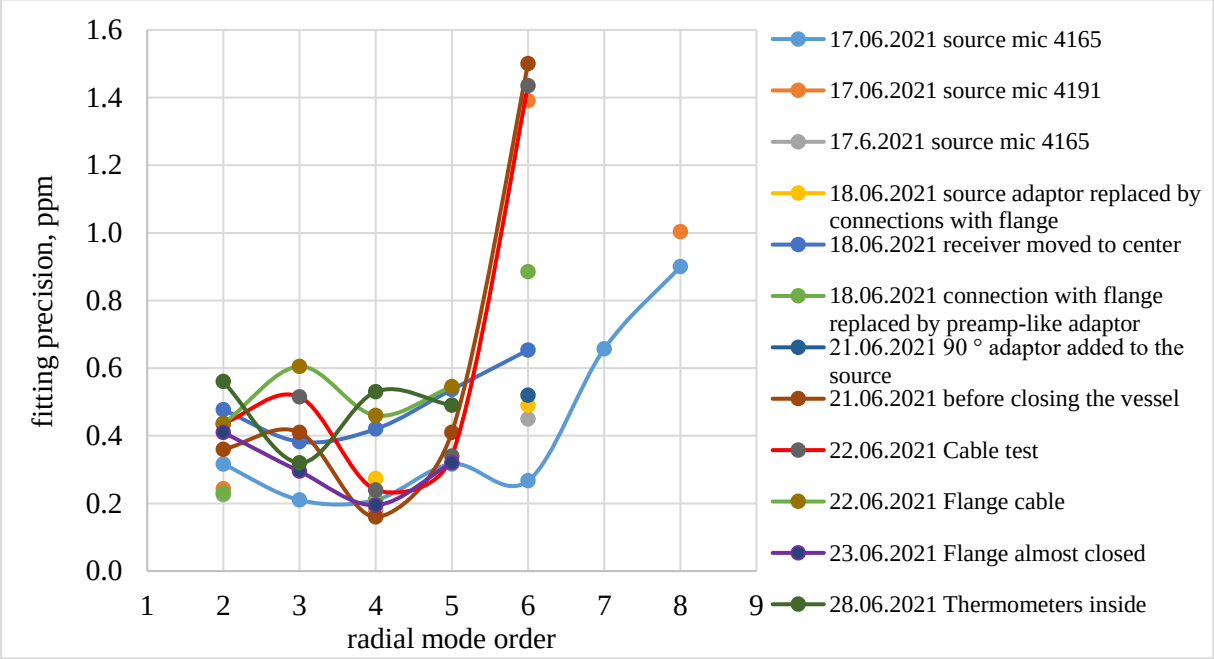

Figure 64: Relative fitting precision of seven purely radial modes, (0,2) to (0,8) in air at ambient temperature and pressure with 40 cm long, 1.6 mm i.d. acoustic waveguides for several different microphonic configurations

5.2.1.5. Measurement in vessel using argon gas and strip heaters

To enable operation with monatomic gas, the resonator was inserted into the gas-tight vessel. Before using the main furnace, it is advantageous to check the condition of the measurement chain after closing the vessel as well as it is to do so after each modification step. The experiment setup is shown in Figure 65. Two IPRTs (simple cable thermometers) were attached to the outer wall of the resonator and connected to Keithley 2001 multimeter, that was acquiring the measured electrical resistance data. The vessel was closed and bolts were tightened repeatedly until satisfactory vacuum level was reached.

Watlow 120v 400w strip heaters were turned around the vessel and using another (third) IPRT (attached to the outer wall of the vessel) and two voltage sources, virtual PID controller controlled the temperature. Side heaters were connected in series as well as central ones and each section was supplied by separated voltage supply.

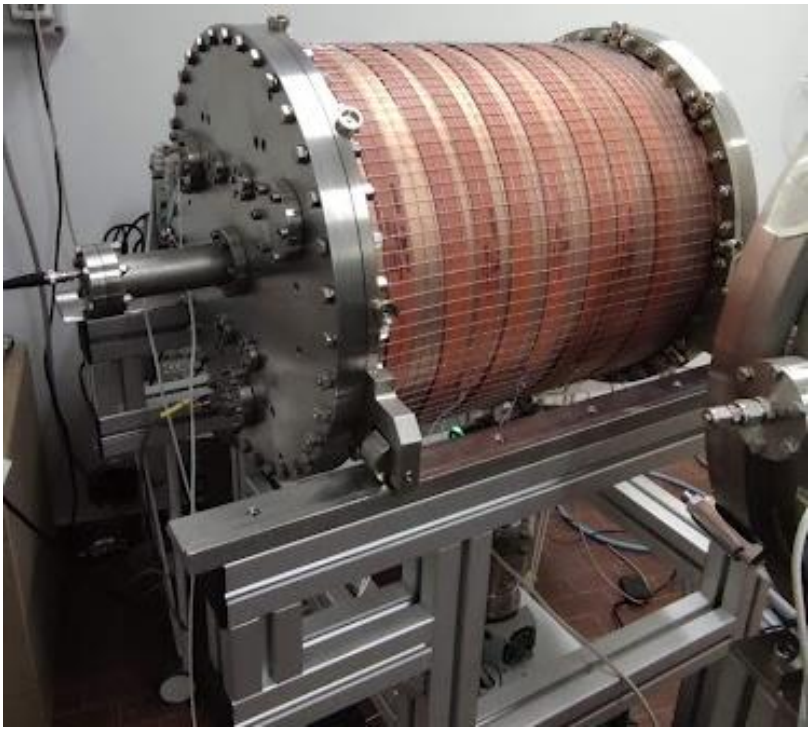

Figure 65: Strip heaters mounted on the vessel

Evacuation of the experimental vessel was carried out with a primary scroll pump (Agilent IDP 7) at the level of $1 \cdot 10^{-2}$ mbar, low limited by the imperfect tightness of the main copper gaskets of the vessel. The pressure of the gas inside the vessel was measured by a quartz pressure transducer (Paroscientific 745). After evacuation of the vessel, it was filled with Ar gas (nominal purity of 99.9999 % as declared by the manufacturer Messer) from the bottle at the pressure of about 1 atm (101.325 kPa). Use of Ar gas allowed to detect all the radial modes up to (0,10) mode. Measurement results for (0,2) mode are shown on Figure 66. Raising temperature had an effect of raising frequency of radial modes.

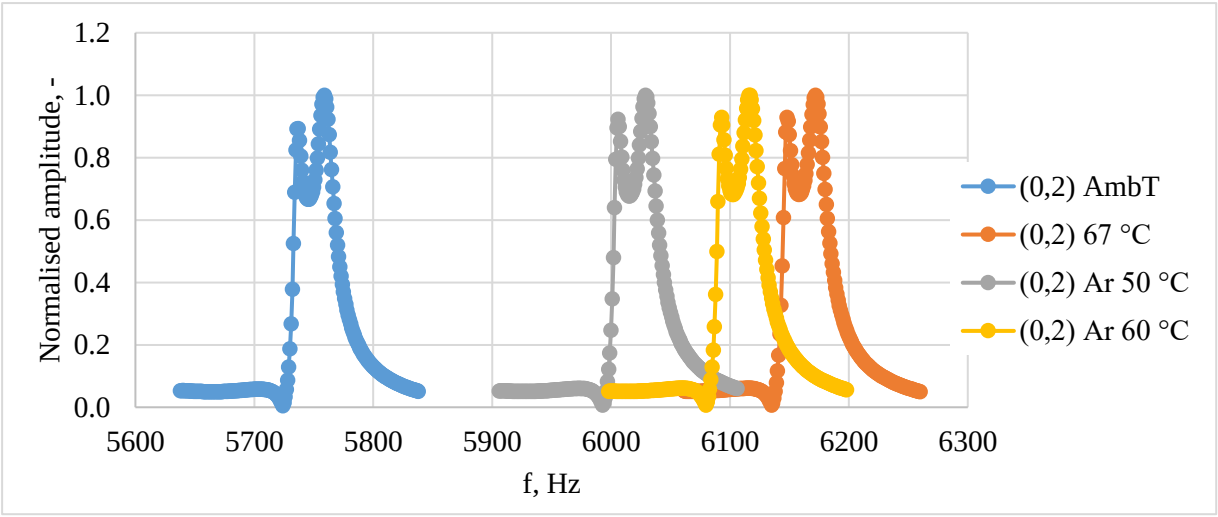

Figure 66: Normalised spectrum of (0,2) mode measured at various temperatures using strip heaters and ambient temperature

Comparison of spectral images for modes (0,2) to (0,10) for measurement with air media at ambient temperature, Ar media at ambient temperature and at approx. 67 °C is shown in Figure 67.

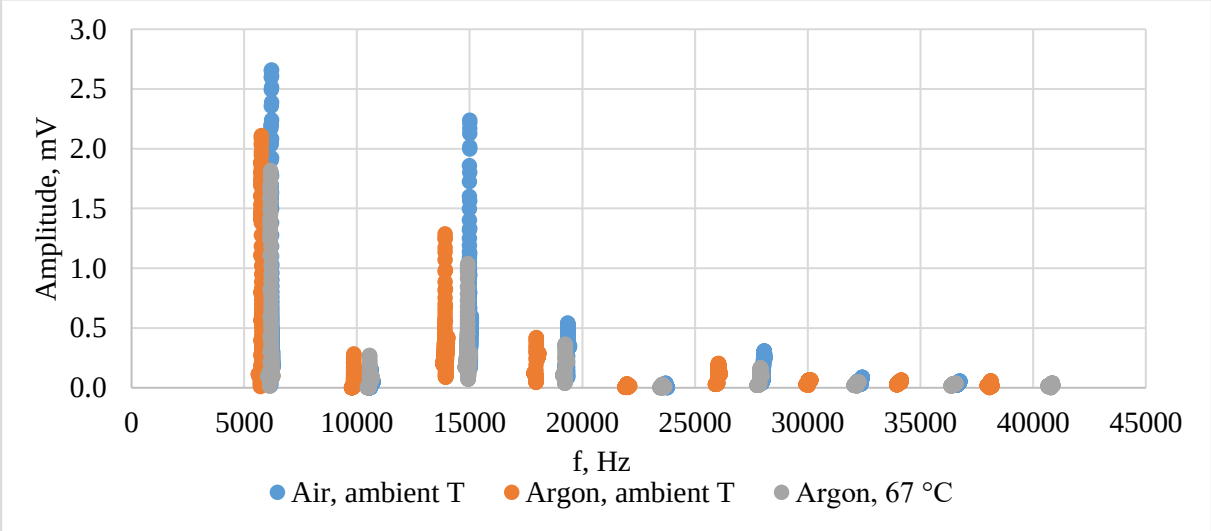

Figure 67: Comparison of spectral images for modes (0,2) to (0,10)

5.2.1.6. Measurement in the vacuum furnace

The vessel inserted into the furnace is shown in Figure 68. The internal volume of the furnace was continuously evacuated at a residual pressure of about $2 \cdot 10^{-2}$ mbar, by a root pump (Leybold Ecodry 40 plus), while the vessel and thus also the resonator were filled by Ar at pressure of 143.5 kPa.

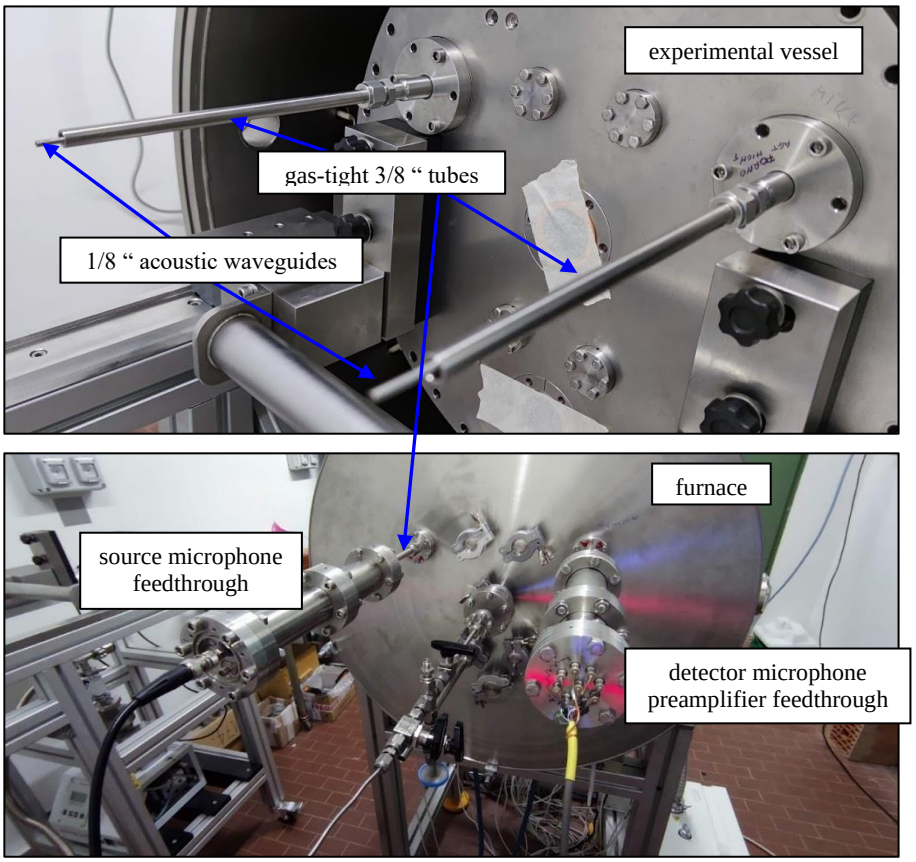

Figure 68: Vacuum and pressure tight connections to microphones and acoustic waveguides

Modes above (0,7) could not be found in spectrum at this stage, probably as an effect of lengthening the waveguides (to the final length of 600 mm) that filtered higher frequencies from transmitted and received signals (signal level generally was of magnitude about 2 μV in the frequency band that corresponds to modes above (0,7)).

Two long-stem 25.5 Ω Chino R800-2 SPRTs were used to estimate the temperature gradient along the cavity in operating conditions. Across each of the head flanges sealing the furnace, a stainless-steel tube (with a length of 60 cm, external diameter of 10 mm and internal diameter of 7.9 mm) served as a thermometer well, allowing insertion and removal of the SPRT (see Figure 69).

Figure 69: SPRT inserted in a thermometry well that is sealed across the head flange of the furnace.

A thermal link between each well and the resonance cavity was provided by a thick long copper ribbon, wrapped around the cavity cylindrical body. The temperature difference across the apparatus recorded was below 4 mK at ambient temperature raising up to 2.5 K in the temperature range between 400 K and 550 K.

Surface thermometer (unspecified J-type thermocouple connected to evaluation and display unit Digi-Sense 91100-00) was installed on the outer wall of the flange (on the side of the furnace, where acoustic waveguides are also located) to allow quick check of the temperature and to avoid damages of microphonic preamplifiers (see Figure 70).

Figure 70: Surface thermometer attached to the flange of the furnace

To reach the temperature of 550 K, the temperature in the furnace was slowly increased, in the course of about one week, until it settled around 550 K with a corresponding increase of the argon pressure up to 270 kPa.

Figure 71 displays the evolving trend of pressure and temperature records. Acoustic data for three modes (0,2), (0,3) and (0,4) were recorded and fitted for a time interval of about 24 hours, while the pressure and the temperature of the AGT was settling very approximately stable around 552 K, 267 kPa. While both quantities appear well correlated, the temperature difference of about 2 K between the readings of two long stem SPRT indicates that an extremely large longitudinal thermal gradient was present across the cylindrical resonator body, representing a major issue of the HTAGT apparatus in its present configuration.

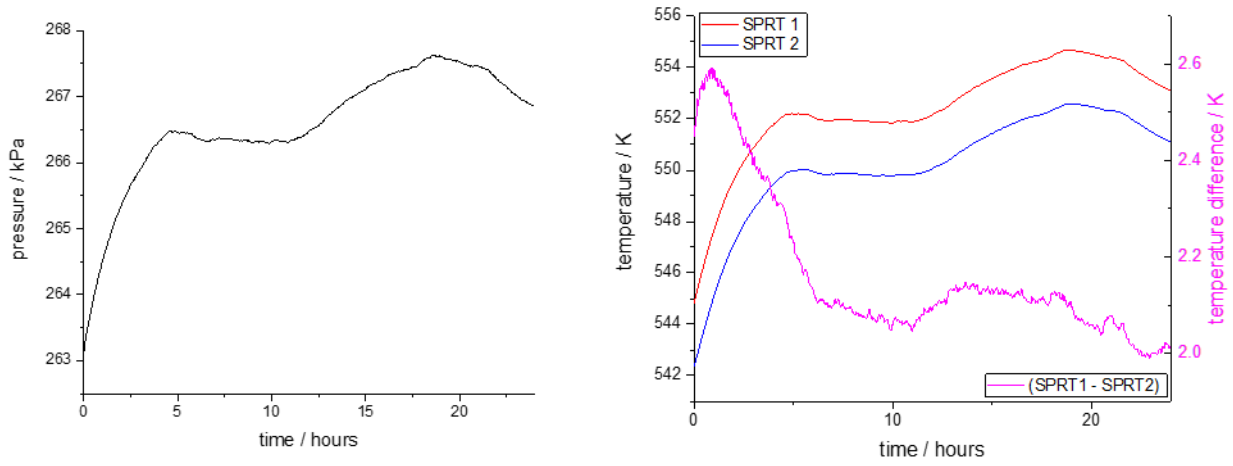

Figure 71: Pressure (left plot) and temperature (right plot) records during 24 hours of acoustic measurements near 550 K, 270 kPa. A large thermal gradient in the order of 2 K persists along the whole record.

The mean relative fitting precision of the frequency of three radial acoustic modes under examination spans between a minimum of 1.0 ppm for mode (0,3) to a maximum of 3.8 ppm for mode (0,4) as indicated in Figure 72.

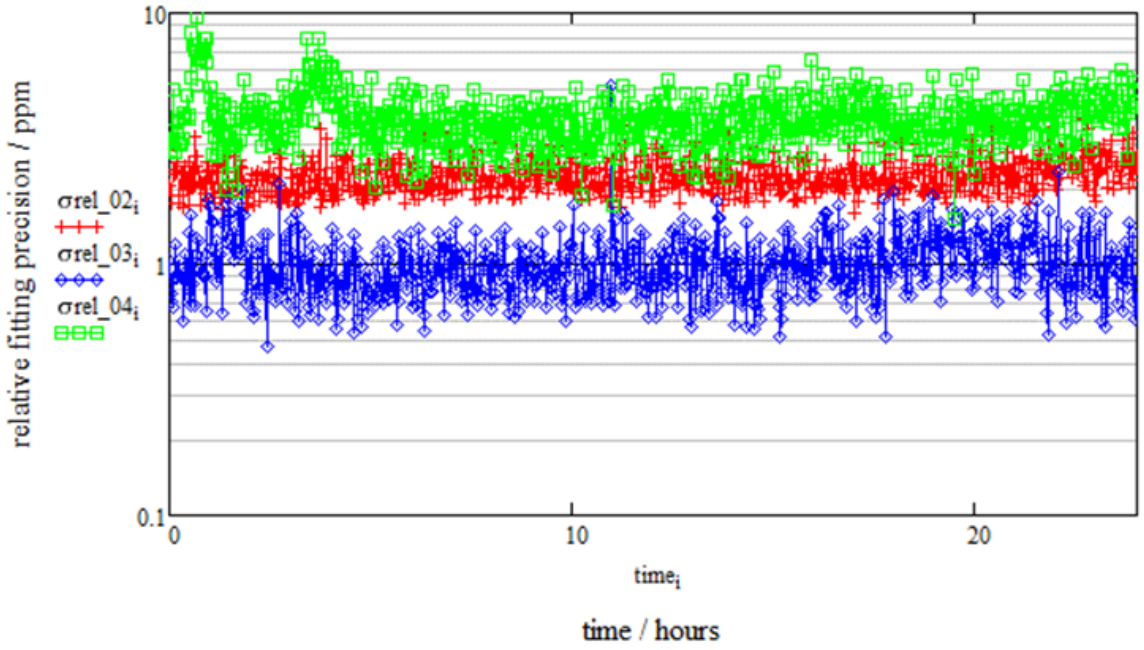

Figure 72: Relative fitting precision of three radial acoustic modes in Ar near 550 K, 270 kPa.

Raw fitted frequency data for the three modes can be normalized, before applying any correction to determine the corresponding speed of sound u_{exp} in Ar using Eq. (17) in the following simplified form:

$$f_{0,n} = \frac{u_{exp} z_n}{2\pi a}, \tag{49}$$

and the estimate of the internal radius of the resonator from previous microwave measurements at 480 K in Eq. (46). These results may be compared to the calculation of the speed of sound u_{calc} at the same temperatures and pressures based on ab initio estimates of the density- and acoustic-virial coefficients of Ar in [63]. The mean relative deviation $(u_{exp} - u_{calc})/u_{calc}$ of this comparison is about 1 %, probably resulting from combination of the large errors in the determination of the experimental temperature T, the composition of the gas, and the imperfect determination of the internal radius a of the cavity.

When the internal consistency of the speed of sound determined from three acoustic modes is examined, the maximum relative discrepancy is about 140 ppm and it can be further reduced by accounting for the various perturbations included in the acoustic model. Perturbation to resonance frequencies due to imperfect geometrical shape of the cavity is considered. By design, it is assumed that the shape closely approximates a triaxial ellipsoid and by the analysis of microwave data in [118], the geometrical parameters $\varepsilon_1 = 3.15\times10^{-3}$ and $\varepsilon_2 = 2.18\times10^{-3}$ were estimated.

These estimates and the analytical model of second-order perturbations of the radial acoustic modes [120] lead to corrected ellipsoid eigenvalues $z_{E(0,n)}$ which are relatively larger than those of a perfect sphere $z_{S(0,n)}$ by 4.7 ppm for mode (0,2), by 13.9 ppm for mode (0,3), and by 27.6 ppm for mode (0,4). These corrected eigenvalues were used to normalize acoustic data from different modes. Applying these geometrical corrections reduces the discrepancy between the acoustic data of mode (0,2) and (0,4) from 140 ppm to 115 ppm (see Figure 73).

In the next step, the thermal boundary layer correction is applied which, in Ar at 552 K and 267 kPa, decreases the resonance frequency by 259 ppm for mode (0,2), 198 ppm for mode (0,3), and 166 ppm for mode (0,4).

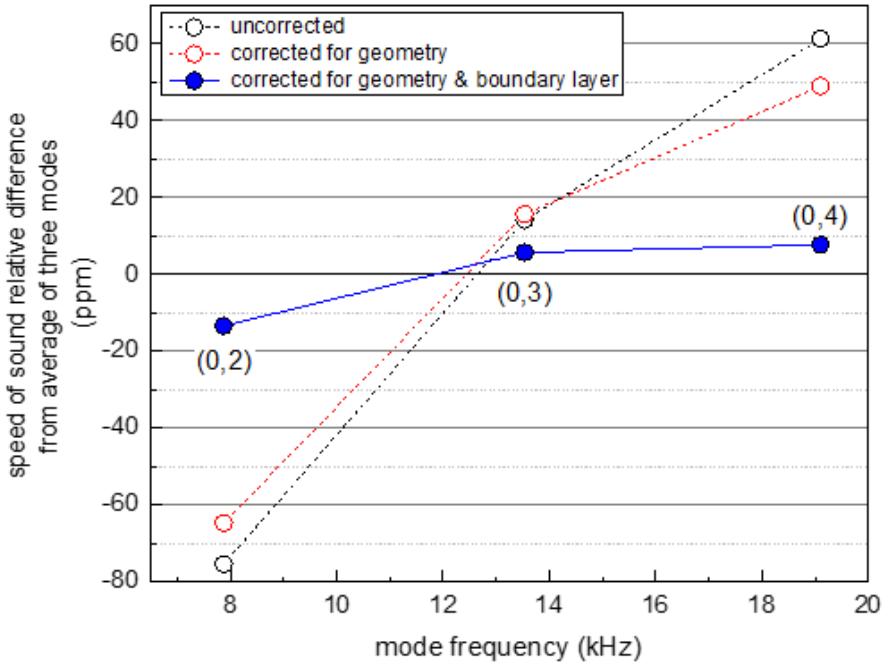

Figure 73: Relative difference of the speed of sound estimated from three radial acoustic modes in Ar near 550 K, 270 kPa

Figure 73 summarizes the progressive reduction of the discrepancy between the speed of sound calculated from three acoustic modes as the geometrical and boundary corrections are applied,

with a final residual relative discrepancy between the acoustic data of mode (0,2) and (0,4) of about 21 ppm.

The measurement results for the radial modes (0,2), (0,3) and (0,4) near 294 K at eight different pressures in the range between 100 kPa and 430 kPa are shown in Figure 74. The fitting precision was in the range of 0.03 ppm (for mode (0,2) at 430 kPa) and 6 ppm (for mode (0,4) at 100 kPa).

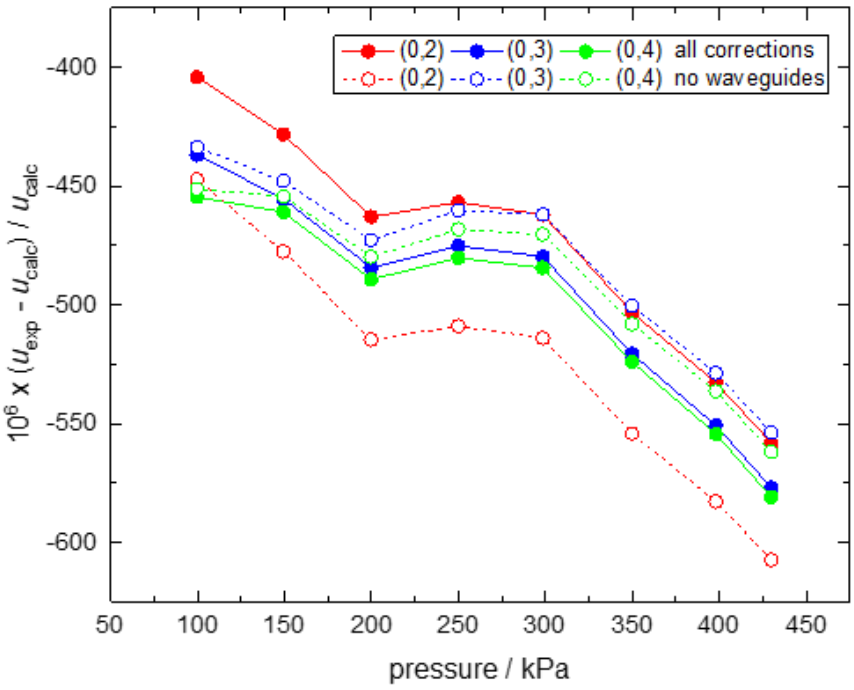

Figure 74: Relative differences of the speed of sound estimated from three radial acoustic modes in Ar at 294 K between 100 kPa and 430 kPa

Relative deviations $(u_{exp} - u_{calc})/u_{calc}$ of the speed of sound vary between −400 ppm at 100 kPa and −600 ppm at 430 kPa. The approximate linear deviation of u_{exp} from u_{calc} can be fitted to provide an experimental estimate $\beta_a^{exp}(294\ K) = (9.43 \pm 0.17) \times 10^{-6}\ cm^3 \cdot mol^{-1}$ of the second acoustic virial coefficient at 294 K, which is inconsistent with the ab initio estimate $\beta_a^{calc}(294\ K) = (10.71 \pm 0.15) \times 10^{-6}\ cm^3 \cdot mol^{-1}$ at the level of seven standard deviations.

5.2.2. Primary Acoustic Gas Thermometry at CMI

The sketch of the stainless-steel resonance cavity present at the CMI is shown in Figure 75. It was obtained from INRiM in 2021. This resonator was previously used for the T-T_{90} measurements in the range of (-38.8344 to 106.85) °C, as described in [65].

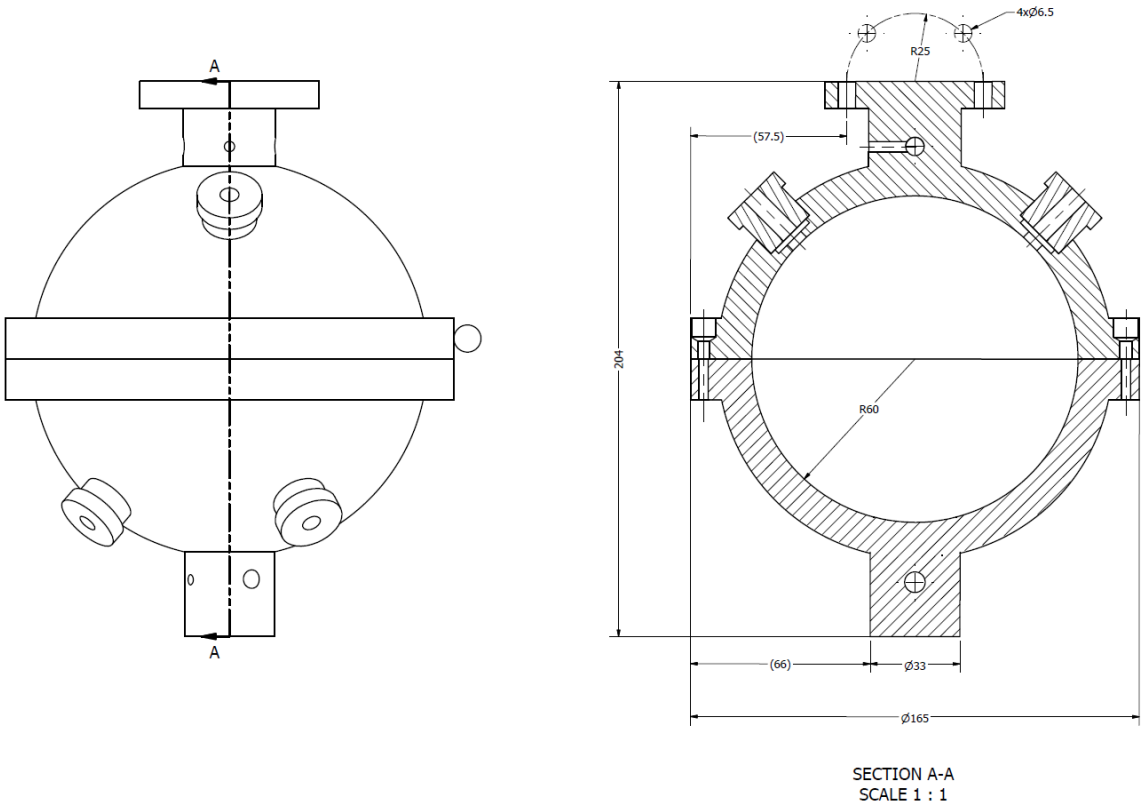

Figure 75: Sketch of the spherical resonator at CMI

Full characterization of the resonator is usually obtained using coordinate measuring machines (as e. g. in [69]). Therefore, a coordinate measuring machine Zeiss XENOS (Figure 76) was used for characterization.

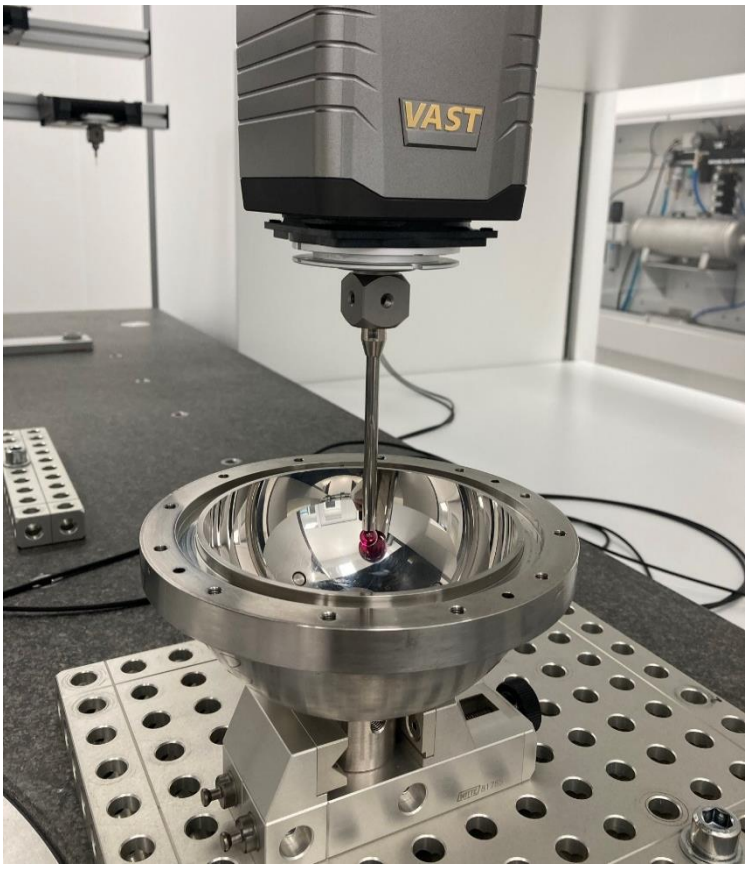

Figure 76: Characterization of the resonator on the Zeiss XENOS coordinate measuring machine

The result of measurement of dimensions (see Figure 77) provides information of the average inner radius a well as deviations from this value. It is 59.99110 mm for the top hemisphere with maximum measured deviation of 0.01410 mm and 59.98450 mm for the bottom hemisphere with maximum deviation of 0.02030 mm. Corresponding measurement uncertainty is 0.86 µm.

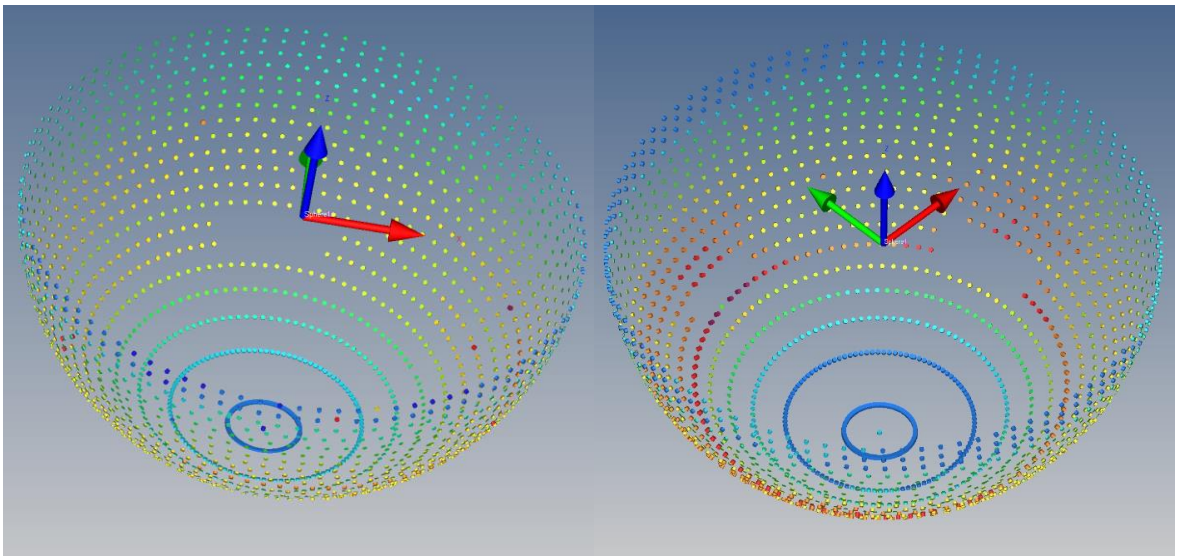

Figure 77: Spatial visualisation of the measured deviations from sphericity values of both hemispheres of the resonator

5.2.2.1. Measurement in ambient environment

The measurement in ambient environment serves to validate the function of the measurement chain. The measurement setup, shown in Figure 78 is very similar to that already described in Section 5.2.1.2.

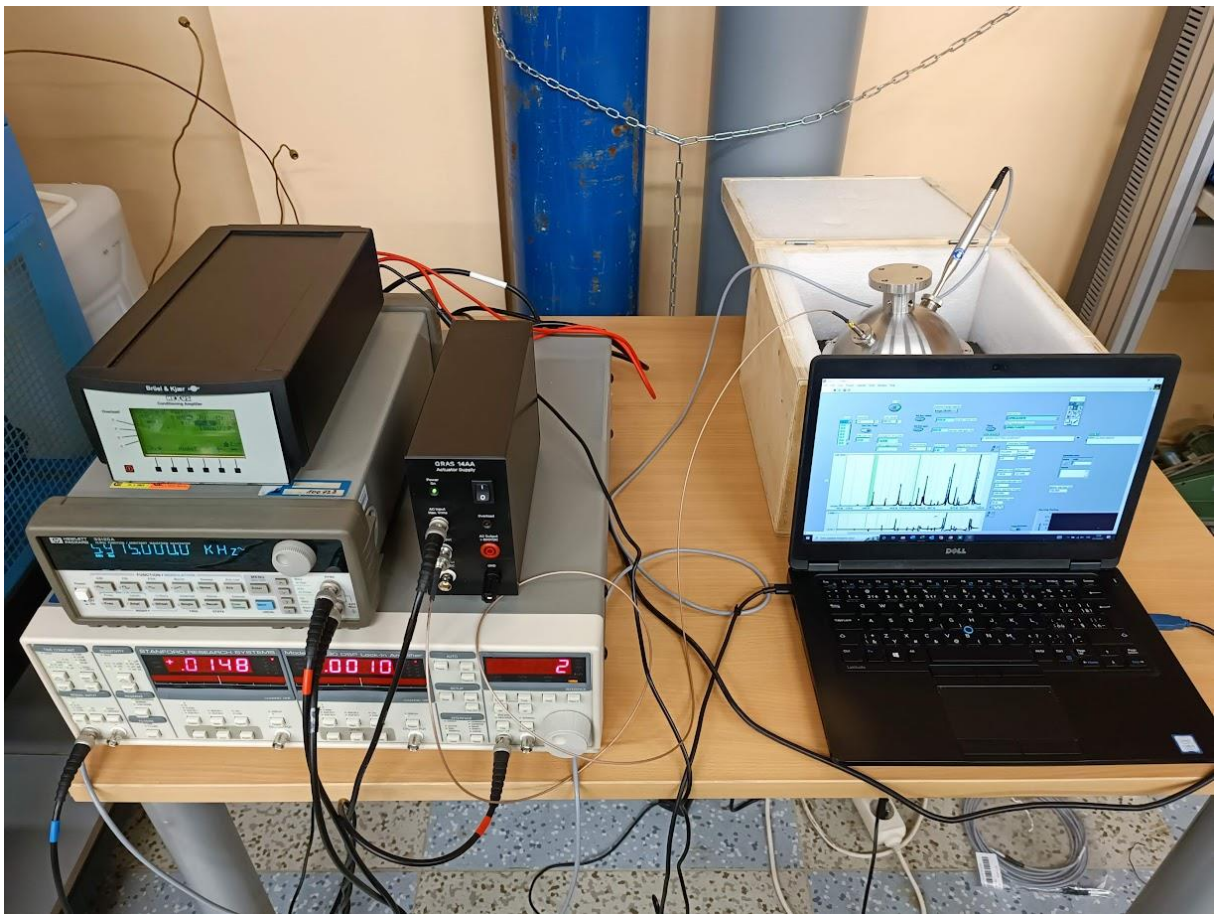

Figure 78: Measurement setup for AGT experiment in ambient environment at CMI

Two Bruel & Kjaer 4939 ¼'' microphones serve to excite and record an acoustic field in the spherical resonator. The source microphone is connected through the G.R.A.S RA0086 Transmitter Adapter and GRAS 14AA Electrostatic Actuator Amplifier to the HP 33120A function generator that also provides a reference signal for the lock-in amplifier. Receiving microphone with Bruel & Kjaer 2669 microphonic preamplifier is connected through the Bruel & Kjaer 2690-A NEXUS Conditioning Amplifier to the measuring channel of the STANFORD RESERCH SYSTEMS SR830 lock-in amplifier. Example of (0,2) resonance mode shape recorded at ambient temperature is shown in Figure 79.

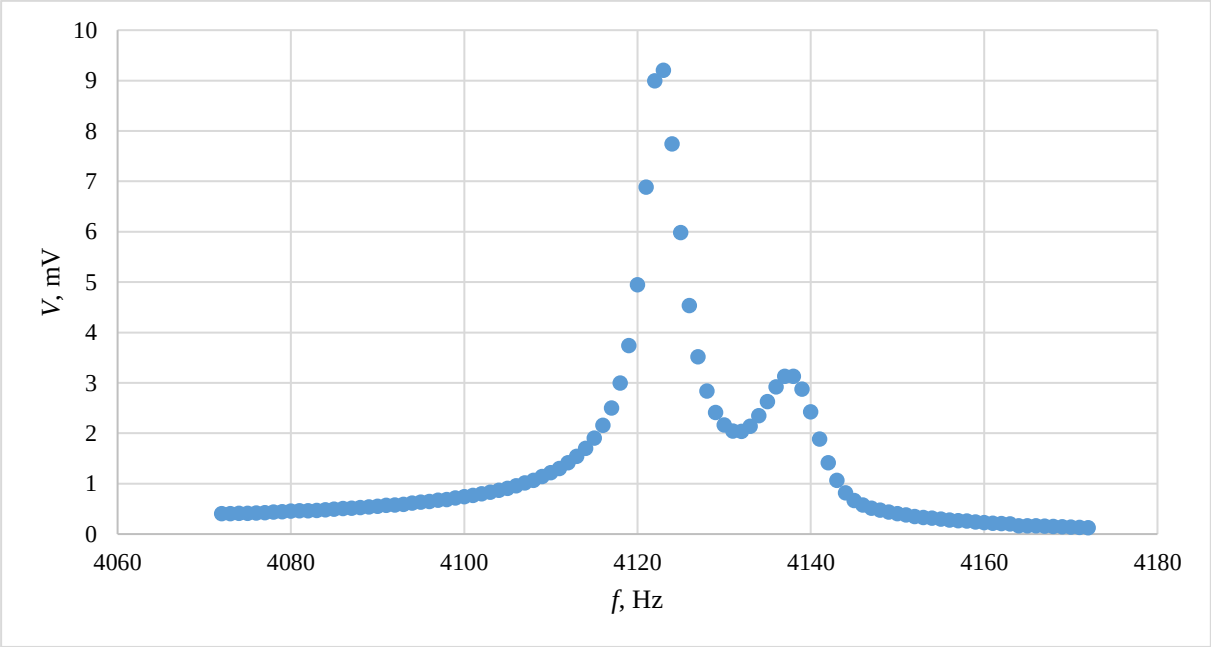

Figure 79: Resonance mode (0,2) at ambient temperature.

First 8 resonance modes were recorded from (0,2) to (0,9) and using Eq. (49), the speed of sound estimations from frequency positions were calculated (see Figure 80). The difference between minimal and maximal value is 0.6 $m \cdot s^{-1}$ and it corresponds to the raise in temperature during the measurement of about 0.8 °C (from 23.6 °C to 24.4 °C).

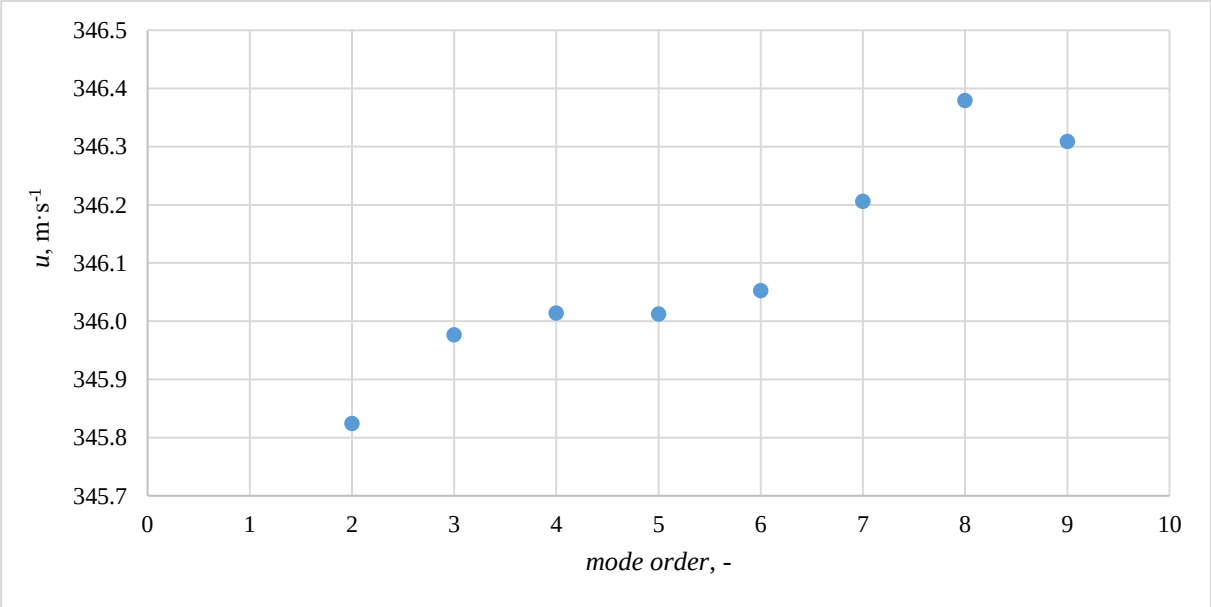

Figure 80: Calculated speed of sound values for 8 resonance radial modes at ambient temperature

5.2.2.2. Measurement in climatic chamber

Measured frequencies of resonance modes can be converted to proper speed of sound values using Eq. (49). As shown in Figure 81, the AGT was compared with ZPA Pt100 IPRT in WEISS Umwelttechnik 125 SB climatic calibration chamber (maintaining stable air temperature) in the range of (-10 to 50) °C at ambient air. This temperature range is given by limitations in technical specifications of acoustic preamplifiers which is (-20 to 60) °C.

Figure 81: Spherical resonance cavity in climatic chamber

INOR IPAQ-HX Temperature Transmitter provided resistance measurement, temperature computation and storing the data in computer. The relation between temperature of IPRT and speed of sound measured in spherical resonator for modes from (0,2) to (0,8) can be found in Figure 82.

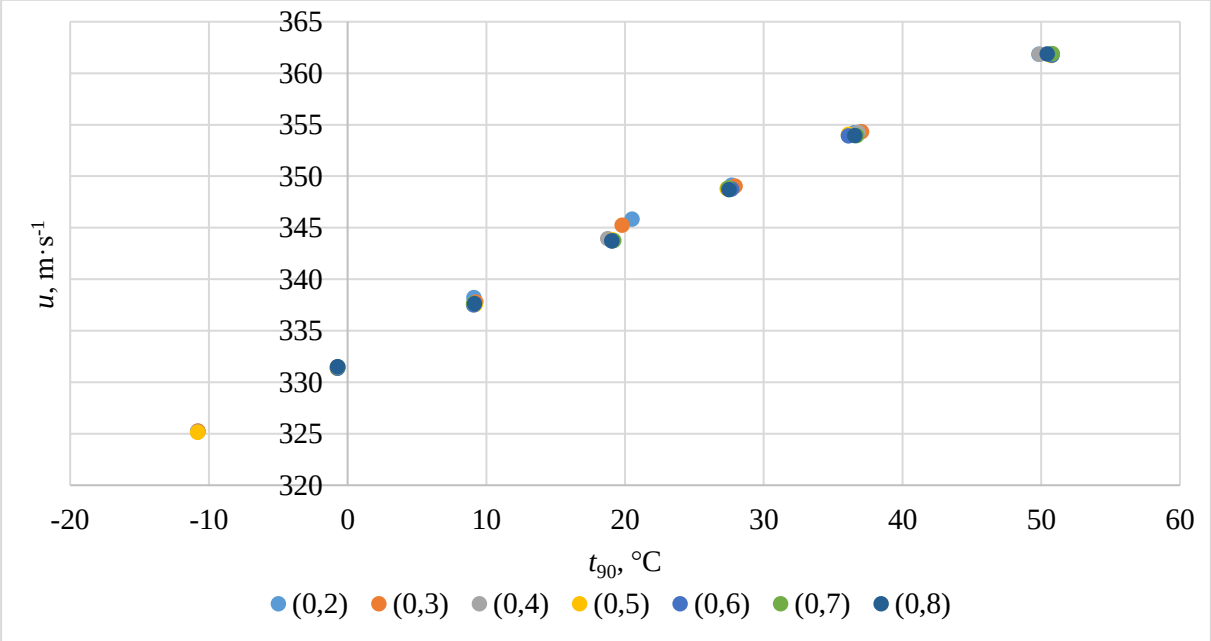

Figure 82: Relation between speed of sound and temperature of IPRT

Temperature can be calculated from the speed of sound using Eq. (23). Differences in calculated thermodynamic temperature and temperature measured by resistance thermometer are shown in Figure 83. It is evident, that not all the radial resonance modes can be reliably used for thermometry purposes in the current configuration and that at temperatures about 50 °C the

system indicates higher instability of results than in other cases which can be caused by proximity to maximum operating temperature of acoustic preamplifiers.

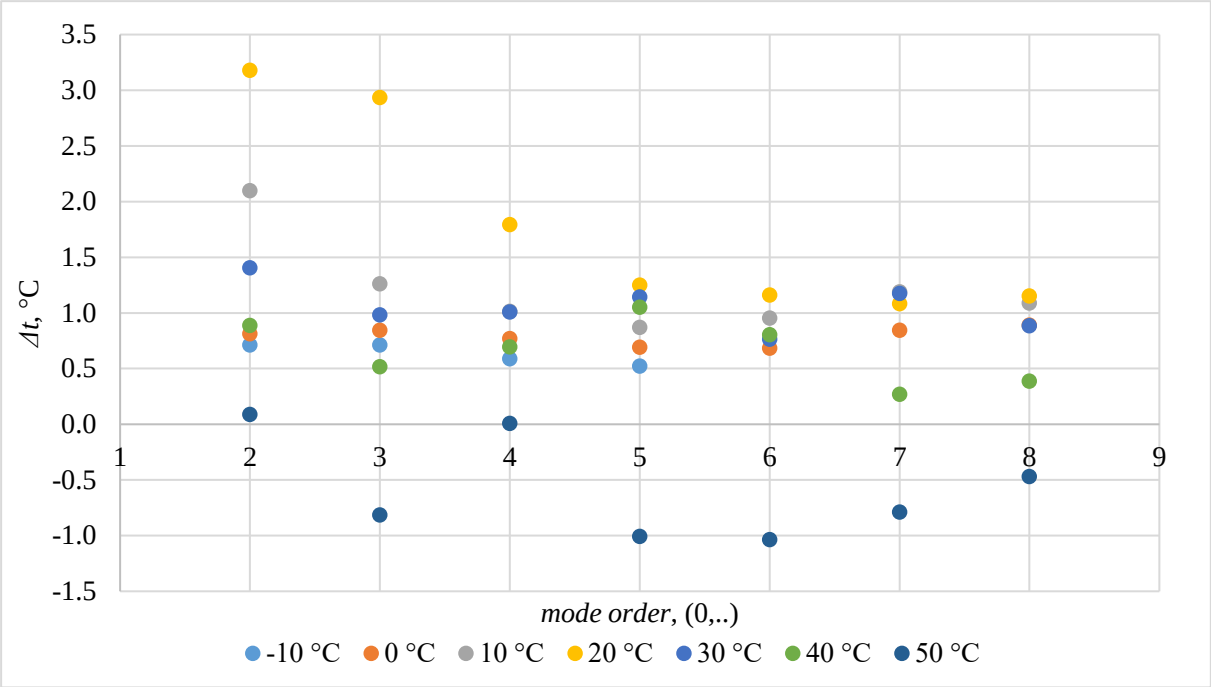

Figure 83: Differences in temperature calculated from speed of sound and temperature measured by IPRT

Resonance modes (0,5) and (0,6) can be followed to make the resonator capable of temperature measurement at ambient air environment in climatic chamber. The detail of previous results (Figure 83) for these two spherical modes is shown in Figure 84.

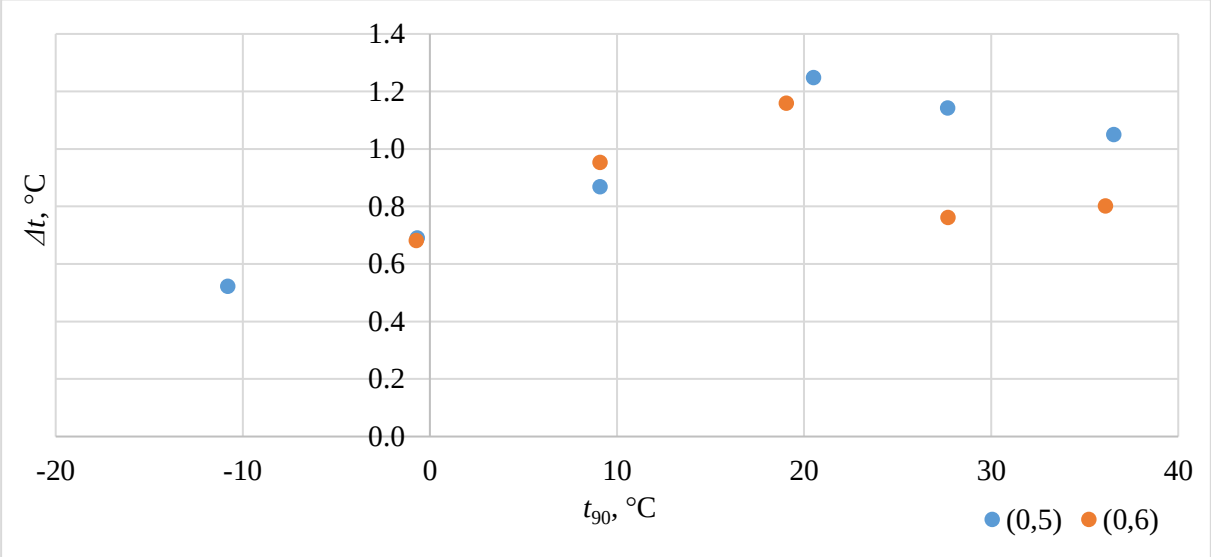

Figure 84: Differences in temperature calculated from speed of sound (at modes (0,5) and (0,6)) and temperature measured by IPRT

The average difference between temperature calculated from the IPRT and from acoustic measurements at resonance modes (0,5) and (0,6) can be caused by the selfheating of industrial resistance thermometer that is usually in order of several tenths of °C in combination with instability of the climatic chamber (up to 0.5 °C according to its calibration certificate) as well as unknown and possible fluctuations of air pressure and composition. The quality of acoustic measurements is usually represented in a form of agreement between resonance modes, i.e. differences from an average u or T value. Relatively high acoustic noise level produced by the chamber itself, during its operation affected the measurement quality.

6. Conclusion

6.1. Meeting the objectives

The practical acoustic thermometer which can be comparable to industrial platinum resistance thermometers was the main objective of this work and is described in Section 5.1. Building a prototype of the practical acoustic thermometer, using single microphone for its operation is described in Section 5.1.1 which meets sub-objective A. The unique design allows the microphone to serve both as a transducer and receiver simultaneously, removing the uncertainty contribution connected to time synchronisation between the transmitter and receiver channel. After the initial calibration, several enhancements were performed in order to minimize the measurement uncertainty. These modifications are described in Section 5.1.2. The development resulted in portable system (Section 5.1.3) that meets sub-objective B. It is capable to measure the thermodynamic temperature in the range from -80 °C to 80 °C (meeting sub-objective C, calibration in Section 5.1.3.2) with the agreement between measured thermodynamic temperature and t_{90} (measured by SPRT) below 0.15 °C (probably limited by imperfect length measurement), excluding temperature of 40 °C, and associated measurement uncertainty ranging from 0.029 °C to 0.043 °C (meeting sub-objective D, uncertainty analysis in Section 5.1.3.3). The microphone is probably at the upper temperature limit of its operation during measurements above 100 °C, leading to higher disagreement between t_{90} (measured by SPRT) and t (measured by PAT).

The result of presented research is comparable to latest achievements in practical acoustic gas thermometry and the resulting PAT device can serve for IPRT calibrations in industrial baths and furnaces with traceability to the thermodynamic temperature scale. High potential of practical acoustic thermometry was proven. Developed industrial acoustic thermometer could serve to introduce thermodynamic means of temperature measurement to industry.

Another task (described in Section 5.2.1) was to assemble the high-temperature apparatus in INRiM and to perform an acoustic measurement at elevated pressure above 430 K to obtain an isotherm and to prove an effectiveness of this apparatus and AGT at high temperatures. Insufficient vessel tightness at 550 K caused the Ar gas to leak in the main furnace, electrical shorting of heating lamps, subsequent destruction of measurement microphones and main pressure transducer. Despite that, measurements in Ar up to 550 K and obtaining an isotherm at 294 K between 100 kPa and 430 kPa was successfully performed. Therefore, the sub-objective E was met only partially.

In addition, the corresponding training and skill accumulation allowed to bring the acoustic gas thermometry into CMI (meeting the sub-objective F), with the preliminary measurements described in Section 5.2.2.

6.2. Further work

The uncertainty of PAT measurement can be furthermore minimized in the future by redesigning the waveguide body to achieve better gas- and pressure-tightness to allow high-pressure measurement in the range up to 1 MPa and by employing microphone capable of operation at higher temperatures. Also, more precise way of length measurement was not yet found, since the best accessible dimensional measurement technique (coordinate measurement machine) is not capable to access the bottom of the waveguide and the X-ray dimensional measurement offers higher measurement uncertainty than method used in this research. The upper temperature limit can be extended by lengthening the waveguide.

The work described in Section 5.2.2 will be followed by measurements in the gas- and pressure-tight vessel using the temperature-controlled system (that are currently in production and will enable measurements in monatomic gas at elevated pressures and temperatures).

7. References

[1] *About EURAMET - EURAMET*. (n.d.). https://www.euramet.org/about-euramet/?L=0. Retrieved on September 5, 2022, from

[2] Velichko, O. N. (2009). Traceability of measurement results at different levels of metrological work. *Measurement Techniques*, *52*(11), 1242–1248. https://doi.org/10.1007/s11018-010-9428-7. Retrieved on May 19, 2019

[3] Machin, G. (2018). The kelvin redefined. *Measurement Science and Technology*, *29*(2), 022001. https://doi.org/10.1088/1361-6501/aa9ddb. Retrieved on June 11, 2019

[4] Bipm. (2018). *Guide to the Realization of the ITS-90 Fixed Points: Triple Point of Water Triple Point of Water*. https://www.bipm.org/documents/20126/41773843/Guide_ITS-90_2_2_TPW-2018.pdf/b4feee2a-3e84-cc30-eba7-94592b247bd2. Retrieved on June 11, 2019

[5] Bipm. (2018). *Guide to the Realization of the ITS-90: Introduction*. https://www.bipm.org/utils/common/pdf/ITS-90/Guide_ITS-90_1_Introduction_2018.pdf. Retrieved on May 30, 2019

[6] Hill, K. D., & Steele, A. G. (2014). The International Temperature Scale: Past, Present, and Future. *NCSLI Measure*, *9*(1), 60–67. https://doi.org/10.1080/19315775.2014.11721675. Retrieved on June 12, 2019

[7] Fischer, J. (2015). Progress towards a new definition of the kelvin. *Metrologia*, *52*(5), S364–S375. https://doi.org/10.1088/0026-1394/52/5/S364. Retrieved on August 9, 2018

[8] Bipm. (2018). *Guide to the Realization of the ITS-90: Metal Fixed Points for Contact Thermometry*. https://www.bipm.org/utils/common/pdf/ITS-90/Guide_ITS-90_2_4_MetalFixedPoints_2018.pdf. Retrieved on March 17, 2021

[9] Bipm. (2018). *Guide to the Realization of the ITS-90: Cryogenic Fixed Points*. https://www.bipm.org/documents/20126/41773843/Guide_ITS-90_2_3_Cryogenic_FP_2018.pdf/8289e448-3de9-4688-804e-1187d9215b83. Retrieved on March 24, 2020

[10] Bipm. (2018). *Guide to the Realization of the ITS-90: Radiation Thermometry*. https://www.bipm.org/documents/20126/41773843/Guide_ITS-90_6_RadiationThermometry_2018.pdf/f346ba40-fb17-b2a9-5641-ea3f0071532e. Retrieved on March 24, 2020

[11] BIPM, Pavillon de Breteuil, F.-92312 S., & Organisation intergouvernementale de la Convention du Mètre. (1997). *TECHNIQUES FOR APPROXIMATING THE INTERNATIONAL TEMPERATURE SCALE OF 1990* (1st ed.). https://www.researchgate.net/publication/236979431_Techniques_for_approximating_the_ITS-90. Retrieved on June 12, 2019

[12] Bipm. (2021). *Guide to the Realization of the ITS-90: Platinum Resistance Thermometry*. https://www.bipm.org/documents/20126/41773843/Guide_ITS-90_5_SPRT_2021.pdf/c4bbbe56-4118-eef7-47cb-3ea234db40b8. Retrieved on June 12, 2019

[13] International standard: *IEC 60751:2022 Industrial platinum resistance thermometers and platinum temperature sensors*, 3rd edition, 47 pg. Available at: https://webstore.iec.ch/publication/63753. Retrieved on January 8, 2023

[14] White, D. R., Ballico, M., del Campo, D., Duris, S., Filipe, E., Ivanova, A., … Yamazawa, K. (2007). Uncertainties in the Realization of the SPRT Sub-ranges of the ITS-90. *International Journal of Thermophysics*, *28*(6), 1868–1881. https://doi.org/10.1007/s10765-007-0271-2. Retrieved on June 12, 2019

[15] Euramet. *EURAMET Calibration Guide No. 8: Guidelines on the Calibration of Thermocouples*. Calibration guide, version 3.0 (02/2019), ISBN: 978-3-942992-55-8. https://www.euramet.org/download/?tx_eurametfiles_download%5Bfiles%5D=37682&tx_eurametfiles_download%5Bidentifier%5D=%252Fdocs%252FPublications%252Fcalguides%252FI-CAL-GUI-

008_Calibration_Guideline_No._8_web.pdf&tx_eurametfiles_download%5Baction%5D=download&tx_eurametfiles_download%5Bcontroller%5D=File&cHash=163bab2a6aa1604eb9128d2db479c78c. Retrieved on March 4, 2019
[16] MSL New Zealand: *MSL Technical Guide 14: Making Sense of Thermocouples – General Guide*, Version 3, July 2019, https://www.measurement.govt.nz/download/23. Retrieved on May 24, 2021
[17] Bentley, R. E. (1998). The use of elemental thermocouples in high-temperature precision thermometry. *Measurement*, *23*(1), 35–46. https://doi.org/10.1016/S0263-2241(98)00007-4. Retrieved on June 12, 2019
[18] Pearce, J. V, Ongrai, O., Machin, G., & Sweeney, S. J. (2010). Self-validating thermocouples based on high temperature fixed points. *Metrologia*, *47*(1), L1–L3. https://doi.org/10.1088/0026-1394/47/1/L01. Retrieved on June 12, 2019
[19] Bipm. (2022). *Guide to the Realization of the ITS-90: Specialized Fixed Points above 0 °C*. https://www.bipm.org/utils/common/pdf/ITS-90/Specialized-FPs-above-0C.pdf. Retrieved on September 2, 2022
[20] Boyes W.: *Instrumentation Reference Book*. (2010). 928 pg., ISBN:978-0-7506-8308-1, https://doi.org/10.1016/C2009-0-25186-5. Retrieved on June 12, 2019
[21] Joachim. (n.d.). *CCT-WG5 on radiation thermometry Uncertainty budgets for realisation of scales by radiation thermometry*. https://www.bipm.org/cc/CCT/Allowed/22/CCT03-03.pdf. Retrieved on June 12, 2019
[22] Saunders, P., Fischer, J., Sadli, M., Battuello, M., Park, C. W., Yuan, Z., … Ugur, S. (2008). Uncertainty Budgets for Calibration of Radiation Thermometers below the Silver Point. *International Journal of Thermophysics*, *29*(3), 1066–1083. https://doi.org/10.1007/s10765-008-0385-1. Retrieved on June 12, 2019
[23] Bedford, R. E., Bonnier, G., Maas, H., & Pavese, F. (1984). Recommended Values of Temperature for a Selected Set of Secondary Reference Points. *Metrologia*, *20*(4), 145–155. https://doi.org/10.1088/0026-1394/20/4/003. Retrieved on June 17, 2019
[24] Steur, P. P. M., & Giraudi, D. (2014). Preliminary Measurements of the Xenon Triple Point. *International Journal of Thermophysics*, *35*(3–4), 604–610. https://doi.org/10.1007/s10765-014-1580-x. Retrieved on June 12, 2019
[25] Ambrose, D. (1957). The triple point of carbon dioxide as a thermometric fixed point. *British Journal of Applied Physics*, *8*(1), 32–34. https://doi.org/10.1088/0508-3443/8/1/309. Retrieved on June 13, 2019
[26] Tew, W. L., & Quelhas, K. N. (1990). Realizations of the Triple Point of Sulfur Hexafluoride in Transportable and Refillable Cells. *J Res Natl Inst Stan*, *123*, 123013. https://doi.org/10.6028/jres.123.013. Retrieved on June 13, 2019
[27] Bipm. (2018). *Guide to the Realization of the ITS-90: Fixed Points for Radiation Thermometry*. https://www.bipm.org/utils/common/pdf/ITS-90/Guide_ITS-90_2_5_RTFixedPoints_2018.pdf. Retrieved on June 12, 2019
[28] Woolliams, E. R., Machin, G., Lowe, D. H., & Winkler, R. (2006). Metal (carbide)–carbon eutectics for thermometry and radiometry: a review of the first seven years. *Metrologia*, *43*(6), R11–R25. https://doi.org/10.1088/0026-1394/43/6/R01. Retrieved on June 14, 2019
[29] Bojkovski, J., Hiti, M., Batagelj, V., & Drnovšek, J. (2011). Design, Construction, and Evaluation of Ni–C Eutectic Fixed Points. *International Journal of Thermophysics*, *32*(7–8), 1800–1810. https://doi.org/10.1007/s10765-011-1034-7. Retrieved on June 12, 2019
[30] Yuan, Z., Wang, T., Lu, X., Dong, W., Bai, C., Hao, X., & Duan, Y. (2011). T 90 Measurement of Co-C, Pt-C, and Re-C High-Temperature Fixed Points at the NIM. *International Journal of Thermophysics*, *32*(7–8), 1744–1752. https://doi.org/10.1007/s10765-011-0993-z. Retrieved on June 14, 2019
[31] Anhalt, K., Hartmann, J., Lowe, D., Machin, G., Sadli, M., & Yamada, Y. (2006). Thermodynamic temperature determinations of Co–C, Pd–C, Pt–C and Ru–C eutectic fixed-

point cells. *Metrologia*, *43*(2), S78–S83. https://doi.org/10.1088/0026-1394/43/2/S16. Retrieved on June 14, 2019
[32] Machin, G., Bloembergen, P., Anhalt, K., Hartmann, J., Sadli, M., Saunders, P., … Yoon, H. (2010). Practical Implementation of the Mise en Pratique for the Definition of the Kelvin Above the Silver Point. *International Journal of Thermophysics*, *31*(8–9), 1779–1788. https://doi.org/10.1007/s10765-010-0834-5. Retrieved on August 21, 2018
[33] Bipm. (2018). *Guide to the Realization of the ITS-90: Fixed Points: Influence of Impurities*. https://www.bipm.org/utils/common/pdf/ITS-90/Guide_ITS-90_2_1_Impurities_2018.pdf. Retrieved on June 12, 2019
[34] Sostmann, H. E., & Tavener, J. P. (n.d.). *FUNDAMENTALS OF THERMOMETRY PART II FIXED POINTS OF THE ITS-90 CONFIDENCE IN THE METAL FREEZING POINTS OF ITS-90*. http://www.isotechna.com/v/vspfiles/pdf_articles/Fixed%20Points%20of%20the%20ITS-90%20and%20Confidence%20in%20the%20Metal%20Freezing%20Points%20of%20ITS-90.pdf. Retrieved on May 30, 2019
[35] Bipm (n.d.). *Estimates of the Differences between Thermodynamic Temperature and the ITS-90*. https://www.bipm.org/documents/20126/2619564/Estimates_Differences_T-T90_2010.pdf/a109650e-6939-3840-974f-cf77f3796e5e. Retrieved on August 23, 2018
[36] Mills, I. M., Mohr, P. J., Quinn, T. J., Taylor, B. N., & Williams, E. R. (2006). Redefinition of the kilogram, ampere, kelvin and mole: a proposed approach to implementing CIPM recommendation 1 (CI-2005). *Metrologia*, *43*(3), 227–246. https://doi.org/10.1088/0026-1394/43/3/006. Retrieved on August 9, 2018
[37] Peruzzi, A., Dobre, M., van Geel, J., Uytun, A., Kalemci, M., Uysal, E., … Davis, C. (2014). Effect of Impurities on Water Triple-Point Cells. *International Journal of Thermophysics*, *35*(6–7), 1084–1096. https://doi.org/10.1007/s10765-014-1702-5. Retrieved on June 27, 2019
[38] Gam, K. S., Kang, K. H., Kim, Y.-G., & Yang, I. (2008). Isotopic Composition of Water Used in Triple-Point Cells. *International Journal of Thermophysics*, *29*(3), 808–814. https://doi.org/10.1007/s10765-008-0414-0. Retrieved on June 27, 2019
[39] Yan, X. K., Zhang, J. T., Wang, Y. L., Ma, C. F., & Duan, Y. N. (2008). Isotopic Effects on the Temperature of the Triple Point of Water. *International Journal of Thermophysics*, *29*(1), 104–111. https://doi.org/10.1007/s10765-007-0321-9. Retrieved on June 27, 2019
[40] Sakurai, H. (2011). *CCT/05-11: Hydrostatic Pressure Correction Coefficient of the Triple Point Cell of Water*. https://www.bipm.org/documents/20126/28439029/working-document-ID-1785/b55e5aa5-5e8d-5d6b-8c8d-4d1ae0024d97/. Retrieved on May 30, 2019
[41] BIPM (2019 June 27): *Thermometry: SI base unit (kelvin)*, webpage. https://www.bipm.org/en/si-base-units/kelvin. Retrieved on June 27, 2019
[42] Fischer J. 2016 Low uncertainty Boltzmann constant determinations and the kelvin redefinition. Phil. Trans. R. Soc. A 374: 20150038. http://dx.doi.org/10.1098/rsta.2015.0038. Retrieved on June 12, 2019
[43] Bipm. (May 2019). *Mise en pratique for the definition of the kelvin in the SI*. 9th edition. https://www.bipm.org/documents/20126/41489682/SI-App2-kelvin.pdf/cd36cb68-3f00-05fd-339e-452df0b6215e?version=1.5&t=1637237805352&download=true. Retrieved on August 21, 2019
[44] Pitre, L., Risegari, L., Sparasci, F., Plimmer, M. D., Himbert, M. E., & Giuliano Albo, P. A. (2015). Determination of the Boltzmann constant *k* from the speed of sound in helium gas at the triple point of water. *Metrologia*, *52*(5), S263–S273. https://doi.org/10.1088/0026-1394/52/5/S263. Retrieved on May 20, 2019
[45] Gavioso, R. M., Benedetto, G., Albo, P. A. G., Ripa, D. M., Merlone, A., Guianvarc'h, C., … Cuccaro, R. (2010). A determination of the Boltzmann constant from speed of sound measurements in helium at a single thermodynamic state. *Metrologia*, *47*(4), 387–409. https://doi.org/10.1088/0026-1394/47/4/005. Retrieved on June 12, 2019

[46] Fischer, J., & Fellmuth, B. (2005). Temperature metrology. *Reports on Progress in Physics*, *68*(5), 1043–1094. https://doi.org/10.1088/0034-4885/68/5/R02. Retrieved on March 1, 2018
[47] White DR, Galleano R, Actis A, Brixy H, Groot M De, Dubbeldam J, et al (1996). The status of Johnson noise thermometry. Metrologia 1996;33:325–35. https://iopscience.iop.org/article/10.1088/0026-1394/33/4/6. Retrieved on April 10, 2019
[48] Bramley, P., Cruickshank, D., & Pearce, J. (2017). The Development of a Practical, Drift-Free, Johnson-Noise Thermometer for Industrial Applications. *International Journal of Thermophysics*, *38*(2), 25. https://doi.org/10.1007/s10765-016-2156-8. Retrieved on April 29, 2019
[49] White DR. (2012). Non-linearity in Johnson noise thermometry. Metrologia 2012;49:651–65. https://iopscience.iop.org/article/10.1088/0026-1394/49/6/651. Retrieved on April 25, 2019
[50] Qu J, Benz SP, Pollarolo A, Rogalla H, Tew WL, White R, et al. (2015). Improved electronic measurement of the Boltzmann constant by Johnson noise thermometry. Metrologia 2015;52:S242–56. https://iopscience.iop.org/article/10.1088/0026-1394/52/5/S242/meta. Retrieved on April 25, 2019
[51] Qu, J., Benz, S. P., Coakley, K., Rogalla, H., Tew, W. L., White, R., … Zhou, Z. (2017). An improved electronic determination of the Boltzmann constant by Johnson noise thermometry. *Metrologia*, *54*(4), 549–558. https://doi.org/10.1088/1681-7575/aa781e. Retrieved on April 30, 2019
[52] Zandt, T., Fellmuth, B., Gaiser, C., Kuhn, A., Merlone, A., Moro, F., & Thiele-Krivoi, B. (2011). Capabilities for Dielectric-Constant Gas Thermometry in a Special Large-Volume Liquid-Bath Thermostat. *International Journal of Thermophysics*, *32*(7–8), 1355–1365. https://doi.org/10.1007/s10765-011-0980-4. Retrieved on May 3, 2019
[53] Gaiser, C., Fellmuth, B., & Zandt, T. (2014). Dielectric-Constant Gas Thermometry and the Relation to the Virial Coefficients. *International Journal of Thermophysics*, *35*(3–4), 395–404. https://doi.org/10.1007/s10765-014-1569-5. Retrieved on May 3, 2019
[54] Gaiser, C., Zandt, T., & Fellmuth, B. (2015). Dielectric-constant gas thermometry. *Metrologia*, *52*(5), S217–S226. https://doi.org/10.1088/0026-1394/52/5/S217. Retrieved on May 30, 2019
[55] Fellmuth, B., Fischer, J., Gaiser, C., Jusko, O., Priruenrom, T., Sabuga, W., & Zandt, T. (2011). Determination of the Boltzmann constant by dielectric-constant gas thermometry. Metrologia, 48(5), 382–390. https://doi.org/10.1088/0026-1394/48/5/020. Retrieved on May 7, 2019
[56] Gaiser, C., Fellmuth, B., & Haft, N. (2008). Primary Dielectric-Constant Gas Thermometry in the Range from 2.4 K to 26 K at PTB. International Journal of Thermophysics, 29(1), 18–30. https://doi.org/10.1007/s10765-007-0318-4. Retrieved on May 2, 2019
[57] Gaiser, C., Zandt, T., Fellmuth, B., Fischer, J., Jusko, O., & Sabuga, W. (2013). Improved determination of the Boltzmann constant by dielectric-constant gas thermometry. Metrologia, 50(6), L7–L11. https://doi.org/10.1088/0026-1394/50/6/L7. Retrieved on May 9, 2019
[58] Fasci, E., Domenica De Vizia, M., Merlone, A., Moretti, L., Castrillo, A., & Gianfrani, L. (2015). The Boltzmann constant from the $H_2{}^{18}O$ vibration-rotation spectrum: complementary tests and revised uncertainty budget. Metrologia, 52(5), S233–S241. https://doi.org/10.1088/0026-1394/52/5/S233. Retrieved on May 3, 2019
[59] Pitre, L., Plimmer, M. D., Sparasci, F., & Himbert, M. E. (2018). Determinations of the Boltzmann constant. Comptes Rendus Physique. https://doi.org/10.1016/J.CRHY.2018.11.007. Retrieved on May 22, 2019
[60] Gianfrani, L. (2016). Linking the thermodynamic temperature to an optical frequency: recent advances in Doppler broadening thermometry. Philosophical Transactions of the Royal Society A: Mathematical, Physical and Engineering Sciences, 374(2064), 20150047. https://doi.org/10.1098/rsta.2015.0047. Retrieved on May 13, 2019
[61] Amodio, P., De Vizia, M. D., Moretti, L., & Gianfrani, L. (2015). Investigating the ultimate accuracy of Doppler-broadening thermometry by means of a global fitting procedure.

Physical Review A, 92(3), 032506. https://doi.org/10.1103/PhysRevA.92.032506. Retrieved on May 10, 2019
[62] Hashemi, R., Povey, C., Derksen, M., Naseri, H., Garber, J., & Predoi-Cross, A. (2014). Doppler broadening thermometry of acetylene and accurate measurement of the Boltzmann constant. The Journal of Chemical Physics, 141(21), 214201. https://doi.org/10.1063/1.4902076. Retrieved on May 13, 2019
[63] Moldover, M. R., Gavioso, R. M., Mehl, J. B., Pitre, L., de Podesta, M., & Zhang, J. T. (2014). Acoustic gas thermometry. Metrologia, 51(1), R1–R19. https://doi.org/10.1088/0026-1394/51/1/R1. Retrieved on March 2, 2018
[64] Pitre, L., Sparasci, F., Truong, D., Guillou, A., Risegari, L., & Himbert, M. E. (2011). Determination of the Boltzmann constant using a quasi-spherical acoustic resonator. Philosophical Transactions of the Royal Society A: Mathematical, Physical and Engineering Sciences, 369(1953), 4014–4027. https://doi.org/10.1098/rsta.2011.0197. Retrieved on May 16, 2019
[65] Benedetto, G., Gavioso, R. M., Spagnolo, R., Marcarino, P., & Merlone, A. (2004). Acoustic measurements of the thermodynamic temperature between the triple point of mercury and 380 K. Metrologia, 41(1), 74–98. https://doi.org/10.1088/0026-1394/41/1/011. Retrieved on May 16, 2019
[66] Segovia, J. J., Vega-Maza, D., Martín, M. C., Gómez, E., Tabacaru, C., & del Campo, D. (2010). An Apparatus Based on a Spherical Resonator for Measuring the Speed of Sound in Gases and for Determining the Boltzmann Constant. *International Journal of Thermophysics*, *31*(7), 1294–1309. https://doi.org/10.1007/s10765-010-0746-4. Retrieved on June 12, 2019
[67] Gao, B., Pan, C., Chen, Y., Song, Y., Zhang, H., Han, D., Liu, W., Chen, H., Luo, E., & Pitre, L. (2018). Realization of an ultra-high precision temperature control in a cryogen-free cryostat. *Review of Scientific Instruments*, *89*(10), 104901. https://doi.org/10.1063/1.5043206. Retrieved on September 6, 2022
[68] Underwood, R., de Podesta, M., Sutton, G., Stanger, L., Rusby, R., Harris, P., Morantz, P., & MacHin, G. (2016). Estimates of the difference between thermodynamic temperature and the International Temperature Scale of 1990 in the range 118 K to 303 K. *Philosophical Transactions of the Royal Society A: Mathematical, Physical and Engineering Sciences*, *374*(2064). https://doi.org/10.1098/RSTA.2015.0048. Retrieved on September 6, 2022
[69] de Podesta, M., May, E. F., Mehl, J. B., Pitre, L., Gavioso, R. M., Benedetto, G., … Flack, D. (2010). Characterization of the volume and shape of quasi-spherical resonators using coordinate measurement machines. *Metrologia*, *47*(5), 588–604. https://doi.org/10.1088/0026-1394/47/5/010. Retrieved on May 28, 2019
[70] Pitre, L., Moldover, M. R., & Tew, W. L. (2006). Acoustic thermometry: new results from 273 K to 77 K and progress towards 4 K. *Metrologia*, *43*(1), 142–162. https://doi.org/10.1088/0026-1394/43/1/020. Retrieved on May 23, 2019
[71] Mehl, J. B. (2009). Second-order electromagnetic eigenfrequencies of a triaxial ellipsoid. *Metrologia*, *46*(5), 554–559. https://doi.org/10.1088/0026-1394/46/5/020. Retrieved on May 27, 2019
[72] Mehl, J. B. (2015). Second-order electromagnetic eigenfrequencies of a triaxial ellipsoid II. *Metrologia*, *52*(5), S227–S232. https://doi.org/10.1088/0026-1394/52/5/S227. Retrieved on May 27, 2019
[73] May, E. F., Pitre, L., Mehl, J. B., Moldover, M. R., & Schmidt, J. W. (2004). Quasi-spherical cavity resonators for metrology based on the relative dielectric permittivity of gases. *Review of Scientific Instruments*, *75*(10), 3307. https://doi.org/10.1063/1.1791831. Retrieved on September 6, 2022
[74] Mehl, J. B., Moldover, M. R., & Pitre, L. (2004). Designing quasi-spherical resonators for acoustic thermometry. *Metrologia*, *41*(4), 295–304. https://www.researchgate.net/publication/231102650_Designing_quasi-

spherical_resonators_for_acoustic_thermometry/link/5bcece5e92851c1816ba5587/download. Retrieved on May 28, 2019
[75] Perkins, R. A., & McLinden, M. O. (2015). Spherical resonator for vapor-phase speed of sound and measurements of 1,1,1,2,2,3,3-heptafluoro-3-methoxypropane (RE347mcc) and trans-1,3,3,3-tetrafluoropropene [R1234ze(E)]. *The Journal of Chemical Thermodynamics*, *91*, 43–61. https://doi.org/10.1016/J.JCT.2015.07.005. Retrieved on May 28, 2019
[76] Gavioso, R. M., Madonna Ripa, D., Steur, P. P. M., Gaiser, C., Truong, D., Guianvarc'h, C., … Dematteis, R. (2015). A determination of the molar gas constant *R* by acoustic thermometry in helium. *Metrologia*, *52*(5), S274–S304. https://doi.org/10.1088/0026-1394/52/5/S274. Retrieved on June 21, 2018
[77] Gavioso, R. M., Benedetto, G., Madonna Ripa, D., Giuliano Albo, P. A., Guianvarc'h, C., Merlone, A., … Cuccaro, R. (2011). Progress in INRiM Experiment for the Determination of the Boltzmann Constant with a Quasi-spherical Resonator. *International Journal of Thermophysics*, *32*(7–8), 1339–1354. https://doi.org/10.1007/s10765-011-1032-9. Retrieved on May 28, 2019
[78] Podesta, M. de, Underwood, R., Sutton, G., Morantz, P., Harris, P., Mark, D. F., … Machin, G. (2013). A low-uncertainty measurement of the Boltzmann constant. *Metrologia*, *50*(4), 354–376. https://doi.org/10.1088/0026-1394/50/4/354. Retrieved on June 12, 2019
[79] Sun, J. P., Zhang, J. T., Zhang, X. Y., Lin, H., & Feng, X. J. (2011). Length Determination of a Fixed-Path Cylindrical Resonator with the Dual Wavelength Laser Interference Method. *International Journal of Thermophysics*, *32*(7–8), 1330–1338. https://doi.org/10.1007/s10765-011-1045-4. Retrieved on May 28, 2019
[80] Underwood, R. J., & Edwards, G. J. (2014). Microwave-Dimensional Measurements of Cylindrical Resonators for Primary Acoustic Thermometry. *International Journal of Thermophysics*, *35*(6–7), 971–984. https://doi.org/10.1007/s10765-014-1726-x. Retrieved on May 28, 2019
[81] Feng, X. J., Zhang, J. T., Lin, H., Gillis, K. A., Mehl, J. B., Moldover, M. R., … Duan, Y. N. (2017). Determination of the Boltzmann constant with cylindrical acoustic gas thermometry: new and previous results combined. *Metrologia*, *54*(5), 748–762. https://doi.org/10.1088/1681-7575/aa7b4a. Retrieved on May 28, 2019
[82] Lin, H., Feng, X. J., Gillis, K. A., Moldover, M. R., Zhang, J. T., Sun, J. P., & Duan, Y. Y. (2013). Improved determination of the Boltzmann constant using a single, fixed-length cylindrical cavity. *Metrologia*, *50*(5), 417–432. https://doi.org/10.1088/0026-1394/50/5/417. Retrieved on May 28, 2019
[83] Preston-Thomas, H. (1990). The International Temperature Scale of 1990 (ITS-90). *Metrologia*, *27*(1), 3. Retrived from https://doi.org/10.1088/0026-1394/27/1/002. Retrieved on May 30, 2019
[84] Stock, M., Davis, R., de Mirandés, E., & Milton, M. J. T. (2019). The revision of the SI—the result of three decades of progress in metrology. *Metrologia*, *56*(2), 022001. https://doi.org/10.1088/1681-7575/AB0013. Retrieved on November 3, 2020
[85] Tiesinga, E., Mohr, P. J., Newell, D. B., & Taylor, B. N. (2021). Codata recommended values of the fundamental physical constants: 2018. *Reviews of Modern Physics*, *93*(2), 025010. https://doi.org/10.1103/REVMODPHYS.93.025010/FIGURES/10/MEDIUM. Retrieved on September 12, 2022
[86] Gavioso, R. M., Madonna Ripa, D., Steur, P. P. M., Dematteis, R., & Imbraguglio, D. (2019). Determination of the thermodynamic temperature between 236 K and 430 K from speed of sound measurements in helium. *Metrologia*, *56*(4), 045006. https://doi.org/10.1088/1681-7575/AB29A2. Retrieved on September 12, 2022
[87] Fellmuth, B., Fischer, J., MacHin, G., Picard, S., Steur, P. P. M., Tamura, O., White, D. R., & Yoon, H. (2016). The kelvin redefinition and its mise en pratique. *Philosophical Transactions of the Royal Society A: Mathematical, Physical and Engineering Sciences*, *374*(2064). https://doi.org/10.1098/RSTA.2015.0037. Retrieved on June 12, 2019

[88] *Strategy Document for Rolling Programme Development from 2021 to 2030 The Consultative Committee for Thermometry 1. General Information on the Consultative Committee for Thermometry*. (n.d.). https://www.bipm.org/documents/20126/41598583/CCT+Strategy/145827b2-4f6a-42ed-bd77-bbffa782e2f7. Retrieved on September 21, 2021

[89] de Podesta, M., Sutton, G., Underwood, R., Legg, S., & Steinitz, A. (2010). Practical Acoustic Thermometry with Acoustic Waveguides. *International Journal of Thermophysics*, *31*(8–9), 1554–1566. https://doi.org/10.1007/s10765-010-0793-x. Retrieved on February 19, 2018

[90] de Podesta, M., Sutton, G., Edwards, G., Stanger, L., & Preece, H. (2015). Practical acoustic thermometry with twin-tube and single-tube sensors. *2015 4th International Conference on Advancements in Nuclear Instrumentation Measurement Methods and Their Applications (ANIMMA)*, 1–6. https://doi.org/10.1109/ANIMMA.2015.7465575. Retrieved on February 20, 2018

[91] Johansson, L., Filtz, J.-R., DeFelice, P., Sadli, M., Plompen, A., Heyse, J., … Keightley, J. (2013). Metrology for new generation nuclear power plants - MetroFission. *2013 3rd International Conference on Advancements in Nuclear Instrumentation, Measurement Methods and Their Applications (ANIMMA)*, 1–8. https://doi.org/10.1109/ANIMMA.2013.6727929. Retrieved on February 19, 2018

[92] Sutton, G., Edwards, G., Veltcheva, R., & de Podesta, M. (2015). Twin-tube practical acoustic thermometry: theory and measurements up to 1000 °C. *Measurement Science and Technology*, *26*(8), 085901. https://doi.org/10.1088/0957-0233/26/8/085901. Retrieved on February 19, 2018

[93] Huang, K. N., Huang, C. F., Li, Y. C., & Young, M. S. (2002). High precision, fast ultrasonic thermometer based on measurement of the speed of sound in air. *Review of Scientific Instruments*, *73*(11), 4022–4027. https://doi.org/10.1063/1.1510576. Retrieved on February 19, 2018

[94] Tsai, W.-Y., Chen, H.-C., & Liao, T.-L. (2005). An ultrasonic air temperature measurement system with self-correction function for humidity. *Measurement Science and Technology*, *16*(2), 548–555. https://doi.org/10.1088/0957-0233/16/2/030. Retrieved on March 9, 2018

[95] Sarabia, E., Llata, J., Robla, S., Torre-Ferrero, C., & Oria, J. (2013). Accurate Estimation of Airborne Ultrasonic Time-of-Flight for Overlapping Echoes. *Sensors*, *13*(11), 15465–15488. https://doi.org/10.3390/s131115465. Retrieved on March 9, 2018

[96] Chia-Chang Tong, Figueroa, J. F., & Barbieri, E. (2001). A method for short or long range time-of-flight measurements using phase-detection with an analog circuit. *IEEE Transactions on Instrumentation and Measurement*, *50*(5), 1324–1328. https://doi.org/10.1109/19.963205. Retrieved on March 9, 2018

[97] Liao, T.-L., Tsai, W.-Y., & Huang, C.-F. (2004). A new ultrasonic temperature measurement system for air conditioners in automobiles. *Measurement Science and Technology*, *15*(2), 413–419. https://doi.org/10.1088/0957-0233/15/2/014. Retrieved on March 9, 2018

[98] Gueuning, F., Varlan, M., Eugene, C., & Dupuis, P. (n.d.). Accurate distance measurement by an autonomous ultrasonic system combining time-of-flight and phase-shift methods. *Quality Measurement: The Indispensable Bridge between Theory and Reality (No Measurements? No Science! Joint Conference - 1996: IEEE Instrumentation and Measurement Technology Conference and IMEKO Technical Committee 7. Conference Proceedings*, *1*, 399–404. https://doi.org/10.1109/IMTC.1996.507414. Retrieved on March 9, 2018

[99] Wei, Y., Gao, Y., Xiao, Z., Wang, G., Tian, M., & Liang, H. (2016). Ultrasonic Al_2O_3 Ceramic Thermometry in High-Temperature Oxidation Environment. *Sensors (Basel, Switzerland)*, *16*(11). https://doi.org/10.3390/s16111905. Retrieved on March 9, 2018

[100] Daw, J. E., Rempe, J. L., & Wilkins, S. C. (2002, November 1). *Ultrasonic Thermometry for In-Pile Temperature Detection*. https://www.osti.gov/biblio/1004265. Retrieved on March 9, 2018

[101] Huger, M., Fargeot, D., & Gault, C. (2002). High-temperature measurement of ultrasonic wave velocity in refractory materials. High Temperatures-High Pressures, 34(2), 193–201. https://www.researchgate.net/publication/243392623_High-temperature_measurement_of_ultrasonic_wave_velocity_in_refractory_materials. Retrieved on May 29, 2019
[102] Yong Jin Lee, Khuri-Yakub, B. T., & Saraswat, K. (1996). Temperature measurement in rapid thermal processing using the acoustic temperature sensor. IEEE Transactions on Semiconductor Manufacturing, 9(1), 115–121. https://doi.org/10.1109/66.484291. Retrieved on May 29, 2019
[103] LEP 1.5.12 Temperature dependence of the velocity of sound in liquids. (n.d.). https://www.nikhef.nl/~h73/kn1c/praktikum/phywe/LEP/Experim/1_5_12.pdf. Retrieved on May 28, 2019
[104] Tavčar, R., Drnovšek, J., Bojkovski, J., & Beguš, S. (2020). Optimization of a Single Tube Practical Acoustic Thermometer. *Sensors 2020, Vol. 20, Page 1529*, *20*(5), 1529. https://doi.org/10.3390/S20051529. Retrieved on May 8, 2021
[105] Kuttruff H. Ultrasonics: Fundamentals and Applications. Springer Netherlands; 1991, 458 pgs., ISBN: 9789401138468. Retrieved on February 20, 2018
[106] Frederiksen E. (2013). Acoustic metrology – an overview of calibration methods and their uncertainties. Int J Metrol Qual Eng;4:97–107. doi:10.1051/ijmqe/2013045. https://www.metrology-journal.org/articles/ijmqe/abs/2013/02/ijmqe130045/ijmqe130045.html. Retrieved on June 12, 2019
[107] Mohr PJ, Newell DB, Taylor BN (2016). CODATA recommended values of the fundamental physical constants: 2014. Rev Mod Phys 2016;88:035009. doi:10.1103/RevModPhys.88.035009. https://journals.aps.org/rmp/abstract/10.1103/RevModPhys.88.035009. Retrieved on June 12, 2019
[108] Fatihah N. and coll., PROPERTY TABLES AND CHARTS (SI UNITS) n.d., https://www.academia.edu/4637146/PROPERTY_TABLES_AND_CHARTS_SI_UNITS_. Retrieved on June 12, 2019
[109] Voldán, M., & Husník, L. (2019). Simple single transducer ultrasonic thermometer using electrostatic actuator. Applied Acoustics, 148, 448–456. https://doi.org/10.1016/J.APACOUST.2019.01.011. Retrieved on June 12, 2019
[110] Messmikrofonkapsel MK 301. (n.d.). https://www.microtechgefell.de/mikrofonkapsel?wl=469-MK301#start. Retrieved on October 14, 2022
[111] *Messmikrofonvorverstärker MV 302*. (n.d.). https://www.microtechgefell.de/mikrofonverstaerker?wl=480-MV302#start. Retrieved on October 17, 2022
[112] Rossi Mario. (1988). *Acoustics and electroacoustics / Mario Rossi ; translated by Patrick Rupert Windsor Roe*. Artech House Norwood, MA. ISBN: 0-89006-255-2
[113] Kuttruff, Heinrich. (2007). *Acoustics : an introduction*. Taylor & Francis. ISBN: 9780415386807.
[114] *Interpolation & Extrapolation VIs - NI*. (n.d.). from https://www.ni.com/docs/en-US/bundle/labview/page/gmath/interp_extrap_pal.html. Retrieved on September 2, 2022
[115] *(PDF) Estimation of molecular weight knowing the mixture composition and Conversion of mole fraction to mass fraction and vice versa*. (n.d.). https://www.researchgate.net/publication/335227807_Estimation_of_molecular_weight_knowing_the_mixture_composition_and_Conversion_of_mole_fraction_to_mass_fraction_and_vice_versa. Retrieved on November 15, 2022
[116] *CODATA Value: molar gas constant*. (n.d.). https://physics.nist.gov/cgi-bin/cuu/Value?r. Retrieved on November 16, 2022

[117] *Stainless Steel 321 - 1.4541 Data Sheet - thyssenkrupp Materials (UK)*. (n.d.). https://www.thyssenkrupp-materials.co.uk/stainless-steel-321-14541.html. Retrieved on December 24, 2022
[118] Kirbas C, Gavioso R M and Madonna Ripa D. (2019). Ses Hizi Ölçümleri Yöntemi Ile Birincil Termometre Tanimi – Primary Thermometry based on Speed Of Sound Measurements Proceedings of the 13th Ulusal Akııstik Kongresi 377-389. https://www.researchgate.net/publication/340114355_Primary_Thermometry_based_on_the_speed_of_sound_measurements. Retrieved on March 1, 2020
[119] Hidnert P. (1922). Thermal Expansion of Copper and some of its Important Industrial Alloys BS Sci. Pap. **17** 91-159. Retrieved on June 12, 2019
[120] Mehl, J. B. (2007). Acoustic Eigenvalues of a Quasispherical Resonator: Second Order Shape Perturbation Theory for Arbitrary Modes. *Journal of Research of the National Institute of Standards and Technology*, *112*(3), 163–173. https://doi.org/10.6028/JRES.112.013. Retrieved on September 23, 2022
[121] Gao, B., Pitre, L., Luo, E. C., Plimmer, M. D., Lin, P., Zhang, J. T., Feng, X. J., Chen, Y. Y., & Sparasci, F. (2017). Feasibility of primary thermometry using refractive index measurements at a single pressure. *Measurement*, *103*, 258–262. https://doi.org/10.1016/J.MEASUREMENT.2017.02.039. Retrieved on May 14, 2019
[122] Bipm. (n.d.). Bureau International des Poids et Mesures: Guide to the Realization to the ITS-90. https://www.bipm.org/utils/common/pdf/ITS-90/Guide-ITS-90-GasThermometry-2015.pdf. Retrieved on September 13, 2019
[123] Fundamental Physical Constants from NIST. (n.d.). https://physics.nist.gov/cuu/Constants/index.html . Retrieved on July 15, 2019
[124] Ripple, D. C., Defibaugh, D. R., Moldover, M. R., & Strouse, G. F. (2003). Techniques for Primary Acoustic Thermometry to 800 K. *AIP Conference Proceedings*, *684*(1), 25. https://doi.org/10.1063/1.1627095. Retrieved on September 22, 2022
[125] Ripple D C, Defibaugh D R, Gillis K A and Moldover M R, Primary Acoustic Thermometer for Use up to 800 K in Proceedings of TEMPMEKO ’99, edited by J. F. Dubbeldam and M. J. de Groot, NMi, Delft, the Netherlands, 418-423 (1999). Retrieved on September 22, 2022

8. List of Publications

8.1. Author's publication on the topic of the doctoral thesis

a. Voldán M, Husník L. **Simple single transducer ultrasonic thermometer using electrostatic actuator**. Applied Acoustics, 1/2019, CTU in Prague, Prague, May 2019, pages 448–456, ISSN 0003-682X, doi:10.1016/J.APACOUST.2019.01.011.

8.2. Other author's publications

b. Strnad R. et al.: **Nepodkročitelné hodnoty nejistot aneb jaká je reálná nejistota kalibrace teploměrů?**, Metrologie, 1/2017, Czech Metrology Institute, Prague, Jan 2017, ISSN 1210-3543.

c. Strnad R., et al.: **Kontaktní měření teploty a jeho návaznost**, Metrologie, 1/2018, Czech Metrology Institute, Prague, Feb 2018, ISSN 1210-3543.

d. Voldán M. and Šindelářová L.: **Vliv ponoru a samoohřevu u odporových snímačů teploty a termoelektrických snímačů teploty**, Metrologie, 1/2018, Czech Metrology Institute, Prague, Feb 2018, ISSN 1210-3543.

e. Kňazovická, L.; Kolík, L.; Kučera, J.; Voldán, M.; Šindelářová, L. **Novinky na OI Praha v oblasti termofyzikálních veličin**, Metrologie. 2022, 31(1/2022), 2-6. ISSN 1210-3543.

f. Voldán M.: **Měření teploty povrchu - nové poznatky**, Metrologie, 1/2018, Czech Metrology Institute, Prague, Feb 2018, ISSN 1210-3543.

g. Merlone A. et al.: **The MeteoMet2 project – Highlights and results**, INRiM, Italy, Nov 2017, DOI: 10.1088/1361-6501/aa99fc

h. Voldán M.: **The Influence of Forest Stands on Temperature Measurement Accuracy in Meteorological Application**, Metrologie, 4/2017, Czech Metrology Institute, Prague, Dec 2017, ISSN 1210-3543

9. Annex A – Uncertainty budgets for practical acoustic thermometer

Table 5: Measurement uncertainty budget for the nominal temperature of -80 °C

Uncertainty source	Value	z_{max}	Dimension	Distribution	k	u_x	Sensitivity	Dimension	u_x for $k=1$, °C	Source
Molar mass from gas composition	0.0399479	3.99E-07	g·mol^{-1}	rectangular	1.732050808	0.0000	5.0E+03	°C·mol·g^{-1}	0.001	gas datasheet
Length of sound path determination	170.88	1.00E-02	mm	Gaussian	2	0.005	2.3E+00	°C·mm^{-1}	0.012	measurement
thermal expansion	0.00056	5.00E-08	m	rectangular	1.732050808	0.000	2.3E+03	°C·m^{-1}	0.000	calculation
Heat capacity ratio	1.667	1.67E-05	-	rectangular	1.732050808	0.00001	1.2E+02	°C	0.001	gas datasheet
Molar gas constant	8.314462618	0.00E+00	J·mol^{-1}·K^{-1}	rectangular	1.732050808	0.0000	2.4E+01	°C·J^{-1}·mol·K	0.000	fixed value, zero uncertainty
Immersion of sensor	0.005	5.00E-03	°C	rectangular	1.732050808	0.003	1.0E+00	°C·°C^{-1}	0.003	estimation
Pressure measurement	100.000	8.00E-03	kPa	Gaussian	2	0.004	0.0E+00	°C·kPa^{-1}	0.000	measurement
Resolution of τ	12.5	1.25E+01	ns	rectangular	1.732050808	0.000	3.1E+05	°C·s^{-1}	0.002	observation and calculation
Time base (short term drift od oscillocope)	1	1.00E+00	ns	rectangular	1.732050808	0.000	3.1E+05	°C·s^{-1}	0.000	device specification
Short term drift of the generator	1	1.00E+00	µHz	rectangular	1.732050808	0.577	0.0E+00	°C·µHz^{-1}	0.000	estimation
Parasitic voltage noise	0	4.00E-03	°C	rectangular	1.732050808	0.002	1.0E+00	°C·°C^{-1}	0.002	estimation
Interpolation	-0.112	0.00E+00	µs	Gaussian	2	0.000	3.1E+05	°C·s^{-1}	0.000	not applicable
Instability of measured environment	0.003	3.00E-03	°C	rectangular	1.732050808	0.002	1.0E+00	°C·°C^{-1}	0.002	estimation
Inhomogeneity of measured environment	0.005	5.00E-03	°C	rectangular	1.732050808	0.003	1.0E+00	°C·°C^{-1}	0.003	estimation
Microphone Characteristic	0	2.00E-03	°C	rectangular	1.732050808	0.001	1.0E+00	°C·°C^{-1}	0.001	estimation
Acoustic noise	0.001	1.00E-03	°C	rectangular	1.732050808	0.001	1.0E+00	°C·°C^{-1}	0.001	estimation
t_{90} temperature measurement	0.008	8.00E-03	°C	rectangular	1.732050808	0.005	1.0E+00	°C·°C^{-1}	0.005	measurement
Other influences	0.001	1.00E-03	°C	rectangular	1.732050808	0.001	1.0E+00	°C·°C^{-1}	0.001	estimation

Uncertainty source	Value	z_{max}	Dimension	Distribution	k	u_x	Sensitivity	Dimension	u_x for $k=1$, °C	Source
A type uncertainty	0.1	0.1	µs	Gaussian	1	0.089	0.044	°C/µs	0.004	data
							Total uncertainty		0.014	
							Expansion coefficient		2	
Temperature, K	193.316									
Temperature, °C	-79.834					*Total rounded expanded uncertainty*, °C			0.029	

Table 6: Measurement uncertainty budget for the nominal temperature of -60 °C

Uncertainty source	Value	z_{max}	Dimension	Distribution	k	u_x		Sensitivity	Dimension	u_x for $k=1$, °C	Source
Molar mass from gas composition	0.0399479	3.99E-07	g·mol^{-1}	rectangular	1.732050808	0.0000	g·mol^{-1}	5.5E+03	°C·mol·g^{-1}	0.001	gas datasheet
Length of sound path determination	170.88	1.00E-02	mm	Gaussian	2	0.005	mm	2.6E+00	°C·mm^{-1}	0.013	measurement
thermal expansion	0.00056	5.00E-08	m	rectangular	1.732050808	0.000	m	2.6E+03	°C·m^{-1}	0.000	calculation
Heat capacity ratio	1.667	1.67E-05	-	rectangular	1.732050808	0.00001	-	1.3E+02	°C	0.001	gas datasheet
Molar gas constant	8.314462618	0.00E+00	J·mol^{-1}·K^{-1}	rectangular	1.732050808	0.0000	J·mol^{-1}·K^{-1}	2.6E+01	°C·J^{-1}·mol·K	0.000	fixed value, zero uncertainty
Immersion of sensor	0.005	5.00E-03	°C	rectangular	1.732050808	0.003	°C	1.0E+00	°C·°C^{-1}	0.003	estimation
Pressure measurement	100.000	8.00E-03	kPa	Gaussian	2	0.004	kPa	0.0E+00	°C·kPa^{-1}	0.000	measurement
Resolution of τ	12.5	1.25E+01	ns	rectangular	1.732050808	0.000	s	3.6E+05	°C·s^{-1}	0.003	observation and calculation
Time base (short term drift od oscillocope)	1	1.00E+00	ns	rectangular	1.732050808	0.000	s	3.6E+05	°C·s^{-1}	0.000	device specification
Short term drift of the generator	1	1.00E+00	µHz	rectangular	1.732050808	0.577	µHz	0.0E+00	°C·µHz^{-1}	0.000	estimation
Parasitic voltage noise	0	4.00E-03	°C	rectangular	1.732050808	0.002	°C	1.0E+00	°C·°C^{-1}	0.002	estimation
Interpolation	0.088	0.00E+00	µs	Gaussian	2	0.000	s	3.6E+05	°C·s^{-1}	0.000	not applicable
Instability of measured environment	0.003	3.00E-03	°C	rectangular	1.732050808	0.002	°C	1.0E+00	°C·°C^{-1}	0.002	estimation
Inhomogeneity of measured environment	0.005	5.00E-03	°C	rectangular	1.732050808	0.003	°C	1.0E+00	°C·°C^{-1}	0.003	estimation
Microphone Characteristic	0	2.00E-03	°C	rectangular	1.732050808	0.001	°C	1.0E+00	°C·°C^{-1}	0.001	estimation
Acoustic noise	0.001	1.00E-03	°C	rectangular	1.732050808	0.001	°C	1.0E+00	°C·°C^{-1}	0.001	estimation
t_{90} temperature measurement	0.006	6.00E-03	°C	rectangular	1.732050808	0.003	°C	1.0E+00	°C·°C^{-1}	0.003	measurement
Other influences	0.001	1.00E-03	°C	rectangular	1.732050808	0.001	°C	1.0E+00	°C·°C^{-1}	0.001	estimation

Uncertainty source	Value	z_{max}	Dimension	Distribution	k	u_x		Sensitivity	Dimension	u_x for $k=1$, °C	Source
A type uncertainty	0.1	0.1	µs	Gaussian	1	0.070	µs	0.042	°C/µs	0.003	data
								Total uncertainty		0.015	
								Expansion coefficient		2	
Temperature, K	213.351										
Temperature, °C	-59.799				*Total rounded expanded uncertainty*, °C					0.030	

Table 7: Measurement uncertainty budget for the nominal temperature of -40 °C

Uncertainty source	Value	z_{max}	Dimension	Distribution	k	u_x		Sensitivity	Dimension	u_x for $k=1$, °C	Source
Molar mass from gas composition	0.0399479	3.99E-07	g·mol^{-1}	rectangular	1.732050808	0.0000	g·mol^{-1}	5.9E+03	°C·mol·g^{-1}	0.001	gas datasheet
Length of sound path determination	170.88	1.00E-02	mm	Gaussian	2	0.005	mm	2.8E+00	°C·mm^{-1}	0.014	measurement
thermal expansion	0.00056	5.00E-08	m	rectangular	1.732050808	0.000	m	2.8E+03	°C·m^{-1}	0.000	calculation
Heat capacity ratio	1.667	1.67E-05	-	rectangular	1.732050808	0.00001	-	1.4E+02	°C	0.001	gas datasheet
Molar gas constant	8.314462618	0.00E+00	J·mol^{-1}·K^{-1}	rectangular	1.732050808	0.0000	J·mol^{-1}·K^{-1}	2.8E+01	°C·J^{-1}·mol·K	0.000	fixed value, zero uncertainty
Immersion of sensor	0.005	5.00E-03	°C	rectangular	1.732050808	0.003	°C	1.0E+00	°C·°C^{-1}	0.003	estimation
Pressure measurement	100.000	8.00E-03	kPa	Gaussian	2	0.004	kPa	0.0E+00	°C·kPa^{-1}	0.000	measurement
Resolution of τ	12.5	1.25E+01	ns	rectangular	1.732050808	0.000	s	4.0E+05	°C·s^{-1}	0.003	observation and calculation
Time base (short term drift od oscillocope)	1	1.00E+00	ns	rectangular	1.732050808	0.000	s	4.0E+05	°C·s^{-1}	0.000	device specification
Short term drift of the generator	1	1.00E+00	µHz	rectangular	1.732050808	0.577	µHz	0.0E+00	°C·µHz^{-1}	0.000	estimation
Parasitic voltage noise	0	4.00E-03	°C	rectangular	1.732050808	0.002	°C	1.0E+00	°C·°C^{-1}	0.002	estimation
Interpolation	0.130	0.00E+00	µs	Gaussian	2	0.000	s	4.0E+05	°C·s^{-1}	0.000	not applicable
Instability of measured environment	0.003	3.00E-03	°C	rectangular	1.732050808	0.002	°C	1.0E+00	°C·°C^{-1}	0.002	estimation
Inhomogeneity of measured environment	0.005	5.00E-03	°C	rectangular	1.732050808	0.003	°C	1.0E+00	°C·°C^{-1}	0.003	estimation
Microphone Characteristic	0	2.00E-03	°C	rectangular	1.732050808	0.001	°C	1.0E+00	°C·°C^{-1}	0.001	estimation
Acoustic noise	0.001	1.00E-03	°C	rectangular	1.732050808	0.001	°C	1.0E+00	°C·°C^{-1}	0.001	estimation
t_{90} temperature measurement	0.005	5.00E-03	°C	rectangular	1.732050808	0.003	°C	1.0E+00	°C·°C^{-1}	0.003	measurement
Other influences	0.001	1.00E-03	°C	rectangular	1.732050808	0.001	°C	1.0E+00	°C·°C^{-1}	0.001	estimation

Uncertainty source	Value	z_{max}	Dimension	Distribution	k	u_x		Sensitivity	Dimension	u_x for $k=1$, °C	Source
A type uncertainty	0.0	0.0	µs	Gaussian	1	0.002	µs	0.041	°C/µs	0.000	data
								Total uncertainty		0.016	
								Expansion coefficient		2	
Temperature, K	233.365							*Total rounded expanded uncertainty*, °C		0.031	
Temperature, °C	-39.785										

Table 8: Measurement uncertainty budget for the nominal temperature of -20 °C

Uncertainty source	Value	z_{max}	Dimension	Distribution	k	u_x		Sensitivity	Dimension	u_x for k=1, °C	Source
Molar mass from gas composition	0.0399479	3.99E-07	g·mol^{-1}	rectangular	1.732050808	0.0000	g·mol^{-1}	6.5E+03	°C·mol·g^{-1}	0.001	gas datasheet
Length of sound path determination	170.88	1.00E-02	mm	Gaussian	2	0.005	mm	3.0E+00	°C·mm^{-1}	0.015	measurement
thermal expansion	0.00056	5.00E-08	m	rectangular	1.732050808	0.000	m	3.0E+03	°C·m^{-1}	0.000	calculation
Heat capacity ratio	1.667	1.67E-05	-	rectangular	1.732050808	0.00001	-	1.5E+02	°C	0.001	gas datasheet
Molar gas constant	8.314462618	0.00E+00	J·mol^{-1}·K^{-1}	rectangular	1.732050808	0.0000	J·mol^{-1}·K^{-1}	3.1E+01	°C·J^{-1}·mol·K	0.000	fixed value, zero uncertainty
Immersion of sensor	0.005	5.00E-03	°C	rectangular	1.732050808	0.003	°C	1.0E+00	°C·°C^{-1}	0.003	estimation
Pressure measurement	100.000	8.00E-03	kPa	Gaussian	2	0.004	kPa	0.0E+00	°C·kPa^{-1}	0.000	measurement
Resolution of τ	12.5	1.25E+01	ns	rectangular	1.732050808	0.000	s	4.5E+05	°C·s^{-1}	0.003	observation and calculation
Time base (short term drift od oscillocope)	1	1.00E+00	ns	rectangular	1.732050808	0.000	s	4.5E+05	°C·s^{-1}	0.000	device specification
Short term drift of the generator	1	1.00E+00	µHz	rectangular	1.732050808	0.577	µHz	0.0E+00	°C·µHz^{-1}	0.000	estimation
Parasitic voltage noise	0	4.00E-03	°C	rectangular	1.732050808	0.002	°C	1.0E+00	°C·°C^{-1}	0.002	estimation
Interpolation	0.087	0.00E+00	µs	Gaussian	2	0.000	s	4.5E+05	°C·s^{-1}	0.000	not applicable
Instability of measured environment	0.003	3.00E-03	°C	rectangular	1.732050808	0.002	°C	1.0E+00	°C·°C^{-1}	0.002	estimation
Inhomogeneity of measured environment	0.005	5.00E-03	°C	rectangular	1.732050808	0.003	°C	1.0E+00	°C·°C^{-1}	0.003	estimation
Microphone Characteristic	0	2.00E-03	°C	rectangular	1.732050808	0.001	°C	1.0E+00	°C·°C^{-1}	0.001	estimation
Acoustic noise	0.001	1.00E-03	°C	rectangular	1.732050808	0.001	°C	1.0E+00	°C·°C^{-1}	0.001	estimation
t_{90} temperature measurement	0.003	3.00E-03	°C	rectangular	1.732050808	0.002	°C	1.0E+00	°C·°C^{-1}	0.002	measurement
Other influences	0.001	1.00E-03	°C	rectangular	1.732050808	0.001	°C	1.0E+00	°C·°C^{-1}	0.001	estimation

Uncertainty source	Value	z_{max}	Dimension	Distribution	k	u_x		Sensitivity	Dimension	u_x for k=1, °C	Source
A type uncertainty	0.0	0.0	µs	Gaussian	1	0.002	µs	0.039	°C/µs	0.000	data
								Total uncertainty		0.017	
Temperature, K	253.369							*Expansion coefficient*		2	
Temperature, °C	-19.781					*Total rounded expanded uncertainty*, °C				0.033	

Table 9: Measurement uncertainty budget for the nominal temperature of 0 °C

Uncertainty source	Value	z_{max}	Dimension	Distribution	k	u_x		Sensitivity	Dimension	u_x for k=1, °C	Source
Molar mass from gas composition	0.0399479	3.99E-07	g·mol^{-1}	rectangular	1.732050808	0.0000	g·mol^{-1}	6.8E+03	°C·mol·g^{-1}	0.002	gas datasheet
Length of sound path determination	170.88	1.00E-02	mm	Gaussian	2	0.005	mm	3.2E+00	°C·mm^{-1}	0.016	measurement
thermal expansion	0.00056	5.00E-08	m	rectangular	1.732050808	0.000	m	3.2E+03	°C·m^{-1}	0.000	calculation
Heat capacity ratio	1.667	1.67E-05	-	rectangular	1.732050808	0.00001	-	1.6E+02	°C	0.002	gas datasheet
Molar gas constant	8.314462618	0.00E+00	J·mol^{-1}·K^{-1}	rectangular	1.732050808	0.0000	J·mol^{-1}·K^{-1}	3.3E+01	°C·J^{-1}·mol·K	0.000	fixed value, zero uncertainty
Immersion of sensor	0.005	5.00E-03	°C	rectangular	1.732050808	0.003	°C	1.0E+00	°C·°C^{-1}	0.003	estimation
Pressure measurement	100.000	8.00E-03	kPa	Gaussian	2	0.004	kPa	0.0E+00	°C·kPa^{-1}	0.000	measurement
Resolution of τ	12.5	1.25E+01	ns	rectangular	1.732050808	0.000	s	4.9E+05	°C·s^{-1}	0.004	observation and calculation
Time base (short term drift od oscillocope)	1	1.00E+00	ns	rectangular	1.732050808	0.000	s	4.9E+05	°C·s^{-1}	0.000	device specification
Short term drift of the generator	1	1.00E+00	µHz	rectangular	1.732050808	0.577	µHz	0.0E+00	°C·µHz^{-1}	0.000	estimation
Parasitic voltage noise	0	4.00E-03	°C	rectangular	1.732050808	0.002	°C	1.0E+00	°C·°C^{-1}	0.002	estimation
Interpolation	-0.073	0.00E+00	µs	Gaussian	2	0.000	s	4.9E+05	°C·s^{-1}	0.000	not applicable
Instability of measured environment	0.003	3.00E-03	°C	rectangular	1.732050808	0.002	°C	1.0E+00	°C·°C^{-1}	0.002	estimation
Inhomogeneity of measured environment	0.005	5.00E-03	°C	rectangular	1.732050808	0.003	°C	1.0E+00	°C·°C^{-1}	0.003	estimation
Microphone Characteristic	0	2.00E-03	°C	rectangular	1.732050808	0.001	°C	1.0E+00	°C·°C^{-1}	0.001	estimation
Acoustic noise	0.001	1.00E-03	°C	rectangular	1.732050808	0.001	°C	1.0E+00	°C·°C^{-1}	0.001	estimation
t_{90} temperature measurement	0.003	3.00E-03	°C	rectangular	1.732050808	0.002	°C	1.0E+00	°C·°C^{-1}	0.002	measurement
Other influences	0.001	1.00E-03	°C	rectangular	1.732050808	0.001	°C	1.0E+00	°C·°C^{-1}	0.001	estimation
Uncertainty source	Value	z_{max}	Dimension	Distribution	k	u_x		Sensitivity	Dimension	u_x for k=1, °C	Source
A type uncertainty	0.0	0.0	µs	Gaussian	1	0.000	µs	0.038	°C/µs	0.000	data
								Total uncertainty		0.017	
Temperature, K	273.385							*Expansion coefficient*		2	
Temperature, °C	0.235					*Total rounded expanded uncertainty*, °C				0.035	

Table 10: Measurement uncertainty budget for the nominal temperature of 20 °C

Uncertainty source	Value	z_{max}	Dimension	Distribution	k	u_x		Sensitivity	Dimension	u_x for k=1, °C	Source
Molar mass from gas composition	0.0399479	3.99E-07	g·mol^{-1}	rectangular	1.732050808	0.0000	g·mol^{-1}	7.2E+03	°C·mol·g^{-1}	0.002	gas datasheet
Length of sound path determination	170.88	1.00E-02	mm	Gaussian	2	0.005	mm	3.4E+00	°C·mm^{-1}	0.017	measurement
thermal expansion	0.00056	5.00E-08	m	rectangular	1.732050808	0.000	m	3.4E+03	°C·m^{-1}	0.000	calculation
Heat capacity ratio	1.667	1.67E-05	-	rectangular	1.732050808	0.00001	-	1.7E+02	°C	0.002	gas datasheet
Molar gas constant	8.314462618	0.00E+00	J·mol^{-1}·K^{-1}	rectangular	1.732050808	0.0000	J·mol^{-1}·K^{-1}	3.5E+01	°C·J^{-1}·mol·K	0.000	fixed value, zero uncertainty
Immersion of sensor	0.005	5.00E-03	°C	rectangular	1.732050808	0.003	°C	1.0E+00	°C·°C^{-1}	0.003	estimation
Pressure measurement	100.000	8.00E-03	kPa	Gaussian	2	0.004	kPa	0.0E+00	°C·kPa^{-1}	0.000	measurement
Resolution of τ	12.5	1.25E+01	ns	rectangular	1.732050808	0.000	s	5.4E+05	°C·s^{-1}	0.004	observation and calculation
Time base (short term drift od oscillocope)	1	1.00E+00	ns	rectangular	1.732050808	0.000	s	5.4E+05	°C·s^{-1}	0.000	device specification
Short term drift of the generator	1	1.00E+00	µHz	rectangular	1.732050808	0.577	µHz	0.0E+00	°C·µHz^{-1}	0.000	estimation
Parasitic voltage noise	0	4.00E-03	°C	rectangular	1.732050808	0.002	°C	1.0E+00	°C·°C^{-1}	0.002	estimation
Interpolation	-0.075	0.00E+00	µs	Gaussian	2	0.000	s	5.4E+05	°C·s^{-1}	0.000	not applicable
Instability of measured environment	0.003	3.00E-03	°C	rectangular	1.732050808	0.002	°C	1.0E+00	°C·°C^{-1}	0.002	estimation
Inhomogeneity of measured environment	0.005	5.00E-03	°C	rectangular	1.732050808	0.003	°C	1.0E+00	°C·°C^{-1}	0.003	estimation
Microphone Characteristic	0	2.00E-03	°C	rectangular	1.732050808	0.001	°C	1.0E+00	°C·°C^{-1}	0.001	estimation
Acoustic noise	0.001	1.00E-03	°C	rectangular	1.732050808	0.001	°C	1.0E+00	°C·°C^{-1}	0.001	estimation
t_{90} temperature measurement	0.004	4.00E-03	°C	rectangular	1.732050808	0.002	°C	1.0E+00	°C·°C^{-1}	0.002	measurement
Other influences	0.001	1.00E-03	°C	rectangular	1.732050808	0.001	°C	1.0E+00	°C·°C^{-1}	0.001	estimation
Uncertainty source	Value	z_{max}	Dimension	Distribution	k	u_x		Sensitivity	Dimension	u_x for k=1, °C	Source
A type uncertainty	0.0	0.0	µs	Gaussian	1	0.000	µs	0.037	°C/µs	0.000	data
								Total uncertainty		0.019	
Temperature, K	293.391							*Expansion coefficient*		2	
Temperature, °C	20.241					*Total rounded expanded uncertainty*, °C				0.037	

Table 11: Measurement uncertainty budget for the nominal temperature of 40 °C

Uncertainty source	Value	z_{max}	Dimension	Distribution	k	u_x		Sensitivity	Dimension	u_x for k=1, °C	Source
Molar mass from gas composition	0.0399479	3.99E-07	g·mol^{-1}	rectangular	1.732050808	0.0000	g·mol^{-1}	7.6E+03	°C·mol·g^{-1}	0.002	gas datasheet
Length of sound path determination	170.88	1.00E-02	mm	Gaussian	2	0.005	mm	3.6E+00	°C·mm^{-1}	0.018	measurement
thermal expansion	0.00056	5.00E-08	m	rectangular	1.732050808	0.000	m	3.6E+03	°C·m^{-1}	0.000	calculation
Heat capacity ratio	1.667	1.67E-05	-	rectangular	1.732050808	0.00001	-	1.8E+02	°C	0.002	gas datasheet
Molar gas constant	8.314462618	0.00E+00	J·mol^{-1}·K^{-1}	rectangular	1.732050808	0.0000	J·mol^{-1}·K^{-1}	3.7E+01	°C·J^{-1}·mol·K	0.000	fixed value, zero uncertainty
Immersion of sensor	0.005	5.00E-03	°C	rectangular	1.732050808	0.003	°C	1.0E+00	°C·°C^{-1}	0.003	estimation
Pressure measurement	100.000	8.00E-03	kPa	Gaussian	2	0.004	kPa	0.0E+00	°C·kPa^{-1}	0.000	measurement
Resolution of τ	12.5	1.25E+01	ns	rectangular	1.732050808	0.000	s	5.9E+05	°C·s^{-1}	0.004	observation and calculation
Time base (short term drift od oscillocope)	1	1.00E+00	ns	rectangular	1.732050808	0.000	s	5.9E+05	°C·s^{-1}	0.000	device specification
Short term drift of the generator	1	1.00E+00	µHz	rectangular	1.732050808	0.577	µHz	0.0E+00	°C·µHz^{-1}	0.000	estimation
Parasitic voltage noise	0	4.00E-03	°C	rectangular	1.732050808	0.002	°C	1.0E+00	°C·°C^{-1}	0.002	estimation
Interpolation	-0.229	0.00E+00	µs	Gaussian	2	0.000	s	5.9E+05	°C·s^{-1}	0.000	not applicable
Instability of measured environment	0.003	3.00E-03	°C	rectangular	1.732050808	0.002	°C	1.0E+00	°C·°C^{-1}	0.002	estimation
Inhomogeneity of measured environment	0.005	5.00E-03	°C	rectangular	1.732050808	0.003	°C	1.0E+00	°C·°C^{-1}	0.003	estimation
Microphone Characteristic	0	2.00E-03	°C	rectangular	1.732050808	0.001	°C	1.0E+00	°C·°C^{-1}	0.001	estimation
Acoustic noise	0.001	1.00E-03	°C	rectangular	1.732050808	0.001	°C	1.0E+00	°C·°C^{-1}	0.001	estimation
t_{90} temperature measurement	0.005	5.00E-03	°C	rectangular	1.732050808	0.003	°C	1.0E+00	°C·°C^{-1}	0.003	measurement
Other influences	0.001	1.00E-03	°C	rectangular	1.732050808	0.001	°C	1.0E+00	°C·°C^{-1}	0.001	estimation
Uncertainty source	Value	z_{max}	Dimension	Distribution	k	u_x		Sensitivity	Dimension	u_x for k=1, °C	Source
A type uncertainty	0.0	0.0	µs	Gaussian	1	0.000	µs	0.036	°C/µs	0.000	data
								Total uncertainty		0.020	
Temperature, K	313.299							*Expansion coefficient*		2	
Temperature, °C	40.149					*Total rounded expanded uncertainty*, °C				0.039	

Table 12: Measurement uncertainty budget for the nominal temperature of 60 °C

Uncertainty source	Value	z_{max}	Dimension	Distribution	k	u_x		Sensitivity	Dimension	u_x for k=1, °C	Source
Molar mass from gas composition	0.0399479	3.99E-07	g·mol^{-1}	rectangular	1.732050808	0.0000	g·mol^{-1}	8.0E+03	°C·mol·g^{-1}	0.002	gas datasheet
Length of sound path determination	170.88	1.00E-02	mm	Gaussian	2	0.005	mm	3.8E+00	°C·mm^{-1}	0.019	measurement
thermal expansion	0.00056	5.00E-08	m	rectangular	1.732050808	0.000	m	3.8E+03	°C·m^{-1}	0.000	calculation
Heat capacity ratio	1.667	1.67E-05	-	rectangular	1.732050808	0.00001	-	1.9E+02	°C	0.002	gas datasheet
Molar gas constant	8.314462618	0.00E+00	J·mol^{-1}·K^{-1}	rectangular	1.732050808	0.0000	J·mol^{-1}·K^{-1}	3.9E+01	°C·J^{-1}·mol·K	0.000	fixed value, zero uncertainty
Immersion of sensor	0.005	5.00E-03	°C	rectangular	1.732050808	0.003	°C	1.0E+00	°C·°C^{-1}	0.003	estimation
Pressure measurement	100.000	8.00E-03	kPa	Gaussian	2	0.004	kPa	0.0E+00	°C·kPa^{-1}	0.000	measurement
Resolution of τ	12.5	1.25E+01	ns	rectangular	1.732050808	0.000	s	6.3E+05	°C·s^{-1}	0.005	observation and calculation
Time base (short term drift od oscillocope)	1	1.00E+00	ns	rectangular	1.732050808	0.000	s	6.3E+05	°C·s^{-1}	0.000	device specification
Short term drift of the generator	1	1.00E+00	µHz	rectangular	1.732050808	0.577	µHz	0.0E+00	°C·µHz^{-1}	0.000	estimation
Parasitic voltage noise	0	4.00E-03	°C	rectangular	1.732050808	0.002	°C	1.0E+00	°C·°C^{-1}	0.002	estimation
Interpolation	-0.171	0.00E+00	µs	Gaussian	2	0.000	s	6.3E+05	°C·s^{-1}	0.000	not applicable
Instability of measured environment	0.003	3.00E-03	°C	rectangular	1.732050808	0.002	°C	1.0E+00	°C·°C^{-1}	0.002	estimation
Inhomogeneity of measured environment	0.005	5.00E-03	°C	rectangular	1.732050808	0.003	°C	1.0E+00	°C·°C^{-1}	0.003	estimation
Microphone Characteristic	0	2.00E-03	°C	rectangular	1.732050808	0.001	°C	1.0E+00	°C·°C^{-1}	0.001	estimation
Acoustic noise	0.001	1.00E-03	°C	rectangular	1.732050808	0.001	°C	1.0E+00	°C·°C^{-1}	0.001	estimation
t_{90} temperature measurement	0.006	6.00E-03	°C	rectangular	1.732050808	0.003	°C	1.0E+00	°C·°C^{-1}	0.003	measurement
Other influences	0.001	1.00E-03	°C	rectangular	1.732050808	0.001	°C	1.0E+00	°C·°C^{-1}	0.001	estimation

Uncertainty source	Value	z_{max}	Dimension	Distribution	k	u_x		Sensitivity	Dimension	u_x for k=1, °C	Source
A type uncertainty	0.0	0.0	µs	Gaussian	1	0.000	µs	0.035	°C/µs	0.000	data
								Total uncertainty		0.021	
Temperature, K	333.062							*Expansion coefficient*		2	
Temperature, °C	59.912					*Total rounded expanded uncertainty*, °C				0.041	

Table 13: Measurement uncertainty budget for the nominal temperature of 80 °C

Uncertainty source	Value	z_{max}	Dimension	Distribution	k	u_x		Sensitivity	Dimension	u_x for $k=1$, °C	Source
Molar mass from gas composition	0.0399479	3.99E-07	g·mol^{-1}	rectangular	1.732050808	0.0000	g·mol^{-1}	8.4E+03	°C·mol·g^{-1}	0.002	gas datasheet
Length of sound path determination	170.88	1.00E-02	mm	Gaussian	2	0.005	mm	4.0E+00	°C·mm^{-1}	0.020	measurement
thermal expansion	0.00056	5.00E-08	m	rectangular	1.732050808	0.000	m	4.0E+03	°C·m^{-1}	0.000	calculation
Heat capacity ratio	1.667	1.67E-05	-	rectangular	1.732050808	0.00001	-	2.0E+02	°C	0.002	gas datasheet
Molar gas constant	8.314462618	0.00E+00	J·mol^{-1}·K^{-1}	rectangular	1.732050808	0.0000	J·mol^{-1}·K^{-1}	4.1E+01	°C·J^{-1}·mol·K	0.000	fixed value, zero uncertainty
Immersion of sensor	0.005	5.00E-03	°C	rectangular	1.732050808	0.003	°C	1.0E+00	°C·°C^{-1}	0.003	estimation
Pressure measurement	100.000	8.00E-03	kPa	Gaussian	2	0.004	kPa	0.0E+00	°C·kPa^{-1}	0.000	measurement
Resolution of τ	12.5	1.25E+01	ns	rectangular	1.732050808	0.000	s	6.8E+05	°C·s^{-1}	0.005	observation and calculation
Time base (short term drift od oscillocope)	1	1.00E+00	ns	rectangular	1.732050808	0.000	s	6.8E+05	°C·s^{-1}	0.000	device specification
Short term drift of the generator	1	1.00E+00	µHz	rectangular	1.732050808	0.577	µHz	0.0E+00	°C·µHz^{-1}	0.000	estimation
Parasitic voltage noise	0	4.00E-03	°C	rectangular	1.732050808	0.002	°C	1.0E+00	°C·°C^{-1}	0.002	estimation
Interpolation	-0.065	0.00E+00	µs	Gaussian	2	0.000	s	6.8E+05	°C·s^{-1}	0.000	not applicable
Instability of measured environment	0.003	3.00E-03	°C	rectangular	1.732050808	0.002	°C	1.0E+00	°C·°C^{-1}	0.002	estimation
Inhomogeneity of measured environment	0.005	5.00E-03	°C	rectangular	1.732050808	0.003	°C	1.0E+00	°C·°C^{-1}	0.003	estimation
Microphone Characteristic	0	2.00E-03	°C	rectangular	1.732050808	0.001	°C	1.0E+00	°C·°C^{-1}	0.001	estimation
Acoustic noise	0.001	1.00E-03	°C	rectangular	1.732050808	0.001	°C	1.0E+00	°C·°C^{-1}	0.001	estimation
t_{90} temperature measurement	0.007	7.00E-03	°C	rectangular	1.732050808	0.004	°C	1.0E+00	°C·°C^{-1}	0.004	measurement
Other influences	0.001	1.00E-03	°C	rectangular	1.732050808	0.001	°C	1.0E+00	°C·°C^{-1}	0.001	estimation

Uncertainty source	Value	z_{max}	Dimension	Distribution	k	u_x		Sensitivity	Dimension	u_x for $k=1$, °C	Source
A type uncertainty	0.0	0.0	µs	Gaussian	1	0.001	µs	0.034	°C/µs	0.000	data
								Total uncertainty		0.022	
								Expansion coefficient		2	
Temperature, K	353.495										
Temperature, °C	80.345					*Total rounded expanded uncertainty*, °C				0.043	

Table 14: Measurement uncertainty budget for the nominal temperature of 100 °C

Uncertainty source	Value	z_{max}	Dimension	Distribution	k	u_x		Sensitivity	Dimension	u_x for k=1, °C	Source
Molar mass from gas composition	0.0399479	3.99E-07	g·mol^{-1}	rectangular	1.732050808	0.0000	g·mol^{-1}	8.8E+03	°C·mol·g^{-1}	0.002	gas datasheet
Length of sound path determination	170.88	1.00E-02	mm	Gaussian	2	0.005	mm	4.1E+00	°C·mm^{-1}	0.021	measurement
thermal expansion	0.00056	5.00E-08	m	rectangular	1.732050808	0.000	m	4.1E+03	°C·m^{-1}	0.000	calculation
Heat capacity ratio	1.667	1.67E-05	-	rectangular	1.732050808	0.00001	-	2.1E+02	°C	0.002	gas datasheet
Molar gas constant	8.314462618	0.00E+00	J·mol^{-1}·K^{-1}	rectangular	1.732050808	0.0000	J·mol^{-1}·K^{-1}	4.2E+01	°C·J^{-1}·mol·K	0.000	fixed value, zero uncertainty
Immersion of sensor	0.005	5.00E-03	°C	rectangular	1.732050808	0.003	°C	1.0E+00	°C·°C^{-1}	0.003	estimation
Pressure measurement	100.000	8.00E-03	kPa	Gaussian	2	0.004	kPa	0.0E+00	°C·kPa^{-1}	0.000	measurement
Resolution of τ	12.5	1.25E+01	ns	rectangular	1.732050808	0.000	s	7.2E+05	°C·s^{-1}	0.005	observation and calculation
Time base (short term drift od oscillocope)	1	1.00E+00	ns	rectangular	1.732050808	0.000	s	7.2E+05	°C·s^{-1}	0.000	device specification
Short term drift of the generator	1	1.00E+00	µHz	rectangular	1.732050808	0.577	µHz	0.0E+00	°C·µHz^{-1}	0.000	estimation
Parasitic voltage noise	0	4.00E-03	°C	rectangular	1.732050808	0.002	°C	1.0E+00	°C·°C^{-1}	0.002	estimation
Interpolation	0.756	0.00E+00	µs	Gaussian	2	0.000	s	7.2E+05	°C·s^{-1}	0.000	not applicable
Instability of measured environment	0.003	3.00E-03	°C	rectangular	1.732050808	0.002	°C	1.0E+00	°C·°C^{-1}	0.002	estimation
Inhomogeneity of measured environment	0.005	5.00E-03	°C	rectangular	1.732050808	0.003	°C	1.0E+00	°C·°C^{-1}	0.003	estimation
Microphone Characteristic	0	2.00E-03	°C	rectangular	1.732050808	0.001	°C	1.0E+00	°C·°C^{-1}	0.001	estimation
Acoustic noise	0.001	1.00E-03	°C	rectangular	1.732050808	0.001	°C	1.0E+00	°C·°C^{-1}	0.001	estimation
t_{90} temperature measurement	0.008	8.00E-03	°C	rectangular	1.732050808	0.005	°C	1.0E+00	°C·°C^{-1}	0.005	measurement
Other influences	0.001	1.00E-03	°C	rectangular	1.732050808	0.001	°C	1.0E+00	°C·°C^{-1}	0.001	estimation
Uncertainty source	Value	z_{max}	Dimension	Distribution	k	u_x		Sensitivity	Dimension	u_x for k=1, °C	Source
A type uncertainty	0.0	0.0	µs	Gaussian	1	0.000	µs	0.034	°C/µs	0.000	data
								Total uncertainty		0.023	
Temperature, K	372.554							*Expansion coefficient*		2	
Temperature, °C	99.404					*Total rounded expanded uncertainty*, °C				0.045	

Table 15: Measurement uncertainty budget for the nominal temperature of 120 °C

Uncertainty source	Value	z_{max}	Dimension	Distribution	k	u_x		Sensitivity	Dimension	u_x for k=1, °C	Source
Molar mass from gas composition	0.0399479	3.99E-07	g·mol^{-1}	rectangular	1.732050808	0.0000	g·mol^{-1}	9.2E+03	°C·mol·g^{-1}	0.002	gas datasheet
Length of sound path determination	170.88	1.00E-02	mm	Gaussian	2	0.005	mm	4.3E+00	°C·mm^{-1}	0.022	measurement
thermal expansion	0.00056	5.00E-08	m	rectangular	1.732050808	0.000	m	4.3E+03	°C·m^{-1}	0.000	calculation
Heat capacity ratio	1.667	1.67E-05	-	rectangular	1.732050808	0.00001	-	2.2E+02	°C	0.002	gas datasheet
Molar gas constant	8.314462618	0.00E+00	J·mol^{-1}·K^{-1}	rectangular	1.732050808	0.0000	J·mol^{-1}·K^{-1}	4.4E+01	°C·J^{-1}·mol·K	0.000	fixed value, zero uncertainty
Immersion of sensor	0.005	5.00E-03	°C	rectangular	1.732050808	0.003	°C	1.0E+00	°C·°C^{-1}	0.003	estimation
Pressure measurement	100.000	8.00E-03	kPa	Gaussian	2	0.004	kPa	0.0E+00	°C·kPa^{-1}	0.000	measurement
Resolution of τ	12.5	1.25E+01	ns	rectangular	1.732050808	0.000	s	7.7E+05	°C·s^{-1}	0.006	observation and calculation
Time base (short term drift od oscillocope)	1	1.00E+00	ns	rectangular	1.732050808	0.000	s	7.7E+05	°C·s^{-1}	0.000	device specification
Short term drift of the generator	1	1.00E+00	µHz	rectangular	1.732050808	0.577	µHz	0.0E+00	°C·µHz^{-1}	0.000	estimation
Parasitic voltage noise	0	4.00E-03	°C	rectangular	1.732050808	0.002	°C	1.0E+00	°C·°C^{-1}	0.002	estimation
Interpolation	0.125	0.00E+00	µs	Gaussian	2	0.000	s	7.7E+05	°C·s^{-1}	0.000	not applicable
Instability of measured environment	0.003	3.00E-03	°C	rectangular	1.732050808	0.002	°C	1.0E+00	°C·°C^{-1}	0.002	estimation
Inhomogeneity of measured environment	0.005	5.00E-03	°C	rectangular	1.732050808	0.003	°C	1.0E+00	°C·°C^{-1}	0.003	estimation
Microphone Characteristic	0	2.00E-03	°C	rectangular	1.732050808	0.001	°C	1.0E+00	°C·°C^{-1}	0.001	estimation
Acoustic noise	0.001	1.00E-03	°C	rectangular	1.732050808	0.001	°C	1.0E+00	°C·°C^{-1}	0.001	estimation
t_{90} temperature measurement	0.010	1.00E-02	°C	rectangular	1.732050808	0.006	°C	1.0E+00	°C·°C^{-1}	0.006	measurement
Other influences	0.001	1.00E-03	°C	rectangular	1.732050808	0.001	°C	1.0E+00	°C·°C^{-1}	0.001	estimation
Uncertainty source	Value	z_{max}	Dimension	Distribution	k	u_x		Sensitivity	Dimension	u_x for k=1, °C	Source
A type uncertainty	0.0	0.0	µs	Gaussian	1	0.000	µs	0.033	°C/µs	0.000	data
								Total uncertainty		0.024	
Temperature, K	392.784							*Expansion coefficient*		2	
Temperature, °C	119.634					*Total rounded expanded uncertainty*, °C				0.047	

Table 16: Measurement uncertainty budget for the nominal temperature of 140 °C

Uncertainty source	Value	z_{max}	Dimension	Distribution	k	u_x		Sensitivity	Dimension	u_x for k=1, °C	Source
Molar mass from gas composition	0.0399479	3.99E-07	g·mol^{-1}	rectangular	1.732050808	0.0000	g·mol^{-1}	9.6E+03	°C·mol·g^{-1}	0.002	gas datasheet
Length of sound path determination	170.88	1.00E-02	mm	Gaussian	2	0.005	mm	4.5E+00	°C·mm^{-1}	0.022	measurement
thermal expansion	0.00056	5.00E-08	m	rectangular	1.732050808	0.000	m	4.5E+03	°C·m^{-1}	0.000	calculation
Heat capacity ratio	1.667	1.67E-05	-	rectangular	1.732050808	0.00001	-	2.3E+02	°C	0.002	gas datasheet
Molar gas constant	8.314462618	0.00E+00	J·mol^{-1}·K^{-1}	rectangular	1.732050808	0.0000	J·mol^{-1}·K^{-1}	4.6E+01	°C·J^{-1}·mol·K	0.000	fixed value, zero uncertainty
Immersion of sensor	0.005	5.00E-03	°C	rectangular	1.732050808	0.003	°C	1.0E+00	°C·°C^{-1}	0.003	estimation
Pressure measurement	100.000	8.00E-03	kPa	Gaussian	2	0.004	kPa	0.0E+00	°C·kPa^{-1}	0.000	measurement
Resolution of τ	12.5	1.25E+01	ns	rectangular	1.732050808	0.000	s	8.2E+05	°C·s^{-1}	0.006	observation and calculation
Time base (short term drift od oscillocope)	1	1.00E+00	ns	rectangular	1.732050808	0.000	s	8.2E+05	°C·s^{-1}	0.000	device specification
Short term drift of the generator	1	1.00E+00	µHz	rectangular	1.732050808	0.577	µHz	0.0E+00	°C·µHz^{-1}	0.000	estimation
Parasitic voltage noise	0	4.00E-03	°C	rectangular	1.732050808	0.002	°C	1.0E+00	°C·°C^{-1}	0.002	estimation
Interpolation	-0.375	0.00E+00	µs	Gaussian	2	0.000	s	8.2E+05	°C·s^{-1}	0.000	not applicable
Instability of measured environment	0.003	3.00E-03	°C	rectangular	1.732050808	0.002	°C	1.0E+00	°C·°C^{-1}	0.002	estimation
Inhomogeneity of measured environment	0.005	5.00E-03	°C	rectangular	1.732050808	0.003	°C	1.0E+00	°C·°C^{-1}	0.003	estimation
Microphone Characteristic	0	2.00E-03	°C	rectangular	1.732050808	0.001	°C	1.0E+00	°C·°C^{-1}	0.001	estimation
Acoustic noise	0.001	1.00E-03	°C	rectangular	1.732050808	0.001	°C	1.0E+00	°C·°C^{-1}	0.001	estimation
t_{90} temperature measurement	0.012	1.20E-02	°C	rectangular	1.732050808	0.007	°C	1.0E+00	°C·°C^{-1}	0.007	measurement
Other influences	0.001	1.00E-03	°C	rectangular	1.732050808	0.001	°C	1.0E+00	°C·°C^{-1}	0.001	estimation
Uncertainty source	Value	z_{max}	Dimension	Distribution	k	u_x		Sensitivity	Dimension	u_x for k=1, °C	Source
A type uncertainty	0.0	0.0	µs	Gaussian	1	0.000	µs	0.032	°C/µs	0.000	data
								Total uncertainty		0.025	
Temperature, K	413.347							*Expansion coefficient*		2	
Temperature, °C	140.197					*Total rounded expanded uncertainty*, °C				0.050	

Table 17: Measurement uncertainty budget for the nominal temperature of 160 °C

Uncertainty source	Value	z_{max}	Dimension	Distribution	k	u_x		Sensitivity	Dimension	u_x for k=1, °C	Source
Molar mass from gas composition	0.0399479	3.99E-07	g·mol^{-1}	rectangular	1.732050808	0.0000	g·mol^{-1}	1.0E+04	°C·mol·g^{-1}	0.002	gas datasheet
Length of sound path determination	170.88	1.00E-02	mm	Gaussian	2	0.005	mm	4.7E+00	°C·mm^{-1}	0.023	measurement
thermal expansion	0.00056	5.00E-08	m	rectangular	1.732050808	0.000	m	4.7E+03	°C·m^{-1}	0.000	calculation
Heat capacity ratio	1.667	1.67E-05	-	rectangular	1.732050808	0.00001	-	2.4E+02	°C	0.002	gas datasheet
Molar gas constant	8.314462618	0.00E+00	J·mol^{-1}·K^{-1}	rectangular	1.732050808	0.0000	J·mol^{-1}·K^{-1}	4.8E+01	°C·J^{-1}·mol·K	0.000	fixed value, zero uncertainty
Immersion of sensor	0.005	5.00E-03	°C	rectangular	1.732050808	0.003	°C	1.0E+00	°C·°C^{-1}	0.003	estimation
Pressure measurement	100.000	8.00E-03	kPa	Gaussian	2	0.004	kPa	0.0E+00	°C·kPa^{-1}	0.000	measurement
Resolution of τ	12.5	1.25E+01	ns	rectangular	1.732050808	0.000	s	8.7E+05	°C·s^{-1}	0.006	observation and calculation
Time base (short term drift od oscillocope)	1	1.00E+00	ns	rectangular	1.732050808	0.000	s	8.7E+05	°C·s^{-1}	0.001	device specification
Short term drift of the generator	1	1.00E+00	µHz	rectangular	1.732050808	0.577	µHz	0.0E+00	°C·µHz^{-1}	0.000	estimation
Parasitic voltage noise	0	4.00E-03	°C	rectangular	1.732050808	0.002	°C	1.0E+00	°C·°C^{-1}	0.002	estimation
Interpolation	-0.354	0.00E+00	µs	Gaussian	2	0.000	s	8.7E+05	°C·s^{-1}	0.000	not applicable
Instability of measured environment	0.003	3.00E-03	°C	rectangular	1.732050808	0.002	°C	1.0E+00	°C·°C^{-1}	0.002	estimation
Inhomogeneity of measured environment	0.005	5.00E-03	°C	rectangular	1.732050808	0.003	°C	1.0E+00	°C·°C^{-1}	0.003	estimation
Microphone Characteristic	0	2.00E-03	°C	rectangular	1.732050808	0.001	°C	1.0E+00	°C·°C^{-1}	0.001	estimation
Acoustic noise	0.001	1.00E-03	°C	rectangular	1.732050808	0.001	°C	1.0E+00	°C·°C^{-1}	0.001	estimation
t_{90} temperature measurement	0.014	1.40E-02	°C	rectangular	1.732050808	0.008	°C	1.0E+00	°C·°C^{-1}	0.008	measurement
Other influences	0.001	1.00E-03	°C	rectangular	1.732050808	0.001	°C	1.0E+00	°C·°C^{-1}	0.001	estimation

Uncertainty source	Value	z_{max}	Dimension	Distribution	k	u_x		Sensitivity	Dimension	u_x for k=1, °C	Source
A type uncertainty	0.0	0.0	µs	Gaussian	1	0.001	µs	0.032	°C/µs	0.000	data
								Total uncertainty		0.026	
Temperature, K	433.215							*Expansion coefficient*		2	
Temperature, °C	160.065					*Total rounded expanded uncertainty*, °C				0.052	

Table 18: Measurement uncertainty budget for the nominal temperature of 180 °C

Uncertainty source	Value	z_{max}	Dimension	Distribution	k	u_x		Sensitivity	Dimension	u_x for k=1, °C	Source
Molar mass from gas composition	0.0399479	3.99E-07	g·mol^{-1}	rectangular	1.732050808	0.0000	g·mol^{-1}	1.0E+04	°C·mol·g^{-1}	0.002	gas datasheet
Length of sound path determination	170.88	1.00E-02	mm	Gaussian	2	0.005	mm	4.9E+00	°C·mm^{-1}	0.024	measurement
thermal expansion	0.00056	5.00E-08	m	rectangular	1.732050808	0.000	m	4.9E+03	°C·m^{-1}	0.000	calculation
Heat capacity ratio	1.667	1.67E-05	-	rectangular	1.732050808	0.00001	-	2.5E+02	°C	0.002	gas datasheet
Molar gas constant	8.314462618	0.00E+00	J·mol^{-1}·K^{-1}	rectangular	1.732050808	0.0000	J·mol^{-1}·K^{-1}	5.0E+01	°C·J^{-1}·mol·K	0.000	fixed value, zero uncertainty
Immersion of sensor	0.005	5.00E-03	°C	rectangular	1.732050808	0.003	°C	1.0E+00	°C·°C^{-1}	0.003	estimation
Pressure measurement	100.000	8.00E-03	kPa	Gaussian	2	0.004	kPa	0.0E+00	°C·kPa^{-1}	0.000	measurement
Resolution of τ	12.5	1.25E+01	ns	rectangular	1.732050808	0.000	s	9.2E+05	°C·s^{-1}	0.007	observation and calculation
Time base (short term drift od oscillocope)	1	1.00E+00	ns	rectangular	1.732050808	0.000	s	9.2E+05	°C·s^{-1}	0.001	device specification
Short term drift of the generator	1	1.00E+00	µHz	rectangular	1.732050808	0.577	µHz	0.0E+00	°C·µHz^{-1}	0.000	estimation
Parasitic voltage noise	0	4.00E-03	°C	rectangular	1.732050808	0.002	°C	1.0E+00	°C·°C^{-1}	0.002	estimation
Interpolation	0.269	0.00E+00	µs	Gaussian	2	0.000	s	9.2E+05	°C·s^{-1}	0.000	not applicable
Instability of measured environment	0.003	3.00E-03	°C	rectangular	1.732050808	0.002	°C	1.0E+00	°C·°C^{-1}	0.002	estimation
Inhomogeneity of measured environment	0.005	5.00E-03	°C	rectangular	1.732050808	0.003	°C	1.0E+00	°C·°C^{-1}	0.003	estimation
Microphone Characteristic	0	2.00E-03	°C	rectangular	1.732050808	0.001	°C	1.0E+00	°C·°C^{-1}	0.001	estimation
Acoustic noise	0.001	1.00E-03	°C	rectangular	1.732050808	0.001	°C	1.0E+00	°C·°C^{-1}	0.001	estimation
t_{90} temperature measurement	0.016	1.60E-02	°C	rectangular	1.732050808	0.009	°C	1.0E+00	°C·°C^{-1}	0.009	measurement
Other influences	0.001	1.00E-03	°C	rectangular	1.732050808	0.001	°C	1.0E+00	°C·°C^{-1}	0.001	estimation
Uncertainty source	Value	z_{max}	Dimension	Distribution	k	u_x		Sensitivity	Dimension	u_x for k=1, °C	Source
A type uncertainty	0.0	0.0	µs	Gaussian	1	0.001	µs	0.031	°C/µs	0.000	data
								Total uncertainty		0.028	
Temperature, K	453.849							*Expansion coefficient*		2	
Temperature, °C	180.699					*Total rounded expanded uncertainty*, °C				0.055	

Table 19: Measurement uncertainty budget for the nominal temperature of 200 °C

Uncertainty source	Value	z_{max}	Dimension	Distribution	k	u_x		Sensitivity	Dimension	u_x for k=1, °C	Source
Molar mass from gas composition	0.0399479	3.99E-07	g·mol^{-1}	rectangular	1.732050808	0.0000	g·mol^{-1}	1.1E+04	°C·mol·g^{-1}	0.003	gas datasheet
Length of sound path determination	170.88	1.00E-02	mm	Gaussian	2	0.005	mm	5.2E+00	°C·mm^{-1}	0.026	measurement
thermal expansion	0.00056	5.00E-08	m	rectangular	1.732050808	0.000	m	5.2E+03	°C·m^{-1}	0.000	calculation
Heat capacity ratio	1.667	1.67E-05	-	rectangular	1.732050808	0.00001	-	2.7E+02	°C	0.003	gas datasheet
Molar gas constant	8.314462618	0.00E+00	J·mol^{-1}·K^{-1}	rectangular	1.732050808	0.0000	J·mol^{-1}·K^{-1}	5.3E+01	°C·J^{-1}·mol·K	0.000	fixed value, zero uncertainty
Immersion of sensor	0.005	5.00E-03	°C	rectangular	1.732050808	0.003	°C	1.0E+00	°C·°C^{-1}	0.003	estimation
Pressure measurement	100.000	8.00E-03	kPa	Gaussian	2	0.004	kPa	0.0E+00	°C·kPa^{-1}	0.000	measurement
Resolution of τ	12.5	1.25E+01	ns	rectangular	1.732050808	0.000	s	1.0E+06	°C·s^{-1}	0.007	observation and calculation
Time base (short term drift od oscillocope)	1	1.00E+00	ns	rectangular	1.732050808	0.000	s	1.0E+06	°C·s^{-1}	0.001	device specification
Short term drift of the generator	1	1.00E+00	µHz	rectangular	1.732050808	0.577	µHz	0.0E+00	°C·µHz^{-1}	0.000	estimation
Parasitic voltage noise	0	4.00E-03	°C	rectangular	1.732050808	0.002	°C	1.0E+00	°C·°C^{-1}	0.002	estimation
Interpolation	-12.217	0.00E+00	µs	Gaussian	2	0.000	s	1.0E+06	°C·s^{-1}	0.000	not applicable
Instability of measured environment	0.003	3.00E-03	°C	rectangular	1.732050808	0.002	°C	1.0E+00	°C·°C^{-1}	0.002	estimation
Inhomogeneity of measured environment	0.005	5.00E-03	°C	rectangular	1.732050808	0.003	°C	1.0E+00	°C·°C^{-1}	0.003	estimation
Microphone Characteristic	0	2.00E-03	°C	rectangular	1.732050808	0.001	°C	1.0E+00	°C·°C^{-1}	0.001	estimation
Acoustic noise	0.001	1.00E-03	°C	rectangular	1.732050808	0.001	°C	1.0E+00	°C·°C^{-1}	0.001	estimation
t_{90} temperature measurement	0.018	1.80E-02	°C	rectangular	1.732050808	0.010	°C	1.0E+00	°C·°C^{-1}	0.010	measurement
Other influences	0.001	1.00E-03	°C	rectangular	1.732050808	0.001	°C	1.0E+00	°C·°C^{-1}	0.001	estimation
Uncertainty source	Value	z_{max}	Dimension	Distribution	k	u_x		Sensitivity	Dimension	u_x for k=1, °C	Source
A type uncertainty	0.0	0.0	µs	Gaussian	1	0.000	µs	0.030	°C/µs	0.000	data
								Total uncertainty		0.030	
Temperature, K	473.818							*Expansion coefficient*		2	
Temperature, °C	200.668					*Total rounded expanded uncertainty*, °C				0.059	

Table 20: Measurement uncertainty budget for the nominal temperature of 220 °C

Uncertainty source	Value	z_{max}	Dimension	Distribution	k	u_x		Sensitivity	Dimension	u_x for k=1, °C	Source
Molar mass from gas composition	0.0399479	3.99E-07	g·mol^{-1}	rectangular	1.732050808	0.0000	g·mol^{-1}	9.7E+03	°C·mol·g^{-1}	0.002	gas datasheet
Length of sound path determination	170.88	1.00E-02	mm	Gaussian	2	0.005	mm	4.5E+00	°C·mm^{-1}	0.023	measurement
thermal expansion	0.00056	5.00E-08	m	rectangular	1.732050808	0.000	m	4.5E+03	°C·m^{-1}	0.000	calculation
Heat capacity ratio	1.667	1.67E-05	-	rectangular	1.732050808	0.00001	-	2.3E+02	°C	0.002	gas datasheet
Molar gas constant	8.314462618	0.00E+00	J·mol^{-1}·K^{-1}	rectangular	1.732050808	0.0000	J·mol^{-1}·K^{-1}	4.7E+01	°C·J^{-1}·mol·K	0.000	fixed value, zero uncertainty
Immersion of sensor	0.005	5.00E-03	°C	rectangular	1.732050808	0.003	°C	1.0E+00	°C·°C^{-1}	0.003	estimation
Pressure measurement	100.000	8.00E-03	kPa	Gaussian	2	0.004	kPa	0.0E+00	°C·kPa^{-1}	0.000	measurement
Resolution of τ	12.5	1.25E+01	ns	rectangular	1.732050808	0.000	s	8.3E+05	°C·s^{-1}	0.006	observation and calculation
Time base (short term drift od oscillocope)	1	1.00E+00	ns	rectangular	1.732050808	0.000	s	8.3E+05	°C·s^{-1}	0.000	device specification
Short term drift of the generator	1	1.00E+00	µHz	rectangular	1.732050808	0.577	µHz	0.0E+00	°C·µHz^{-1}	0.000	estimation
Parasitic voltage noise	0	4.00E-03	°C	rectangular	1.732050808	0.002	°C	1.0E+00	°C·°C^{-1}	0.002	estimation
Interpolation	66.748	0.00E+00	µs	Gaussian	2	0.000	s	8.3E+05	°C·s^{-1}	0.000	not applicable
Instability of measured environment	0.003	3.00E-03	°C	rectangular	1.732050808	0.002	°C	1.0E+00	°C·°C^{-1}	0.002	estimation
Inhomogeneity of measured environment	0.005	5.00E-03	°C	rectangular	1.732050808	0.003	°C	1.0E+00	°C·°C^{-1}	0.003	estimation
Microphone Characteristic	0	2.00E-03	°C	rectangular	1.732050808	0.001	°C	1.0E+00	°C·°C^{-1}	0.001	estimation
Acoustic noise	0.001	1.00E-03	°C	rectangular	1.732050808	0.001	°C	1.0E+00	°C·°C^{-1}	0.001	estimation
t_{90} temperature measurement	0.020	2.00E-02	°C	rectangular	1.732050808	0.012	°C	1.0E+00	°C·°C^{-1}	0.012	measurement
Other influences	0.001	1.00E-03	°C	rectangular	1.732050808	0.001	°C	1.0E+00	°C·°C^{-1}	0.001	estimation
Uncertainty source	Value	z_{max}	Dimension	Distribution	k	u_x		Sensitivity	Dimension	u_x for k=1, °C	Source
A type uncertainty	0.0	0.0	µs	Gaussian	1	0.000	µs	0.032	°C/µs	0.000	data
								Total uncertainty		0.027	
Temperature, K	492.690							*Expansion coefficient*		2	
Temperature, °C	219.540					*Total rounded expanded uncertainty*, °C				0.054	